Ageing, microstructure and magneto-structural relations in room temperature magnetocaloric materials

Madhu Chennabasappa

Numero ordre these : 4970

THÈSE

PRÉSENTÉE A

L'UNIVERSITÉ BORDEAUX 1

ÉCOLE DOCTORALE DES SCIENCES CHIMIQUES

Par Madhu CHENNABASAPPA

POUR OBTENIR LE GRADE DE

DOCTEUR

SPÉCIALITÉ : Physico-Chimie de la Matière Condensée

Ageing, microstructure and magneto-structural relations in room temperature magnetocaloric materials

Directeur de recherche : M. Olivier TOULEMONDE et M. Bernard CHEVALIER

Soutenue le : 12 Décembre 2013

Après avis de :

M. HARDY, Vincent	Directeur de Recherche CNRS, CRISMAT, Caen	Rapporteur
M. ISNARD, Olivier	Professeur des Universités, Institut Néél, Grenoble	Rapporteur

Devant la commission d'examen formée de :

M. MAGLIONE, Mario	Directeur de Recherche CNRS, ICMCB, Bordeaux	Président
M. HARDY, Vincent	Directeur de Recherche CNRS, CRISMAT, Caen	Rapporteur
M. ISNARD, Olivier	Professeur des Universités, Institut Néél, Grenoble	Rapporteur
M. TAILHADES, Philippe	Chercheur, CIRIMAT-LCMIE, Toulouse	Examinateur
M. CHEVALIER, Bernard	Directeur de Recherche,CNRS Emérite, ICMCB, Bordeaux	Examinateur
M. TOULEMONDE, Olivier	Maître de Conférence, Bordeaux1, ICMCB, Bordeaux	Examinateur

Dedicated to

My Teachers, my Dad-Mom, my Family

Felicitating completing nearly three decades of contribution for their individual fields,

Dr Bernard CHEVALIER

Dr Claude DELMAS

Dr Jean-Claude GERNIER

Kannada Vachanas (sayings) of Veerashiva philosophers (Sharanas) of the 12th century:

ಕಳಬೇಡ, ಕೊಲಬೇಡ,	**Transliteration:**	**Translation:**
ಹುಸಿಯ ನುಡಿಯಲು ಬೇಡ,	**kaLabEDa kolabEDa,**	**Do not Steal, Do not kill**
ಮುನಿಯ ಬೇಡ,	**husiya nuDiyalu bEDa,**	**Do not speak a Lie**
ಅನ್ಯರಿಗೆ ಅಸಹ್ಯಪಡಬೇಡ.	**muniya bEDa,**	**Do not be Angry with any one**
ತನ್ನ ಬಣ್ಣಿಸಬೇಡ,	**anyarige asahyapaDabEDa.**	**Do not feel Disgust for others**
ಇದಿರ ಹಳಿಯಲು ಬೇಡ.	**tanna baNNisabEDa,**	**Do not indulge in Self-praise**
ಇದೇ ಅಂತರಂಗಶುದ್ಧಿ.	**idira haLiyalu bEDa.**	**Do not Humiliate any one**
ಇದೇ ಬಹಿರಂಗಶುದ್ಧಿ.	**idE aMtaraMgaSuddhi!**	**This is your Inward Purity**
ಇದೆ ನಮ್ಮ ಕೂಡಲಸಂಗನನೊಲಿಸುವ	**idE bahiraMgaSuddhi!**	**This is your outward Purity**
ಪರಿ.	**ide namma kUDalasaMgananolisuva pari.**	**This is the way to win the Lord Kudala Sangama!**

Table of contents

Chapter 5: General conclusion and perspectives

Chapter 6: Appendix, Remerciements

Résumé détaillé du manuscrit de thèse de Monsieur Madhu Chennabasappa, intitulé «**Ageing, microstrucutre and magneto-structural relations in room temperature magnétocaloric materials**», soutenue à l'Université de Bordeaux I le 12 décembre 2013.

Le travail de thèse de Madhu Chennabasappa est un travail expérimental en sciences des matériaux à l'interface entre la cristallochimie, la physique du solide et la corrosion de surface. Il aborde différents aspects allant des plus fondamentaux comme la synthèse, la caractérisation cristallochimique et la nature des transitions de phases de matériaux « oxydes » ou « intermétalliques » jusqu'aux plus applicatifs avec, l'étude et l'analyse des effets de vieillissement en milieux aqueux des surfaces exposées au liquide caloporteur et les conséquences sur les propriétés magnétocaloriques.

Le manuscrit a été construit de tel sorte que le cœur de chaque chapitre soit centré sur la présentation des résultats obtenus par famille de matériaux avec un état de l'art et une conclusion générale.

Chapitre 1 : Etat de l'art

Ce chapitre propose une vue d'ensemble de l'effet magnétocalorique et de son utilisation pour la réfrigération magnétique. Il est constitué d'une présentation de généralités sur l'effet magnétocalorique comprenant sa définition et un développement des aspects thermodynamiques qui lui sont propres. Puis, un historique est réalisé afin de surligner les avantages de la réfrigération magnétique et d'exposer les dispositifs actuels rencontrés à travers le monde en surlignant leurs performances. Finalement, un tour d'horizon des

matériaux connus à ce jour est présenté afin de situer la pertinence des choix d'études au regard de la performance escomptée des matériaux pour la réfrigération magnétique selon la nature chimique « oxyde » ou « intermétallique » des matériaux.

Chapitre 2 : Vieillissement de $Gd_6Co_{1.67}Si_3$ en milieu aqueux.

Ce chapitre est consacré à l'étude du comportement du composé $Gd_6Co_{1.67}Si_3$ en milieu aqueux en s'attachant aux modifications microstructurales dues au vieillissement dans des conditions proches de celle d'utilisation potentielles comme régénérateur. A l'aide de différentes techniques complémentaires d'analyses chimiques de surfaces (Microscopie électronique à balayage, spectroscopie Auger et spectroscopie de photoélectrons) et de diffraction de rayons X, il a été permis d'attribuer la dégradation du matériau à la formation d'une structure en « oignon » avec une couche SiO_x-Gd_2O_3 à la surface du matériau tandis que le cobalt est dissous dans l'eau dé-ionisée. Une réduction significative de la corrosion est obtenue par l'utilisation d'un milieu aqueux alcalin comme liquide caloporteur.

Il est à noter que le même type d'étude a été effectuée sur deux autres matériaux appartenant aux familles exposées aux chapitres 3 et 4 qui, même si elles sont moins complètes, ont permis de confirmer l'établissement de processus électrochimiques spontanées lors de la corrosion.

Chapitre 3 : Les Phases d'Heusler Ni-Cu-Mn-Ga

Ce chapitre est consacré aux phases $Ni_2Mn_{1-x}Cu_xGa$ et $Ni_2Mn_{0.75+d}Cu_{0.25}Ga$. Les substitutions consistent à rapprocher simultanément la transition structurale martensitique ($T_{M/A}$) et la transition ferromagnétique (T_C) vers la température ambiante afin de reproduire les effets

magnétocaloriques géants proposés dans la littérature. Une étude détaillée et systématique des propriétés magnétiques et structurales par diffraction de rayons X met en lumière leurs effets croisés avec les propriétés de mémoire de forme. L'étude de l'impact de la stœchiométrie cationique, de l'état massif ou pulvérulent du matériau, des traitements thermiques subis par le matériau sur les propriétés magnétocaloriques a permis une illustration spectaculaire du rôle de la microstructure.

Chapitre 4 : Les manganites $Pr_{1-x}Sr_xMnO_3$

Ce chapitre porte sur les composés $Pr_{1-x}Sr_xMnO_3$ avec $0.25 \leq x \leq 0.45$ qui présente une température d'ordre ferromagnétique autour de la température ambiante. C'est un système connu pour avoir un diagramme de phases complexe. En s'appuyant sur la diffraction de rayons X (laboratoire et synchrotron) et la diffraction de neutrons, des mesures AC et DC de la susceptibilité magnétique, le diagramme de phases a été complété avec l'observation d'un crossover Pnma-Imma dans la dépendance en x à température ambiante au voisinage de la transition d'ordre ferromagnétique et mais aussi en température pour x fixe. Les propriétés magnétocaloriques des phases ont alors été caratérisées.

General Introduction

Durability, the combination of performance and consistency, is the preliminary figure of merit for any device promising potential application. In this regard, it is always preferred to test the device or material for long and repeated reproducibility of the properties before launching into working model. This thesis is dedicated for one of such test on materials highlighted for use in *room temperature magnetic refrigeration* because magnetic refrigeration is promising in terms of energy consumption, safety and efficiency and more importantly is believed to be good replacements/alternatives for gas compressor based domestic refrigeration.

The magnetic refrigeration is based on the so-called magnetocaloric effect (MCE) referring to a temperature change of a material when it is exposed to a change of the applied magnetic field. Surely, there have been a lot of new materials put forward as potential for room temperature applications from different disciplines such as oxides, intermetallics. Leading to giant magnetocaloric materials such as $Gd_5Si_2Ge_2$, Heusler alloys through extensive material research. An attempt to give summary of the exciting science that evolved during course of these discoveries is made in the introduction chapter. The theoretical approaches that are recently proposed to distinguish first and second order transition and the related advances in theoretical treatment of entropy data are introduced. Progress on the prototypes and working materials towards realization of complete working unit is summarized in the end of this chapter.

One major concern that still needs to be addressed with magnetocaloric materials is the effect of heat transfer fluid on the chemical and physical stability of the material. There are very few efforts to explore the durability of these materials once put into functional units. We make an effort to study in detail the microstructural effect of the working fluid on the material with duration of exposure, often addressed as *ageing*. To move forward in the ageing direction we choose three different class of material: *Gd-based* $Gd_6Co_{1.67}Si_3$, *Heusler alloy* $Ni_2Mn_{0.75}Cu_{0.25}Ga$ and *perovskite oxide* $Pr_{0.66}Sr_{0.34}MnO_3$. These materials were subjected for the process of heat transport artificially and the resulting microstructural changes on surface of the material in relation with the changes in the magnetic properties are studied.

Chapter 2 is dedicated for detailed studies of ageing on $Gd_6Co_{1.67}Si_3$. The ageing on the samples were performed followed by microprobe, depth profile and X-ray photoelectron spectroscopy characterizations. Schematic picture of the process of corrosion resulting in oxide layer on surface has been proposed and explained based on spectroscopy studies with validation using spontaneous electrochemical oxidation. Few remedies to reduce the resulting corrosion is proposed and also demonstrated in case of $Gd_6Co_{1.67}Si_3$ by performing similar durability test under higher pH condition, in our case, using KOH as working solution. Based on the outcomes the spontaneous electrochemical reactions is claimed to be potentiostatic rather than the galvanostatic that was proposed in most of the previous reports.

In the chapter 3 to follow, we present the studies on one of the Heusler alloy (X_2YZ), $Ni_2Mn_{0.75}Cu_{0.25}Ga$ derived from Ni_2MnGa by intentionally replacing Mn by Cu in order to merge low temperature T_M (martensitic transition- structural) and high temperature T_C (magnetic transition). Interestingly, this result in shift of merged T_C to near room temperature characterized with high entropy change. In literature the "*magneto-crystalline*" transition has been highlighted to be responsible for the so called "*giant magnetocaloric effect*" observed in the compound. In this chapter, the composition $Ni_2Mn_{0.75}Cu_{0.25}Ga$ is readdressed for its reproducibility and criticality of synthesis condition with focus mainly on manganese concentration and its effect on observed physical properties. As it is believed the so obtained magnetism has been accounted to contribution from Mn along with negligible contribution from Ni. Even though the compound $Ni_2Mn_{0.75}Cu_{0.25}Ga$ was studied extensively by very few groups, the structural detail of this compound is still not addressed convincingly. We make an attempt to solve the nuclear structure, through neutron diffraction experiments. Based on the outcomes we also propose the model for possible mixing of Cu which should preferentially occupying X site than the proposed classical Cu occupying Y site resulting in $Ni_{2-x}Mn_{1-y}Cu_xNi_yGa$ with x and y=0.25 . Heusler alloys are also known for their "*shape-memory effect*", the property known for the large lattice contraction-expansion near their structural transition – giving rise to *elastic effect*. So it is also interesting to investigate the effect of microstructure on physical properties. We have demonstrated the effect of grain size, shape on the observed magnetic properties in some of these compounds. Considering Heusler alloys to

be much economical and exhibit high entropy change impacting towards good candidate for magnetocaloric refrigeration, ageing is performed on one of the compositions. Initial glimpse of the ageing is presented with the promise of long period durability compared to other magnetocaloric material is presented in the final part of the chapter. However, in these materials the narrow temperature span (narrow ΔS) due to first order transition remains a concern as it influences the relative cooling power (RCP) which is one of the major MCE figures of merit. Interestingly, as shown for *Gd-based* $Gd_6Co_{1.67}Si_3$ material, the ageing process is chemically selective but here with Ni and Cu remaining stable.

Oxide based materials have often been preferred in terms of large scale production, stability and reproducibility making them one of the favorites towards applications/technological transfer. Perovskite oxide manganite, $Pr_{1-x}Sr_xMnO_3$ within the limit $0.25<x<0.45$ inherit metal to insulator transition along ferromagnet to paramagnetic transition hence known to be metallic-ferromagnet. Interestingly, they exhibit the magnetic transition around room temperature making them interesting for MCE. Compositions with in the regime shows reasonable magnetocaloric properties and few have been successfully tested by implanting with in prototypes. Such facts encourage us to test them for their sustainability under the influence of the working fluid. However, contrary reports on magnetic entropy reported with in this interesting region prompt us to first define better candidate – one with higher entropy change near room temperature. Such a study is depicted on chapter 4. For which we synthesis several compositions with in the limit and present the observed entropy change against the composition. In the literature there exists detailed nuclear and magnetic phase diagram over temperature for rest of the limits for the $Pr_{1-x}Sr_xMnO_3$ system (i.e., $0<x<0.25$ and $0.45<x<1$ – the antiferromagnet insulators). But not for metallic-ferromagnet region ($0.25<x<0.45$) which is indeed more interesting for room temperature magnetocaloric effect. This has been addressed in detail with proposed nuclear and magnetic phase diagram based on the nuclear diffraction experiments. During the ageing test, the electrochemical stability of $Pr_{0.66}Sr_{0.34}MnO_3$ is shown and the highlighted carbone shell is understood considering electrocatalytic reduction of CO_2 into CH_4 at the manganite surface.

Chapter 1

Advances in Magnetocaloric Effect, Magnetocaloric Materials towards realization of room temperature magnetic refrigeration - a general introduction

1.1. Introduction:

Realization of magnetocaloric refrigeration involves contribution from several interdisciplinary such as material science, numerical modeling (thermodynamic, magnetic field distribution …), device engineering, and so on. Initial phase of the chapter serves as very brief introduction to the history and developments of refrigeration in general and contributions from various fields towards realization of efficient magnetocaloric refrigerator. Following this is an introduction to thermodynamics of MCE, where in the differences between the observed transition and related properties are explained. Most of the potential Magnetocaloric Materials (MCM) from different class of materials that have been put forward by several pioneers in the field focusing room temperature application is summarized. In later stage of the chapter, the technical reasons and efforts made towards realization of a completely functioning cooling unit in the form of prototypes are briefed. Before conclusion, the aim and the approach of the thesis are proposed.

1.1.1. Brief history of refrigeration:

Even though refrigeration has become very part of household, industry and cryogenics in recent days, the history of refrigeration goes back to ages. First time small amount of ice was artificially created by William Cullen (1756), at University of Glasgow by creating partial vacuum in diethyl ether container. Soon in 1758 Benjamin Franklin and John Hadler at Cambridge University confirmed the evaporation of highly volatile liquids could be used to drive down the temperature of an object. First refrigerator based on vapor-compressor refrigeration cycle concept was designed by Oliver Evans (1805). Almost two century (1820) back the first refrigeration was demonstrated by Michael Faraday who liquefied ammonia using high pressure and low temperatures. Jacob Perkins built the first practical refrigerating machine in 1834 which used ether in a vapor compression cycle. Refrigerators with toxic gases such as ammonia, methyl chloride, methyl formate and sulfur dioxide working as refrigerants were put into operation leading to some fatal accidents. After several revision and improvements refrigerators, refrigerants safe enough to be working in the household came to existence in late 1920s. Where in synthetic refrigerants based on chlorofluorocarbon (CFC) followed by hydro chlorofluorocarbon (HCFC) and hydro fluorocarbon (HFC) were used as refrigerants. Even though these were less harmful compared to their predecessors in terms of safety. They were later diagnosed to be cause for depleting atmospheric ozone layer, a natural

protective layer against harmful solar ultraviolet radiations. Vapor-compression cycle which is basis for the gas compressor refrigerators used in most of the present household refrigerators is displayed in Figure 1 (right).

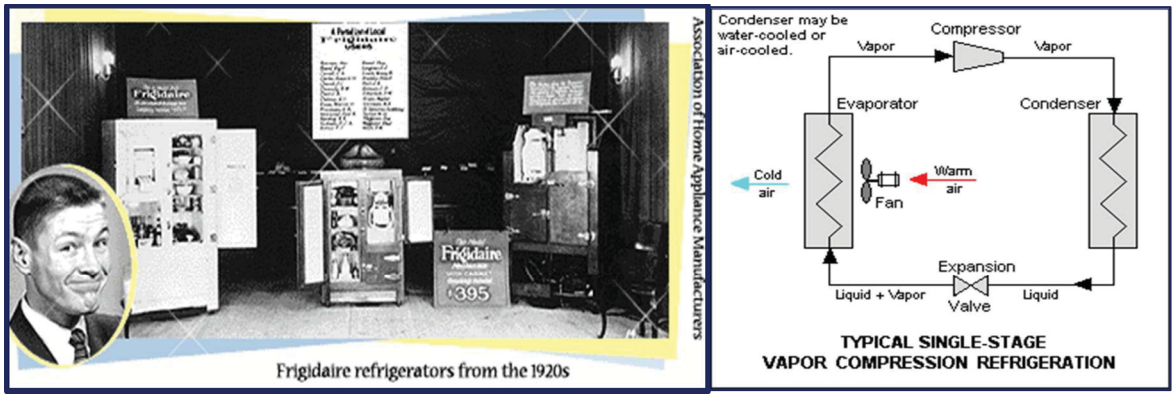

Figure 1 : Example of early refrigeration systems, left: One of the oldest commercial promotion of Frigidaire refrigerators (http://www.keepitcool.com/history_of_the_refrigerator2.htm). Right: schematic representation of working vapor-compression refrigeration system.

The modern era belongs to environment friendly material research, there have been dedicated efforts in this direction in several field such as sustainable energy solar cells, Solid oxide fuel cells (SOFC), lithium-ion batteries, lead free relaxors, thermoelectrics and so on. One such interesting field is the environmentally clean and energy efficient refrigeration around ambient temperature for domestic application based on magnetocaloric effect, an effect which will be introduced in detail in the following sections. This solid-state caloric cooling was already proposed to achieve ultra-low cryogenic temperatures of mK [1, 2].

1.1.2. Magnetocaloric effect and magnetic refrigeration:

Change in temperature of material near its magnetic or/and structural transition termed as *MagnetoCaloric Effect* (MCE) is making its way for future cooling devices. Most of the literature highlight MCE to be first observed by Emil Warburg in 1881 [3]. However, recent reinvestigations into the history have revealed the fact that the effect was discovered and introduced for first time by Pierre Weiss and Auguste Piccard in 1917 [4, 5].

The particular change of temperature can be utilized in cooling defined space without any involvement of gas or compressors, with lowered power requirements and hence their potentiality to replace gas compression based household refrigeration/cooling systems. The materials inheriting the property have been annotated as *MagnetoCaloric Materials* (MCM). The coexistence of both structural and magnetic transitions – *magnetostructural* - in

particular has helped in observing so called the giant magnetocaloric effect. The classical definition for the magnetocaloric is often stated as,

"A temperature change of a magnetic material near its magnetic transition under an applied magnetic field".

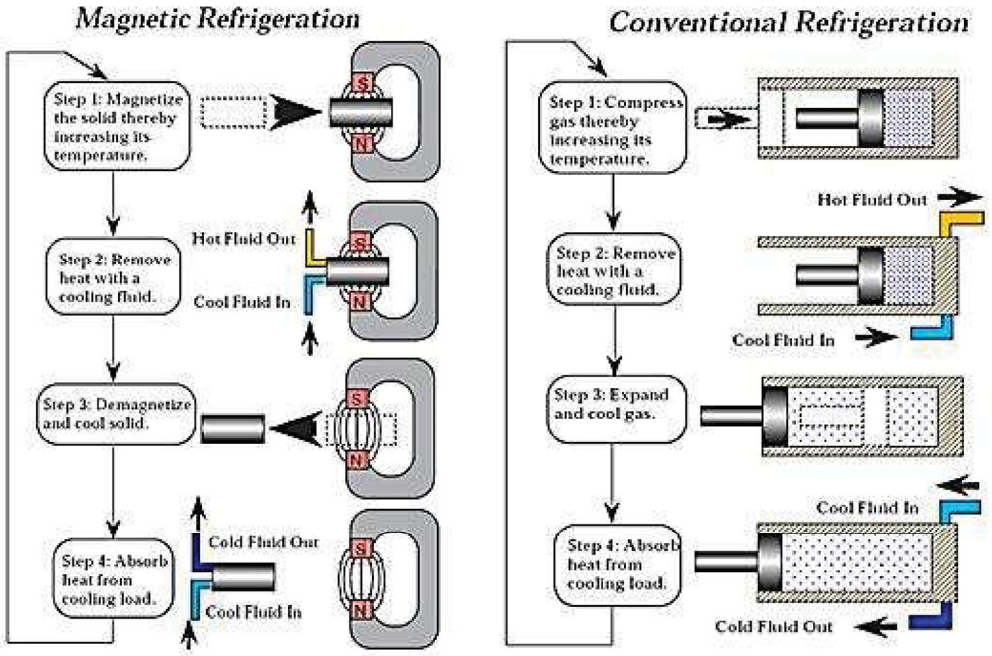

Figure 2: Schematic comparing magnetocaloric driven refrigeration with that of gas compressed refrigeration Source: http://eng.whmfc.cn/category/32/.

Figure 2 gives schematic representation of working principle of magnetic cooling and compares the same to that of gas compressed refrigeration. By allowing MCM to experience external magnetic field near magnetic transition temperature, one allow the temperature of material increases (step 1). The excess heat is removed through external fluid or air (step 2). Now the material is set free of applied field (step 3), the temperature of the material is lowered (reverse process of step 1). The lowered temperature of the material is used to cool the desired space (step 4). Till date widespread research and advances is in progress mostly in magnetocaloric materials alongside quite number of prototypes being put forward as replica of magnetic refrigeration and air-conditioning units for ambient temperature [6]. All though MCM's have found to be successful in cryogenic applications to obtain temperatures below 4K (liquid helium temperature), it is not yet commercialized for room temperature cooling either in the form of refrigeration or air-conditioning.

1.2. Thermodynamics view of magnetocaloric effect

Any material that undergo change of the order parameter from non-zero to zero near the transition will experience a change in entropy associated with the latent heat of the system, it serves as the origin of any caloric effects observed. The magnitude of entropy when high enough will result in large change in the temperature of the material making it potential for cooling applications.

1.2.1. First order versus second order transitions

To well understand change of entropy it is important to know the different type of influence which play major role. The observed entropy mainly arises due to change in symmetry/*alignment of spin* near ordering/*Curie point* if we consider, for instance, around structural/*magnetic* transition. The degree of ordering differs from each material and also type of ordering. If the ordering is continuous and extends over reasonable temperature range, then it is said to be *second order* (Figure 3 *a1*). And in case if the ordering is quick resulting in sharp/abrupt/discontinuous transition then it is said to be *first order* (Figure 3*b1*). In very few cases it can also be due to uncompleted transitions occurring nearby but not at same point, generally termed as *induced* magnetic transition.

C P Bean explains first and second transition by comparing them respectively to free and clamped systems (Figure 3c1) [7]. For case of second order transition, the ferromagnetic interactions occur between magnetic moments on each atom site. In such case, one can consider saturated magnetization or perfect long range ordering will decrease with increasing temperature due to thermal randomization. The fall in magnetization follows Brillouin function, resulting in smooth, controlled transition, hence named 'clamped' (Figure 3 a1, dotted line in c1). The first order on other hand, along with ordered magnetic spins magnetization is described to be strong function of interatomic spacing resulting from a noticeable change in volume of the system. In such system one can expect distortion/strain of the lattice that helps reduce loss of magnetization compared to clamped system. Such changes can also result to maintain the magnetization at temperatures higher than the actual magnetization transition T_0. At sufficient higher temperatures (T_{crit}) the decrease of magnetic spins cause diminution of lattice strain now the magnetization which is controlled mostly by distortion (termed as 'unclamped' or 'free') has to follow discontinues/sharp path (Figure 3 b1) unlike controlled decrease in second order (Figure 3 a1) which is function of mostly ordered magnetic spins. Such discontinuity in first order transition will normally result in large

entropy which is due to loss of magnetic order as well as the one associated with lattice entropy due to change in volume. When temperature is decreased in such system, the magnetization is not re-established until true magnetic ordering temperature (T_0 -***Figure 3***c). Hence most of the warming-cooling magnetization curve of first order exhibit thermal hysteresis ($T_{crit} - T_0$).

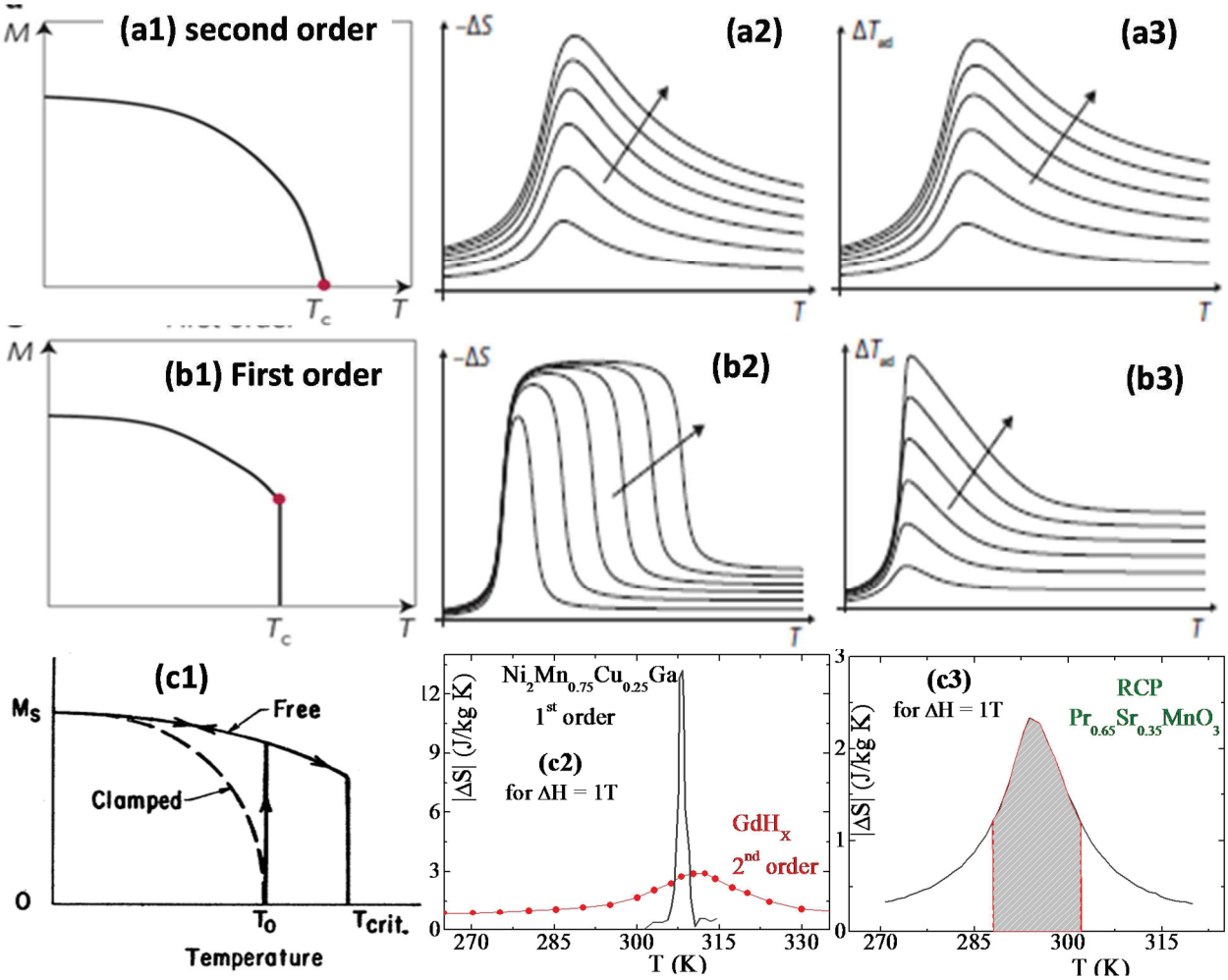

Figure 3: General curve profile for magnetization as function of temperature observed in (a1) First, (b1) second [8] and (c1) comparing both [7]. Typical shape, peak profile for entropy change (ΔS) (a2 & b2), adiabatic temperature change (ΔT_{ad}) (a3 & b3) for second & first order transitions [9]. Some examples of ΔS from literature (c2),(c3).

Several debates have been made in past concerning the effect of nature of transition – *first or second* – on the observed entropy change. Each one has their own advantage as well as drawbacks. The peak profile of different physical entities observed in case of first and second order transitions are summarized in Figure 3 (a1-a3, b1-b3). The entities entropy

change, adiabatic temperature change for second order transitions (Figure 3 a2, a3) exhibit broader profile while same for its counterpart i.e. first order are much sharper (Figure 3 b2, b3). Figure 3 c2 where the entropy change of $Ni_2Mn_{0.75}Cu_{0.25}$ (1^{st} order transition) and GdH_x (2^{nd} order) obtained under identical probe conditions help to better visualize these changes. The effect of external magnetic field on each parameter is also shown. For second order transition both ΔS and ΔT curves show increase in peak height as well as peak broadening with increasing field (Figure 3 a2, a3). Whereas in case of first order ΔT seems to follow similar trend, on other hand ΔS show different behavior. The peak height starts to be constant with application of higher field, with increase of only peak width (Figure 3 b2).

Relative cooling power define (RCP), which gives crucial weightage for MCM's, is expressed as integral under the entropy curves. The area under the shaded curve in gives the Figure 3 c3 gives the RCP for $Pr_{0.65}Sr_{0.35}MnO_3$. Considering broad peak shape, one expects materials with second order transition to be potential over first order once. However, even though the peak profiles are sharp for first order transitions they are having much larger magnitude (Figure 3 c2), hence tagged with the term *giant caloric effects*. And the total credential, RCP, is most of the times end up to be order of magnitude comparable to once from second order. One of the major drawbacks of first order is their inherent properties of magneto-crystalline anisotropy or thermal-field hysteresis. Coefficient of performance (COP) is similar reliability factor favored by few researchers over RCP. It is expressed in terms of the subtracted heat because of the magnetocaloric effect (Q_0) and the work done (L), $COP = Q_0/L$.

Theoretical approach to distinguish the first and second order transitions was well explained way back by Landau and Lifshitz in 1940's. C P Bean, D S Rodbell, S K Banerjee improve and confirmed the validity of these theories by applying them to experimental data [7, 10]. Later Anthony Arrott, John E Noakes and others proposed *critical behaviors* to better understand and differentiate each of them [11].

1.2.2. Intrinsic effects:

The intrinsic properties that are responsible for the entropy change (ΔS) associated with magnetocaloric materials will be discussed here. Observed entropy in case of magnetocaloric materials might not be simple as it looks in most of the case, i.e., change in the magnetic contribution. Such change in entropy may also be attributed to different contributions such as lattice/structural (that we just see in first order transition) or electronic or orbital in individual

or in few cases as combined form. It is important to take into account this fact before assigning and evaluating the observed entropy change of any material. Much generalized (but not complete) equation for change in entropy of given system can be written as [12],

$$\Delta S = \Delta S_e + \Delta S_L + \Delta S_m + \Delta S_O + \cdots$$

Each term in the equation signify the following,

ΔS_e is the Electronic entropy, defined by, $S_e = \gamma T$. Ex: *electrocaloric, FeRh*, [13]

ΔS_L is the Lattice entropy is given by, $S_L = \frac{L}{T_t} = mR\left[-3\ln\left(1 - e^{-\theta_D/T}\right) + 4D\left(\frac{\theta}{T}\right)\right]$. Ex: *magnetoelastic [14]*.

Relation for magnetic entropy is $S_m = RLn(2J+1) = -\left(\frac{\partial F}{\partial T}\right)_H$ Ex: *gadolinium*, [12]

ΔS_0, represents the entropy change due to orbital degeneracy. Ex. Manganites,

The observed entropy can be just due to magnetic exchange as in gadolinium, from lattice as in shape memory alloys, or combined effect of structure and magnetic as in $Gd_5Si_2Ge_2$ with equal contribution from both effect. In some special case such as heusler alloys, entropy is defined by three contributions vibrational ΔS_{vib}, conduction electrons ΔS_{el} and magnetic subsystem ΔS_{mag} [15]. Similarly in some manganite oxides, we have entropy from magnetic and electronic along with that due to orbital degeneracy.

1.2.3. External influences

External factors such as pressure, magnetic field play important role on observed entropy change near transition. In some case the external field might enhance the total entropy and may induce the entropy change in few others. In one of the observations in case of $Nd_{0.5}Sr_{0.5}MnO_3$, increasing and decreasing of magnetic field at constant temperature below metal-insulator transition resulted in a clear hysteresis in resistivity against field curve. The width of this hysteresis increased with lowered temperature. Even though it was first and only case observed, it was reported that a first order like transition, electronic (metal-insulator), can be caused by applying external field [16]. Similar phenomenon of field induced entropy change enhancement is observed near structural transition in case of $Ni_{55}Mn_{20}Ga_{25}$ heusler alloy metallic foams [17]. External field applied in specific crystallographic direction on $Ba_{0.3}Sr_{1.7}Co_2Fe_{12}O_{22}$ single crystal resulted in sign change of magnetocaloric effect due to gradual collapse of heliconical magnetic order [18]. However the ΔS_M observed is very low to realize this composition in magnetic refrigerant.

It should be noticed that almost every material inherits caloric effects (thermal response) near transition or/and due to changes in the external fields such as mechanical, electrical, magnetic fields. The above discussed cooling effect can be extended to be associated with change of other physical phenomenon of any material that results change of entropy near transition. Some of these are briefed below:

a. Electrocaloric – Even though first report came back in 1960's for the electrocaloric effect which is classically defined as, "change in the temperature of the material upon application or withdrawal of electric field under adiabatic conditions" [19]. It did not gain further focus as the highest obtained electrocaloric effect among studies was very small, 2.5k in 750V for bulk $Pb_{0.99}Nb_{0.02}(Zr_{0.75}Sn_{0.20}Ti_{0.05})_{0.98}O_3$ sample. Recently thin films of $PbZr_{0.95}Ti_{0.05}O_3$ brought back interest by showing impact change of 12K in 25V around ferroelectric Curie temperature (222 °C) [20]. For the electrocaloric materials the entropy change is defined by, $\Delta S = -\frac{1}{\rho}\int_{E_1}^{E_2}\left(\frac{\partial P}{\partial T}\right)dE$ and the temperature change using, $\Delta T = -\frac{1}{\rho}\int_{E_1}^{E_2}\frac{T}{C}\left(\frac{\partial P}{\partial T}\right)dE$ in both cases, P is polarization, *C* is specific heat capacity, ρ is density and E_1, E_2 corresponds to starting, final applied fields. Much recently entropy change was observed in multiferroics two-phase composite, $La_{0.7}Sr_{0.3}MnO_3/Pb(Mg_{1/3}Nb_{2/3})O_3$-$PbTiO_3$, where the combined effect of both voltage and magnetic field influence the observed latent heat [21].

b. Elastocaloric/ piezocaloric – The change in length/ of the material near its transition under influence of external field (uniaxial stress, magnet) can give rise to the change in entropy termed as Elastocaloric. For instance, such effect is observed in Heusler shape memory alloy Ni-Mn-Ga where both external applied magnetic field and compression stress (mechanical stress) increase the observed entropy change of the structural phase transition[22, 23].

c. Barocaloric – Refers to change in temperature/entropy of the material with application of external adiabatic pressure. External pressure and magnetic field along with temperature are demonstrated to trigger the polymorphism. Polymorphic transformations can lead to minimizing free energy of many solids. On basis of this concept, barocaloric effect was demonstrated on the magnetocaloric prototype $Gd_5Si_2Ge_2$ under hydrostatic pressure. Entropy change observed under moderate applied pressure were comparable to those obtained by magnetocaloric effect. This was further supplemented with direct measurements of temperature change of the material [24, 25].

d. Thermoelectric – In 1838 Henrich Lenz demonstrated water drop placed on junction of metal wires of bismuth and antimony, by applying current in one direction resulted in freezing of the water drop and on reversing the current direction water drop melted. Phenomenological explanation of such effect is based on Peltier effect. In 1950's Abram Ioffe suggested semiconductors as potential thermoelectric materials for home refrigeration. Following which several materials were explored concluding in Bi_2Te_3/Sb_2Te_3 alloys to be the top performers at room temperature [26]. Thermoelectric materials could produce only moderate amount of cooling (COP≈10%), failing to overcome gas compressor based refrigeration (COP≈60%) in terms of efficiency by long way. To positive side thermoelectric cooling is potentially used in surgery for cooling the instrument used for extracting the crystalline lens out of the eye. The fact that such effect which requires higher ZT and Seebeck coefficients has been achieved mostly with selenides/tellurides/arsinides/sulphides/antimony based materials which are quite hazardous, carcinogenic is the other drawback of the thermoelectric cooling.

e. Thermoacoustic – Around 1859, P L Rijke demonstrated sound waves (acoustics) with in closed system (tube) can induce change in temperature of the system (later better known as Rijke tube) [27, 28]. This has also been successfully demonstrated [29]. To mention other use of this effect, researchers at Los Alamos National laboratory using their early stage prototype of thermoacoustic heat engine have efficiently (efficiency up to 30%) liquefied 140 gallons of natural gas per day.

1.2.4. Magnetocaloric effect a theoretical view

Alongside experimental efforts, theoretical verifications and predictions have also played greater role in understanding basics and further improve performance of different physical properties. And so is its part in magnetocaloric – let it be in understanding basics of magnetism/entropy, materials (discussed below), or improving performance in prototypes (magnet-design, explain heat transport and so on). In which regards lot of advances has been made leading to several models and theories [9]. This subsection gives very basics of the theoretical background on magnetism and derivation of magnetocaloric effect.

Basic theoretical explanations for the magnetic behavior like *type of transition* (ferro/antiferro/ferri/para/dia); *nature of transition* (first/second); and so on goes long time back. Initially, the thermodynamics for first[7] and second[10] order transitions from yester

years is recollected. Following which is the summary of advances in theoretical treatments that are made in recent years to well characterize materials inherit properties.

Thermodynamics of second order magnetic transition

From thermodynamical theory of second order transition developed by Landau and Lifshitz, the thermodynamic potential ϕ near transition point can be expanded using Taylor series,

$$\phi(T,P,J) = \phi_0 + aJ^2 + bJ^4 + \cdots \qquad (i)$$

Where J is order parameter which can assume infinitely small values, a and b are functions of pressure (P) and temperature (T) and ϕ_0 is a constant. This has been successfully implied for Curie point transition in ferromagnets considering, $J = J_T/J_0$ with $J_T$and J_0representing the spontaneous magnetizations per unit mass respectively at any given temperature T°K and at 0°K. Restricting the series to J^4 and including magnetostatic field energy (JH), we can rewrite (i) as,

$$\phi(T,P,J) = \phi_0 + aJ^2 + bJ^4 - JH \qquad (ii)$$

At equilibrium near Curie point one expects, $\partial\phi/\partial J = 0$, applying this to (ii) we get,

$$\alpha\sigma + \beta\sigma^3 = H \qquad (iii)$$

Where, σ specify experimentally observed specific magnetization, while α=2a, β=4b are new constant incorporating a, b, J_0.

Eq. (iii) can be rewritten as $\alpha + \beta\sigma^2 = H/\sigma$

$$or \quad (H/\sigma - \alpha) = \beta\sigma^2 \qquad (iv)$$

For thermodynamic reasoning β should always take positive values, it can be deduced experimentally (from (D)) as slopes of linear isothermal magnetization plots of H/σ against σ^2 (comparing (iv) with y=mx+c). And at Curie point α=0. In most case to follow here after, σ the specific magnetization or spontaneous magnetization per unit mass is represented by M.

Thermodynamics of first order magnetic transition

C P Bean and D S Rodbell first proposed theory for first order magnetic transition [7]. They consider collection of interacting magnetic dipoles with interactions that can be well approximated by the molecular field model. Thermodynamics for caloric effects in system with magneto-structural couplings has been very well demonstrated recently [22].

Over the years some of the theoretical analysis techniques, such as critical exponent and universal curves, that help better understand the difference between first and second order transitions are developed [30].

1.3. Characterization and measurements

The figure of merit for magnetocaloric materials: Potential of any material for its magnetocaloric applications is judge on following properties they exhibit. Individual researchers have their own favorite entity as figure of merit, here is list of most of them along with their meanings. *Entropy change (ΔS)* is change in total entropy of the system under influence of external field (magnet, pressure, etc). This has become one of the common entities in most of the reports and analysis. *Adiabatic temperature change (ΔT)* – change of temperature change under influence of external forces (magnetic, mechanical stress) is more realistic measure of MCM, most case it is evaluated through indirect measurements as direct measurements are not yet accessible by large population of scientists. Adiabatic temperature change due to MCE *Relative cooling power (RCP)/Refrigerant Capacity (RC)* is believed to be much relevant credential to evaluate the MCMs as it is described as the work function of the material [31]. Most reliable figure of merit for any given refrigerator/cooling cycle is the *Coefficient of Performance (COP)* and is defined as the ratio of amount of cooling produced to the energy input [32]. To note, all along the thesis, the credentials of the magnetocaloric materials are often addressed with magnitude of the observed entropy change (ΔS) and/or adiabatic temperature change (ΔT).

Performance of any MCM is evaluated by means of the entropy change and adiabatic temperature change that they exhibit. The so observed entropy change/adiabatic temperature change can be probed either by direct measurements or through indirect measurements [33]

1.4. 1. Direct measurements:

Direct measurements involve the measurement of adiabatic change in temperature (ΔT) of the material by subjecting it to magnetic field changes. The first proposal to measure MCE directly by using thermocouple was back in 1921 by Weiss [34]. Till date there are quite good number of proposed experiments that claim to be able to record such change in temperature accurately and even so under higher applied fields[35]. Few of them which work on different principles are briefed here. It is to be noted that most of them are yet to be

commercialized and standardized to be used in lab like any other instruments such as SQUID or DSC.

1.4. 2. Indirect measurements

Most of the direct measuring facilities are very recently developed compared to the time at which MCE was introduced. Even though the direct measurements are frequently addressed as 'classical MCE evaluating tool', we should also be aware that most of the MCM were explored based on indirect measurements. And still need to address some of complication such as requirement of the high cost, high end technology and engineering, along with questions about accuracy. These facts leave most of the researchers to go for much affordable, ease of availability and standardized measurements.

Indirect measurements are based on probing magnetization or heat capacity and further applying Maxwell's relations to evaluate the entropy and temperature change of the system. So it normally involves two steps *measurements* and *calculations* in obtaining magnetocaloric effect.

1.4.2. 1. Measurements

(a) Magnetization as function of applied field at constant temperature, $M(H)_T$, followed by extraction of isothermal magnetic entropy ΔS_M.

(b) Heat capacity by calorimetric method under zero and various external applied field strength.

1.4.2. 2. Calculations

From the magnetization measurements one can obtain magnetization as function of field at constant temperature $M(H)_T$ or magnetization as function of temperature at constant applied field $M(T)_H$. We can link magnetization with the entropy through thermodynamic Maxwell equation,

$$\left(\frac{\partial S}{\partial H}\right)_T = \left(\frac{\partial M}{\partial T}\right)_H \quad by\ integrating\ over\ the\ magnetic\ field\ H,$$

$$\Delta S_M(T)_{\Delta H} = \int_{Hi}^{Hf} \left\{ \left(\frac{\partial M(T,H)}{\partial T} \right) dH \right\} \qquad \cdots (1)$$

Similarly, adiabatic temperature change can be related to magnetization and heat capacity by the expression,

$$\Delta T_{ad}(T)_{\Delta H} = \int_{Hi}^{Hf} \left\{ \left(\frac{T}{C(T,H)} \right)_H \left(\frac{\partial M(T,H)}{\partial T} \right)_H dH \right\} \qquad \cdots (2)$$

Where, Hi, Hf represents respectively the initial and final applied fields in the isotherm. C(T, H) the heat capacity as function of temperature and applied field, ∂M the change in magnetization obtained at adjacent temperatures T_{i+1} and T_i. ∂T is difference in temperature, T_{i+1}-T_i. There exist few debates that the Maxwell equation is not the best to evaluate MCE in materials undergoing first-order magnetostructural phase transition (FOMPT) where anisotropy in isothermal (metamagnetism) curves is, in most case, inevitable [36]. To avoid overestimate of the entropy change using equation (1) few authors claimed Clausius-Claperyon (CC) (defined as equation (3)) to give more reliable MCE. This will be further discussed in chapter 3.

$$\Delta S_M(T,B) = -\Delta M \frac{dH_c}{dT} \qquad \cdots (3)$$

Direct measurements are highlighted to be better way to characterize MCMs with first order transition where entropy change due to structural change would be more important and indirect measurements might fade this[35, 37]. Going further some of the direct measurements are able to demonstrate the effect of magneto-crystalline anisotropy taking advantage of ease of changing field direction that their device designing offers[38]. In case of first order transition in $MnFeSi_{0.25}P_{0.75-x}Ge_x$, the effect of remnant magnetization or anisotropy leading to different entropy change values under different measurement conditions have been demonstrated [39]. In some cases, we can expect the convergence of both direct and indirect measurements [40]. So extreme care is necessary while analyzing first order transitions as sometimes it might be linked with other physical properties such as elasticity which by themselves can be reason for the observed entropy change [41, 42]

1.4. Magnetocaloric materials explored

Material scientists from different disciplines through their efforts have introduced wide variety of materials that exhibit high magnitude of magnetocaloric effect over complete range temperature (from milli K to several hundred Kelvin)[43]. This subsection is restricted to summarize materials of different class (intermetallics, oxides, arsenides or simple element like Gd) that show promising magnetocaloric performance in and around ambient temperature. Even then, as the number of these materials is quite large we still may miss some of them. One can refer to some of the dedicated reviews on magnetocaloric materials that have been presented in literature [9, 30, 43, 44].

1.4.1. Intermetallics

Intermetallics are always favored over other class of materials due to the potential entropy change that they exhibit even under very low applied field. There are several efforts that were successful to explore new potential, reliable, and cost effective magnetocaloric material for ambient temperature applications. Further subsections deal in detail the properties of each class of materials such as structure, magnetic and magnetocaloric properties. Also special view has paid on their advantage and disadvantage towards being promising materials for real applications.

1.4.1.1. Gd-based intermetallics

Gadolinium with magnetic transition around room temperature (T_c = 294K) was initially proposed to be potential prototype material for room temperature magnetic refrigeration. Later on several groups worked extensively on gadolinium based compositions to explore a potential material with higher magnetocaloric effect. In due course, V K Pecharsky and K A Gschneidner reported giant magnetocaloric effect exhibited by one of the compounds from rich Gd-Si-Ge phase diagram [43]. They propose $Gd_5Si_2Ge_2$ an equal mixture of Gd_5Si_4 and Gd_5Ge_4 as giant magnetocaloric material characterized with high entropy change around room temperature. Even though compounds from Gd-Si-Ge system are potential enough lower temperature (T_{MCE} =276 K) and the inclusion of low abundance germanium is small concern. The other ternary diagram of interest is Gd-M-Si (M = Co, Ni), after several combinations, several new phase exhibiting good magnetocaloric effect at lower temperatures were reported. Only compound with in this phase diagram to exhibit magnetic transition near room temperature, reported till date, is $Gd_6M_{1.67}Si_3$ [45]. Much detail description about this compound is presented in introduction of chapter 2. Several binary combinations of gadolinium with other elements were also explored such as Gd_4M_3 (M=Bi, Sb) which show moderate MCE around their second order magnetic transition. The compound Gd_4Bi_3 has its Curie temperature around 332 K and Gd_4Sb_3 at 264 K with reasonable MCE. The solid solutions between these two alloys $Gd_4(Bi_xSb_{1-x})_3$ help tune the transition to near room temperature, for instance, $Gd_4(Bi_{0.5}Sb_{0.5})_3$ show $T_C \approx$ 288 K and $Gd_4(Bi_{0.75}Sb_{0.25})_3$ $T_C \approx$ 308 K [46].

Table 1: Magnetocaloric materials for near room temperature applications – Intermetallics (RCP- Relative Cooling Power; SC – Single Crystal; †- calculated from ΔS peak; -- – data insufficient/not available); ΔH is change is applied magnetic field http://icmp.imr.ac.cn/ss07/PPT/deBoer/deboer16.pdf

Material	Magnetic Transition		Properties and Performance						Reference
	Type	Order	Tc K	| ΔS| J/KgK	ΔT K	ΔH k Oe	δS_{FWHM} † K	RCP † J/kg	
Gadolinium-based									
Gd	Ferro – Para	2nd	294	4.5 8.5	5.5 11	20 50			Phys Rev Lett 78, 4494 and Phys Rev B 57, 3478 Cost ≈ 20€/kg
$Gd_5Si_2Ge_2$	FerroI–FerroII Ferro – Para	1st 2nd	276 299	14 2	7 0.8	20 20			Phys Rev Lett 78, 4494 Cost ≈ 60€/kg
$Gd_6Co_{1.67}Si_3$	Ferro – Para	2nd	294	2.8	2.93	20			Chem Mater 20, 2977
$Gd_6Ni_{1.67}Si_3$	Ferro – Para	2nd	310	2.93	3.1	20			
Gd_7Pd_3									Intermetallics 10, 731
$Gd_{90}Tb_{10}$	Ferro – Para	2nd	286						JMMM 316, e558 RevSciInstrum 83, 083902
La-Fe-Si based									
$LaFe_{11.7}Si_{1.3}$ $LaFe_{11.2}Co_{0.6}Si_{1.3}$ $LaFe_{11}Co_{0.9}Si_{1.1}$	Ferro-Para	1st	190 265 294	26.2 8.7 7.4		20		157 148 163	J Phys Cond Mater 19, 236230
Heusler Alloys – X_2YZ – Ni_2MnZ									
$Ni_{55.2}Mn_{18.6}Ga_{26.2}$ or $Ni_{2.208}Mn_{0.744}Ga_{1.048}$	Ferro – Para	1st	320	9 20.4		15 50			J Phys Cond Mater 16, L39 Cost ≈ 10€/kg
$Ni_2Mn_{0.75}Cu_{0.25}Ga$	Ferro – Para	1st	308	28 65		20 50	2 2	-- 84	Appl Phys Lett 88, 192511
MnFe(P,As), Fe-Pt and others									
MnAs	Ferro – Para	1st	310 *318*	20 *30*		20 *50*			Physica A 358, 123 *Appl Phys Lett 79, 3302* Cost ≈ 10€/kg
$MnFeP_{0.5}As_{0.5}$	Ferro – Para	1st	300	14.5 18		20 50			Nature 415, 150 Cost ≈ 7€/kg
$Mn_{1.28}Fe_{0.67}P_{0.48}Si_{0.52}$	Ferro – Para	1st	290	16		20			Adv Energy Mater 1, 1215
MnP-*SC* *H along <100>* *H along <010>* *H along <010>*	Ferro – Para		291	 1.2 2.1 2.5		20	 -- 22 28		Phys Rev B 77, 104439
Mn_5Ge_3	Ferro – Para	2nd	298	3.8 9.3		20 50	35 46		J Alloys Comps 337, 269
$Fe_{80}Pt_{20}$ $Fe_{79}Pt_{21}$	Ferro – Para	1st	240 285	11 31.3 10 25.2		20 50 20 50	18 15 20 18		Appl Phys Lett 90, 222504
$TbCo_2$									
Intermetallic with carbon, hydrogen, boron intercalation									
Gd ribbon GdH_x ribbon			293 312	2.74 2.91		10	-- --	-- --	J Alloys Comp 377, 72
$Gd_{0.98}B_{0.02}$ $Gd_{0.93}B_{0.07}$	Ferro – Para		298	2.8 2.8		10		79.5 87.5	Solid State Comm 131, 97
$Gd_{0.975}C_{0.025}$ $Gd_{0.91}C_{0.09}$	Ferro – Para		296 300	2.8 2.4		10		90.1 81.3	J Alloys Comp 387, 6
$LaFe_{11.6}Si_{1.4}$ $LaFe_{11.6}Si_{1.4}C_{0.2}$ $LaFe_{11.6}Si_{1.4}C_{0.4}$	Ferro – Para	1st 1st 2nd	200 230 250	20 17 7		19	10 12 15	200 204 105	JAP 111, 07A927
$LaFe_{11.6}Si_{1.4}H_{1.6}$	Ferro-Para	1st	334		3.59	19.3			Adv Mater 22, 3735 Cost ≈ 8€/kg
$LaFe_{10.98}Co_{0.92}Si_{1.1}B_{0.2}$	Ferro-para	1st	295	6.2		20	27		Proced ThermagV Grenoble, 173

1.4.1.2. *La-Fe-Si based materials*

La-Fe-Si based intermetallics are believed to have more potential other than Gd-based intermetallics for room temperature applications and probably next well studied in this regard [47]. The objective for exploring new materials to supplement the rare earth Gd and less abundance Ge based material lead way for several materials and one of the successive emergent is La-Fe-Si based intermetallic. Even though it carry rare earth La, it was interesting as it was successive to obtain large entropy change alongside reach the main objective to some extent. The parent compound $LaCo_{13}$ and $LaFe_{13}$. A new family by replacing cobalt by Fe and/or Si lead to series $La(Co_{1-x}Fe_x)_{13}$, $La(Co_{1-x}Si_x)_{13}$ and La(Fe, Co, $Si)_{13}$. It was highlighted as low cost material.

1.4.1.3. MnAs, MnP, MnAs1-xPx, MnFe(P, As)

Considering low cost and high abundance of manganese, some researchers focused their material exploration on manganese based materials. First of which was MnAs and MnP family of materials. To achieve transition near 300K, it is necessary to replace more than 50 at % P by As in case of $MnFeP_{1-x}As_x$. MnAs first-order magnetic transition is coupled to a crystallographic one from hexagonal (ferromagnetic) to orthorhombic (paramagnetic) inducing a great magneto-elastic coupling. Colossal MCE was observed in MnAs under hydrostatic pressure [48]. Colossal differs from giant magnetocaloric effect by an order of magnitude greater. Further the effect of pressure on the observed MCE was extended for other compounds such as GdGeSi alloys. Even though these materials are believed to exhibit giant magnetocaloric effect around room temperature, the toxicity of the composition is a concern for them to be realized in the large production and applications. However till date a lot of work is in progress to either in explore new materials (such as $MnFeSi_{0.25}P_{0.75-x}Ge_x$) or to simplify the manufacturing process to push them towards application [39].

1.4.1.4. *Heusler alloys*

Heusler alloys have general form of X_2YZ. Focusing near room temperature magnetocalorics several combinations with X any transition metal such as Ni, Co; Y again a transition metal (here we restrict to Mn) and Z is one of the group IIIA, IVA and VA elements have been explored. Other than magnetocaloric, compositions from this system also exhibit other interesting physical properties such as memory effect, anisotropy, metamagnet transition and shape memory effect [49]. This particular class of materials are claimed to be

low cast, ease in manufacture and environmental friendly compared to other intermetallics. Nickel and manganese based $Ni_2Mn_{1\pm x}Z_{1\pm x}$ (Z = Ga, In, Sn, Sb, Al) are most explored materials in recent days due to the giant magnetocaloric effect around structural or first order transition [50]. Compositions from $Ni_2Mn1\text{-}xCu_xGa$ system have shown promising magnetocaloric effect close to room temperature [51]. More details on Heusler alloys will be presented in introduction of the chapter 3.

1.4.1.5. *Hydrogen, boron, carbon insertion*

Enhancement of magnetic properties and hence the magnetocaloric effect has been observed in few intermetallics up to insertion of hydrogen or boron or carbon [52, 53]. However for most of these materials the long time stability is still need to be addressed [54]. Some of these materials along with their physical properties are summarized in the Table 1.

Note: In Table 1 the cost of some of the materials as calculated by Prof Frank de Boer is also listed. However, it should be noticed these values for each material are subject to change with time depending on the price of constituent elements and manufacturing technique involved. They are provided for general comparison only.

1.4.2. Oxides

Dedicated efforts have been made by material scientists in the field of oxides to compete with the giant magnetocaloric intermetallics materials. Oxides are favored over intermetallics in comparison with cost, ease of manufacturing in large scale, stability and reproducibility [55]. Oxide based magnetocaloric materials exhibiting modest figure of merit around ambient temperature are summarized in the Table 2.

Manganese based perovskite oxide

Manganese based perovskites always stand up front in the regard, with success in attaining magnetocaloric figure of merits compared to gadolinium. However, only few of them are discussed in detail here, with much detailed work to follow in chapter 4. Perovskite manganites, $RMnO_3$ (R=lanthanide), general have structure that is shown in Figure 4a. By replacing A-site by alkaline equal amount of Mn^{3+} is forced to have Mn^{4+}. Recalling super exchange theory and GKA rules of interaction, we know that, $Mn^{3+}—O^{2-}—Mn^{3+}$ (as in $LaMnO_3$) or $Mn^{3+}—O^{2-}—Mn^{4+}$ (as in $CaMnO_3$) have antiferromagnetic ground state.

However, in very rare cases the orbital ordering can influence Mn^{3+} to be ferro magnetically coupled to Mn^{3+} (as in $LaMnO_3$). With introduction of Mn^{4+} we can expect some Mn^{3+}—O^{2-}—Mn^{4+} interactions which according to double exchange theory should give raise to ferromagnetic interaction [56] (as observed in $La_{0.7}Ca_{0.3}MnO_3$) .

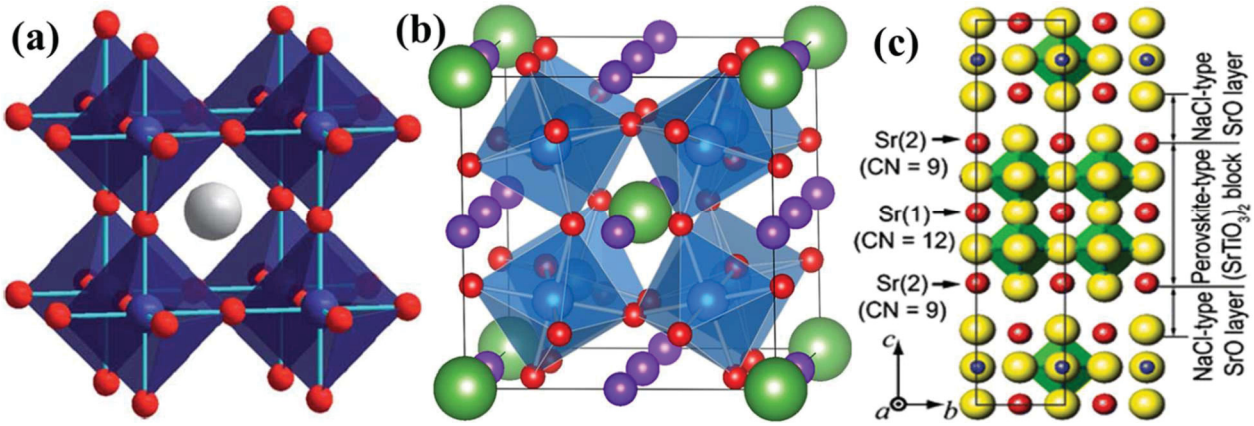

Figure 4 General structure for (a) ABX_3 perovskite A-site cations is represented by grey spheres, B-site cations by blue spheres and the anions by smaller red spheres [J Mater Chem 20, 5785] (b) $AA'_3B_4O_{12}$ A-site ordered double perovskite, A, A', B and O atoms are represented by green, purple, blue and red spheres [Scientific Reports 2, 449] and (c) Layered manganites $R_3Mn_2O_7$ ($Sr_3Ti_2O_7$-type) R is normally mix of lanthanide (La, Pr, Nd, Sm) and alkaline(Ca, Ba, Sr) [DOI: 10.1007/s10832-008-9455-9].

Some of the $La_{1-x}A_xMnO_3$ (with A=Sr, Ca, Ba) series show first order transitions with promising magnetocaloric effect. But they lack T_C near ambient temperature as they order either at low temperature (Ex: $La_{0.6}Ca_{0.4}MnO_3$) [57] or at higher temperatures (Ex: $La_{0.6}Sr_{0.4}MnO_3$) [58]. In order to shift the T_C near to room temperature, some even tried solid solution between materials with high temperature T_C and once with low temperature T_C MCMs [58]. In an Efforts/attempts to increase the transition temperature in case of $La_{0.7}Ca_{0.3}MnO_3$ by introducing Ag in place of Ca resulted in partial success as transition temperature increased (in the series $La_{0.7}(Ca_{1-x}Ag_x)_{0.3}MnO_3$ – T_C=250K for x=0 and T_C = 270K for x=0.1) [59]. Meanwhile the magnetic transition lost first order nature and became more second order with increasing Ag concentration. It resulted in decrease of observed entropy hence magnetocaloric effect. At higher doping levels impurity phase starts to appear and hence limiting the highest reachable T_C to270K which is still low to be considered for ambient applications.

In a similar way, replacing Mn in lanthanum based manganite $La_{0.67}Sr_{0.33}MnO_3$, with Fe result in slight increase of T_C but lowered magnetocaloric performance. Same effect was

observed with B site cation doping, when chromium was introduced into manganese site in case of $Pr_{0.6}Sr_{0.4}Mn_{1-x}Cr_xO_3$ and $Pr_{0.6}Ca_{0.4}Mn_{1-x}Cr_xO_3$, former compositions resulted decrease in the entropy and later result in increase of entropy change **[60]**.

Table 2: Few magnetocaloric materials for near room temperature applications – Oxides. (SC-single crystal); RCP in bold suggest the values are as reported in literature.

Material	Magnetic Transition		Performance						Reference
	Type	Order	Tc K	| ΔS| J/KgK	ΔT K	ΔH k Oe	FWHM K	RCP J/kg	
Perovskite manganates									
$Pr_{0.63}Sr_{0.37}MnO_3$-*SC*	Ferro – para	2nd	305	2.57 8.52		10 50			J Appl Phys 97, 10M306
$Pr_{0.6}Sr_{0.4}MnO_3$ $Pr_{0.55}Eu_{0.05}Sr_{0.4}MnO_3$ $Pr_{0.50}Eu_{0.10}Sr_{0.4}MnO_3$ $Pr_{0.45}Eu_{0.15}Sr_{0.4}MnO_3$	Ferro – para	2nd	303 283 -- 260	2.46 2.16 1.99 2.23		20		**78.6** **100.9** **111.2** **5** **159.4**	Solid State Comm 151, 1579
$Pr_{0.9}Pb_{0.1}MnO_3$ $Pr_{0.6}Pb_{0.4}MnO_3$ $Pr_{0.5}Pb_{0.5}MnO_3$	Ferro-para		150 254 253	3.91 3.68 3.34		13.5			J Appl Phys 99, 08Q108
$La_{0.6}Ca_{0.4}MnO_3$	Ferro – Para	1st	260	2.6 3.8	1.1 1.7	10 20	14 20		JMMM 208, 85
$La_{0.80}Ag_{0.20}MnO_3$	Ferro – Para		278	3.4		10	9		JMMM 222, 110
$La_{0.83}Ag_{0.17}MnO_3$ $La_{0.80}Ag_{0.20}MnO_3$ $La_{0.78}Ag_{0.22}MnO_3$	Ferro-Para		290 296 300	2 2.4 2.9		10			Physica B 319, 168
$La_{0.67}Ba_{0.33}MnO_3$			292	1.48		50		161	J Appl Phys 79, 373
			332	3.51		50		235	Mater Lett 65, 2093
$La_{0.7}Ca_{0.2}Ba_{0.1}MnO_3$									Physica B 405 2733
$La_{0.8}Ca_{0.2}MnO_3$ $La_{0.67}Ca_{0.33}MnO_3$	Ferro-Para	1st	230 257	5.5 4.3		15			Phys Rev Lett 78, 1142
$La_{0.70}Sr_{0.30}MnO_3$ $La_{0.825}Sr_{0.175}MnO_3$ $La_{0.875}Sr_{0.125}MnO_3$	Ferro-para	2nd	348 260 180	--	0.8 0.7 0.4	8.2	--	--	Phys. Solid State 46, 1081
$La_{0.72}(Ca_{1-x}Sr_x)_{0.28}MnO_3$									J Mater Res 24, 1585
Perovskite Ferrites, Cobaltites, Double perovkites, Layered Perovskites									
CrO_2	Ferro - Para	2nd	396	5.1		15			
$SrFe_{1-x}Co_xO_{3\pm d}$; x =0.5	Ferro-Para	2nd	330	2.2 4	0.9 1.8	20 50		**80** **258**	J Solid State Chem 184, 3228
Ba_2FeMoO_6 Bulk and Nanorod	Ferro – Para	2nd	340 349	1.09 1.54		10	16.7 14.63	18.2 22	Eur Phys J B 41, 213 JMMM 282, 151
$NdBaMn_2O_6$	Para-Ferro-Antiferro	2nd	290 210	1.2 -0.6		20			
$La_{1.4}Ca_{1.6}Mn_2O_7$	Ferro – Para	1st	270		11.3 16.8	20 50			Appl Phys Lett 81 3416

Other oxides

CrO_2 is probably the simplest oxide which exhibit large magnetocaloric effect, but unfortunately, at slightly higher than the room temperature. With hope to attain transition at

lower temperature and to improve MCE, this oxide was extensively study in different forms, first of them was nanoparticles [61]. Magnetocaloric effect of acicular CrO_2 nanoparticles/ nanorods with two different lengths were evaluated and found that particles with length of 400 nm yield large entropy value of 5.1 J/kg K as compared to 2.25 J/kgK by particles of 260 nm length with applied field of 1.5T near their second order magnetic transition (T_C = 396K) [14].

Cobaltite and ferrite based perovskite oxides can also be considered as good candidates. Stoichiometric $SrFeO_3$ with iron formal valence of Fe^{4+} is metallic upto 300K, with screw antiferromagnet arrangement below Néel temperature T_N =134K [62]. By replacing Fe with Co, $SrFe_{1-x}Co_xO_3$ one can expect some ferromagnetic interaction. By introducing Fe in place of Co, Kawasaki et.al., synthesized under high pressure interesting series of compositions, $SrFe_{1-x}Co_xO_{3-\delta}$ ($0\leq x\leq 1$, $\delta\leq 0.06$), that exhibit ferromagnetic Curie temperature around 300K [63]. The saturation magnetization was explained based on ferromagnetic alignment of Fe^{4+} ions ($4\mu_B$) and Co^{4+} ions ($1.8\mu_B$). While $SrCoO_3$ which was obtained by electrochemical oxidation to get complete Co^{4+} turn out to be metallic ferromagnet with T_C=280K [64].

Much recently, detailed studies on magnetocaloric effect in case of $SrFe_{0.5}Co_{0.5}O_{3-\delta}$ obtained by electrochemical oxidation process was carried out by O. Toulemonde et. al., showing modest MCE figure of merit values around second order ferromagnet transition (T_C=330 K) in samples with almost stoichiometric oxygen ($\delta\approx 0$). These results suggest other compositions in the series might also exhibit similar MCE around room temperature [65]. However, it should be noted that the transport properties of these compounds are very sensitive to the oxygen stoichiometric which in turn is controlled by synthesis route. In an alternative study the authors also demonstrated the sample, $SrFe_{0.5}Co_{0.5}O_{3-\delta}$ ($\delta\approx 0.17$) obtained in similar process and after storing in air for one year (*termed air ageing*) results in the loss of oxygen [66]. This loss of oxygen accounted to the decrease in transition temperature (T_C=305 $K_{virgin\ phase}$ to 293±5 $K_{aged\ phase}$), as well the magnetization/magnetic contribution. Hence decrease in total entropy of the sample. Interestingly, the broadened magnetic transition due to *air ageing* maintains the total refrigerant capacity as that of starting material.

Ordered double-perovskite, $A_2B'B''O_6$, which carry twice the molecular weight to that of ABO_3 – type perovskites, they have been much recently explored for ambient magnetocaloric effect. A-site ordered perovskite, $RBaMn_2O_6$ (R = La, Pr, Nd…), is described

to have significant structure where in MnO_2 square sublattice is sandwiched by two types of rock-salt layers, rare earth oxide RO and alkaline oxide BaO which are different in sizes resulting in the MnO_6 octahedron to be distorted in non-centrosymmetric manner. $PrBaMn_2O_6$ exhibits much lower magnetocaloric effect. Its analog $NdBaMn_2O_6$ display two transitions when cooled from high temperature first one a second order paramagnetic to ferromagnetic at T_C = 290K with 'normal' magnetocaloric effect with ΔS = 2.5J/kg K under applied magnetic field change ΔH=5 T [67]. Second magnetic transition from ferromagnetic to antiferromagnetic at carrying 'inverse' magnetocaloric effect, ΔS = 1.4 J/kg K (ΔH=5 T). However, these results are important in sight that single low-temperature magnetic transition ($T_C \approx 140K$) in disordered $Nd_{0.5}Ba_{0.5}MnO_3$ was replaced with two transitions in ordered double-perovskite $NdBaMn_2O_6$. Ba_2FeMoO_6 was prepared by two different synthesis routes and the MCE for both cases was reported. First synthesis was by wet chemistry which result in bullrush-like crystallites with diameter 130 nm and high aspect ratio larger than 15. These crystallites show sharper magnetic transition (T_C=340K) and the large entropy of 1.34 J/kg K in applied field change of 10k Oe. While sample obtained by conventional solid state synthesis resulted inhomogeneous aggregates of granules with different shape and size showing broader transition characterized with entropy change of 1.09 J/kg K [68]. The double perovskite La_2NiMnO_6 exhibits lower magnetocaloric effect.

Two-layered $A_3B_2O_7$-type perovskite (Figure 4 c) in particular $La_{2+2x}Ca_{1+2x}Mn_2O_7$ have been recently highlighted potential for room temperature magnetocaloric effect. $La_{1.4}Ca_{1.6}Mn_2O_7$ have been reported to exhibit large magnetocaloric effect around first order transition, $T_C \approx 270$ K [69]. Some efforts to push the transition to slightly higher temperatures did not give fruitful results, as in case of $La_{1.6}Ca_{1.4}Mn_2O_7$ the Curie temperature was shifted to 171 K with entropy change of 3.8 J/kgK with change in applied field of 1.5 T. These compounds are even reported with contrary values for transition temperature and entropy [69, 70]. So they are yet to be established in terms of reproducibility for phase purity (co-existence of morsel phase) and consistency of observed entropy. Also as they are having transition temperature slightly lower to ambient, they may still need to be optimized to obtain higher temperatures.

1.4.3. Thinfilms, nanoparticles, ribbons and single crystals

Engineering of microstructure of the materials, with enhanced surface area ratio, has helped in enhancement of the magnetocaloric effect in some of the materials (oxides and

intermetallics). In such regard lot of trials have been made to obtain nanoparticles [71], microstructure (ribbons in particular) [72], thin films [73] and so on. Thin films of magnetocaloric materials are shown to be potential for local cooling of processors in supercomputers used for high end computing.

Nanoparticles of $Pr_{0.7}Sr_{0.3}MnO_3$ are reported to show higher entropy change ($T_C \approx$ 235K ΔS = 3J/kg K, ΔH=2T) compared to their bulk counterpart [71]. $Ba_2Fe_{1+x}Mo_{1-x}O_6$ nonorods prepared by wet chemistry which assure high stoichiometry and homogeneity compared to samples synthesized by conventional techniques exhibit sharper transition and higher entropy change [74]. For x=0 the entropy observed in case of nano rods is 1.54 J/kgK around T_C = 349 K as compared to samples from solid state synthesis which show 1.09 J/kgK under applied field change of 10k Oe. Such effect does not follow same trend in all case for instance in case of $La_{1.4}Ca_{1.6}Mn_2O_7$ samples obtained by sol-gel process showed way low magnetocaloric effect compared to the bulk once [75].

1.5. Progress in device development

With the knowledge of materials nature – physical properties, chemical stability and limitations implied thereby – the next obvious step is the designing and implementation of the material into application. Here is when the engineering play key role from device designing to implement materials towards obtaining fine working unit. This section brings together prototypes proposed and developed in order to mimic a complete functional unit and hence aid evaluation of any material for its magnetocaloric refrigeration potential. It is worth to acknowledge the efforts from numerical modeling groups in complement explanation of experimental results such as magnet field strength, heat extract/transport, distribution of entropy with in material and so on [76]. Such modeling is essential in understanding, optimizing design as well as performance of the prototype/working unit. However here we do not include details of any of these modeling, as it is in divergent direction to that of the scope of the thesis [30, 77].

1.5.1. Prototypes and Magnetocaloric refrigeration realized

Initial stage reciprocating magnetic refrigerators was tested back in 1979 for operating in temperature range of 2 to 4K [2]. The working material in this prototype was $Gd_2(SO_4)_3 \cdot 8H_2O$. Thereafter magnetocaoric refrigeration protoype desiging and testing has

established as an independent field of research bringing together material scientists and device engineering. There are several prototypes put forward by different research groups. It is worth mentioning, review by Bingfeng Yu et.al., where they bring together the magnetic refrigeration and heat pump prototypes operating in near room temperatures, which are established prior to 2010 [77]. This review not just mentions nearly 41 prototypes that were put forward but also gives detailed explanation of basic principle, design and working of some of them. We suggest reader to refer the review for more details. Here we are going to summarize the basic aspects differentiating the prototypes developed in the Table 3.

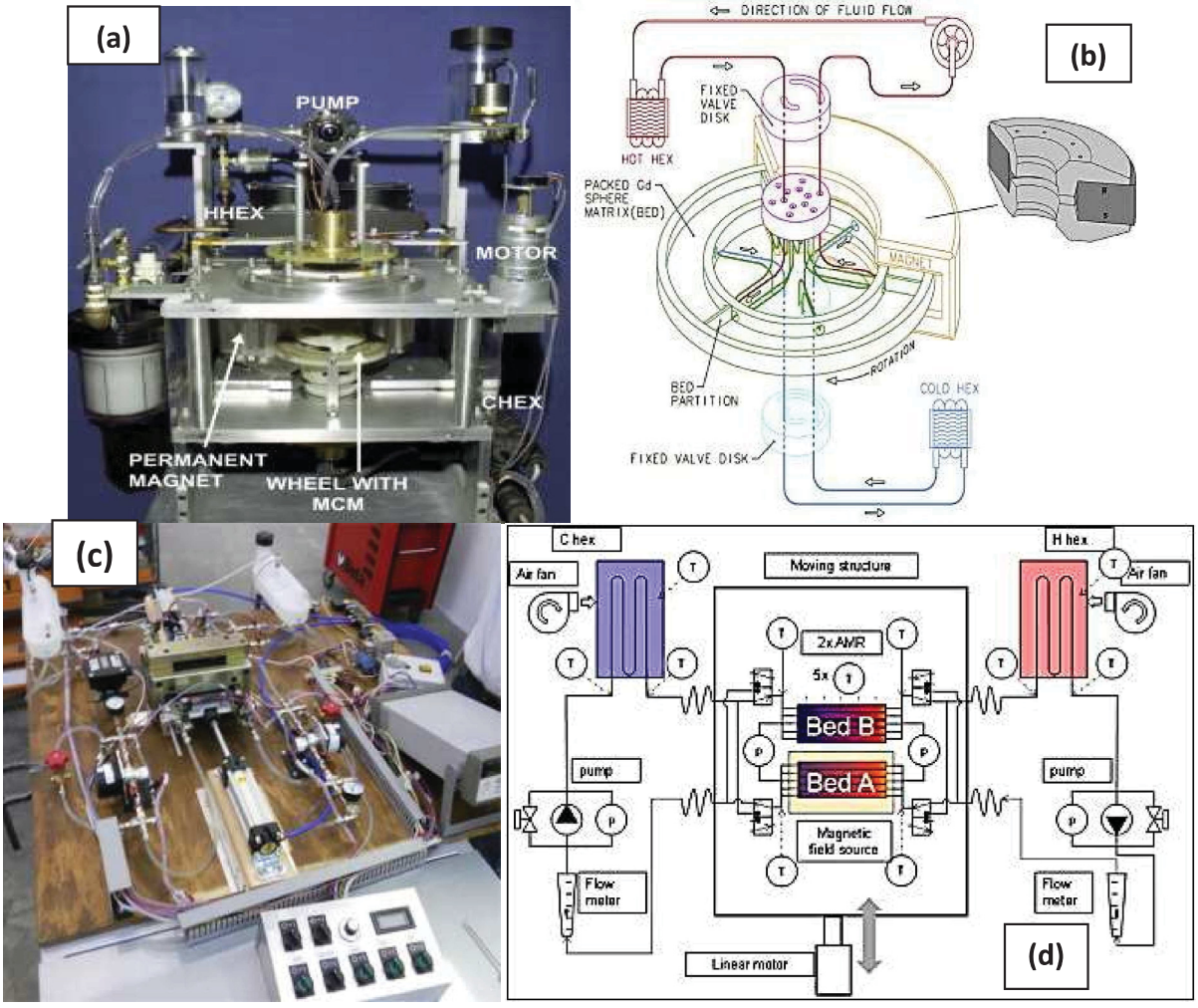

Figure 5: Rotating bed magnetic refrigerator (a) photographic image (b) schematic representation [78]. (c, d) Corresponding images for Linear reciprocating magnetic refrigerator [79].

The proposed prototypes/devices are differentiated mainly on their working principle and design. Based on design one can widely distinguish two types of magnetocaloric devices, *(i) rotary* (rotation of magnetocaloric material or rotation of magnetic field source) and *(ii) linear* (linear motion of magnetocaloric material or linear movement of the magnetic field

source). The external magnetic field is either an permanent magnetic or superconducting magnet.

Table 3 List of proposed prototypes proposed for near room temperature magnetocaloric devices

Prototype Name, Inventors, Lab or Company	Working Material	Operation mode	Magnet	Physical Quantities and Performance		Reference or Source
				ΔT K	Cooling power	
Astronautics Corporation of America(2001)	La-Fe-SiH_x		Rotating NdFeB B=1T		400 W	
Chubu Electronics and Toshiba refrigerator (2002/2003)	Gadolinium spheres	Reciprocating	Superconducting 4 T	21	100 W	Hirano N., Paper No. K7.002 Am. Phys. Soc. Meeting March 4, Austin, Texas
	$Gd_{1-x}Dy_x$ layered bed	Reciprocating /rotary	Rotating perm 0.6/0.76T	27/10	40/60 W	
Magnetocaloric Demonstrator Prototype (MDP) Cooltech Applications	(2007) Gadolinium plates (80 g Gd) Tc=20°C		Rotating NdFeB 1T			
	(2013) GdTb (0.55 Kg)	2 AMR stages	1.3 Tesla	42		
Lab. D'Electrotechnique Grenoble, France	Gd foil	Reciprocating	0.8 T permanent	4	8.8	IEEE Trans. Magn. 30 3349 (2003).
Universida de Estadual de Campinas, Brazil	Gd pins and ethylalcohol as heat transport	Rotary 0.5Hz	2.3 T electro-magnet	11		

The photographic image and schematic diagram of the rotating bed magnetic refrigerator designed by Astronautics Corporation of America laboratory is presented in Figure 5 (a) and (b) [78]. A wheel/bed of magnetocaloric material (Gd) rotates continuously across assembly of permanent magnet (in form of arc). The MCM bed is in contact with two heat exchangers pumps (CHEX – cold heat exchanger) and (HHEX – hot heat exchanger) which contain heat transport fluid that facilitate the removal/transport of the heat generated during each magnetocaloric cycle. Figure 5 (c) and (d) display the photographic and

schematic diagrams for a linear reciprocating magnetic refrigerator [79]. The MCM is placed in the Bed A and Bed B, each of which is connected with heat exchanger C hex, H hex. A source of magnetic field (T – block in faint yellow just below Bed A) moves linearly between each of the MCM Bed, and the fluid is pumped alternatingly to transport the heat generated during MCE cycle.

One main fact to be noticed irrespective of the configuration is the necessity of the heat transport medium to transport the heat generated by the material into the refrigeration space or the heat sink. The most preferred medium in this case is fluid with good heat transport properties and high physical-chemical stability with time. The material used in most of the case is predominantly the Gd-based material or La-Fe-Co-Si based intermetallics.

Several models have been put forward with very much improved design, accuracy and performance. C R J Bahl et.al, report a versatile linear magnetic refrigeration test device built based on principle of active magnetic regenerator (AMR). They argue that their device allowed variation and control of many experimental parameters (heat transfer fluid – direction/speed; magnitude of applied magnetic field; cycle timing variation). They test MCE of sheets of gadolinium under different experimental conditions that is mentioned. Further they optimize the design of the test device based on results from two-dimensional numerical model [80].

1.5.2.Performance or ageing

In the couple of paragraph to follow, we summarize the efforts that have been made to test material in either on prototype d or magnetocaloric tester under much realistic environment – filed, stress and flow of fluid for moderate duration. Such testing will address the '*performance*' of a material in real time application. Before winding the subsection, very few experiments that have tried to address 'ageing' or corrosion of the magnetocaloric materials after exposing to heat transport fluid are also briefed. These experiments will address the '*stability'* of the material with time. Any given material should exhibit equal degree of better 'performance' and 'stability' if it has to be considered for potential in application.

Considering the complications involved in characterizing magnetocaloric materials especially when the observed entropy change involves contributions from different phenomenon like magnetic, lattice and orbital. It is advised to grade the material in terms of direct temperature change observed. With most of the prototypes offering precise

characterization factors/values, one can explore them to characterize MCM's. Also this will help to evaluate physical and chemical stabilities of material under working environment. We shall recollect results on some of the potential materials that have been subjected in magnetocaloric testers. Olivier Gutfleisch measured adiabatic temperature (ΔT_{ad}) change of $La(Fe,Si)_{13}$ samples for several cycles employing direct measurements technique [81]. The $LaFe_{11.6}Si_{1.4}$ bulk sample loses the mechanical integrity during cycling and broke eventually after 4th cycle. It was further demonstrated that by using porous material with slightly reduced performance, it was able to maintain the mechanical stability.

V Hardy et. al. have recently produced in large scale the perovskite manganite, $Pr_{0.65}Sr_{0.35}MnO_3$, and subjected to test on magnetic refrigeration system in order to evaluate the potential of the material in applications [82]. This material showed magnetocaloric figure of merits close to that of the prototype material Gd. Alongside they had good stability with time with no or minimal damages. The results will be further discussed in detail in chapter 4.

Very few attempts are made to address the possible reactions that occur for the material due to interaction of working fluid with the MCM. First report came from Canepa et. al. where they subject different gadolinium based materials to flux of typical heat transport fluids, water and air, for about one year [83]. Their choices of materials for the study are Gd, $Gd_5Si_{1.9}Ge_{2.1}$ and $Gd_{75}Cd_{25.}$ The other report is on La-Fe-Co-Si based intermetallic reported by Min Zhang et al [84]. These two reports will be detailed in the introduction of chapter 2.

1.6. The blue print – preview of the thesis

One of the most common features on almost every prototype proposed is the transfer of heat from MCM into refrigeration space by using transport fluid. There are not much work dedicated towards understanding the interaction of such fluid with material and further consequence of the same on material. The performance and stability of different promising material against the flux of working fluid is artificially mimicked and its effect on surface of the working material is studied. Much concentration is paid on the microstructural changes on surface that can explain the phenomenon of corrosion. The physical damage such as erosion that can occur from the exposure of material to the flux of heat transport fluid is also investigated. For the choice materials we consider the factors that they exhibit reasonable, reproducible MCE around room temperature (≈300K), environmental friendly, low toxic, and

ease for manufacture scaling. They were, as well, from different class of materials - oxides and intermetallics - to make our study quite generalized and versatile.

Taking into account the amount of raw materials needed if the composition is realized in application it is important in capitalistic view to consider lower cost of element along with higher elemental abundance (Figure 6). Further for the reproducibility in industrial scale, the cost of manufacturing also needs to be accounted. Cost of few of the materials is also mentioned in Table 1(highlighted in red). So is the choice of the heat transport fluid which needs to satisfy several key points - low cost, low toxicity, non-flammable, non-corrosive, biodegradable, good thermal conductivity, low viscosity for easy flow as well as stability against all possible external stress (magnetic field, pressure)[‡].

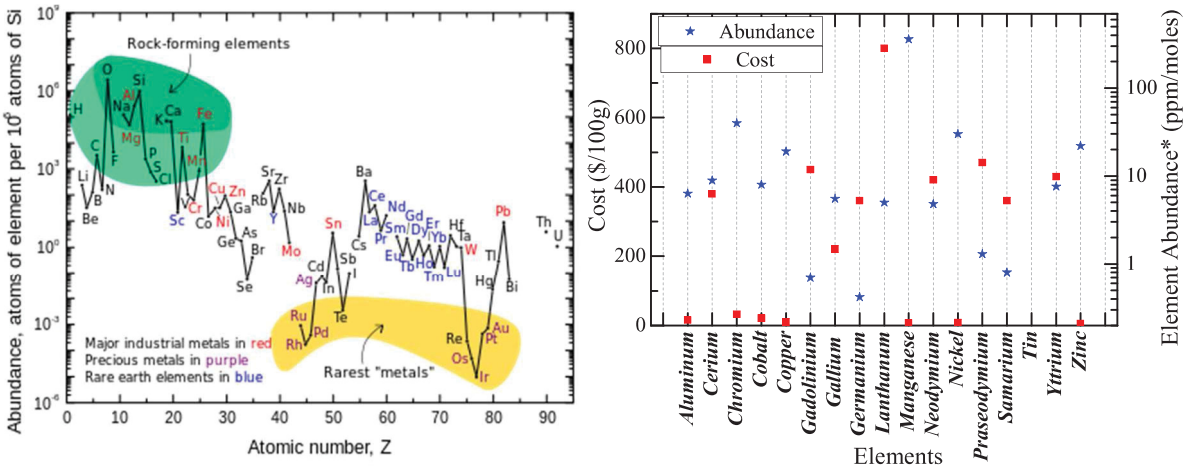

Figure 6 : Left - Relative abundance of elements in earth's upper continental crust (WebElements.com, Israel Science and Technology Homepage, Jefferson Lab). Right panel: Cost and abundance of the elements - For simplicity, the lower the height of red solid square and higher that of blue solid star the better the element for large scale production [Data from Chemicool Periodic Table. Chemicool.com. 18 Oct. 2012].

Table 4 summarizes the physical properties of different fluids which have potential thermal transport features. One fluid which tops most of the credibility's listed is non-other than the deionized water. Such facts indeed justify the choice of water as transport fluid in most of the prototypes that were discussed previously in section 1.5. All these prompt us to consider deionized water as thermal transport fluid in our initial tests.

Table 4 : Physical properties of few thermal transport fluids

Fluid	Physical properties					Cost	Remarks
	Viscosity† 10^{-6} m^2/s	Boiling °C	Freezing °C	Heat Capacity J/kg K	Thermal conductivity $W\ m^{-1}\ K^{-1}$	€/l	
Generic							
DI Water	1	100	0	4.18	0.609		<4%(NaCl+$MgCl_2$+$CaCl_2$)
Air				1.007	0.0262		300K, (N,21%O+0.93% Ar+0.04%CO_2) (1 atm)
10% Ethanol +DI H_2O	1.23	133 to 145	-9	4.33	0.52		pH = 12;
Ethyl alcohol	1.5	79	-117		0.171		Ethanol
Methyl alcohol	0.75	65	-98		0.202		Methanol
Saturated Ammonia (NH_3)	266	-33	-78		0.507		
Commercially available							
Freon R11 Freon R12					0.093 0.071		
Mineral oil (VG2)			-7.5	1.6	0.16		
Alcohol based							
2-Propanol							
Propylene glycol	5	-60	189	2.5	0.20		
Ethylene glycol	18	198	-11	2.39	0.258		
Glycerine	1200	180	20		0.285		
Glycerol			-15	3.97	0.481		
Other miscellaneous salts solution							
Sodium Chloride					6.5		
Potassium hydroxide							
Virgin Olive Oil	0.93			2.0	0.17		

†Kinematic viscosity: cSt - centistokes (cgs physical unit) 1cSt = 1 $mm^2 \cdot s^{-1}$ =$10^{-6} m^2 \cdot s^{-1}$ (SI physical unit) ‡Doctoral Thesis Åke Melinder, KTH, Sweden (2007)

For better visualization entropy curves from literature for different materials (both from intermetallics & oxides) are plotted in Figure 7. Keeping in mind the most tested material being Gd-based material we wish to investigate ageing on one material from this family. Also comparing the price and other aspects discussed earlier we have made $Gd_6Co_{1.67}Si_3$ as our choice from traditional Gd-based family. As it was well characterized and reproduced several times from our group as well as by few others. We are able to synthesis the desired compound and start the ageing treatment on the material. This allows us sufficient time with in the period of thesis to perform ageing for reasonable period, follow up with possible remedies that might reduce or stop the damage that was caused for the material during the first run.

Heusler alloy which are not yet subjected to such ageing test, with its unique features of first order transition and giant magnetocaloric effect convey us to choose them as one of the potential material. As the synthesis condition and heat treatments play crucial role on observed physical properties, we have spent some time to standardize the conditions of

$Ni_2Mn_{0.75}Cu_{0.25}Ga$ before actually subjecting the material for age testing. During optimization we detail the effect of Mn-concentration and microstructure of the sample on the nature of transition and magnitudes of observed entropy.

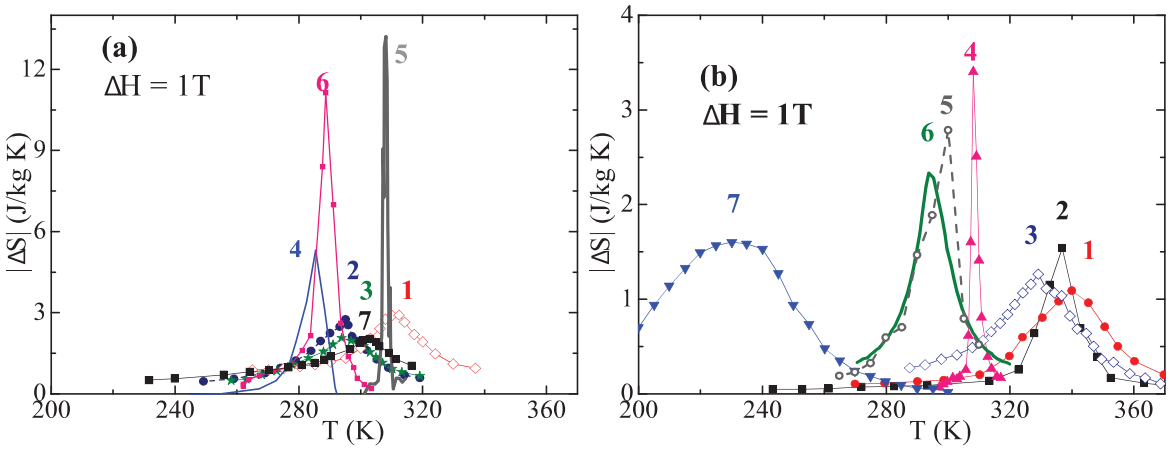

Figure 7: Total entropy change observed around room temperature in case of few selected materials (a) Intermetallics: *1 GdH; 2 Gd metal; 3 Nano Gd; 4 $Ni_{50-x}Co_xMn_{35}In_{15}$ ribbons; 5 $Ni_2Mn_{0.75}Cu_{0.25}Ga$; 6 $Mn_{1.28}Fe_{0.67}P_{0.48}Si_{0.52}$; 7 $Gd_6Co_{1.67}Si_3$* (b) Oxides: *1 bulk Ba_2FeMoO_6; 2 nano Ba_2FeMoO_6; 3 $SrFe_{0.5}Co_{0.5}O_3$; 4 $La_{0.8}Ag_{0.2}MnO_3$; 5 $La_{0.78}Ag_{0.22}MnO_3$; 6 $Pr_{0.65}Sr_{0.35}MnO_3$; 7 nano $Pr_{0.7}Sr_{0.3}MnO_3$*

If we recall section 1.4.2 and table 2, oxides with potential room temperature MCE possibly are: $La_{2-2x}Ca_{1+2x}Mn_2O_7$ or $La_{1-x}Ag_xMnO_3$. For comparison entropy curves from literature for different oxide materials are plotted in Figure 7 b. These materials however pose few questions about reproducible giant magnetocaloric, presence of impurity or competing phases [85]. Encounter of such difficulties on other phase encourage us to probe $R_{1-x}A_xMnO_3$ (R- rare earth lanthanides such as La, Pr, Nd, Sm; A – alkaline elements such as Sr, Ca, Ba) for ageing. From the magnetic phase diagram of these perovskite in literature we derive $Pr_{1-x}Sr_xMnO_3$ within the ferromagnetic metallic region, $0.3 \leq x \leq 0.45$ to be better candidate, as we can have composition with near room temperature transition over large range of x compared to any other combination of lanthanides and alkaline elements. The composition with moderate MCE figure of merit was first defined by preparing several samples with different x in the limit of interest and then the selected material was treated for ageing. In the context to obtain optimized composition we realize lack of convincing phase diagram (nuclear and magnetic) for the metallic-ferromagnet regime, so through detailed neutron diffraction experiments we have made efforts to solve nuclear and magnetic structures of the compositions $Pr_{1-x}Sr_xMnO_3$ ($0.25 \leq x \leq 0.45$). $Pr_{0.65}Sr_{0.35}MnO_3$ was tested

directly on a magnetic refrigeration system for its reliable performance by V Hardy et. al., [82]. Their preliminary results confirm the composition to exhibit reliable refrigeration capabilities as well the temperature spans reached were comparable to the so called room temperature magnetocaloric prototype material gadolinium. Such results convince our belief of $Pr_{1-x}Sr_xMnO_3$ to be moderate room temperature magnetocaloric material.

1.7. Reference:

1. Giauque, G.W., *A thermodynamic treatment of certian magnetic effects. A proposed method of producing temperatures considerably below 1 absolute.* Journal of American Chemical Society, 1927. **49**: p. 1864.
2. J. A. Barclay, O. Moze, and L. Paterson, *A reciprocating magnetic refrigerator for 2-4 K operation: Initial results.* Journal of Applied Physics, 1979. **50**: p. 5870.
3. Warburg, E., *Magnetische Untersuchungen.* Annalen der Physik, 1881. **249**(5): p. 141-164.
4. Weiss, P. and A. Piccard, *Le phénomène magnétocalorique.* J. Phys. Theor. Appl., 1917. **7**(1): p. 103-109.
5. Smith, A., *Who discovered the magnetocaloric effect?* The European Physical Journal H, 2013. **38**(4): p. 507-517.
6. Steven L Russek and C.B. Zimm, *Potential for cost effective magnetocaloric air conditioning systems.* International Journal of Refrigeration, 2006. **29**: p. 1366.
7. C P Bean and D.S. Rodbell, *Magnetic Disorder as a First-order Phase Transformation.* Physical Review, 1962. **126**: p. 104.
8. Nordblad, P., *MAGNETOCALORIC MATERIALS Strained relations.* Nature Materials, 2013. **12**: p. 11.
9. Anders Smith, et al., *Materials Challenges for High Performance Magnetocaloric Refrigeration Devices.* Advanced Energy Materials, 2012. **2**: p. 1288.
10. Banerjee, B.K., *On a generalised approach to first and second order magnetic transitions.* Physics Letters, 1964. **12**(1): p. 16.
11. Anthony Arrott and J.E. Noakes, *APPROXIMATE EQUATION OF STATE FOR NICKEL NEAR ITS CRITICAL TEMPERATURE.* Physical Review Letters, 1967. **19**: p. 786.
12. H. Oesterreicher and F.T. Parker, *Magnetic cooling near Curie temperatures above 300 K.* Journal of Applied Physics, 1984. **55**: p. 4334.
13. K. Kreiner, et al., *Evolution of the electronic specific heat and magnetic order in $(Fe_{1-x}Ni_x)Rh$.* Journal of Magnetism and Magnetic Materials, 1998. **177-181**: p. 581.

14. Xiao-Yu Zhang, Yajie Chen, and Z.-Y. Li, *Large magnetocaloric effect in chromium dioxide with second-order phase transition.* Journal of Physics D: Applied Physics, 2007. **40**: p. 3243.

15. V. V. Khovailo, et al., *Entropy change at the martensitic transformation in ferromagnetic shape memory alloys $Ni_{2+x}Mn_{1-x}Ga$.* Journal of Applied Physics, 2003. **93**: p. 8483.

16. H Kuwahara, et al., *A First-Order Phase Transition Induced by a Magnetic Field* Science, 1995. **270**: p. 961.

17. Carlo Paolo Sasso, et al., *Enhanced field induced martensitic phase transition and magnetocaloric effect in $Ni_{55}Mn_{20}Ga_{25}$ metallic foams.* Intermetallics, 2011. **19**: p. 952.

18. Li-Qin Yan, et al., *Field- and temperature-induced evolution of the magnetocaloric effect in $Ba_{0.3}Sr_{1.7}Co_2Fe_{12}O_{22}$ single crystals with heliconical magnetism.* Journal of Physics: Condensed Matter, 2013. **25**: p. 256006.

19. Scott, J.F., *Electrocaloric Materials.* Annual Review of Materials Research, 2011. **41**: p. 229.

20. A. S. Mischenko, et al., *Giant Electrocaloric Effect in Thin-Film $PbZr_{0.95}Ti_{0.05}O_3$.* Science, 2006. **311**: p. 1270 - 1271.

21. Ch. Binek and V. Burobina, *Near-room-temperature refrigeration through voltage-controlled entropy change in multiferroics* Applied Physics Letters, 2013. **102**: p. 031915.

22. P. O. Castillo-Villa, et al., *Caloric effects induced by magnetic and mechanical fields in a $Ni_{50}Mn_{25-x}Ga_{25}Co_x$ magnetic shape memory alloy.* Physical Review B, 2011. **83**: p. 174109

23. Erell Bonnot, et al., *Elastocaloric Effect Associated with the Martensitic Transition in Shape-Memory Alloys.* Physical Review Letters, 2008. **100**: p. 125901.

24. Ya. Mudryk, et al., *Polymorphism of $Gd_5Si_2Ge_2$ The equivalence of temperature, magnetic field, and chemical and hydrostatic pressures.* Physical Review B, 2005. **71**: p. 174104.

25. Suheyla Yuce, et al., *Barocaloric effect in the magnetocaloric prototype $Gd_5Si_2Ge_2$.* Applied Physics Letters, 2012. **101**: p. 071906.

26. Gerald Mahan, Brian Sales, and J. Sharp, *THERMOELECTRIC MATERIALS: NEW APPROACHES TO AN OLD PROBLEM.* Physics Today, 1997. **50**: p. 42-47.

27. S. Backhaus and G.W. Swift, *A thermoacoustic Stirling heat engine.* Nature, 1999. **399**: p. 335 - 338.

28. Swift, G.W., *Thermoacoustic Engines and Refrigerators.* Physics Today, 1995. **48**: p. 22 - 28.

29. Daniel A. Russell and P. Weibull, *Tabletop thermoacoustic refrigerator for demonstrations.* American Journal of Physics, 2002. **70**: p. 1231 - 1233.

30. Franco, V., et al., *The Magnetocaloric Effect and Magnetic Refrigeration Near Room Temperature: Materials and Models.* Annual Review of Materials Research, 2012. **42**(1): p. 305-342.

31. M.E. Wood and W.H. Potter, *General analysis of magnetic refrigeration and its optimization using a new concept: maximization of refrigerant capacity.* Cryogenics, 1985. **25**: p. 667.

32. Fabio Canepa, Myrta Napoletano, and S. Cirafici, *Magnetocaloric effect in the intermetallic compound Gd_7Pd_3.* Intermetallics, 2002. **10**: p. 731.

33. Bernd Wolfa, et al., *Magnetocaloric effect and magnetic cooling near a field-induced quantum-critical point.* PNAS, 2011. **108**: p. 6862.

34. Weiss, P., *Le phénomène magnéto-calorique.* J. Phys. Radium, 1921. **2**(6): p. 161-182.

35. B R Gopal, R Chahine, and T.K. Bose, *A sample translatory type insert for automated magnetocaloric effect measurements.* Review of Scientific Instruments, 1997. **68**: p. 1818 - 1822.

36. Cui, W., W. Liu, and Z. Zhang, *The origin of large overestimation of the magnetic entropy changes calculated directly by Maxwell relation.* Applied Physics Letters, 2010. **96**(22): p. 222509-3.

37. A M Aliev, A B Batdalov, and V.S. Kalitka, *Magnetocaloric Properties of Manganites in Alternating Magnetic Fields.* JEPT Letters, 2009. **90**: p. 663 - 666.

38. J Kamarád, J Kaštil, and Z. Arnold, *Practical system for the direct measurement of magneto-caloric effect by micro-thermocouples.* Review of Scientific Instruments, 2012. **83**: p. 083902.

39. O. Tegus, Bao Li-Hong, and S. Lin, *Phase transitions and magnetocaloric effects in intermetallic compounds MnFeX (X=P, As, Si, Ge).* Chinese Physics B, 2013. **22**: p. 037506.

40. Porcari, G., et al., *Convergence of direct and indirect methods in the magnetocaloric study of first order transformations: The case of Ni-Co-Mn-Ga Heusler alloys.* Physical Review B, 2012. **86**(10): p. 104432.

41. O. Tegus, et al., *Magnetic-phase transitions and magnetocaloric effects.* Physica B, 2002. **319**: p. 174.

42. Barcza, A., et al., *Giant Magnetoelastic Coupling in a Metallic Helical Metamagnet.* Physical Review Letters, 2010. **104**(24): p. 247202.

43. K A Gschneidner Jr, V K Pecharsky, and A.O. Tsokol, *Recent developments in magnetocaloric materials.* Reports on Progress in Physics, 2005. **68**: p. 1479.

44. Zhong, W., C.-T. Au, and Y.-W. Du, *Review of magnetocaloric effect in perovskite-type oxides.* Chinese Physics B, 2013. **22**(5): p. 057501.

45. Etienne Gaudin, et al., *Structural and Magnetocaloric Properties of the New Ternary Silicides $Gd_6M_{5/3}Si_3$ with M = Co and Ni.* Chemistry of Materials, 2008. **20**: p. 2972.

46. Niu, X.J., et al., *Crystallography, magnetic properties and magnetocaloric effect in $Gd_4(Bi_xSb_{1-x})_3$ alloys.* Journal of Magnetism and Magnetic Materials, 2001. **234**(2): p. 193-206.

47. Britt Rosendahl Hansen, et al., *Properties of magnetocaloric $La(Fe,Co,Si)_{13}$ produced by powder metallurgy.* Journal of Magnetism and Magnetic Materials, 2010. **322**: p. 3447-3454.

48. Gama, S., et al., *Pressure-Induced Colossal Magnetocaloric Effect in MnAs.* Physical Review Letters, 2004. **93**(23): p. 237202.

49. Kreissl, M., et al., *The influence of atomic order on the magnetic and structural properties of the ferromagnetic shape memory compound Ni_2MnGa.* Journal of Physics: Condensed Matter, 2003. **15**(22): p. 3831.

50. Igor Dubenko, et al., *Magnetocaloric effectsin Ni–Mn–X based Heusler alloys with X= Ga, Sb,In.* journal of Magnetism and Magnetic Materials, 2009. **321**: p. 754.

51. Stadler, S., et al., *Magnetocaloric properties of $Ni_2Mn_{1-x}Cu_xGa$.* Applied Physics Letters, 2006. **88**(19): p. 192511.

52. Gajdzik, M., et al., *Strongly enhanced Curie temperature in carbon-doped Mn_5Ge_3 films.* Journal of Magnetism and Magnetic Materials, 2000. **221**(3): p. 248-254.

53. Lyubina, J., et al., *La(Fe,Si)$_{13}$-based magnetic refrigerants obtained by novel processing routes.* Journal of Magnetism and Magnetic Materials, 2009. **321**(21): p. 3571-3577.

54. Krautz, M., et al., *Reversible solid-state hydrogen-pump driven by magnetostructural transformation in the prototype system $La(Fe,Si)_{13}H_y$.* Journal of Applied Physics, 2012. **112**(8): p. 083918.

55. Kuhn, L.T., et al., *Magnetic refrigeration at room temperature – from magnetocaloric materials to a prototype.* Journal of Physics: Conference Series, 2011. **303**(1): p. 012082.

56. Zener, C., *Interaction between the d-Shells in the Transition Metals. II. Ferromagnetic Compounds of Manganese with Perovskite Structure.* Physical Review, 1951. **82**(3): p. 403-405.

57. Suemitsu, M., et al., *Magnetocaloric effect of $La_{0.7-x}Pr_xCa_{0.3}MnO_3$ perovskites.* Journal of Alloys and Compounds, 2013. **551**(0): p. 195-199.

58. Nasri, M., et al., *Investigation of structural, magnetocaloric and electrical properties of $La_{0.6}Ca_{0.4-x}Sr_xMnO_3$ compounds.* Physica B: Condensed Matter, 2013. **408**(0): p. 104-109.

59. Debnath, J.C., et al., *Large magnetic entropy change near room temperature in $La_{0.7}(Ca_{0.27}Ag_{0.03})MnO_3$ perovskite.* Journal of Alloys and Compounds, 2011. **509**(8): p. 3699-3704.

60. Suresh Kumar, V. and R. Mahendiran, *A comparison of magnetocaloric effect in $Pr_{0.6}A_{0.4}Mn_{1-x}Cr_xO_3$(A=Ca and Sr; x= 0 and 0.04).* Solid State Communications, 2010. **150**(31–32): p. 1445-1449.

61. Xiaoyu Zhang, et al., *A potential oxide for magnetic refrigeration application: CrO_2 particles.* Journal of Physics: Conmdensed Matter, 2006. **18**: p. L559.

62. Takayoshi Takeda, Yasuo Yamaguchi, and H. Watanabe, *Magnetic Structure of $SrFeO_3$.* Journal of the Physical Society of Japan, 1972. **33**: p. 967.

63. S. Kawasaki, M. Takano, and Y. Takeda, *Ferromagnetic Properties of $SrFe_{1-x}Co_xO_3$ Synthesized under High Pressure.* Journal of Solid State Chemistry, 1996. **121**: p. 174.

64. P. Bezdicka, et al., *Preparation and Characterization of Fully Stoichiometric $SrCoO_3$ by Electrochemical Oxidation.* Z. anorg. allg. Chem., 1993. **619**: p. 7.

65. C. Yin, et al., *Unusual oxidation states give reversible room temperature magnetocaloric effect on perovskite-related oxides $SrFe_{0.5}Co_{0.5}O_3$.* Journal of Solid State Chemistry, 2011. **184**: p. 3228.

66. O. Toulemonde, et al., *Magnetic and Magnetocaloric Properties of $SrFe_{0.5}Co_{0.5}O_{3\pm y}$ upon Oxidation and Reduction: A Heterogeneous Distribution of the Oxidation States.* Chemistry of Materials, 2012. **24**: p. 1128.

67. Q. Zhang, et al., *Coexistence of inverse and normal magnetocaloric effect in A-site ordered $NdBaMn_2O_6$.* Applied Physics Letters, 2010. **96**: p. 242506.

68. W. Zhong, a., et al., *Magnetocaloric effect in ordered double-perovskite Ba_2FeMoO_6 synthesized using wet chemistry.* The European Physical Journal B, 2004. **41**: p. 213.

69. Hong Zhu, Hao Song, and YuHeng Zhang, *Magnetocaloric effect in layered perovskite manganese oxide $La_{1.4}Ca_{1.6}Mn_2O_7$.* Applied Physics Letters, 2002. **81**: p. 3416.

70. E. Tas¸ arkuyu, et al., *Effect of high temperature sintering on the structural and the magnetic properties of $La_{1.4}Ca_{1.6}Mn_2O_7$.* Journal of Alloys and Compounds, 2011. **509**: p. 3717.

71. Rabindra Nath Mahato, et al., *Large magnetic entropy change in nanocrystalline $Pr_{0.7}Sr_{0.3}MnO_3$.* Journal of Applied Physics, 2010. **107**: p. 09A943.

72. Dunhui Wang , et al., *Enhanced Curie temperature and magnetic entropy change in H-doped Gd ribbon* Journal of Alloys and Compounds, 2004. **377**: p. 72.

73. Moya, X., et al., *Giant and reversible extrinsic magnetocaloric effects in La0.7Ca0.3MnO3 films due to strain.* Nat Mater, 2013. **12**(1): p. 52-58.

74. W. Zhong, et al., *Magnetocaloric effect above room temperature in the ordered double-perovskite $Ba_2Fe_{1+x}Mo_{1-x}O_6$.* journal of Magnetism and Magnetic Materials, 2004. **282**: p. 151.

75. R. Dudric, et al., *Magnetic properties and magnetocaloric effect in $La_{1.4-x}Ce_xCa_{1.6}Mn_2O_7$ perovskites synthesized by sol–gel method.* Journal of Materials Science, 2012. **47**: p. 3125.

76. M. Risser, C.V., C. Muller, A. Noume, *Improvement and application of a numerical model for optimizing the design of magnetic refrigerators.* International Journal of Refrigeration, 2013. **36**: p. 950 - 957.

77. Bingfeng Yu, et al., *A review of magnetic refrigerator and heat pump prototypes built before the year 2010.* International Journal of Refrigeration, 2010. **33**: p. 1029.

78. Zimm, C., et al., *Design and performance of a permanent-magnet rotary refrigerator.* International Journal of Refrigeration, 2006. **29**(8): p. 1302-1306.

79. Tagliafico, L.A., et al., *Preliminary experimental results from a linear reciprocating magnetic refrigerator prototype.* Applied Thermal Engineering, 2013. **52**(2): p. 492-497.

80. C. R. H. Bahl, et al., *A versatile magnetic refrigeration test device.* Review of Scientific Instruments, 2008. **79**: p. 093906.

81. Lyubina, J., et al., *Novel Design of $La(Fe,Si)_{13}$ Alloys Towards High Magnetic Refrigeration Performance.* Advanced Materials, 2010. **22**(33): p. 3735-3739.

82. F. Guillou, et al., *Development of a new magnetocaloric material used in a magnetic refrigeration device.* EPJ Web of Conferences, 2012. **29**: p. 00021.

83. Canepa, F., et al., *Ageing effect on the magnetocaloric properties of Gd, $Gd_5Si_{1.9}Ge_{2.1}$ and on the eutectic composition $Gd_{75}Cd_{25}$.* Journal of Physics D: Applied Physics, 2008. **41**: p. 155004.

84. Zhang, M., et al., *Corrosion behavior of magnetic refrigeration material La–Fe–Co–Si in distilled water.* Journal of Alloys and Compounds, 2011. **509**(8): p. 3627-3631.

85. Joly V L Joseph, Joy P A, and D.S. K, *Comment on "Giant magnetoresistance of the $La_{1-x}Ag_xMnO_3$ polycrystalline inhomogeneous granular system" [Appl. Phys. Lett. 77, 723 (2000)].* Applied Physics Letters, 2001. **78**(23): p. 3747-3748.

Chapter 2

Microstructural changes due to ageing under deionized water flux on surface of $Gd_6Co_{1.67}Si_3$

2.1. Introduction

In recent years there was great quest for search of magnetocaloric materials for applications in ambient temperature cooling applications [1, 2]. This has contributed to discovery of many potential materials which promise high cooling power as summarized in the previous chapter. To know the criticality of these materials in terms of reproducibility and the stability in the real time applications it is necessary that the material is tested for strain-stress like the variations in temperature, magnetic field, environment, pressure and so on that it might undergo during the operation. In similar discipline it is also worth to investigate the interaction of working fluid (used to transfer heat from sample to work space), the so called *ageing effect*, of these materials in order to know the reliability and improve their performance (if necessary) with time [3-5]. There exist very few such investigations to date.

The first one was by Canepa *et al* who conducted a detailed ageing under influence of different refrigerant fluids (air, water, ethylene glycol, alcohol propylic and Freon 245) on Gd, $Gd_5Si_{1.9}Ge_{2.1}$ and $Gd_{75}Cd_{25}$ [3]. They reported that Gd and Gd-based intermetallics undergo corrosion followed by erosion which eventually decreases their performance with time of exposure to the fluid. Effort to protect the surface from the corrosion by gold coating also failed as after six month the corrosion is much enhanced even compared to the uncoated sample. They put forward concept of galvanic corrosion and explained formation of $Gd(OH)_3$ on the surface of the material. Interestingly, they observe no change in the magnetocaloric performance of their material until 100 days. More recently Min Zhang *et al* demonstrated a rapid corrosion followed by degradation of the compound $La(Fe_{0.94}Co_{0.06})_{11.7}Si_{1.3}$ even by just placing it in distilled water for 15 days [4]. They conclude the final product on surface due to corrosion to be La_2O_3, γ-Fe(OOH), $Co(OH)_2$ and H_2SiO_3. They also propose an electrochemical preferential corrosion that results in decrease of the weight. In contrast to previous study of Gd-based compounds, they observe a drastic decrease in maximum magnetic entropy for the La-based compound whereas such materials are still subject to extended studies [6]. In most of the prototypes and reports on ageing, distilled water has been highlighted to be better heat transport fluid comparing its physical properties with other heat transfer fluids (refer Table 4 of chapter 1), so we choose distilled water as working fluid in our experiments [7]. Furthermore, the use of pure distilled water as heat exchange medium without adding any antioxidant was done on purpose. Indeed, this choice allows us to

carefully study the chemical effects of the water on the material to be able to control them in the future.

$Gd_6Co_{1.67}Si_3$ material was reported with detailed structural, magnetic properties and more recently for its room temperature magnetocaloric effect (MCE) by E Gaudin *et al* [8, 9]. In brief, $Gd_6Co_{1.67}Si_3$ is one of the most thermodynamically stable compositions derived from ternary phase diagram of Gd-Co-Si. It crystallizes in hexagonal symmetry and adopts $Ce_6Ni_{1.67}Si_3$-type structure ($P6_3/m$ space group). $Gd_6Co_{1.67}Si_3$ exhibit second order ferromagnetic to paramagnetic transition at T_C = 294 K and this is the unique composition in this phase diagram to exhibit T_C around room temperature as most of the other compositions have lower T_C. Magnetic entropy change (ΔS= 2.9 J/K kg; ΔH= 2 T) and adiabatic temperature (ΔT= 3 K; ΔH= 2 T) change of this material are also quite promising considering the fact that $Gd_6Co_{1.67}Si_3$ contains only 56 at% of Gd. This particular composition has been successfully reproduced in terms of purity, magnetization and observed magnetocaloric effect by few other groups. [10, 11] $Gd_6Ni_{1.67}Si_3$ crystallizes in the same space group, exhibit similar entropy change, and adiabatic temperature change. But it has T_C= 310 K slightly higher to its iso-structural $Gd_6Co_{1.67}Si_3$. Neutron diffraction experiments show that magnetic contribution in these compounds is mainly from Gd, while Ni and Co showed negligible contribution to the magnetic properties. Considering all these facts, $Gd_6Co_{1.67}Si_3$ can be regarded as one of the potential material for room temperature application, so we decide to study its ageing effect. In this report we present x-ray diffraction, detailed microstructure changes, surface analysis and magnetization results during ageing of $Gd_6Co_{1.67}Si_3$ in flux of distilled water. In initial stage we compare parallel results on pure gadolinium to make better understanding of the observed phenomenon.

The first attempt of 'Ageing' in deionized water flux (imitated as heat transport fluid) on one of the promising room temperature MagnetoCaloric Material (MCM) $Gd_6Co_{1.67}Si_3$ is presented in this chapter. Initial part deals with the proposal of model for corrosion process based on microscopic studies and spontaneous electrochemical oxidation. In forthcoming section experimental confirmation of the proposed model based on ICP and X-ray photoelectron spectroscopy (XPS) are presented. Detailed XPS of $Gd_6Co_{1.67}Si_3$ is also presented in the context. Before concluding the chapter one of the possible solutions to reduce the corrosion by choice of different working fluid is demonstrated.

2.2. Synthesis and ageing setup

$Gd_6Co_{1.67}Si_3$ was prepared from high pure elements Gd (99%), Co (99.9%) and Si (99.9%). Each element cut and well-polished to remove possible oxidation on surface with maintained stoichiometry were arc melted in pure argon atmosphere. Arc melting was repeated two more time by reversing the ingot to ensure homogeneity. Further as prepared ingots were sealed in evacuated quartz tube and annealed at 800° C for month followed by air quenching. Thin slabs of approximately 1.5 – 2mm thinkness, 8mm length and 4 mm wide were cut from annealed sample using diamond anvil cutter (figure 1(a)) to perform the ageing. These slabs were well polished to ensure smooth surface and then exposed for ageing.

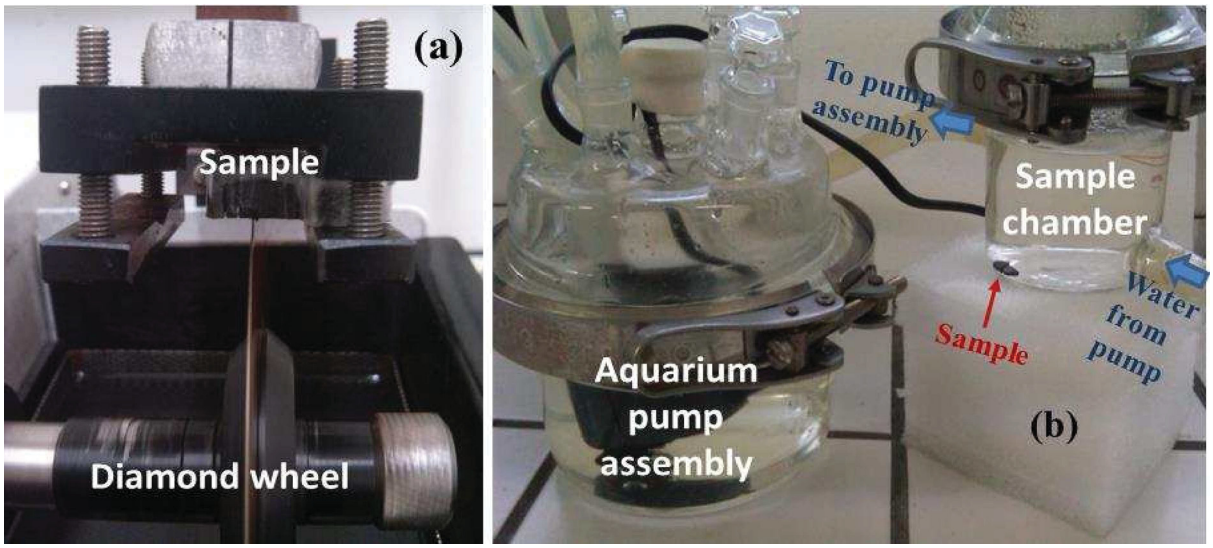

Figure 1 : (a) Sample cut into thin slabs with help of diamond wheel. (b) View of ageing set showing aquarium pump assembly and sample chamber.

For ageing, $Gd_6Co_{1.67}Si_3$ was treated with continuous constant flux of water, we use small aging set-up to artificially stimulate the heat transfer and this is conceptually similar to the one reported [4]. To brief, two cells one with aquarium pump other one containing sample are interconneted by tubing to facilitate commute of water flow(figure 1 b). Water is pumped from the reservoir (aquarium pump assembly) into sample chamber with constant flux with the aid of aquarium pump (EHEIM compact 300). Samples in the form of the slab presented in other cell experience this flux. The exposed slabs are periodically (every month) analyzed (chemical and physical) to understand systematically the effect of ageing.

Phase purity of as cast and annealed ingot was confirmed from powder x-ray diffraction performed on Philips 1050 diffractometer. Magnetic measurements were

performed on MPMS SQUID instrument (Quantum Design, USA). Elemental analysis was performed on Electron Probe Micro Analyzer (EPMA) (CAMECA SX 100 - Bruker AXS) equipped with 3 different spectroscopes WDS (Wavelength-Dispersive Spectroscopy), EDS (Energy-Dispersive Spectroscopy) and SDDD (Silicon Drift Detector). Depth profile analysis was carried out on Auger electron spectroscopy (VG microlab 310F) equipped with sputter ion gun. ICP-OES (Induced Couple Plasma – Optical Emission Spectroscopy) measurements were performed on Varian 720-ES. X-ray photoelectron spectroscopy (XPS) was performed using VG Scientific 220 i-XL ESCALAB spectrometer with a monochromatized AlKα source (hν=1486.6eV) at 70 W under pressure of 10^{-7} Pa in the chamber. The spot size is about 180 μm in diameter. The full spectra (0-1350eV) were obtained with constant pass energy of 150eV and high resolution spectra at constant pass energy of 40eV or 20eV.

2.3. Results and discussion

2.3.1. Structural Characterization

X ray diffraction (XRD) on powder of the annealed sample revealed phase purity. We are able to refine the structure in hexagonal *P6₃/m* space group with "$Ce_6Ni_{1.67}Si_3$" type structure as reported in the literature. [9] Figure 2(a) compares the X-ray diffraction on powder and thin slab of starting samples, showing broader peaks observed for slabs against sharp peak profile for powder. These broader x-ray patterns makes difficult to perform qualitative analysis. However, we are able to profile match them and the results are displayed in figure 2 (b) and (c). As prepared sample was profile matched with the proposed *P6₃/m* space group (a=b=11.838(1) Å, c=4.161(3) Å, α=β=90° and γ=120°). For aged samples we could only obtain reasonable profile fit after taking into account a Gd_2O_3 (*Ia-3*; a=b=c= 10.797(1) Å and α=β=γ=90°) [ICSD #41270] secondary phase. The Bragg position marked as A in Figure 2 c corresponds to $Gd_6Co_{1.67}Si_3$ phase while B the Gd_2O_3. Compared to $Gd_6Co_{1.67}Si_3$ such changes are better visualized on after exposure of gadolinium slab to water flux in figure 2(d). The Gd_2O_3 contribution is highlighted with '*' symbols, which are very low in the staring slab of Gd. Interestingly, our results highlight a corrosion phenomenon resulting in the formation of Gd_2O_3 oxide somewhat contrary to the formation of $Gd(OH)_3$ hydroxides in case of $Gd_5Si_{1.9}Ge_{2.1}$, $Gd_{75}Cd_{25}$, Gd-rich materials [3].

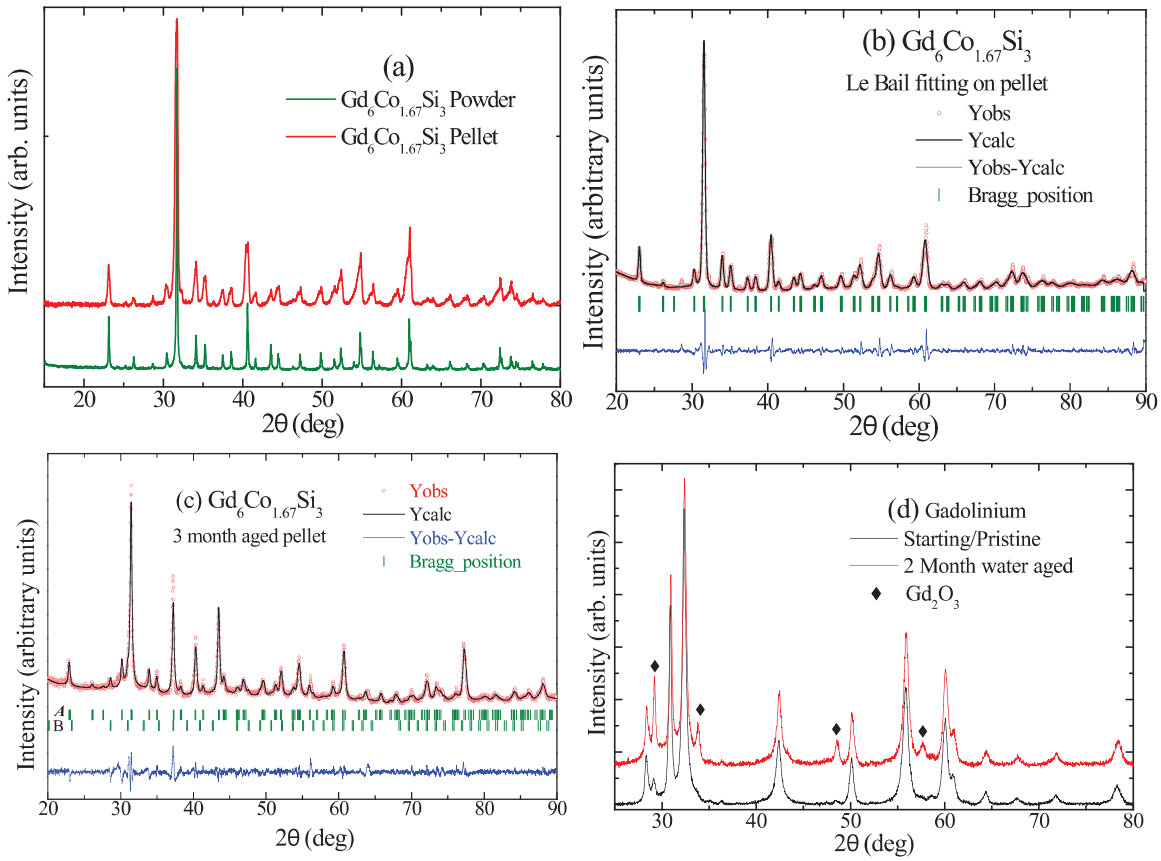

Figure 2:X-ray diffraction patterns: (a) comparing starting material in powder and slab form. Le Bail or profile matching for: (b) staring material, (c) 3 months aged. (d) Comparison of starting and 2 months aged Gd.

2.3.2. Microstructural studies

A. Electron Probe Microscope Studies

To well understand the surface morphology and to check the distribution on overall surface compositional changes during ageing we have performed EPMA, since only crystalline Gd_2O_3 is observed on XRD. Backscattering image of starting and three month aged sample shows clear change in morphology due to water flux and/or corrosion reactions, with smoother surface for starting (figure 3 a) and more rough surface morphology for aged sample (figure 3 b). We perform elemental analysis following atomic % mapping on starting slab. Despite some rich siliceous domains homogeneous elemental distribution is observed on entire surface (figure 3 c). The atomic mapping confirmed nominal composition $Gd_6Co_{1.67}Si_3$ all along scanned area (to note, the random oxygen signal observed is mainly due to exposure

of sample surface to atmosphere). While similar elemental mapping on 3 months aged sample display heterogeneous distributions of elements along with high oxygen signal (figure 3 d).

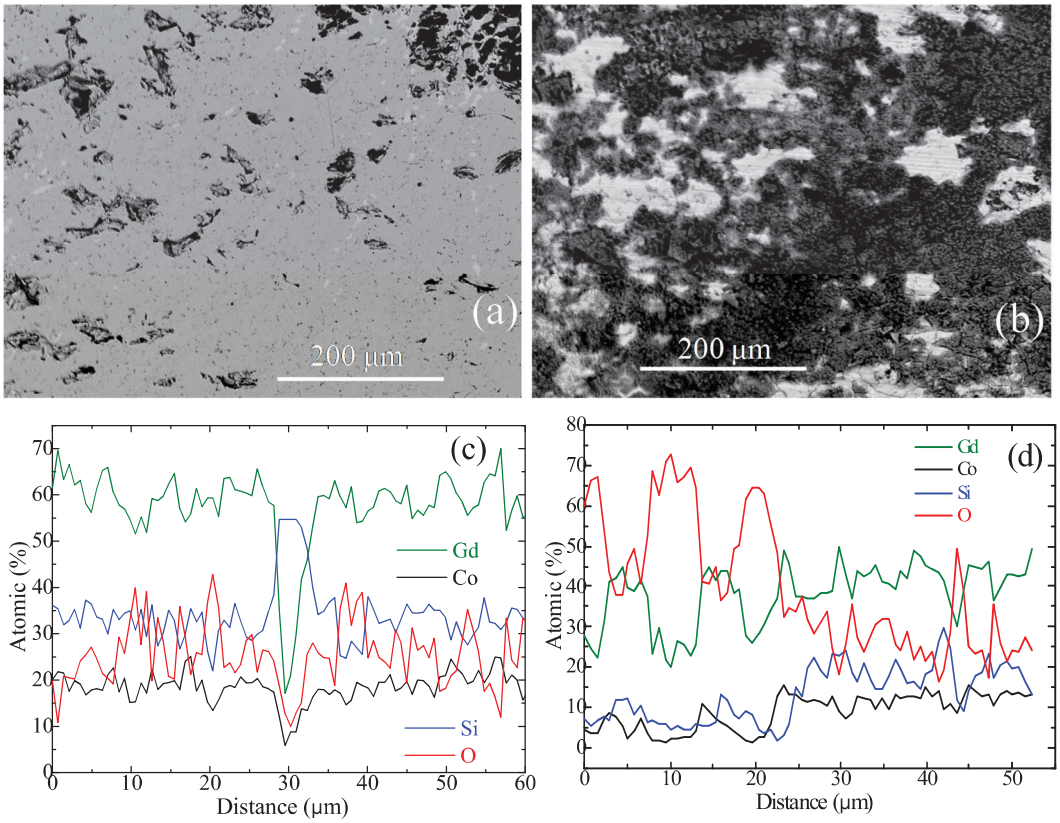

Figure 3 : Backscattered images of (a) starting and (b) 3 months aged samples obtained from EPMA. Elemental analysis along selected surface of the (c) starting and (d) 3 months aged samples.

To study the effect of ageing on microstructure and elemental distribution, more detailed experiments on two months aged sample were performed and the results are tabulated in figure 4(a-f). In some portion a valley like structure is highlighted in red-dotted line on figure 4 (a). This suggests an erosion process around grain boundary due to interaction of flux. Figure 4 (c – f) displays elemental mapping for all the constituent elements along with that of oxygen within the same area. One can notice that the elemental distribution is heterogeneous unlike starting composition which showed better homogeneity of composition with lower trace of oxygen throughout scanned area. While on aged (figure 4 b) there are $Gd_6Co_{1.67}Si_3$ phase poor region corresponding to the oxygen rich region. Atomic % mapping on selected region (containing both oxygen rich and oxygen poor region) was performed and results are displayed in figure 3 (b). Markings S and E correspond to the starting and end

point of the mapping. This mapping confirms that oxygen poor region corresponds to the original composition of $Gd_6Co_{1.67}Si_3$ and with careful analysis one can notice that oxygenated region is rich in Gd content compared to the content of Si or Co. This is in agreement with our XRD pattern matching with Gd_2O_3 crystallographic phase and with no contribution from either Si or Co.

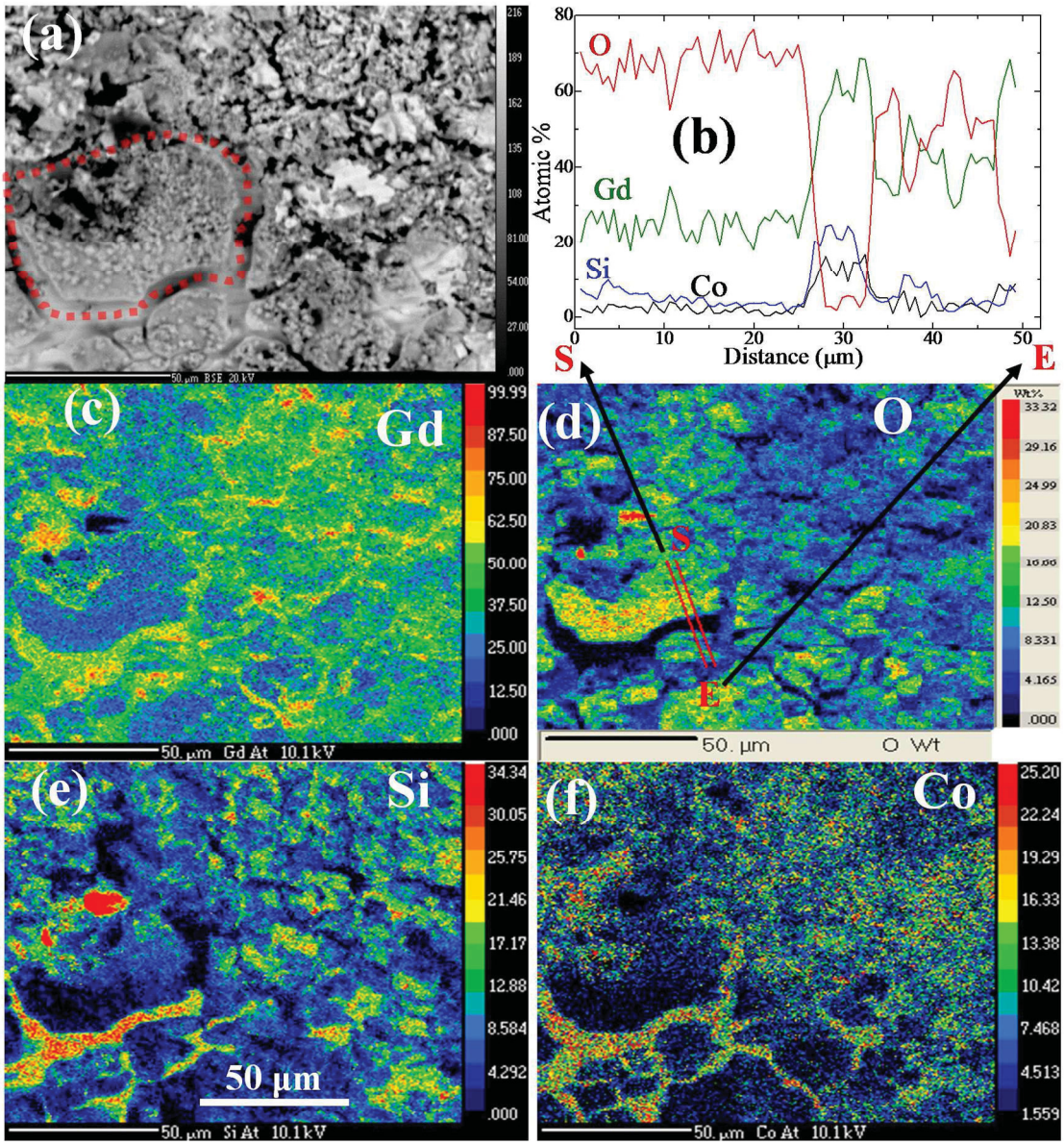

Figure 4: (a) Backscattered image of 2 months aged sample slab. Elemental mapping of: (c)Gd-Gadolinium, (d) O-oxygen, (e)Si-Silicon and (f)Co-Cobalt area under study is same as that of (a). (b) selected area elemental analysis in terms of atomic percentage (S refers to start point and E the End point).

B. Depth Profile Analysis by Auger:

We have further performed depth profile analysis using Auger spectroscopy. It will address whether the oxygen layer is constrained to the surface or is penetrated into the sample with time. Auger spectroscopy is equipped with ion sputtering chamber; sputtering facilitates controlled etching of surface and Auger spectroscopy help in elemental analysis. The elemental detection is based on the auger spectral analysis of the element under study, the instrument has depth resolution of around 2 to 5 nm which is advantage to obtain precise and systematic study along depth of corrosion. The photographic images of the starting and 2 months aged Gd slab are presented in figure 5 a. The staring pose shining smooth surface compared to the aged one where in some dark parts are observed suggesting possibility of partial surface oxidation. As seen in figure 5 (b), the depth profile on the pristine gadolinium show smaller layer (≈150 nm) of oxygen, after ageing for period of 2 months it has oxidation layer up to depth of 600 nm and confirms our previous results from XRD and EPMA.

The surface of as prepared sample $Gd_6Co_{1.67}Si_3$ shows surface oxidation up to 75 nm likely due to atmosphere exposure of sample (figure 5 (c)) as already seen on the previous section. However, for two months ageing this depth increase to around 800 nm and after three months exposure the depth of oxygen is around 1200 nm (figure 5 (d) and (e)). From these studies we propose that water flux results in formation of oxide layer, thickness of which increase with time of exposure. If one observe carefully on these histograms of aged sample (for example figure 5(d)), it can be noticed that on top layer (say up to 100 nm) there is only Si signal along with that of oxygen (marked with dotted line (i)). After which Gd signal increase along with decrease in Si signal and still there is no contribution in Co signal (some place up to dotted line (ii)). Only after 600 nm thickness we find nominal composition of starting material. Similar results were observed on different spots of the 2 months aged material. Based on these observations we propose that ageing leads to oxide formation on surface of the material which takes the form of "core-shell": the outer most layer to be SiO_x, followed by Gd_2O_3 as seen on XRD and the core to be the original composition of the material (figure 5 (f)).

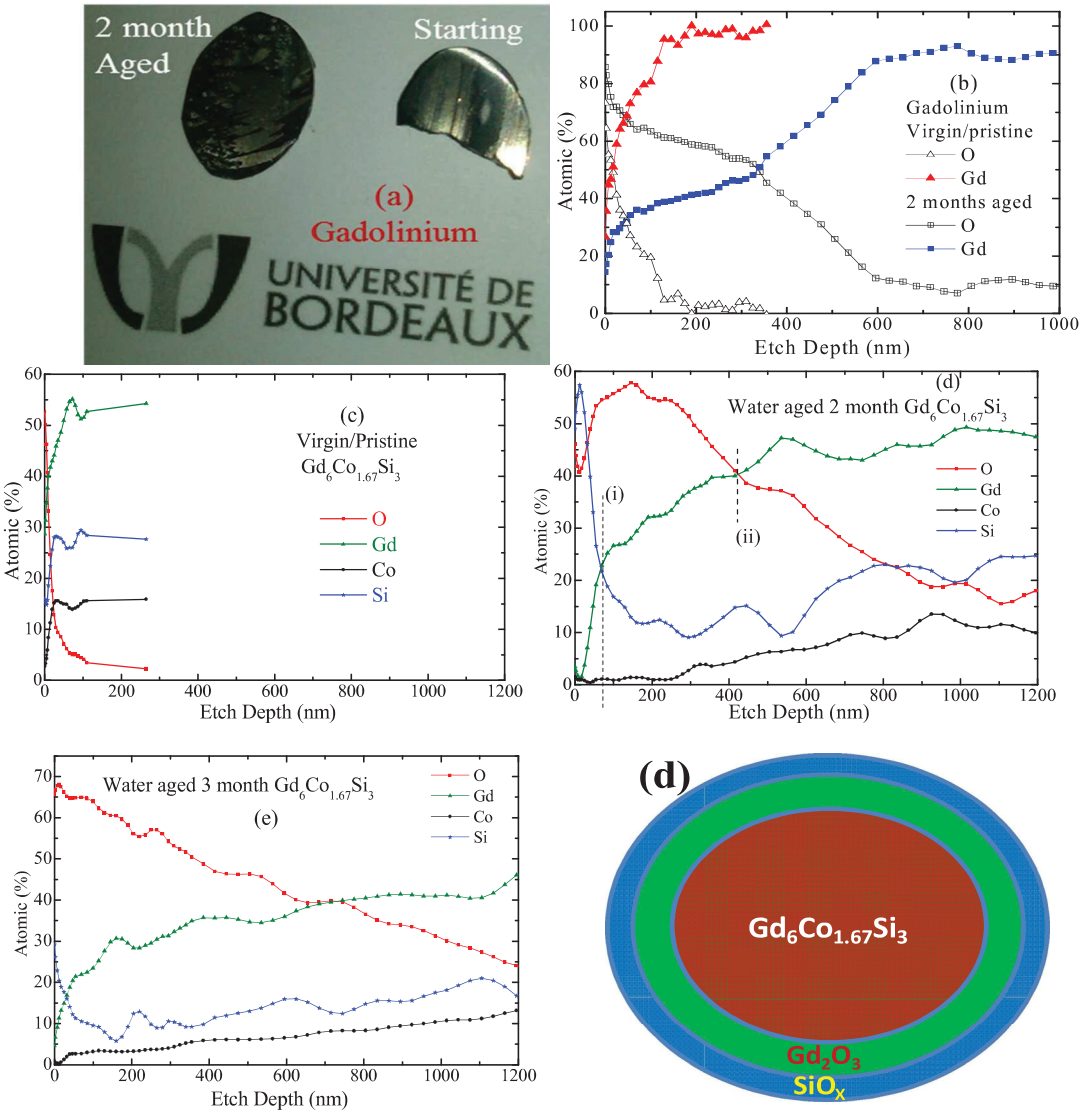

Figure 5: (a) photographic image of 2 month aged and starting Gadolinium (Gd). Depth profile using Auger spectroscopy on (b) Gd (aged and starting) followed by for $Gd_6Co_{1.67}Si_3$ (c) starting, (d) 2 months aged and (e) 3 months aged material. (f) Proposed core-shell model of formation of oxide layer on surface of the material.

2.3.3. Spontaneous electrochemical reaction:

As just introduced on the previous paragraph, flux of the working fluid introduces competition between corrosion and erosion phenomena. The oxidation of the surface can be explained based on the single metal corrosion phenomenon because of bubble O_2 which becomes the cathode, into the water introduced on the ageing set-up. The tendency for a reaction to occur follows the order of the electrochemical potentials that are tabulated in

Table 1. Based on their relative values, the overall corrosion can be suggested as follows. At initial stage cobalt metal on $Gd_6Co_{1.67}Si_3$ slab is corroded as further illustrated. Following the gamma rule electrochemical, the reaction between the most negative i.e., oxidation of Gd takes place with reduction of O_2 resulting in: $3O_{2(g)} + 2\ H_2O + 4Gd \rightarrow 12\ OH^- + 4Gd^{3+}$ …(7). Our coupled XRD and EMPA analyses unambiguously suggest that the expected Gd^{3+}_{aq} cation is replaced by the oxide Gd_2O_3 more stable than the hydroxide $Gd(OH)_3$ within our experimental conditions resulting in a passivation surface around the $Gd_6Co_{1.67}Si_3$ slab material. One can point out that Si can be corroded at different level of oxidation state. It follows the successive change in redox potential required for the spontaneous reaction from Si^{II}-O (E^0 = -0.8eV) → $Si^{IV}O_2$ (E^0= -0.9eV) → $Si^{IV}O_3^{2-}$ (E^0= -1.7eV). Such stepped corrosion can explain the time dependent SiO_x thickness along the total thickness of corroded layer and should introduced a Si heterogeneous oxidation state on the SiO_x sub-layer. And finally, from equation (1) and (2) we can obtain new equation (8) as, $O_{2(g)} + 2\ H_2O + 2Co \rightarrow 4\ OH^- + 2Co^{2+}_{(aq)}$ …(8) which will result in Co^{2+}_{aq} within water. This explaining the lack of cobalt on surface of the aged samples as observed on the deep profile analysis.

Table 1: Electrochemical reaction details for selected metals and metal oxides along with required potential (E^0). [12]

Oxidation/reduction	E^0 (eV)	Electrochemical reaction
O_2/OH^-	**+0.401**	$O_2 + 2H_2O + 4e^- \leftrightarrow 4OH^-$ **(1)**
Co^{2+}/Co	**-0.28**	$Co^{2+} + 2e^- \leftrightarrow Co$ **(2)**
SiO/Si	**-0.80**	$SiO + e^- + 2H^+ \leftrightarrow Si + H_2O$ **(3)**
$Si^{IV}O_2/SiO$	**-0.90**	$SiO_2 + 2e^- + 2H^+ \leftrightarrow SiO + H_2O$ **(4)**
$Si^{IV}O_3^{2-}/SiO$	**-1.697**	$SiO_3^{2-} + 4e^- + 4H^+ \leftrightarrow SiO + 2H_2O$ **(5)**
Gd^{3+}/Gd	**-2.30**	$Gd \Leftrightarrow Gd^{3+} + 3e^-$ **(6)**

The overall ageing hence results in the formation of core-shell like oxide layer on the pristine sample, the thickness of the such layer varies with ageing time. This can be illustrated on Figure 5 d and e, the lines marked as (ii) (crossover of Gd and O) around 400 nm in former case can be roughly considered as the thickness of Gd_2O_3 layer. With careful observation on Figure 5 e (further ageing) the same spot is shifted to around 700 nm. So ageing results in the growth of thin Gd_2O_3 layer around the parent phase. Such chemical nature change of Gd^{3+}

cation (from Gd^{3+}_{aq} to Oxide Gd^{3+}_{s} or hydroxyde Gd^{3+}_{s}) is known to be in relation with acidity decreases of the solvant when Pourbaix diagram is plotted. To definitely conclude on the single metal corrosion phenomenon, one must demonstrate the presence of $Co^{2+}_{(aq)}$ and $SiO_3^{2-}_{(aq)}$ within the water flux and a distribution of silicium oxidation state at the surface of the slab.

2.3.4. Chemical Analysis

A. ICP analysis

From above mentioned spectroscopic studies (section 2.2) we never come across the state of cobalt on the surface of the sample until we observe nominal composition, there are two possibilities: (i) Co dissipates into the material (Co vacancies) but this is not possible as the maximum Co occupancy is limited to 1.67 for this particular composition [8, 9]. As just suggested from spontaneous electrochemical reaction (equation (7)) the dissolution of Co_{aq} into the water flux is better possibility. To insure this possibility of corrosion of the material we performed ICP-OES analysis of the fluid from the ageing cell. Three trials of fluids from the sample chamber were withdrawn to perform the ICP study. In all of these three solutions we find higher content of cobalt in the fluid (Co/Gd =1.22 as compared to starting Co/Gd=0.28), this gives better picture of the overall effect of ageing. Interestingly, we also extract Si/Gd=0.86 against the starting Si/Gd=0.5 which suggest that Si is also corroded within is $SiO_3^{2-}_{(aq)}$ form from ICP of the fluid.

B. Chemical state by X-ray photoelectron spectroscopy (XPS)

In order to better understand the chemical state of each of the constituent element, detailed XPS analyses are performed. Considering the fact that there is no detailed study on parent compound $Gd_6Co_{1.67}Si_3$, we will first present detailed XPS analysis on the compound itself. Thereafter detailed XPS studies on aged samples will be presented.

The in-situ scratch facility with our XPS machine helps to get rid of surface contamination possibly due to atmospheric exposure of the material. This is demonstrated on pristine material which is not subjected to any ageing treatment as shown in figure below.

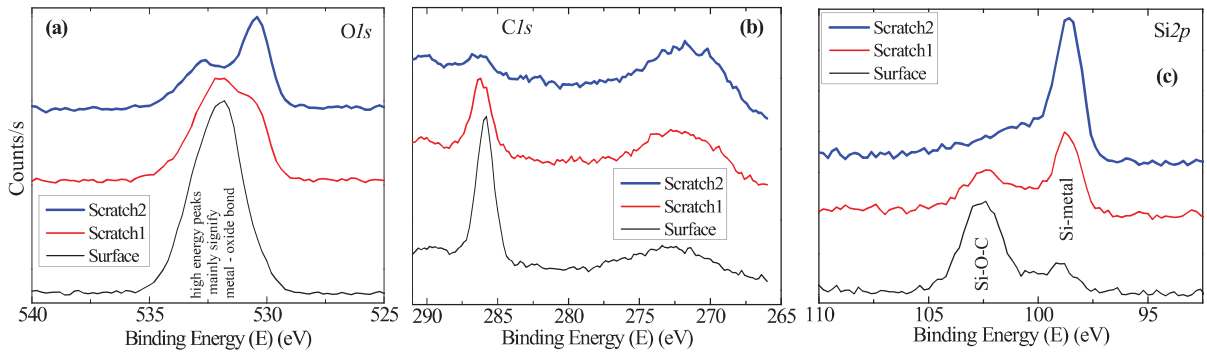

Figure 6: XPS spectra of (a) *O1s* (b) *C1s* and (c) *Si2p* on pristine $Gd_6Co_{1.67}Si_3$ demonstrating effect of scratching to remove carbon and oxygen contamination due to atmospheric exposure of sample.

In figure 6 (a - c), 'Surface' refer to spectra acquired on sample directly without any treatment, while 'Scratch1' and 'Scratch2' correspond to the consequent spectra after in-situ scratching first and second time. Even though the depth of scratch is no measureable as the scratching is done manually, by comparing to Auger spectroscopy one can have rough estimate of the position of depth. As evident from the figure (a, b), spectra from surface indicate large amount of carbon and oxygen which decrease with depth. Direct effect of the presence of these on the constitutional elements (Gd/Co/Si) of sample along same depth, for example Si is also demonstrated in figure 6 (c). Oxygen and carbon are non-constituent species of our material treated to be contaminant due to atmospheric exposure of the sample. One can also utilize ion sputtering for etching instead of manual scratch to get better precise depth information. However sample etching by sputtering can give rise to artifacts such as bombardment-induced damage resulting in broadening of peaks which directly effects factor analysis in data treatment [13]. As effects due to ageing are in submicron or nano-scale we have to also take into account possibility of sputter damage on corroded surface on the sample surface which hinder further qualitative analysis [14].

Chemical state of the Gd and $Gd_6Co_{1.67}Si_3$

X-ray photoelectron Spectroscopy was performed on pure gadolinium and pristine compound $Gd_6Co_{1.67}Si_3$ to know the initial chemical state of the constituent elements which will serve as reference to understand chemical state of aged material.

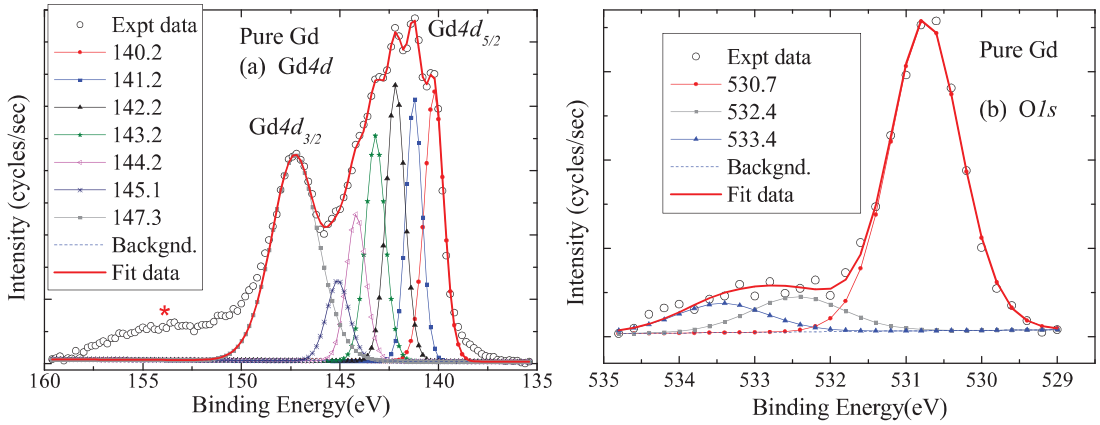

Figure 7: XPS spectra from pure gadolinium after removing carbon by 2 times in-situ scratch (a) *Gd4d* and (b) *O1s* spectra.

We have performed detailed qualitative chemical state analysis on the final scratched sample of pure Gd using least square fitting and the results are tabulated in figure 7. Our analysis is based on the phenomenological rule allowing the prediction of relative binding energy position depending on the degree of ionic and/or covalent character in the bonding of metal oxides. For example, from $ZrSiO_4$ to SiO_2 materials, an increase of both the O*1s* (531.3 eV → 532.7 eV) and Si*2p* (101.8 eV → 103.15 eV) features is seen in relation with the increase of the ionic character of the Si-O bonding [15].

4d Energy spectra of gadolinium, in general, exhibits two peaks Gd$4d_{5/2}$ and one broader Gd$4d_{3/2}$ (≈147.5 eV) [16]. These doublets correspond to ^{9}D final states and ^{7}D state and are separated by 5eV due to spin-orbit interactions. First peak Gd$4d_{5/2}$ exhibits mutiplet structure (seven peaks) which has been explained because of 4d-4f (super-Coster-Kronig) decay process in the final state. Figure 7 (a) displays Gd*4d* spectra for pure gadolinium after eliminating the carbon contamination. We are able to fit the spectra by considering all the possible splitting we are able to obtain all peaks proposed for ^{9}D final states and ^{7}D states. The remaining broad peak marked with '*' is the Plasmon energy-loss satellite that is observed in most of the lanthanides (Sc, Y, La, Eu). For O1s, the prominent peak is assigned to Gd-O bond (530.7 eV) [16], and smaller secondary broad peaks can be due to residual C-O bonding.

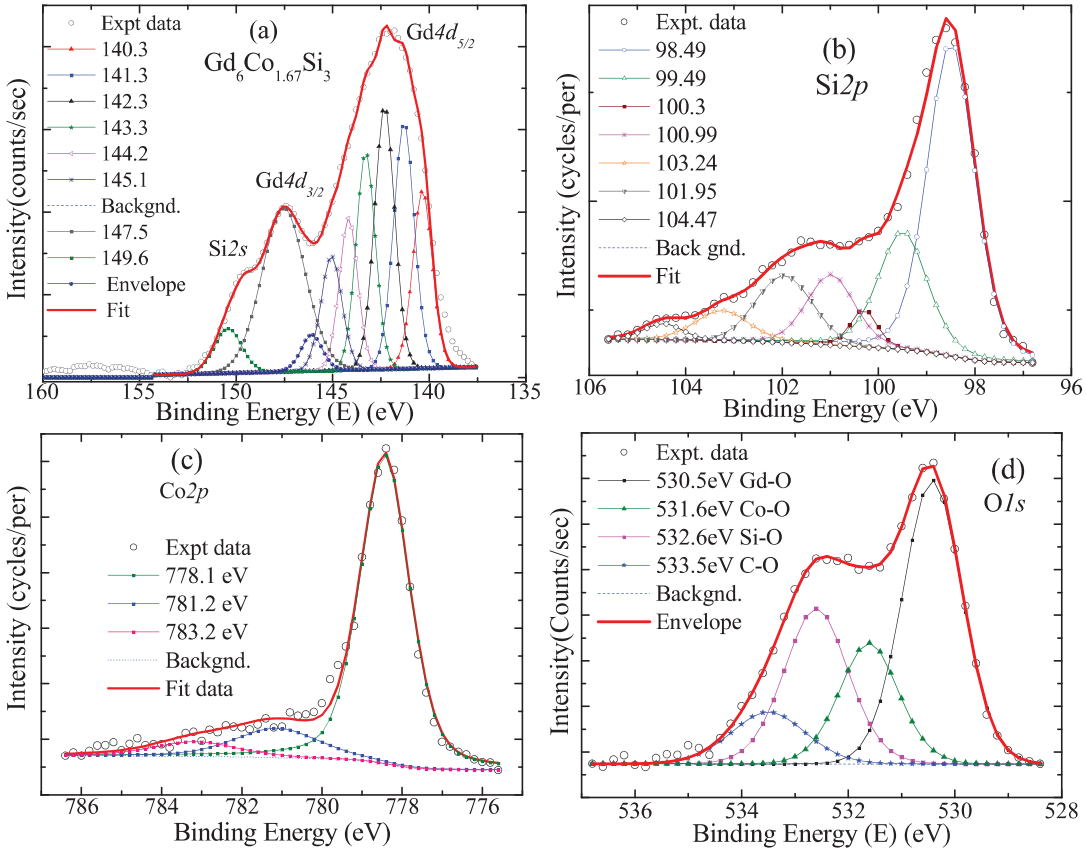

Figure 8: XPS spectra for pristine $Gd_6Co_{1.67}Si_3$ (c) Gd4d-Si2s, (d) Si2p, (e) Co*2p*, (f)O1s.

Much similar results are obtained on Gd*4d* from the pristine sample (Figure 8 a), along with Si*2s* (149.6eV), binding energy of which overlap with that of Gd*4d*. Silicon can have five different oxidation states namely metallic Si (designated here after as S^0), Si_2O (Si^1), SiO (Si^2), Si_2O_3 (Si^3) and SiO_2 (Si^4) [17]. Each of these individual oxidative states exhibit distinct peak positions features in Si*2p* energy spectra. Our analyses suggest that Si remain mostly in Si^0 configuration when dissolved in $Gd_6Co_{1.67}Si_3$ matrix, with smaller amount of S^1 and minor Si^2, S^3 spin-orbit state ((Figure 8 b).

Cobalt has fewer stable chemical states compared to silicon however the characterization can be tedious if proper care is not taken. Cobalt metal is characterized by two sharp peaks (Co$2p_{3/2}$ and Co$2p_{1/2}$) and on oxidation or hydration these peaks get broaden. These peaks also inherit with them smaller satellite structure due to Plasmon loss process.[18] Studies on different oxidation states of cobalt have confirmed unique positions and peaks shape [19]. Co-metal's photoelectron energy spectrum has one single, sharp peak for Co$2p_{3/2}$ (778.1eV) along with weaker satellite (781.1eV, 783.1eV). On oxidation to CoO $2p_{3/2}$ peak

broadens (780eV, 782.2eV) and intensity of satellite peak increase (785.5eV, 786.5eV). In case of $Co(OH)_2$ which has peak around 780.4eV and 782.2eV, the satellite peak is further pronounced and broadened (786eV, weaker 790.4eV). For Co_3O_4 main peak is characterized by three peaks (779.6, 780.9, 782.2eV) and relatively smaller satellite at higher energies (weaker 785.2, 789.5eV). From phenomenological treatment of Co*2p*$_{3/2}$ spectra of our sample data we infer that cobalt remain mostly in metallic form with preferable Co^{2+} state (Figure 8 c). Oxygen O*1s* spectra (Figure 8 d) with low intensity is observed even after removal of most of the carbon. We assign the four individual peaks to be linked to Gd-O as also seen on pure gadolinium, along with Co-O, Si-O and C-O from residual carbon.

Along corroded layer after three month ageing

To know the specific metal-oxide species that is formed on surface during ageing, especially the Si-O bonding and to corroborate it with a stepped corrosion proposed for silicon, detailed X-ray Photoelectron Spectroscopy (XPS) measurements are performed on aged sample. XPS were performed on unscratched and scratched surface (Figure 9 (a) and (b)) to probe the first corroded layers. This is how in-situ scratch facility also turns useful when we wish to explore the chemical state of the corroded layer.

On the unscratched slab, in agreement with Auger measurements we do not observe any trace of *Co2p* and *Gd4d* spectra on the surface. We only observe Si*2p* and O*1s* spectra which are treated and discussed in detail as follows. Fitting of Si*2p* was made taking into account all possible Si-oxidation states expected: (i) Si^0 oxidation states from pristine $Gd_6Co_{1.67}Si_3$ exhibiting Si*2p* at 98.8 eV (ii) Si^{+4} from 102.5 eV [20] on amorphous material to 103.15 eV on crystalline one's for SiO_2 bonding. [15] For intermediate oxidation of Si^{+2} a signature peak appears at 100.5 eV i.e. at interval of 1.7 eV with respect to Si^0 position. [21, 22] We were able to fit the Si*2p* spectra with three spin-orbit doublets centered at 101.7 eV (19%), 102.7 eV (56%) and 104.4 eV (25%) with theirs corresponding areas. We suggest that these features are due to Si-C-O bonding since we do not scratch the surface, amorphous more covalent SiO_2 bonding and more ionic SiO_3^{2-} bonding respectively. Further we fit O*1s* as shown in figure 5(b) considering O*1s* peak at 530.5 eV for Gd-O bonding from atmosphere exposure as seen on Gd metal slab and pristine $Gd_6Co_{1.67}Si_3$ slab, and at 531.7 eV [20] on amorphous material and 533 eV on crystalline one's [15] for SiO_2 bonding. In our case we observe 4 peaks at energies 530.8 eV (13%), 532.2 eV (30%), 533.2 eV (34%) and 534.3 eV

(23%) with their respective area. Once again, since the surface was not scratched, we suggest the feature at 532.2 eV originated from Si-C-O bonding due to air exposure. If the feature at 530.8 eV is related to Si-O-Gd bonding interface, we suggest the features at 533.2 eV and 534.3 eV correlated to the more covalent SiO_2 bonding and more ionic SiO_3^{2-} bonding respectively. The main contributions of the both Si2p and O1s spectra would be due to $Si^{4+}O_x$-type bonding with a mixture of covalent and ionic character in between SiO_2 and SiO_3^{2-} species. However, to definitively support the stepped spontaneous reaction from Si^{II}-O (E^0 = -0.8 eV) → $Si^{IV}O_2$ (E^0= -0.9 eV) → $Si^{IV}O_3^{2-}$ (E^0= -1.7 eV) at the slab/water interface, we should see a decrease of the more ionic species after scratching the surface in-situ.

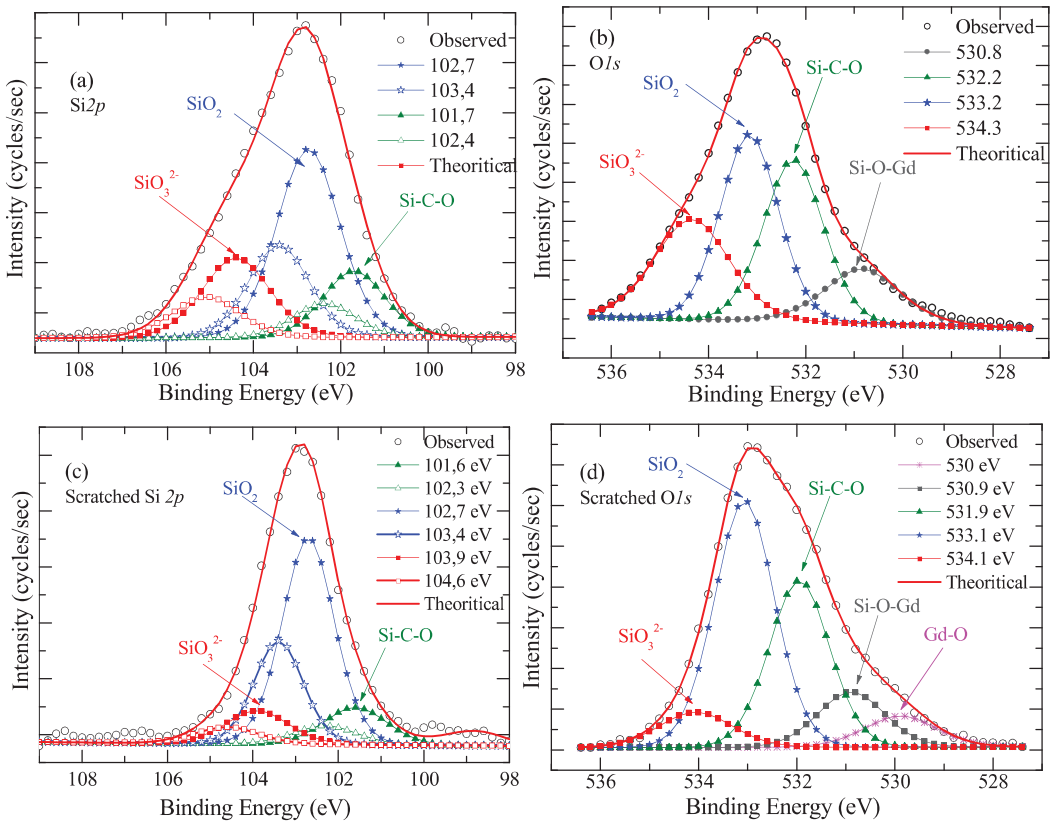

Figure 9: X-ray photoelectron spectrum from surface of aged material: on surface (a) Si2p (b) O1s; after scratch (c) Si2p (d) O1s.

Spectra resulting from scratched surface show extra contributions of oxidized *Gd4d* peaks but still we do not observe any *Co2p* spectra. These observations make us believe we are still in the corroded region far from the core consisting original $Gd_6Co_{1.67}Si_3$. As previously, we focus our study on the Si*2p* and O*1s* spectra (Figure 9 (c) and (d)). The Si*2p*

was also fit by using spin-orbit doublets with the main peaks centered at 101.6eV (16%), 102.7eV (70%) and 103.9eV (14%) and O*1s* peak was now fitted using 5 peaks centered at 529.9eV (7%), 530.9eV (10%), 532eVeV (30%), 533 eV (45%) and 534 eV (8%.) [23] The new O*1s* peak around 530 eV is likely due to Gd-O type bonding in relation with the oxidation observed on the top of a metal Gd slab exposed to air. Interestingly, the relative areas of the main features at 102.8 eV on Si*2p* and 533.1 eV on O*1s* spectra resulting from SiO_2 bonding are unambiguously enhanced with the scrapping procedure eliminating the top corroded layers Si-O-C and SiO_3^{2-} bonding-type. This tendency in the distribution of SiO_3^{2-} /SiO_2 on the top layer of the shell is definitively link with our hypothesis of time dependent variation of SiO_x layer based on electrochemical corrosion. Because the difference on the standard reduction potentials between SiO/Si and SiO_2/SiO couples is low, the SiO oxide is not stable as further supported by our XPS study.

In conclusion, with time of exposure to water flux, the cobalt is first oxidized to Co^{2+}_{aq} allowing its dissolve to the water and resulting in a "pristine $Gd_6Co_{1.67}Si_3$ core" / "Gd_2O_3-SiO_x shell". The so formed oxide-corroded layer of silicon wears out when SiO_3^{2-} ionic species is formed exposing gadolinium at surface of sample. Interestingly, Gd_2O_3 would act as a passivation layer that slows down the Co dissolution. This step is reflected as decrease in SiO_x sub layer thickness in parallel to an increase of Gd_2O_3 thickness with time and supported by our XPS studies.

2.3.5. Physical properties

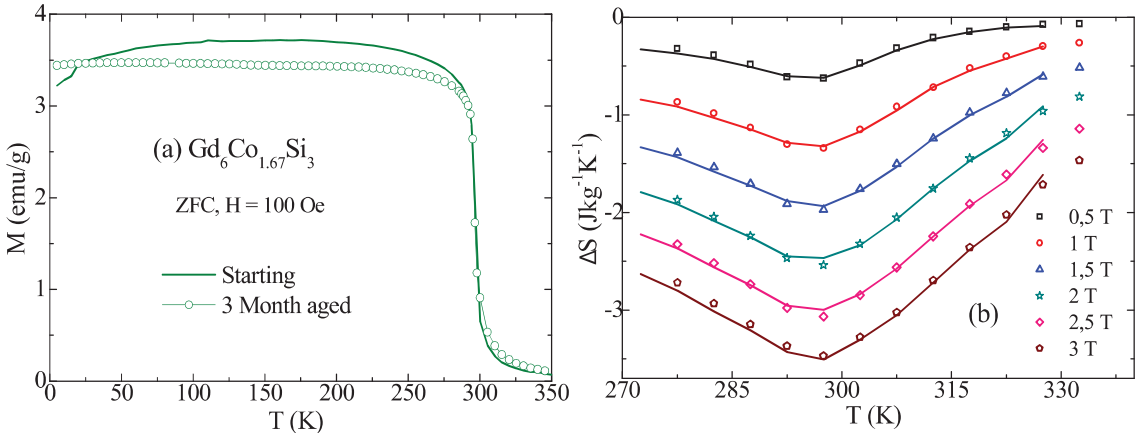

Figure 10: (a) ZFC magnetization as function of temperature. (b) Entropy change. For both graphs solid line signifies starting and open symbols are for 3 months aged material.

Since the chemical (corrosion) and mechanical (erosion) actions of the water flux into $Gd_6Co_{1.67}Si_3$ slab material are highlighted and understood, we present the central part of our study i.e. the MCE performance of the material before and after ageing by evaluating the T_C, isothermal curves and magnetic entropy change. Figure 10 (a) compares the magnetization as function of temperature for starting and 3 month aged samples which confirm no change in the abrupt jump from paramagnetic to ferromagnetic (T_C) after ageing. The entropy changes for these two samples are calculated from the isothermal curves obtained around the magnetic transition and results are shown in Figure 10 (b). After three month of ageing and with oxide layer of around 1.2 μm, we observe no change in T_C or entropy change. This result is highly promising compared to La-Fe-Co-Si system which shows considerable decrease in total entropy because of the paramagnetic character of the Gd_2O_3 passivation layers. The aging phenomenon does not change the total spin density of the core/shell material compare to these of the pristine one. It is also worth to note our compounds undergo much less mechanical damage in the present ageing conditions for which we do not control the water flow. So we propose that Gd-based intermetallics are better choice of materials for the practical implementation in household applications compared to La-Fe-Co-Si system. Gd-based intermetallics could also be alternate to perovskite related manganites [24] for which their corrosion resistance is underway. Some preliminary results will be presented in chapter 4.

2.4. Effect of different fluids

Considering the fact that water is only one of the options for heat transport fluid and there are several commercialized and non-commercial options available which have their unique advantages, we preform ageing effect with few other fluids. Water is regarded perfect fluid with excellent heat transfer, health, safety and low cost. One of the problem is its freezing point(°0 C) to overcome few suggest use of anti-freezing agent such as salt($CaCl_2$, $MgCl_2$, LiB_2, etc.), alcohols, glycols or non-ageous fluids(mineral oils, synthetics). One of the comparatively safe, stable, low cost solution is the mixture of ethanol and DI H_2O which is believed to lower the freezing point compared to pure DI H_2O itself. Such mixing of ethanol is also believed to help reduce the surface tension.

The second case is a follow up of the results from our initial ageing which was presented in detail in section 2.3. We described that the starting/triggering of the corrosion was dissolution of Co_{aq} by following the spontaneous electrochemical reaction. This was

followed by similar reaction occurring on Si and Gd. The interest here is to arrest the reaction of Co by using fluid with higher pH in order to reduce corrosion (described below) if it follows our hypothesis as described in section 2.3.3. For simplicity we choose KOH for our study however there can also be other choice. In couple of sections to follow we summarize the glimpse of initial ageing in KOH solution, experiments with 10% ethanol are still in progress so they are not discussed here.

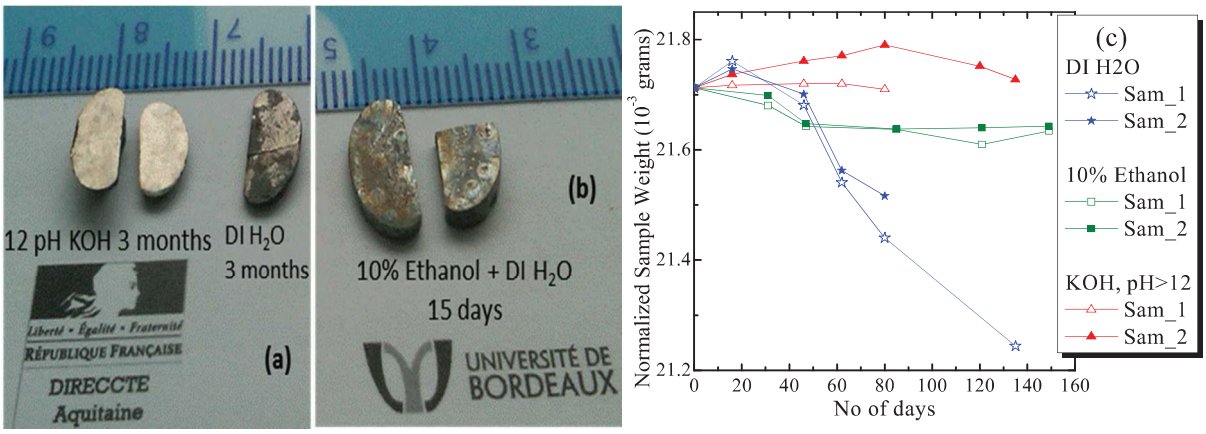

Figure 11: Effect of ageing under different heat transport fluids left to right 3month aged in KOH of pH≥12 alongside DI H_2O aged for same period. 15 days aged in 10% ethanol solution. Change in mass of sample with duration of exposure to different fluids - DI H_2O, 10% ethanol + DI H_2O, KOH (with pH>12) solution

Two initial photographic snaps presented in Figure 11(a) helps in comparing physical damage caused by different fluid during ageing. As evident surface of samples treated with KOH still keep their smooth and metallic nature while once treated with DI H_2O or 10% ethanol + DIH_2O mixture starts changing their appearance with dark deposition on surface. Tracking the weight loss during ageing can also provide rough estimate about possible erosion of the sample. Even though this might not account for qualitative analysis, one can still compare the degree of erosion due to different fluids. Our observation of weight loss during ageing are shown in Figure 11 (c), where weight loss for atleast two samples for each fluid was followed to have reliability and reproducibility. It follows that erosion due to DI H_2O is higher as compared to 10%ethanol mixture and that for KOH is the lowest among them. So this is considerable observation in order to understand the physical damage caused by each fluid and can relate the higher elemental traces that we observe in ICP as discussed in section 2.3.4.

Case study using KOH solution with pH≈12 to 13

Following the pH diagram/Pourbiaux diagram for cobalt (in left of Figure 12 (a)), we propose two solutions: ***(i)*** considering the Co to be stable for potential less than 1 for complete pH range and from prototypes we know the magnetocaloric material in the working unit is place in regular channels. We can think to apply constant negative potential Eh = -1.5 or -2 for the working material, with assumption that such external potential do not affect the overall magnetocaloric properties. ***(ii)*** From Figure 12 (a) one can infer by choosing the fluid which has pH above 9 one should reduce dissolution of Co_{aq} into fluid instead should facilitate $Co(OH)_2$ precipitation on surface which can act as protective layer. If our hypothesis of corrosion which was explained on basis of spontaneous electrochemical reaction is valid then, $Co(OH)_2$ precipitation should arrest, or at least, slower the corrosion process. To brief the hypothesis, erosion of Co followed by exposure of Si for further corrosion. So the gadolinium based intermetallic was further age treated with KOH solution of pH≥12. Results for initial couple of months of ageing are discussed here. After ageing sample for 3months in KOH there were hardly any changes in physical appearance (Figure 11 a) or on x-ray diffraction (not shown) compared to the starting material.

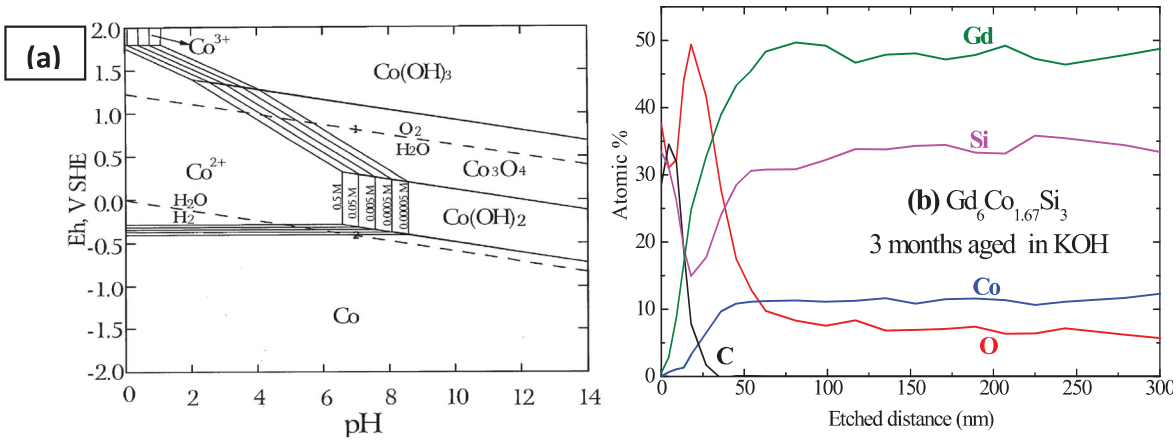

Figure 12: Pourbiaux diagram for Cobalt. Depth profile using Auger for three month KOH solution aged sample.

To confirm the unchanged state of the sample and to probe possibility of the elemental changes at lower dimension undetectable either by visualization or even by xrd, depth profile was performed. As seen in Figure 12 (b), initial profile (≈20 nm) display carbon which can be considered to the one observed on pristine due to contamination. However a sharp increase in oxygen profile is observed (≈30 nm) followed by decrease to lowest at depth of around 100 to 200 nm. Nominal composition of the compound is observed after depth of 150 nm. This

particular depth profile is much similar to the one of the pristine sample. Exception is on the nature of cobalt; on pristine sample cobalt does not appear until other compositional elements appear (Figure 5 c) where as we observe small trace of cobalt even just after removal of carbon in present case.

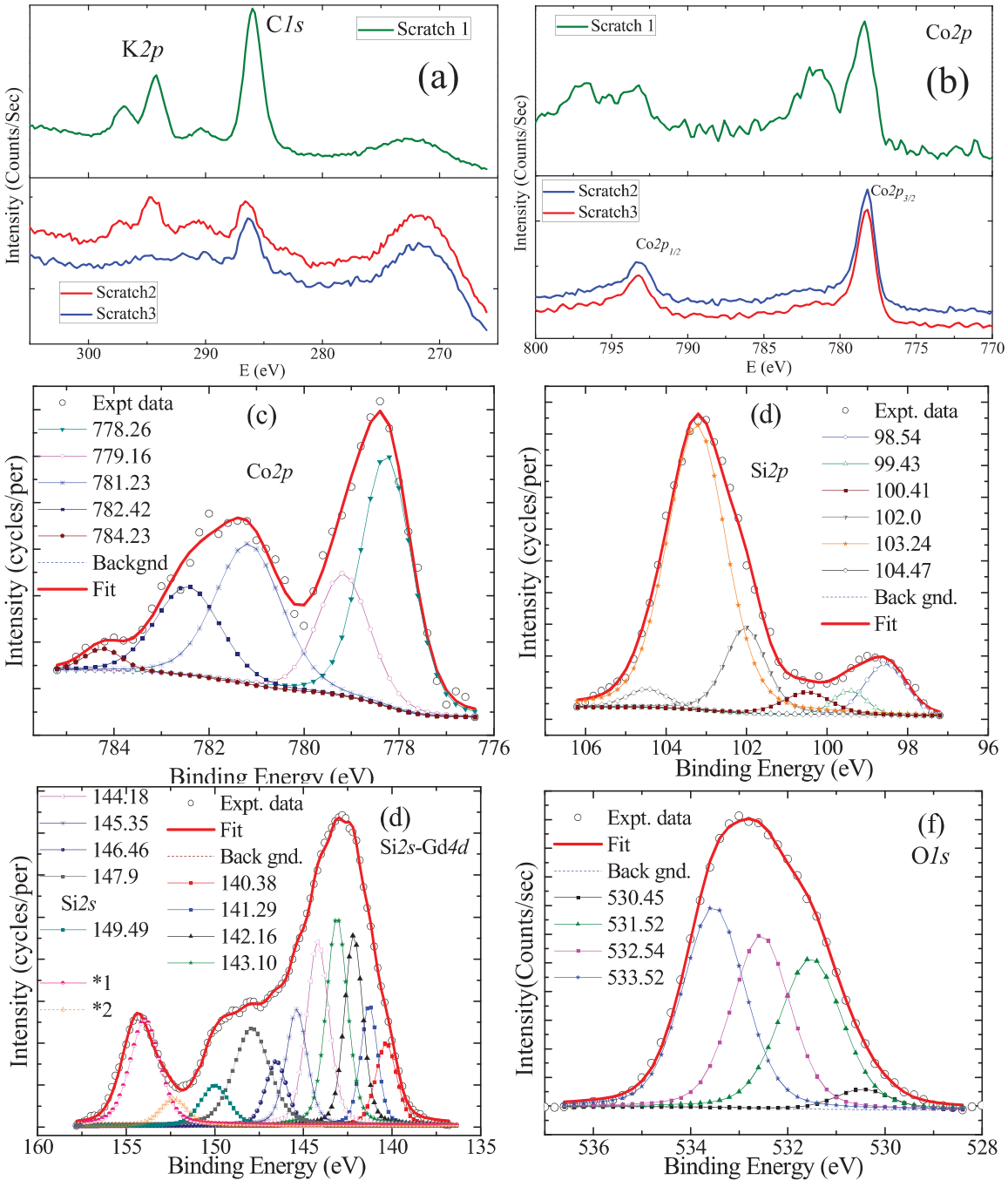

Figure 13: XPS studies on three month aged in KOH. (a) and (b) selective spectra to highlight spectral change along depth. Fits for spectra from surface (c)Co*2p*, (d) Si*2p*, (e) Si*2s*-Gd*4d* and (f) O*1s*

We further perform XPS on the 3 month KOH aged sample to better understand possible specific anion attachment on each of the element Gd, Co and Si. XPS spectra were collected around different depth after in-situ scratch of sample, Scratch 1 corresponds to top layer after small scratch, Scratch 2 and Scratch 3 are after removal of further layer. Scan over complete range of binding energy showed some trace of potassium (K*2p*) on surface and with scratching this disappear even before complete removal carbon Figure 13 (a). So we confirm that these trace might be due to heat transport KOH solution that stay on surface after removal of sample from ageing cell and show no kind of bonding with our sample. And there is no reaction of potassium with the sample.

Figure 13 (b) confirms the presence of cobalt starting from the surface contrary to what our previous study on DI H_2O aged sample where cobalt appears only after removal of core-shell oxide layer. In the present case it is also interesting to note the secondary peak associated with Co$2p_{3/2}$ and Co$2p_{1/2}$ (Figure 13 (b)). As discussed in section 2.3.4 the XPS of pristine sample, this is signature of cobalt linked with oxide-hydride or oxygen [Thin Solid films 384, 23; [19]]. To recall, XPS studies on pristine or DI H_2O aged sample confirm that cobalt mostly stays in its metallic form without any oxidation (section 2.3.4). So it is necessary to evaluate the Co2p peak observed on surface to well characterize nature of cobalt.

Qualitative analysis of fitting on the KOH aged sample according to binding energy dependence on the bonding between elements and/or metal-oxides, are summarized in Figure 13 (c to d). The Co2p, Si2p spectra convince the oxidation of cobalt and silicon. Cobalt is in particularly in hydroxide form, preferentially $Co(OH)_2$, which is confirmed from the nature of intensity and binding energies of the Co$2p_{3/2}$ satellite peaks observed at 781.23eV and 782.42eV.[19]

Silicon oxidation looks to result in SiO_2 (Figure 13 d). However, careful observation of Si^0, Si^1, Si^2 contribution highlight the oxidation seems to be at lower rate in present case as compared to DI H_2O ageing (Figure 9 a, c) where we do not observe these oxidation states of silicon until we reach much deeper of corrosion layers. Also we do not see much oxide contribution on Gd*3d* (Figure 13 e) the features of which remains to be much similar to the one of pristine sample (Figure 8 a) suggesting gadolinium is protected from corrosion. From depth profile and XPS analysis we believe our hypothesis of corrosion process is true and so is the theory put forward to reduce corrosion by using heat transport fluid with higher pH.

2.5. Conclusion

We have presented detailed chemical and microstructural analysis of ageing process in constant flux of water on the ternary silicide $Gd_6Co_{1.67}Si_3$. Core-shell model of formation of SiO_x-Gd_2O_3 on surface of $Gd_6Co_{1.67}Si_3$ is proposed based on XRD, EMPA and depth profile by Auger spectroscopy analysis. The cobalt on surface was found to be corroded to Co^{2+}_{aq} and dissolve to the water as supported by ICP and XPS analysis. Further, XPS confirms the oxide at top surface to be mainly SiO_x without much trace of hydroxide but with a time dependant thickness related to spontaneous single metal corrosion phenomenon involving the two couple SiO_2/SiO and SiO_3^{2-}/SiO_2 and resulting in SiO_3^{2-} ionic species dissolution at the end of the oxidation process. That is why a final $Gd_6Co_{1.67}Si_3$/Gd_2O_3 interface is suggested. Remarkably the bulk magnetocaloric effect is unaltered even with this micron length oxide layer on surface because of the paramagnetic Gd_2O_3 passivation layer. Alongside detailed electronic structure of $Gd_6Co_{1.67}Si_3$ through XPS studies is presented.

Effort to reduce the corrosion by using appropriate fluid is carried out by using KOH as heat transport fluid. Drastic reduction in the corrosion observed in this case is due to self-coating of $Co(OH)_2$ following hypothesis put forward on basis of spontaneous electrochemical reaction. The ageing experiments with KOH, DIH_2O and 10% ethanol for longer duration of time, for 8 months or more are under way and will be presented in separate publications. Depending on the outcomes of these experiments, we believe it will give realistic analysis and confirm whether the material is potential for applications.

2.6. References

1. O Tegus, et al., *Transition-metal-based magnetic refrigerants for room-temperature applications.* Nature, 2002. **415**: p. 150.

2. K A GschneidnerJr, V K Pecharsky, and A.O. Tsokol, *Recent developments in magnetocaloric materials* Reports on Progress in Physics, 2005. **68**(6): p. 61.

3. F Canepa, et al., *Ageing effect on the magnetocaloric properties of Gd, $Gd_5Si_{1.9}Ge_{2.1}$ and on the eutectic composition $Gd_{75}Cd_{25}$.* J. Phys. D: Appl. Phys., 2008. **41**(15): p. 10.

4. Min Zhang, et al., *Corrosion behavior of magnetic refrigeration material La–Fe–Co–Si in distilled water.* Journal of Alloys and Compounds, 2011. **509**: p. 3627.

5. M Balli, et al., *Implementation of $La(Fe, Co)_{13-x}Si_x$ materials in magnetic refrigerators: Practical aspects.* Materials Science and Engineering B, 2012. **177**: p. 629.

6. Julia Lyubina, et al., *Novel $La(Fe,Si)_{13}$ /Cu Composites for Magnetic Cooling.* Advanced Energy Materials, 2012. **2**(11): p. 1323.

7. Anders Smith, et al., *Materials Challenges for High Performance Magnetocaloric Refrigeration Devices.* Advanced Energy Materials, 2012. **2**: p. 1288.

8. Etienne Gaudin, et al., *Structural and Magnetocaloric Properties of the New Ternary Silicides $Gd_6M_{5/3}Si_3$ with M = Co and Ni.* Chemistry of Materials, 2008. **20**: p. 2972-2980.

9. Etienne Gaudin, Franc¸ois Weill, and B. Chevalier, *Structural, Magnetic and Electrical Properties of the Ternary Silicide $Gd_6Co_{1.67}Si_3$ Derived from the Hexagonal $Ho_4Co_{3.07}$ (or $Ho_6Co_{4.61}$) Type Structure.* Z. Naturforsch., 2006. **61b**: p. 825-832.

10. S Narayana Jammalamadaka, et al., *Magnetic anomalies in $Gd_6Co_{1.67}Si_3$ and $Tb_6Co_{1.67}Si_3$.* J. Phys. Condens. Matter, 2008. **20**: p. 425204-425209.

11. Shen Jun, et al., *Magnetocaloric effect in $Gd_6Co_{1.67}Si_3$ compound with a second-order phase transition.* Chinese Physics B, 2008. **17**(6): p. 2268-2271.

12. Haynes, W.M., ed. *CRC Handbook of Chemistry and Physics*. 93 ed. 2012 -2013, CRC Press.

13. S Oswald and R. Reiche, *Binding state information from XPS depth profiling: capabilities and limits.* Applied Surface Science, 2001. **179**: p. 307-315.

14. Erik Lewin, et al., *Influence of sputter damage on the XPS analysis of metastable nanocomposite coatings.* Surface & Coatings Technology, 2009. **204**: p. 455-462.

15. M. J. Guittet, et al., *Bonding and XPS chemical shifts in $ZrSiO_4$ versus SiO_2 and ZrO_2 Charge transfer and electrostatic effects.* Physical Review B, 2001. **63**(12): p. 125117.

16. J A Gupta, et al., *Interfacial layer formation in Gd_2O_3 films deposited directly on Si(0 0 1).* Applied Surface Science, 2001. **173**: p. 318-326.

17. G Hollinger and F.J. Himpsel, *Probing the transition layer at the SiO_2-Si interface using core level photoemission.* Applied Physics Letters, 1984. **44**: p. 93-95.

18. Andrew P Grosvenor, et al., *Examination of the Bonding in Binary Transition-Metal Monophosphides MP (M) Cr, Mn, Fe, Co) by X-Ray Photoelectron Spectroscopy* Inorganic Chemistry, 2005. **44**: p. 8988-8998.

19. Mark C Biesinger, et al., *Resolving surface chemical states in XPS analysis of first row transition metals, oxides and hydroxides: Cr, Mn, Fe, Co and Ni.* Applied Surface Science, 2011. **257**: p. 2717-2730.

20. D. Löffler, et al., *Growth and Structure of Crystalline Silica Sheet on Ru(0001).* Physical Review Letters, 2010. **105**(14): p. 146104.

21. F. J. Himpsel, et al., *geometry-Dependent Si(2p) Surface Core-Level Excitations for Si(111) and Si(100) Surfaces.* Physical Review B, 1980. **45**: p. 1112.

22. G. Hollinger and F.J. Himpsel, *Probing the transition layer at the SiO_2-Si interface using core level photoemission.* Applied Physics Letters, 1984. **44**: p. 93.

23. Amauri J. Paula, et al., *Surface Chemistry in the Process of Coating Mesoporous SiO_2 onto Carbon Nanotubes Driven by the Formation of Si-O-C Bonds.* Chemistry - A European Journal, 2011. **17**: p. 3228.

24. Christian R. H. Bahl, et al., *High performance magnetocaloric perovskites for magnetic refrigeration.* Applied Physics Letters, 2012. **100**: p. 121905.

Chapter 3

Cu-doped Ni_2MnGa Heusler alloy – The effect of composition and microstructure on structure, magnetism and magnetocaloric effect, sustainability against ageing in water thereafter

3.1. Introduction

Even though Gd-based materials are in top priority as the magnetocaloric materials, the cost and the abundance of gadolinium becomes barrier to realize them in application of large scale. Mn-Fe-As-P, La-Fe-Si are projected as better alternatives, the first one has toxic concern the second one has been demonstrated to be less stable for cycling [1]. The Ni-Mn-R (R being main group element) based intermetallic Heusler alloys with first order transition are proposed to be low toxic, cost effective alternatives [2]. Their stability for the working environment and their performance reproducibility are yet to be explored. These factors make us believe Cu-doped Ni_2MnGa based material to be interesting for the present study.

In the beginning of this chapter a brief introduction to Heusler alloys is provided. Special attention is paid on relating structure, composition and the magnetic properties. The possible ordering-disordering of elemental atoms in crystal structure of the Heusler alloy is depicted. Experimental investigations to obtain optimized composition that exhibit the giant magnetocaloric effect around room temperature in the system $Ni_2Mn_{1-x}Cu_xGa$ (x=0.2, 0.25 and 0.3) are first summarized. Then we demonstrate the role of Mn concentration, microstructural effects and heat treatment on the observed magnetocaloric properties (transition temperature, entropy change) in the series $Ni_2Mn_{0.75+\delta}Cu_{0.25}Ga$. Before concluding the chapter, results of initial ageing on one of the Heusler composition are presented.

3.1.1. Heusler alloy

German chemist Friedrich Heusler was first to study Heusler alloys long back in 1903. He proposed Cu_2MnAl to be ferromagnetic even though none of the constituent by themselves has any ferromagnetic properties [3], whereas the detailed crystal structure for this alloy was given almost two decades later [4]. Heusler alloys in general were however subjected for broader research only after 1960's, leading to several compositions exhibiting unique and interesting physical properties [5]. Depending on the stoichiometry of composition two distinct families of Heusler alloys exist: (i) Half-Heusler with 1:1:1 compositional stoichiometry represented by *XYZ (*Figure 1 *b)*; (ii) Full-Heusler or commonly addressed as Heusler phase having 2:1:1 stoichiometry (X_2YZ) *(*Figure 1 *c)*. Both are widely

studied and individually form a large family by themself. We will restrict our discussions to the family of full- Heusler. ***X_2YZ*** represents the general formula for Heusler composition, X and Y representing mostly transition metal element, whereas Z normally one of the main group element (i.e., group III, IV, V elements). In some case Y is replaced with alkaline earth or rare earth element. The possible combinations of different elements was pictorially represented with unique colors (Figure 1 a) representing each site by T Graf et al [6]. Cu_2MnAl is considered as the prototype of Heusler compound. Following the IUPAC nomenclature, the element with larger amount is represented in beginning (Cu), followed by rest (Mn, Al) with main group element (Al) ending the composition. The crystal structure of Heusler alloy is shown in Figure 1 b. X atoms are in the center of the cubic cell (highlighted by black lines). The cubic cell is formed with Y and Z atoms in the alternating edges of the cube Figure 1 b. In case of half Heusler, one of the X atoms in adjacent cubic cell is missing (replaced with 'voids' - as regularly addressed) leaving four simple cubes and four X-atoms body-centered cube in Heusler structure (Figure 1 c) [7].

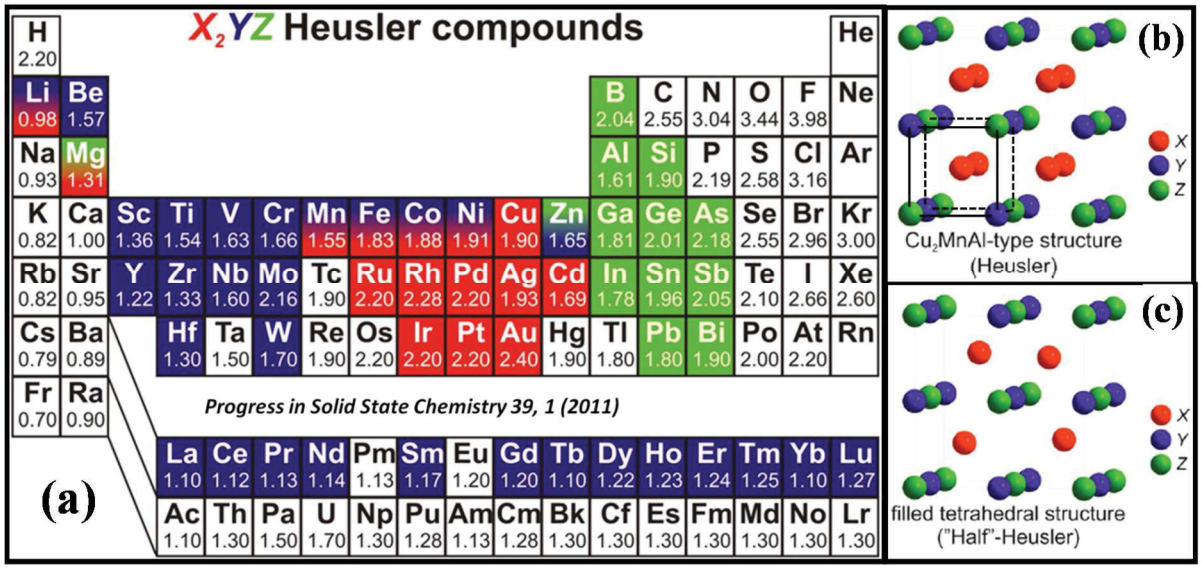

Figure 1 : (a) Periodic table displaying possible elemental combinations for X, Y and Z site of the Heusler phase. Atomic arrangement in the crystal structure of (b) Heusler (c) Half-Heusler phase.

The site preference (X/Y/Z) of the 3d elements in the Heusler alloy structure is determined by the number of their valence electrons. Depending on the combination of atoms in X, Y and Z sites, the total valence state of the Heusler composition can be

controlled [8]. The valence state is defined by the total number of free electrons. Thereby different compounds with unique physical properties can be derived such as semiconductors/half-metals/metallic/superconducting alloys or magnetic/spin-glass/non-magnetic alloys. Some of these alloys have shown promising multiferroic, half-metallic, magnetoelastic properties [9].

We shall restrict our discussion here to only alloys showing magnetocaloric effect. In Heusler alloys it is well known that the physical properties (structural and magnetic transitions) are decided on electron concentration defined by the valence electron to atom ratio. The number of valence electrons per atom for Ni ($3d^8$, $4s^2$), Mn ($3d^5$, $4s^2$), Cu ($3d^{10}$, $4s^1$) and Ga ($3d^{10}$, $4s^2$, $4p^1$) atoms is 10, 7, 2 and 3 respectively. Then the electron concentration (e/a) for alloys consisting these elements can be defined as [10],

$$\frac{e}{a} = \frac{10 \times (Ni_{at.\%}) + 7 \times (Mn_{at.\%}) + 2 \times (Cu_{at.\%}) + 3 \times (Ga_{at.\%})}{Ni_{at.\%} + Mn_{at.\%} + Cu_{at.\%} + Ga_{at.\%}} \quad \cdots \quad (1)$$

Among the Heusler series, Ni-Mn based Ni_2MnZ (Z= Ga, Sn, In) systems have shown great promise in magnetocaloric effect [11]. Within which Ni-Mn-Ga series are comparatively widely studied and has advantage of inhabiting more compositions with transitions close to ambient temperature than the rest of them.

Our choice of magnetocaloric material Ni-Mn-Ga is also known as the Magnetic Shape Memory Alloys (MSMAs) with potential technological applications. Ni-Mn-Ga based magnetically controlled shape memory alloys are proposed to be good shape memory actuators and sensors [12, 13]. With possibility of observing giant strain induced by applying external magnetic field [14], in response of which they exhibit large change in length (ΔL/L) and hence volume (ΔV/V). Hence giving rise to the structural transition inheriting large entropy change. Most of the compounds exhibit separate magnetic and structural transitions [15]. Very few have been engineered to have combined magnetic and structural transition. Much recently they are discovered to show much larger entropy change commonly termed as giant magnetocaloric effect across such magneto-structural transition.

3.1.2. The structural deviations - Ordering-disordering of atoms and the modulation

The atomic arrangement which is the distribution of the atoms (X, Y and Z) on the specific lattice sites (*8c*, *4b* and *4a*), depends on: **(a)** the preference of occupancy of the constituent elements i.e., X, Y, Z; **(b)** on the thermodynamic conditions used for their synthesis (like final temperature, cooling rates) versus the fully ordered one. Disordered structures are classified based on the degree of deviation, a brief account of these structures as proposed in the literature is summarized in the following [9].

(i) Ordering with preferential site occupancy

Depending on the site occupancy priority of the given atom 'A', it would prefer to occupy either of X/Y/Z atomic sites in X_2YZ. Such priority of occupancy can also lead the same atom to occupy two different sites resulting in mixing of elements in different sites. Consider the Heusler unit cell shown in Figure 2 a, by shifting all positions by (1/4, 1/4, 1/4) with respect to the standard Fm-3m cell (Figure 1 b) one can make CsCl superstructure visible. The CsCl- like superstructure is defined by the combination of two binary alloys crystallizing in the CsCl-type structure. The fully ordered unit cell of cubic $L2_1$ structure that is shown in Figure 2 a can be considered as CsCl-type unit cell (highlighted by blue in Figure 2 a) where Y or Z at body center of the cube and X atoms occupying all the corners (compared to figure 1 where X atom was at centre with Y atoms occupying the alternative corners). Structure of the ideal Heusler alloy can be obtained by combining 8 similar cells with alternating Y and Z- centered simple cubic cells. The ideal Heusler Cu_2MnAl or $L2_1$ cubic structure crystallize in *Fm-3m* space group as described in 3.1.1. In this structure, both of the X atoms (Cu atoms) are located in 8c (1/4, 1/4, 1/4) Wyckoff position and form a primitive cubic sub lattice. Adjacent cubes of this X_2 sublattice are filled alternating by Y (Mn atoms) at 4a (0, 0, 0) and Z (Al atoms) on the 4b (1/2, 1/2, 1/2) site.

When the Y and Z atoms are evenly distributed among them than 4a, 4b become equivalent while X still in 8c site, such arrangement results in the CsCl-type or *B2* disorder structure as shown in Figure 2 b. The resulting structure with reduced symmetry is defined using *Pm-3m* space group with lattice parameter close to the parent $L2_1$. Similarly, with random distribution of X and Y or X and Z will give raise to BiF_3-type or DO_3 disorder described with 8c≈4a or 8c≈4b within *Fm-3m* space group. A very rare disorder arrangement

is where in X on one of the fcc sublatttices mix with Y atoms and X on other sub lattice with Z atoms result in NaTl-type or *B32a* structure. This structure is defined using *Fd-3m* with X atoms on 8a (0, 0, 0), and Y, Z atoms on 8b (1/2, 1/2, 1/2) positions. All these are partially disordered states, if in case all the atoms are randomly distributed irrespective of the site a complete disordered state with bcc lattice called tungsten-type or *A2* structure results in Figure 2 c. New structure with further reduced symmetry is defined using *Im-3m* space group.

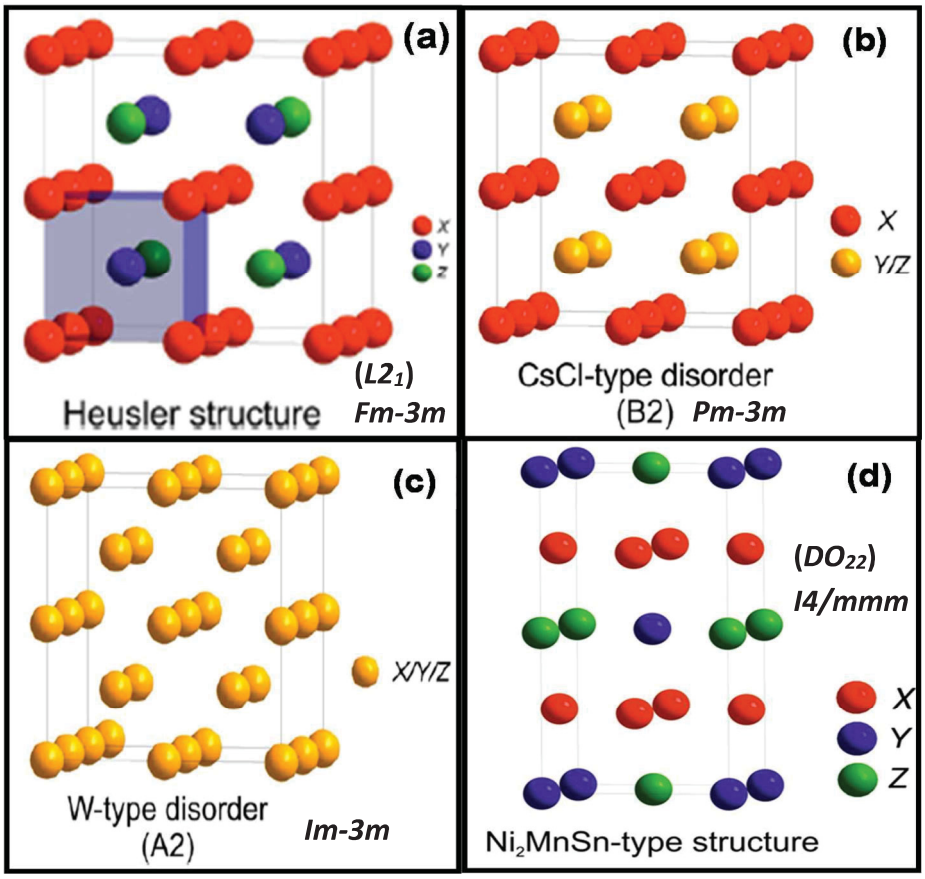

Figure 2: (a to d) Different possible ordering depending on the preferential atomic occupancy of element in cubic phase Heusler structure.

There are different notations used in representing the disordered structure, such as ICSD, *Strukturberichte (SB)*, Pearson, general formula. We have used two of these notations throughout our discussion, for instance; (i) Cu_2MnAl is structure type notation according to ICSD; (ii) $L2_1$ is its equivalent in *Strukturberichte (SB)* system. Table summarizing all these

order-disorder structures along space group and different notations used to represent them will be provided in appendix H.

Each phase results in specific super lattice reflections which are reflected as peaks on diffracted pattern having unique intensity and help in distinguishing them. The calculated diffraction patterns for A2, B2 and $L2_1$ structure for Cu_2MnAl are presented in Figure 3 a. As we move from A2 to B2 we can observe new peaks marked in blue arrows they represent super reflections for B2 phase. B2 to $L2_1$-type structure further introduce additional reflections (red arrows) and these are super lattice reflections for $L2_1$. The value of the lattice parameter for B2 phase is most of the time considered as half of that for $L2_1$ phase, i.e., $a_{B2} = 1/2 \cdot a_{L21}$ [16].

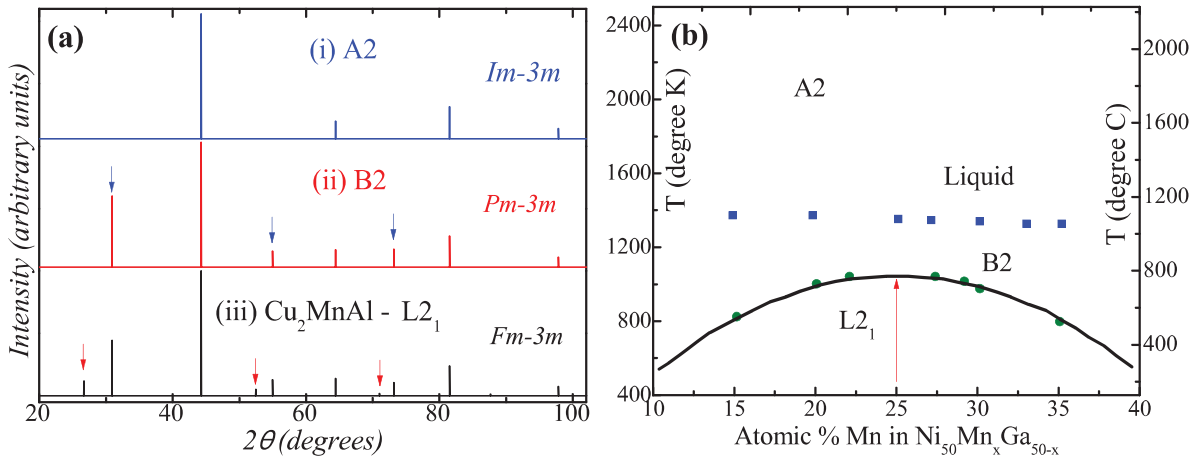

Figure 3 : (a) comparison of super lattice reflections for different cubic ordering (b) Cubic symmetry ordering temperatures for $Ni_{50}Mn_xGa_{50-x}$ [Scripta Mater 40, 1095].

Such chemical ordering depends greatly on the synthesis temperature and further steps followed for annealing. Detailed studies of the effect of temperature on chemical ordering in the case of Ni-Mn-Ga alloy are reported independently by Overholser et. al., [17] and few other researchers. The temperature dependent phase stability for the $Ni_2Mn_xGa_{2-x}$ reported based on experimental investigations is presented in Figure 3 (b) where it is clear that A2 phase stabilize at higher temperature, B2 phase is stabilized in intermediate temperatures in the liquid state and $L2_1$ phase at lower temperature. Red arrow in Figure 3 (b) highlights the parent compound Ni_2MnGa for which B2 to $L2_1$ transformation takes place around 780 °C. It is clear that the change in Mn and/or Ga concentration imply the transition

temperature of B2 - $L2_1$ to shift to lower temperatures. However the A2 to B2 structure transition temperature remains almost constant over the composition range. So for a given composition, it is possible to have mixed phase of $L2_1$ and B2 structures if the thermal heat treatments are in intermediate temperatures. Such phase co-existence has been demonstrated in case of $Ni_{50}Mn_{25}Ga_{20}Al_5$ as against single phase of $L2_1$ in $Ni_{50}Mn_{25}Ga_{25}$ or B2 in $Ni_{50}Mn_{25}Ga_{25}Al_5$ [16].

(ii) Tetragonal distortions

The so called martensitic transition in Ni_2MnGa results in structural transformation from high temperature cubic ($L2_1$) to low temperature tetragonal structure around 210 K. Considering all above mentioned factors, after ageing at higher temperatures (T>850 °C) following slow cooling, the transformation sequence is reported as $B_2 \rightarrow L2_1$.

The tetragonal structure such as $L1_0$ is normally attained at much lower temperatures, most of the case below room temperature. $L1_0$ unit cell is tetragonally distorted i.e., elongation or compression of cubic cell during martensitic distortion. The resulting tetragonal unit cell from elongation of unit cell is displayed in Figure 2 d. Early neutron diffraction experiments have showed the tetragonal modified structure to have lattice parameters a_t= 5.922 Å and c_t= 5.566 Å, along with some extra peaks attributed to modulation of the transformed lattice [18]. Geometrically, the transformation of cubic (FCC-Face Centered Cubic) to tetragonal (quadratic) takes place due to lowering of symmetry and the peaks are expected to split. Consider the d spacing for tetragonal system with a=b≠c, $\frac{1}{d^2} = \frac{h^2+k^2}{a^2} + \frac{l^2}{c^2}$. From this we infer that peaks such as $(111)_{FCC}$ will not split while the other peaks such as $(200)_{FCC}$, $(311)_{FCC}$ will split. For example, $(311)_{FCC}$ will split into $(113)_{DO22}$ and $(311)_{DO22}$ these two peaks will however have same d-spacing value. Such splitting will differ depending on the degree of deformation employed during transition.

Martensitic transformations are most often referred as ***first order, diffusion less; shear (displaced) solid-state structural changes***. In such transformations atoms move in well-organized manner relative to their neighbors. So the deformation can be described as combination of homogeneous lattice deformation described as “Bain Distortions” and “shuffles”. In a homogeneous lattice deformation, one Bravais Lattice is converted to another by the coordinated shift of atoms. The lattice invariant deformations such as slip or

twinning come in to act to minimize the stain energy due to Bain strain and to keep martensitic lattice undisturbed. The resulting shape deformation due to remaining strain after lattice invariant shear is taken care by elastic or plastic deformation of parent phase. Hence, the product phase after martensitic transformations inherits the same composition, atomic order and lattice defect as of the parent phase.

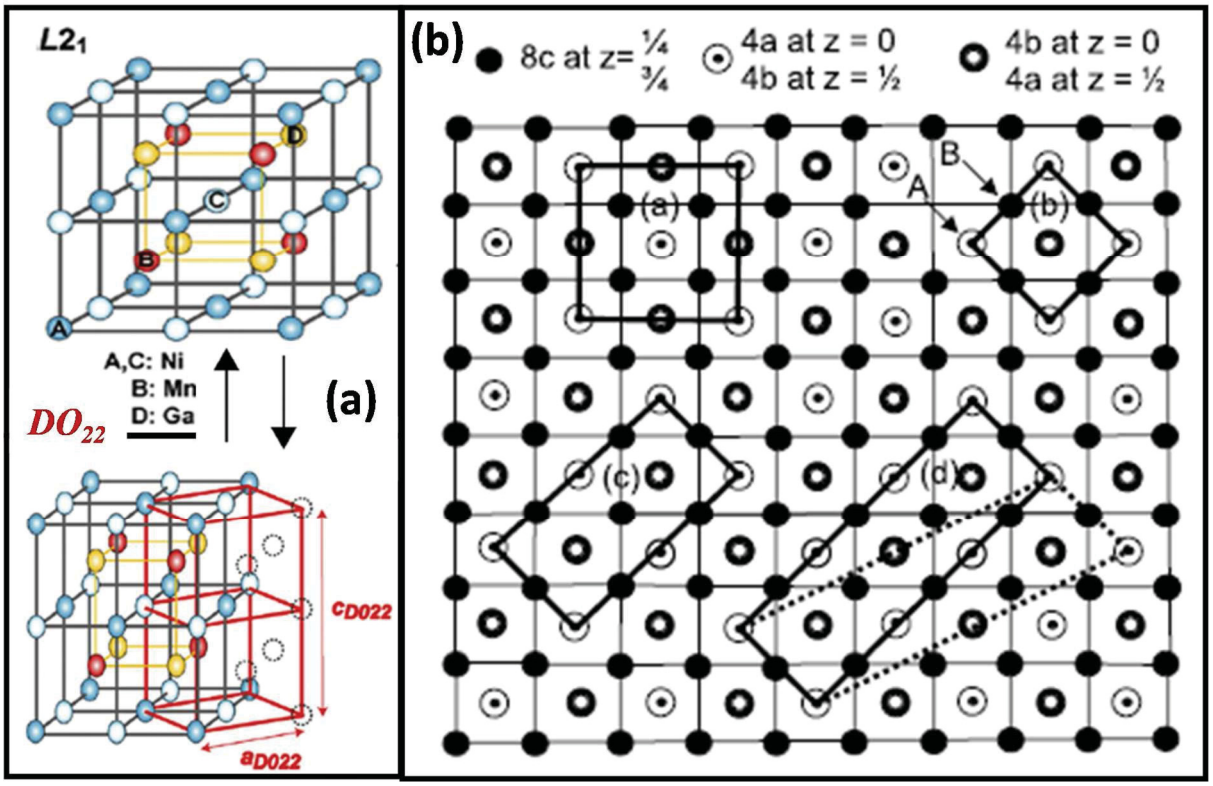

Figure 4: Scheme of Bain transformation of martensitic transformation (a) construction of tetragonal from cubic unit from [19] (b) cubic symmetry transformation to lower symmetry of tetragonal, orthorhombic and monoclinic as viewed on cubic lattice [20].

Figure 4 (a) illustrate the construction of one particular tetragonal unit cell from the cubic unit cell. The a-axis of DO_{22}-type structure (a_{DO22}) is chosen to be rotated in the c-plane by 45° from the a-axis of the $L2_1$ structure, the newly formed tetragonal unit cell is highlighted in red. Depending on value of this new *a* parameter two distinct tetragonal structures are formed namely DO_{22} and $L1_0$. DO_{22} unit cell is defined using lattice parameter $a=a_{cubic} \cdot \sqrt{2}/2$ while the $L1_0$ has unit cell with $a= \sqrt{2}\, a_{cubic}$ and the value of c remains the same in either case.

(iii) Modulation

Transitions from cubic to tetragonal involve intermediate steps such as shear/twisting of the lattice. The so twisted structures can themselves crystalize in valid crystal structures with much lowered symmetry (either orthorhombic or monoclinic). The schematic of the route followed by Bain transformation from simple cubic symmetry to monoclinic symmetry is summarized in Figure 4 b. The figure illustrates the construction of different unit cells on (001) projection of $L2_1$ Heusler structure is shown in Figure 4 b. (a) represents the cubic $L2_1$ cell *Fm-3m* which serve as basic unit. (b) is unit cell for body centred tetragonal *I4/mmm* constructed by 45° rotaion of a-axis so that it forms long c axis as explained before. (c) four-fold modulated orthorhombic cell Pmma b-axis is $[001]_{cubic}$(d) three-fold orthorhombic structure *Pnnm* represented by solid line and three-fold monoclinic cell *C2/m* by dotted line [20].

Over course of studies, a new super-structure was reported during martensitic transformation of Ni_2MnGa. So formed new structure, named as pre-martensitic was described to be orthorhombic structure obtained by repeating (tripling) of one of the side $<110>_{cubic}$ on the parent $L2_1$ phase. This is represented by (d) in Figure 4 b. The lattice parameters of so formed orthorhombic unit cell with *Pnnm* symmetry could be linked to parent cubic cell as, $a_{ortho} = 1/\sqrt{2}a_{cubic}$; $b_{ortho} = 3/\sqrt{2}a_{cubic}$; $c_{ortho} = a_{cubic}$. On further cooling the same Ni_2MnGa below 200K appearance of new orthorhombic super-cell with $b_{ortho}=7/\sqrt{2}a_{cubic}$ was also reported. Even the tetragonal structure itself can be considered two-fold modulated structure. It is also possible for the material to inherit mixed phase between two or more crystal structures after martensitic transformation. At low temperature $Ni_{2.18}Mn_{0.82}Ga$ single crystal was shown to exhibit two phase namely, orthorhombic and a monoclinic structure, which transfer to single cubic phase after martensitic transition [21].

Most of the tetragonal or modulated (orthorhombic/monoclinic) structures detailed above are obtained with ordered $L2_1$ cubic structure as the starting composition. In case of the ordered B2 cubic (*Pm-3m*) structure, as observed in TiNi, the first or second order martensitic transformations will result in either tetragonal (B2, *P4/mmm*), orthorhombic (B19, *Pcmm*) or R-phase or monoclinic (B19', *P21/m*) [22, 23]. In similar perspective, the

transformation of high temperature A2 (BCC, Im-3m) to lower symmetry has been explained based on the subgroup relation between the phases [24].

Table 1: Summary of symmetry, lattice parameter for different non-modulated and modulated structures.

Space group	Material	Lattice parameter a Å α °	b Å β °	c Å γ °	Type	Unit cell	Reference and remarks
Non-modulated							
Cubic *		2.901 90	2.901 90	2.901 90	A2 *Im-3m*	Body centered cubic	J Phys D Appl Phys 45, 295001
	$Ni_2MnGaAl_{0.2}$	2.901 90	2.901 90	2.901 90	B2 *Pm-3m*	Body centered cubic	Intermetallics 18, 2090
	Ni_2MnGa	5.822 90	5.822 90	5.822 90	$L2_1$ *Fm-3m*	Face centered cubic	J Phys III France, 2 739
Tetragonal 2M	$Ni_{2.12}MnGa_{0.88}$	3.865 90	3.865 90	6.596 90	DO_{22} *I4/mmm*	c/a>1; Face centered tetragonal	[25]
	$Ni_{2.2}Mn_{0.8}Ga$	5.482	5.482	6.488	*P4/mmm*	c/a>1; Face centered tetragonal	Materials Transactions, Vol. 45, No. 8 (2004) pp. 2661 [26]
	$Ni_{2.13}Mn_{1.06}Ga_{0.81}$	7.65	7.65	6.60	$L1_0$	c/a<1; Face centered tetragonal	Alloy8 of [27]
Modulated							
5M/10M, Monoclinic *I12/m1, P12/m1*	melt spun $Ni_{2.06}Mn_{0.94}Ga$	4.2 90	5.5 90.5	21.0 90	Five-layered, (3-2) stacking	c/a<1; body-centred tetragonal	Alloy2 of [27] Unit cell is orthorhombic
14M/7R/7M, Monoclinic *C2/m*	melt-spun $Ni_{2.13}Mn_{1.06}Ga_{0.81}$	4.26 90	5.43 94.3	29.54 90	Seven-layered; $(5\text{-}2)_2$ stacking	Body-centred monoclinic	*'Communsurate' modulated* Alloy 4, 8 of [27] PRB 82, 214423
Orthorhombic *Pnnm*	$Ni_{2.33}Mn_{0.64}Ga_{1.03}$	4.3 90	5.4 90	21.0 90	Ten-layered	The lattice is orthorhombic	*'Incommunsurate' modulated* Alloy 5, 7 of [27]

**depending on the ordering which is linked with the synthesis and heat treatments. For more details please refer appendix H.*

Modulated structures can be explained as due to the creation of vacancies or the excess ions within the lattice following off-stoichiometric of the composition. The so formed vacancies force the structure to be slightly distorted to account them. In order to take care

of the distortion the symmetry must be reduced and hence structure is either orthorhombic or monoclinic depending on the degree of the distortion. More detailed explanation on type of symmetry and the space group used to describe them can be found elsewhere [19, 20, 27, 28].

3.1.3. Ni_2MnGa – Tuning martensitic and austenitic for T_C around room temperature

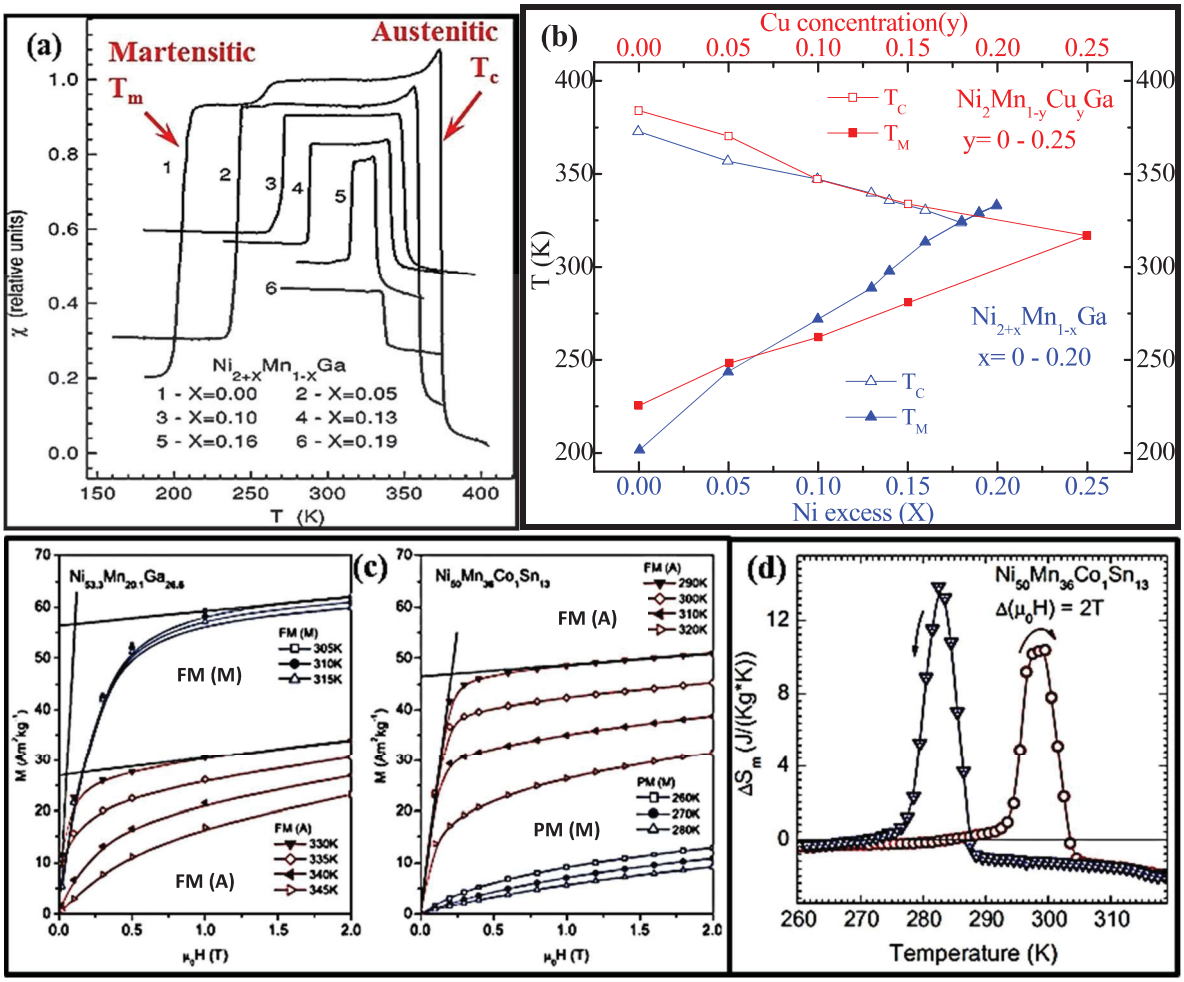

Figure 5: (a) Magnetization curve for the parent Ni_2MnGa. (b) Merging of structure and magnetic transition with varying Mn concentration, Mn replaced with Ni (data in blue from [29]) ; with Cu (data in red from [30]). Effect of existence of T_M, T_A on hysteresis and hence entropy (c)Isothermal magnetization curves in FM(Austenitic) and FM (Martensitic) region [11]. (d) Entropy from M(T) measured upon cooling (triangles) and heating (circles) for Ni-Mn-Sn [Phys Rev B 81, 214406].

Martensitic, austenitic transitions [31] : Ni_2MnGa is characterized by a magnetic transition (paramagnet to ferromagnet) around T_C = 376 K and a secondary drop while cooling and the raise on heating around T_M = 202 K as shown in Figure 5 a (sample 1). The former magnetic transition (T_C) occurs within the cubic phase. The cubic phase is known as

named "***austenitic***". The abrupt drop/raise in magnetization around T_M is due to first order structural transition (tetragonal to cubic). This structural transition is often addressed as ***"martensitic transition"*** *(T_M)*. Change in lattice parameter and structure is highlighted as cause for such sudden drop in magnetism.

Heusler alloys show abrupt or large change in lattice parameters near their structural transition against applied external field (pressure or magnetic field). The change in length (shape) of the alloy around its structural transition is well demonstrated in the case of $Ni_{50}Mn_{25-x}Co_xGa_{25}$ [32]. It was also confirmed such change in length of the material is strong dependent of applied external field, with increase of external pressure or magnetic field resulted in increase of length. This intern results in steep increase in the entropy or total cooling power of the material.

The external applied force such as stress, magnetic field, electric field can play large impact on the martensitic and magnetic transformations [33]. It was reported that applied magnetic fields can induce larger strains of up to 6.5% around martensitic phase transition along [001] in case of Ni_2MnGa single crystal [14]. Such strains result in larger entropy change. In $Ni_{51.5}Mn_{22.7}Ga_{25.8}$ even change of low field (0.9 T) results a considerable amount of entropy change (4.1 J/kg K) around the transition (197 K) [34]. It was further proposed that by varying the concentration of Ni or Mn one can achieve magnetic transition or/and martensitic transition close to room (sample 6 in Figure 5 a). The merging of transition temperatures in case of Ni_2MnGa is illustrated in Figure 5 a (sample 1 to sample 6). There were some efforts to push either T_C or T_M near room temperature without losing the inherited large entropy change [35]. Several groups made effort to shift T_M or/and T_C towards mark of 294 K [36].

Replacing Mn with small proportion of Ni, $Ni_{2.19}Mn_{0.81}Ga$, helped in merging both structure transformation and magnetic transition at 345K (blue line in Figure 5 b) accompanied by giant magnetic entropy change of 20 J/kg K in the magnetic field change of 1.6 T [37]. The merged magnetic transition was much higher to consider for ambient temperature. In same direction, substitution of Co on Ni site result in shift of T_M, T_A to higher temperature, while T_C remains at much higher temperature [38].

Increase in Curie temperature with ferromagnetic Co substitution in place of Mn was assigned to the enhancement of the total exchange interaction of the system. While with

substitution of non-magnetic Cu, $Ni_2Mn_{1-x}Cu_xGa$ one reduces the magnetic exchange interactions with in the system and hence lowering the T_C [30]. Introduction of copper also increase the martensitic transition to higher temperature and merge it with magnetic transition as we approach $Ni_2Mn_{0.75}Cu_{0.25}Ga$ (demonstrated by data in red, Figure 5 b). In the article to follow, the authors report, an enhanced entropy change due to co-existence of both transitions. The entropy change of 64 J kg^{-1} K^{-1} at 308K for magnetic field change ΔH= 5T was observed [39]. It was also shown with very small variation of composition ($0.245 \leq x \leq 0.26$) the temperature at which entropy occurs can be varied without any large difference in entropy value.

By changing the stoichiometry one was able to achieve the transitions at desired temperatures. However, in the process the usual atomic arrangements were considerably affected. Under such circumstances it is difficult for the compound to still keep the higher cubic symmetry. In few cases, the symmetry of the system is further reduced to maintain the stability of the compound. As the constituent elements Ni, Mn, Cu are having quite close properties (ionic radii, stable charge), it was advantage for the new composition to still retain the parent structure with slight rearrangement of the excess (deficient) atoms (vacancies) on different sites.

Apart from shifting T_C/T_M to near room temperature, the disadvantage of T_M and T_A when occurs separately, is that they impose problem with observed entropy depending on cooling or heating cycle (Figure 5 c and d). For instance in $Ni_{53.3}Mn_{20.1}Ga_{26.6}$, the observed entropy during cooling (which correspond to martensitic transition) is much lower compared to the one during heating (austenitic) [11]. This may not be true for all case, entropy change during cooling and heating for $Ni_{50}Mn_{36}Co_1Sn_{13}$ is almost same. However, changes in adiabatic temperature corresponding to each transition are contrary. Such converse effects can be one of the drawbacks in realizing these materials in real application. The magnetocaloric effect observed around martensitic transition is characterized by the crossover of magnetization isotherms, the observed entropy change is negative such effect is termed as Inverse magnetocaloric effect [40].

Finally it is important to note that the symmetry of structure play direct role on the nature of transition, as in case of CuZn, the transition is continuous or second order during its cation ordering transition from disordered A1-type structure to ordered $L1_2$-type

structure. In similar scenario, cation ordering transition between disordered A2-type to an ordered B2-type structure in $AuCu_3$ turns out to be discontinuous or first ordered. It should be noted that in the latter case, both the structures have lower symmetry compared to the former once. Following the change in Gibbs free energy there should be larger latent heat near the transition for discontinuous phase transitions compared to the continuous transitions where a negligible or no latent heat is seen. This suggest that the transitions involving lower symmetry should yield larger latent heat compared to the once involving the symmetric systems.

3.2. Experimental Investigations

We have several subsections with in this section. First one deals with synthesis route followed to obtain the samples. Next sections deal in detail respectively (i) reproduce large entropy change in Cu doped system, $Ni_2Mn_{1-x}Cu_xGa$; (ii) Effect of Mn concentration $Ni_2Mn_{0.75\pm\delta}Cu_{0.25}Ga$, (iii) heat treatment on magnetic properties and entropy change in $Ni_2Mn_{0.75\pm\delta}Cu_{0.25}Ga$ (δ= 2.5 at % excess Mn). To address them individually, we present systematic results of xrd, magnetic and elemental analysis in each case. In last couple of subjection the significance of microstructure and valence electron concentration to observe giant magnetocaloric effect (large entropy change) is discussed.

3.2.1. Synthesis

Samples were prepared from pure elements of Ni (Alfa Aesar 99.9%), Mn (Strem Chemicals 99.9%), Cu (Goodfellow 99.99%) and Ga (Strem Chemicals 99.99%). Stoichiometric amount of each of the elements was cut, well-polished (Figure 6 a) and arc melted in argon atmosphere (Figure 6 b). Arc melting was repeated two times more by reversing ingot (Figure 6 c) each time to ensure homogeneous mixing of the elements. To obtain homogenization, the final ingot was sealed in evacuated quartz tube (Figure 6 d) to subject to further heat treatments at 800°C followed by either slow cooling or quenching into ice cooled water as reported in literature and shown in Table 2. The conditions for our samples will be specified in the upcoming text.

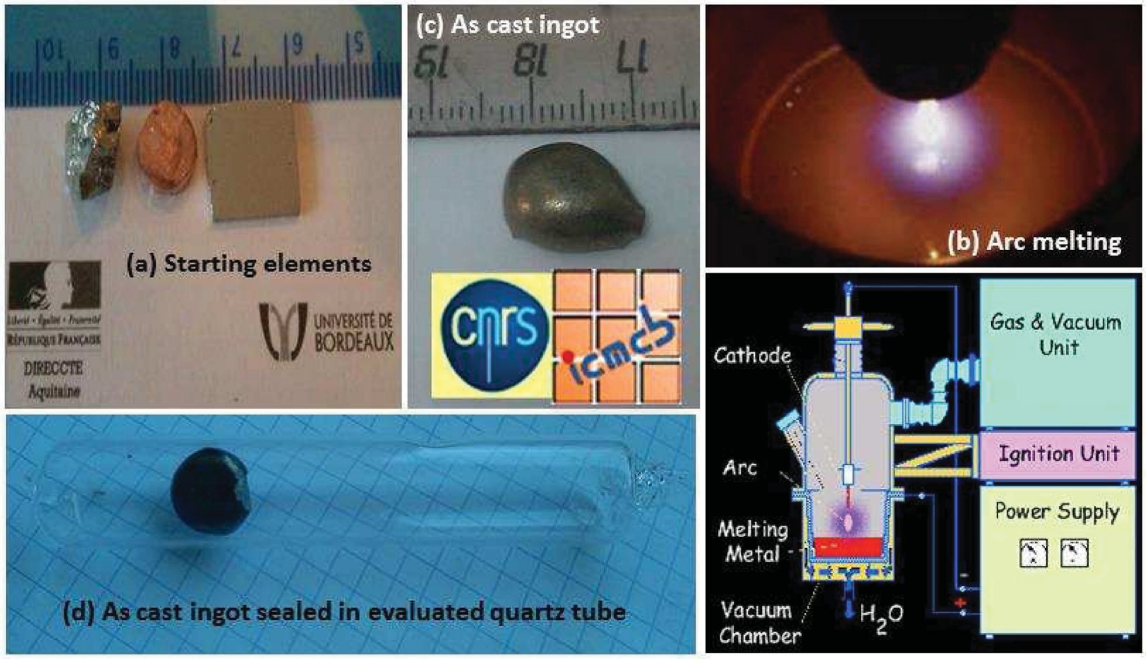

Figure 6 : Sample synthesis (a) polished starting elements. (b) Ingot after three arc melting. (c) As Cast ingot sealed in evacuated quartz to perform heat treatment.

Table 2 : Comparison of synthesis condition, structure, magnetic and MCE properties as reported in literature.

Sl no	Composition	Structure at room temp	Synthesis Condition	MCE figure of merit			Reference
				T_M, T_A K	T_C K	|ΔS|(J/kg K) ΔH=1, 3, 5T	
1	Ni_2MnGa^{sc}		Single crystal	314, 316	370	**2**, --, 18.5	[41]
2	$Ni_2Mn_{0.90}Cu_{0.10}Ga$	L21 - cubic	800 °C, 6 days in vacuum furnace and slowly cooled to RT	250	360	-----	[42] [30]
	$Ni_2Mn_{0.85}Cu_{0.15}Ga$	biphasic † and ‡		280	335	1.39 (@T_M), 1.79 (@T_C) ΔH=2T	
	$Ni_2Mn_{0.75}Cu_{0.25}Ga$	Tetragonal		**308**	**308**	**12**, 44, 65	
3	$Ni_{2.04}Mn_{0.99}Ga_{0.97}$	Cubic	850 °C for 9 days, quenched into ice water	280	363	**3.5** (274 K)	[43]
	$Ni_{2.11}Mn_{0.95}Ga_{0.94}$	Tetragonal		338	354	**7** (290 K)	
	$Ni_{2.21}Mn_{0.74}Ga_{1.05}$	Tetragonal		**320**	**320**	**15.6** (@ 317 K)	
4	$Ni_{2.16}Mn_{0.84}Ga$		827 °C for 9 days and quenching in ice water	313	330		[29]
	$Ni_{2.19}Mn_{0.81}Ga$			**324**	**324**		

† Austenetic - Cubic at high temperatures, space group *Fm-3m*, *a*=*b*=*c*=0.582nm. ‡ Martensitic - tetragonal at low temperature space group *I4/mmm*, *a*=*b*=0.592; *c*=0.557nm. ^{SC} - single crystal.

After heat treatment phase purity was checked on PANalytical X-ray diffractometer on powdered samples (λ_{Cu} ≈ 1.5406 Å). Elemental distribution analysis was performed on

Electron Probe Micro Analyzer (EPMA – CAMECA SX 100) equipped with 3 different spectroscopes WDS (Wavelength-Dispersive Spectroscopy), EDS (Energy-Dispersion Spectroscopy) and SDDD (Silicon Drift Detector) from Bruker AXS. Magnetic measurements were performed on MPMS SQUID instrument (Quantum Design, USA). X-ray photoelectron spectroscopy (XPS) was performed using VG Scientific 220 i-XL ESCALAB spectrometer with a monochromatized AlKα source (hν=1486.6eV) at 70 W under pressure of 10^{-7} Pa in the chamber. The spot size is about 180 µm in diameter. High resolution spectra at constant pass energy of 40eV or 20eV. For ageing thin slabs were cut using diamond wheel as it was described in chapter 2.

3.2.2. $Ni_2Mn_{1-x}Cu_xGa$ with x=0.2, 0.25 and 0.3

In order to reproduce the so-called giant magnetocaloric effect around room temperature in doped Ni_2MnGa systems. We initially choose two compositions which show large entropy change (Table 2) namely *(i) $Ni_2Mn_{0.75}Cu_{0.25}Ga$ (T_C ≈ 308 K) [39] (ii) $Ni_{2.21}Mn_{0.74}Ga_{1.05}$ (T_C ≈ 320 K) [43]*. Even after following careful heat treatment procedures mentioned for each of them in the literature, we never obtain so called giant MCE.

To better understand the possible reason, we prepare and characterize three different copper concentration with x= 0.2, 0.25 and 0.3 in the series $Ni_2Mn_{1-x}Cu_xGa$. Sample are obtained after annealing the as cast ingot at 800 °C for 145 hours followed by slow cooling (1.5 °C/min) [39].

As previously pointed out, a structural transition along with magnetic transition has been reported from tetragonal (*I4/mmm*, for $T<T_C$) to cubic (*Fm-3m*, for $T>T_C$) for $Ni_2Mn_{1-x}Cu_xGa$ with x=0.25. Further, the enhancement in entropy change for this particular composition of the series has been highlighted as due to merging of structural (T_M) and magnetic (T_C) transitions. Figure 7 (a) summarize the room temperature powder x-ray diffraction patterns for the samples under study. As seen samples with different copper level, *$Ni_2Mn_{0.7}Cu_{0.3}Ga$* and *$Ni_2Mn_{0.75}Cu_{0.25}Ga$* showed single tetragonal phase whereas *$Ni_2Mn_{0.8}Cu_{0.2}Ga$* looks to be mixture between cubic and tetragonal. This is possible if the magneto-structural or just structural transition is around room temperature at which the diffraction patterns were collected. It is also interesting to note the change in position of peak (*2 0 0*) next to the intense peak. With increasing Cu concentration this peak seems to

shift to lower angle (Figure 7 b), along with decrease in intensity relative to intensity of (*1 1 2*) peak. This is one of the signature for decreasing tetragonality of the system.

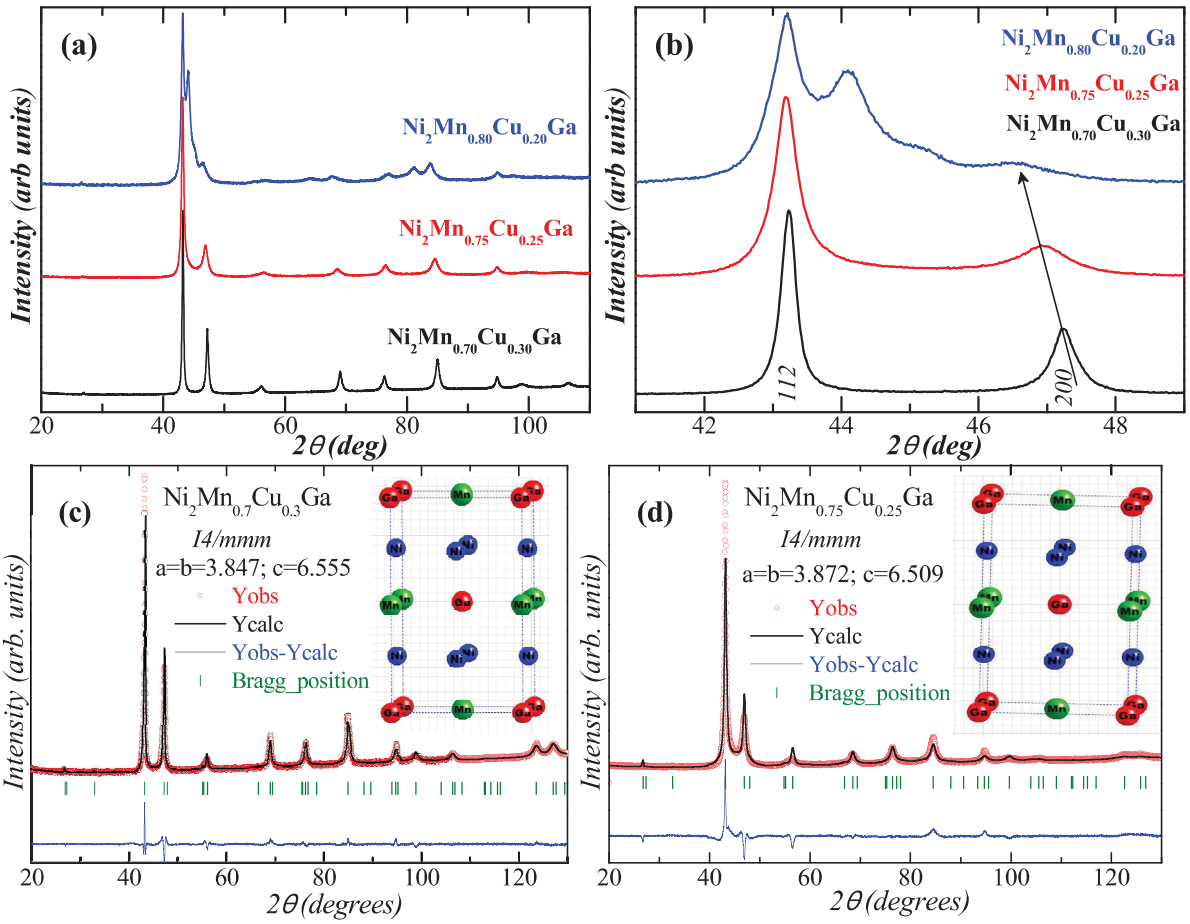

Figure 7: Room temperature x-ray diffraction pattern (a) variation of Cu concentration. (b) Expand view around intense peak demonstrating movement of (2 0 0) reflection with varying Cu (black arrow). Rietveld refinements results on (c) x=0.3 and (d) x=0.25.

Reitveld refinement was performed on $Ni_2Mn_{0.7}Cu_{0.3}Ga$ using tetragonal DO_{22} *I4/mmm* with a= b = 3.847(3) Å, c = 6.555(4) Å and resulting fits are displayed in Figure 7 c. The fit on this pattern is quite comparable to those that are reported for $Ni_{2.24}Mn_{0.75}Ga$ [26], but the reliability factors of our fit are slightly high(

Table 3). Starting from similar atomic position and unit cell parameters the refinement on $Ni_2Mn_{0.75}Cu_{0.25}Ga$ yield a=3.872 Å, c=6.509 Å, while the overall goodness of fit starts to fade with increase in value of reliability factors, Rp=4.85; Rwp=7.51; and χ^2=12.8 (Figure 7 d).

Table 3: Unit cell parameters and atomic positions from refinements of $Ni_2Mn_{1-x}Cu_xGa$ (x=0.30, 0.25).

	$Ni_2Mn_{0.7}Cu_{0.3}Ga$	$Ni_2Mn_{0.75}Cu_{0.25}Ga$
Space group	*I4/mmm*	*I4/mmm*
a Å, b Å	3.8477	3.8746
c Å	6.5544	6.5003
Ni (x, y, z); Biso	(0.00, 0.50, 0.25); 0.59	(0.00, 0.50, 0.25); 2.69
Mn, Cu	(0.00, 0.00, 0.50); -0.38	(0.00, 0.00, 0.50); -1.18
Ga	(0.00, 0.00, 0.00); -1.76	(0.00, 0.00, 0.00); 2.97
χ^2	5.46	18.4
Rp	3.89	5.11
Rwp	5.51	8.97

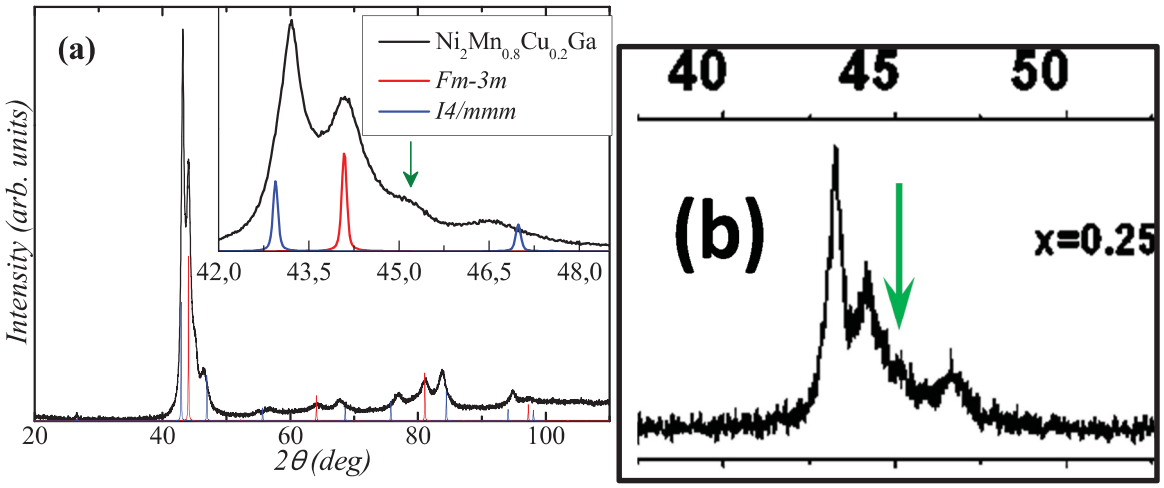

Figure 8: XRD pattern for $Ni_2Mn_{0.8}Cu_{0.2}Ga$ (a) Comparison of experimental spectra with calculated spectra of cubic *Fm-3m* and tetragonal *I4/mmm*. Inset display peaks between 2θ= 42° & 48°. Expand view around intense peak (2θ=45°) of $Ni_2Mn_{1-x}Cu_xGa$ data from [30]) demonstrating extra peak (green arrow) for x=0.25.

As mentioned before, for $Ni_2Mn_{0.8}Cu_{0.2}Ga$, a combination of tetragonal and cubic should give relative good fit for the observed x-ray pattern (Figure 8 a). However, during profile matching followed by Rietveld refinement we observe the discrepancy of considering the tetragonal phase. A careful observation, (inset of Figure 8 a) highlights shoulder peak around 2θ = 45° which is not accounted by either of the phase. Features close to our

observation can also be seen on some of the reports for example in $Ni_2Mn_{0.75}Cu_{0.25}Ga$ (green arrow in Figure 8 b), however none of the earlier reports address such difference [30].

We consider the possibility of other cubic phase that can be present due to the disordered atomic arrangements during synthesis by arc melting and further steps of heat treatment. During synthesis by arc-melting all compositions are mostly quenched from their melt in the vacuum. However in these experimental conditions the heat conduction during quenching might not be homogeneous as the base of the sample in contact with copper crucible (cooled with water) will quench much faster than the upper most surface and hence creating temperature gradient within ingot (inset (i) of Figure 9 a). If we recall most of the Ni-Mn-Ga systems have their different ordering temperatures highly populated in very close intervals around the liquid phase (Figure 3 (b)). Even small delay in cooling can result in ingot inheriting multiphase due to different ordering. As the temperature used for further heat treatment is mostly below this line of liquid state we can expect the annealed samples to still have trace of high temperature along with other lower temperature phases depending on path chosen for cooling (slow cooling or quenching). Considering these possibilities, profile matching was performed with more than one cubic phase along with tetragonal phase. Reasonable fit is obtained using the combination of 3 phases – ***DO_{22}*** or ***$L1_0$*** (low temperature tetragonal phase), ***$L2_1$*** (Cubic austenite, martensitic phase) and ***A2*** (phase stabilized at the highest temperature). However the Rietveld refinements on the resulting composite phase never converge to reasonable fit.

Brown et al based on the high neutron powder diffraction experiments have shown that Ni_2MnGa undergoes multi stage structural transitions at low temperatures [44]. Against the classical cubic (*Fm-3m*) to tetragonal (*I4/mmm*) transition at martensitic transition, the diffraction patterns confirmed new sequence of transition to occur: Cubic Heusler $L2_1$ structure (*Fm-3m*, a = 5.82 Å, 400K to 260K) → precursor/pre-martensitic phase (*Pnnm*, b=3a between 260 and 200K) → martensitic phase (*Pnnm*, *b* = 7*a*, from 200 K down to 20 K). Most of the off-stoichiometric compounds of Ni_2MnGa have also been reported to show similar deviations from the tetragonal structure [27]. Such deviation was encountered by taking into account the modulation of the structure.

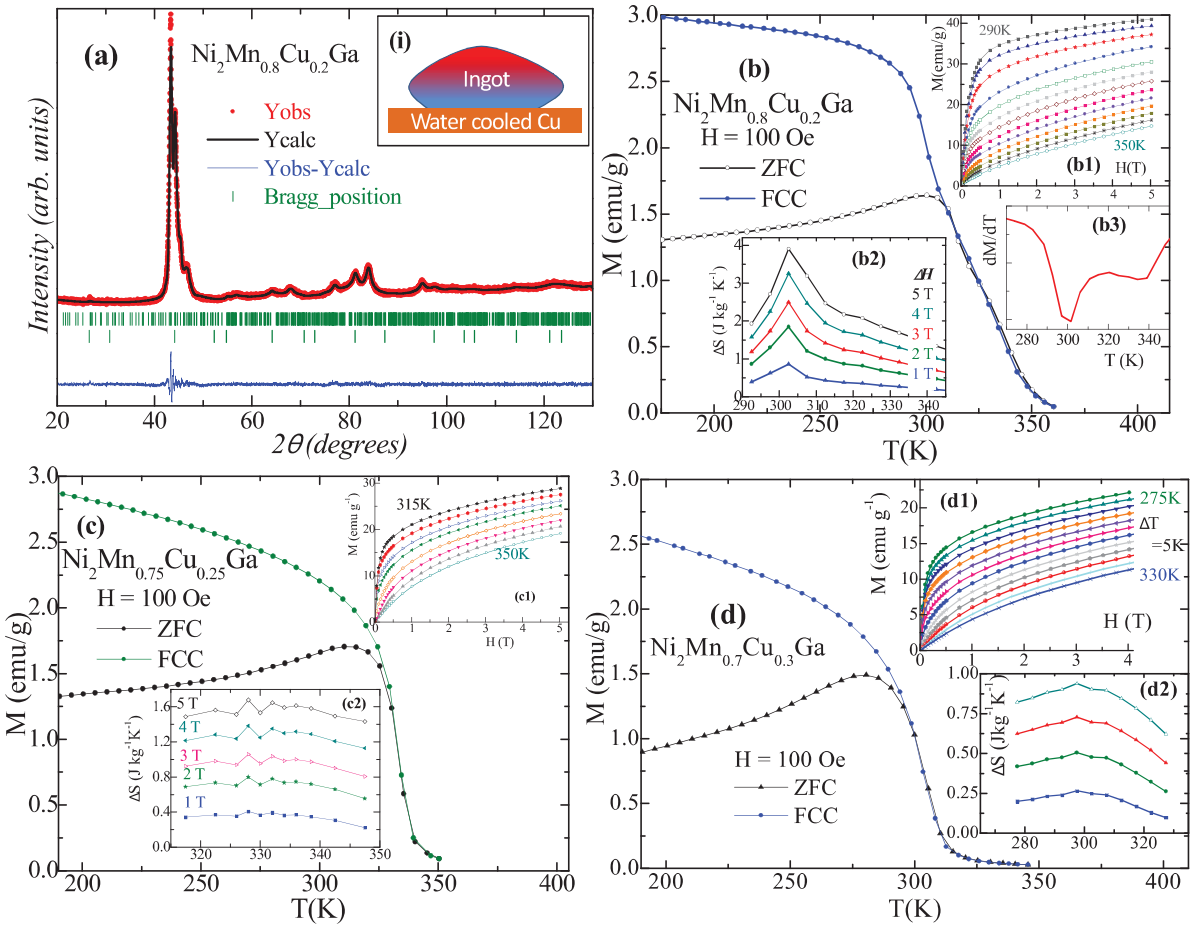

Figure 9: For the powder samples - (a) Le-bail fit for $Ni_2Mn_{0.8}Cu_{0.2}Ga$ using monoclinic + cubic phase. Temperature dependence of magnetization for (b) $Ni_2Mn_{0.8}Cu_{0.2}Ga$ (c) $Ni_2Mn_{0.75}Cu_{0.25}Ga$ and (d) $Ni_2Mn_{0.7}Cu_{0.3}Ga$. Their corresponding isothermal magnetization curves and entropy change are presented in insets.

Initial profile matching was carried out on xrd pattern of $Ni_2Mn_{0.8}Cu_{0.2}Ga$ using above-mentioned orthorhombic as well as monoclinic modulated structures (3.1.3 (ii)). Reasonable profile fit with lower residue, reliability factors was obtained only for 14M/7R, with space group *I12m/1* and lattice parameters a=4.182, b=5.472, c=29.389, α=γ=90°, β=94.21° (Figure 9 a).

Even though powder x-ray diffraction gives good knowledge of the possible arrangement of atoms in the unit cell through super lattice reflections and peak splitting. High background noise mostly due to x-ray absorption of some of constituent elements, along with several possible peaks at same diffraction angle from multiphase makes qualitative analysis of these diffraction peaks slightly tedious. So it is necessary to make diffraction patterns at temperatures (low or higher than the room temperature) where only

single phase exists. High temperature x-ray diffraction will be performed on these samples to address these issues. The constituent elements of our sample i.e., Ni, Mn, and Cu have much close x-ray scattering lengths (Table 4); this becomes limiting factor in order to well establish the site occupancy of each of the elements. It is therefore necessary to characterize the structure using better elemental sensitive probes such as neutron diffraction that can better distinguish each of the elements. Electron diffraction technique has been demonstrated to be more precise tool in characterizing the modulated structures [45]. So we look forward to address crystal structure of $Ni_2Mn_{0.8}Cu_{0.2}Ga$ using these two techniques in near future.

Table 4 : Physical properties of the constituent elements of $Ni_2Mn_{1-x}Cu_xGa$.

Element	Density g cm^{-3}	Melting °C	Boiling °C	x-ray	Neutron
				Atomic scattering factor/length	
Manganese (Mn)	7.21	1246	2061	24.99	-3.73
Nickel (Ni)	8.908	1455	2913	27.98	10.3
Copper (Cu)	8.96	1084	2562	28.98	7.718
Gallium (Ga)	5.91	29.76	2204		

Ni_2MnGa as a forth mentioned exhibits two transition lower martensitic transition (T_M=202K) and magnetic ordering with higher Curie temperature T_C=376 K[29]. By introducing 25% of Cu in place of Mn these two transitions are believed to be merged and shifter towards room temperature (318 K) along with enhanced entropy change to give giant magnetocaloric effect. Magnetization measurements as function of temperature were performed under constant applied field of 100 Oe from 15 K to 350 K for three samples and are summarized in (here data is presented by highlighting the region only around transition for better display). In all the measurements to follow, we use constant notation to represent measuring conditions, ZFC for data collected warming from low temperature before which sample was Zero Field Cooled; FCC for Field Cooled Cooling; FCW – Field Cooled Warming conditions. Here magnetization data was collected on the powder sample.

$Ni_2Mn_{0.8}Cu_{0.2}Ga$ exhibits ferromagnetic to paramagnetic transitions from 350 K to 300 K, the derivative of the curve show two peaks at 300 K and 334 K suggesting the transition to be two stepped (Figure 9 b3). Isothermal magnetization curves are probed

between 350 K and 290 K at regular temperature interval of 5 K which are displayed in inset Figure 9 b1. These isotherm curves are characteristics of second order ferromagnet to paramagnet transition, and they do not exhibit any anisotropic nature that was reported for $Ni_2Mn_{0.75}Cu_{0.25}$. The entropy change calculated using these curves had moderate but low values (0.86, 1.85, 2.5, 3.9 J kg^{-1} K^{-1} for applied field of 1, 2, 3, 4, 5 T) and no giant magnetocaloric effect is seen (Figure 9 b2). These values are observed at 302 K which corresponds to the first transition on magnetic curve. While a shoulder like signature at low value of entropy change is seen around 330 K which correspond to second transition on magnetic curve.

Magnetization curves of other two samples $Ni_2Mn_{1-x}Cu_xGa$ (x=0.25, 0.3) showed a single magnetic transition at 334 K and 303 K (Figure 9 c and d). The temperature observed for x=0.25 is very high compared to 308 K reported for same composition. Again there was no signature of any anisotropy in all isothermal curves probed between 350 K and 315 K (Figure 9 c1, d1). For much surprise, the entropy changes for these samples are still very low (Figure 9 c2, d2).

Table 5: Electron Probe Micro Analysis (EPMA) results on $Ni_2Mn_{1-x}Cu_xGa$.

Element →	**Targeted composition**				**From EPMA – normalized to Ni**			
Composition↓	**Ni**	**Mn**	**Cu**	**Ga**	**Ni**	**Mn**	**Cu**	**Ga**
X= 0.20	2	0.80	0.20	1	2	0.74	0.20	0.93
X=0.25	2	0.75	0.25	1	2	0.67	0.24	0.92
X=0.30	2	0.70	0.30	1	2	0.65	0.29	0.90

Elemental distribution analysis were carried out using EPMA. The backscattered image characterized with single contrast region over complete probe area confirm single phase at micron level. Elemental distribution on all the samples were obtained and the results are tabulated in Table 5. It is evident from the table that for all the composition there is loss of Mn (7.5 at. % to 10 at. %) and Ga (7 at. % to 10 at. %) making the over all composition to be off-stoichiometry. Variation of T_M and T_C depends strongly on concentration of individual elements. The so observed low values of entropy change, in our case, can be due to this off set of composition. The lowered Mn and Ga concentration than the targetted can mainly be to the lower boiling point of these elements [Table 4].

3.2.3. $Ni_2Mn_{0.75+\delta}Cu_{0.25}Ga$ compensating for the Mn loss

The major magnetic contribution in $Ni_2Mn_{0.75}Cu_{0.25}Ga$ is reported to be from Mn as confirmed by neutron and very small magnetic contribution from Ni as proposed from x-raymagnetic circular dichroism (XMCD) experiments [46]. Hence observed entropy changes will be reflected of Mn concentration. We observe loss of Mn during arc melting as Mn tends to be volatile for the arc, the qualitative analysis of the loss was also addressed by EPMA analysis in previous subsection. Addition of Mn can also be used to interpret the effect of Mn concentration within the matrix and its influence on observed magnetic and entropy changes. To compensate such loss we have further prepared three compositions by accounting excess atomic percentage of Mn in $Ni_2Mn_{0.75}Cu_{0.25}Ga$ from the start instead of adding in between melting [47]. The contribution of gallium can also be considered, however we will focus our studies only on content of manganese.

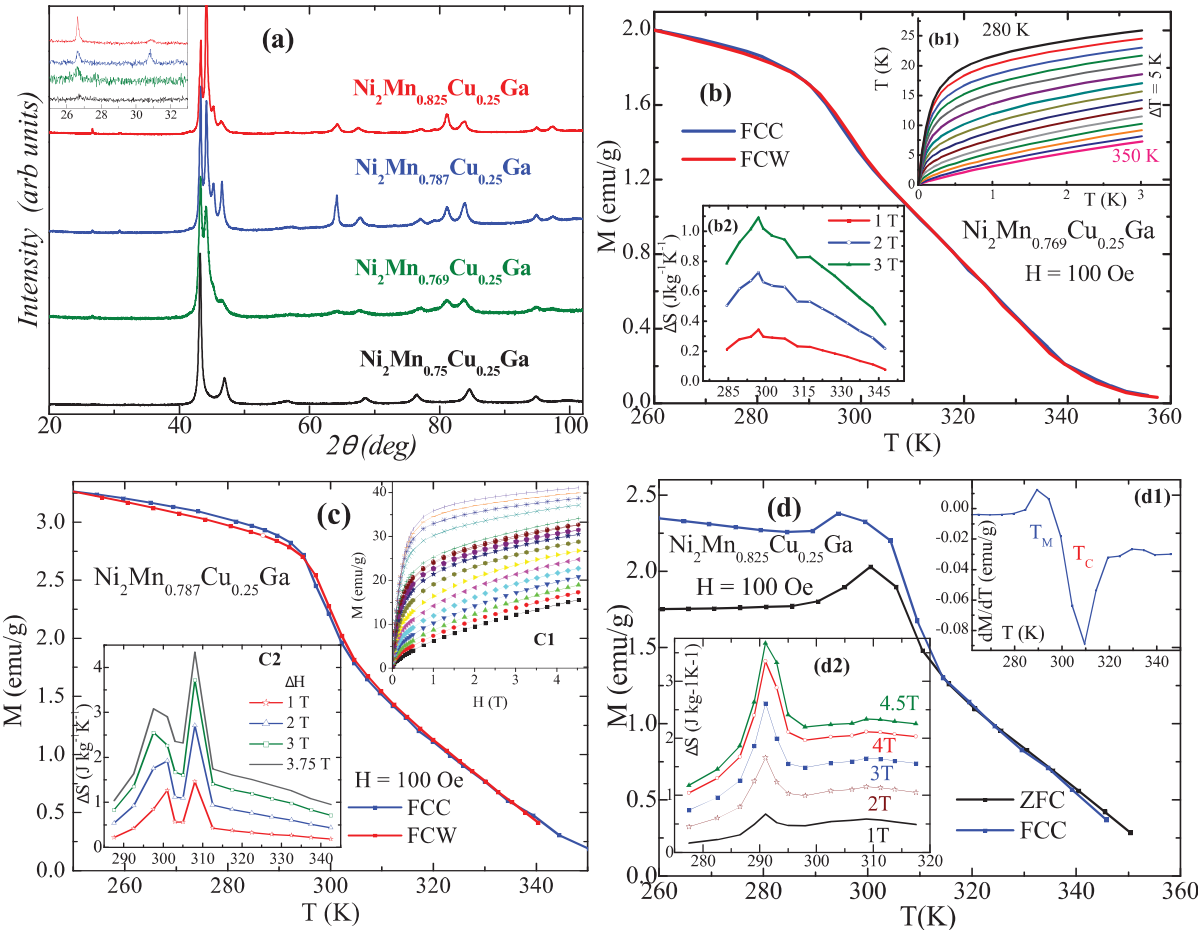

Figure 10: (a) X-ray diffraction for all three excess Mn concentrations on $Ni_2Mn_{0.75+\delta}Cu_{0.25}Ga$. Magnetization and entropy change for (b) 2.5, (c) 5 and (d) 10 at % excess Mn.

Three different compositions, with $Mn_{0.769}$, $Mn_{0.787}$ and $Mn_{0.825}$ which correspond to 2.5, 5 and 10 at % excess Mn on $Ni_2Mn_{0.75}Cu_{0.25}Ga$ parent compound are prepared. The final sample are obtained by annealing the as cast sample at 800°C for 145 hours followed by slow cooling, as described in previous section 3.2.2. The powder x-ray diffractions for these three samples along with parent compound $Ni_2Mn_{0.75}Cu_{0.25}Ga$ are presented in Figure 10 (a). All the samples have structure which deviate from regular tetragonal unit cell. The inset shows the appearance of some extra peaks as we move from $Mn_{0.75}$ sample to higher Mn doping. These peaks are superstructure peaks that can give information about different ordering. Justifying we have to consider multiple cubic phase in few case, for example $Ni_2Mn_{0.787}Cu_{0.25}Ga$ where two equal intensity peaks are visible. However, our attempt to refine did not yield reliable fits as discussed for $Ni_2Mn_{0.8}Cu_{0.2}Ga$, so may be one of the orthorhombic/monoclinic modulated structures is better solution. To address this effectively we need some high-resolution electron diffraction experiments.

The magnetization on resulting samples with 2.5 at % ($Ni_2Mn_{0.769}Cu_{0.25}Ga$), 5 at % ($Ni_2Mn_{0.787}Cu_{0.25}Ga$) and 10 a t% excess Mn ($Ni_2Mn_{0.825}Cu_{0.25}Ga$) are summarized in Figure 10 (b to d).

From Figure 10 b, $Ni_2Mn_{0.769}Cu_{0.25}Ga$ has two transitions $T_{C1} \approx 298$ K, $T_{C2} \approx 324$ K (obtained from differentiating FCC/FCW curve) much similar to $Ni_2Mn_{0.8}Cu_{0.2}Ga$. The isothermal magnetization curves across the transition (between 350 K and 280K) show features more likely of second order like magnetic transition (Arrott plot). The entropy change calculation from these curves result in very low values (ΔS = 0.34, 0.73, 1.09 J $kg^{-1}K^{-1}$).

Sample with 5 at % excess Mn showed a single wide second order ferromagnetic magnetic like transition around room temperature (Figure 10 c). On differentiating the curve we observe two distinct ordering T_{C1}= 298 K, T_{C2} = 306 K. These are reflected on entropy curve where in two maximum are exhibited around 306K and 295K. The peak values at 306 K are 1.46, 2.71 and 3.72 $Jkg^{-1}K^{-1}$ for field change of 1, 2 and 3T.

While magnetic behavior of $Ni_2Mn_{0.825}Cu_{0.25}Ga$ has different features a small raise in magnetization across T_M = 291.5 K and a ferromagnetic ordering around T_C = 308 K (inset d1 of Figure 10 d). The entropy change (inset d1, Figure 10 d) calculated across these transition

show large value across T_M (ΔS=0.67, 1.65, 2.61 $Jkg^{-1}K^{-1}$ for ΔH=1, 2, 3T) compared to the once around T_C (ΔS=0.58, 1.14, 1.65 $Jkg^{-1}K^{-1}$).

Table 6: Microprobe analysis for the $Ni_2Mn_{0.75+\delta}Cu_{0.25}Ga$ with δ representing the excess of Mn.

Composition - excess of Mn in terms of		$Ni_2Mn_{0.75+\delta}Cu_{0.25}Ga$ Targeted composition				From EPMA – normalized to Ni			
at %	δ	Ni	Mn	Cu	Ga	Ni	Mn	Cu	Ga
2.5	**0.019**	2	0.769	0.25	1	2	0.72	0.24	1.01
5	**0.037**	2	0.787	0.25	1	2	0.75	0.25	0.98
10	**0.075**	2	0.825	0.25	1	2	0.79	0.25	0.85

To evaluate the overall stoichiometry of the compositions elemental analysis was carried out on well-polished samples of all the three composition. The results are tabulated in Table 6, it is quite clear that there is still low content of manganese in final composition as compared to the starting or targeted compositions. For 10 at % excess of Mn sample the resulting composition as obtained from EPMA is $Ni_2Mn_{0.79}Cu_{0.25}Ga_{0.85}$. In this case we propose the excess Mn to be on the Ga site making the composition as $Ni_2Mn_{0.75}Cu_{0.25}Ga_{0.85}Mn_{0.04}$. [Science China 55 295] It is interesting to observe sample targeted for 5 at % excess of Mn results in $Ni_2Mn_{0.75}Cu_{0.25}Ga_{0.98}$ which is close to composition reported for the giant magnetocaloric effect [39]. So we should expect large entropy change for this sample to be consistent with reports. However, the magnetization show two transition against one sharp transition reported. Also the highest observed entropy change being 1.45, 2.71 and 3.71 $Jkg^{-1}K^{-1}$ against reported values of 12, 44 and 65 $Jkg^{-1}K^{-1}$ for field change of 1, 2 and 3 T respectively. There are few results in literature which report slightly lower values such as 8, 17, 26 $Jkg^{-1}K^{-1}$ these are still larger than the values observed in our case [47]. In the same report it was also shown that with decreasing Mn content the martensitic transition increases however the giant entropy change is still maintained even till 6% loss of manganese. So there should be other phenomenon responsible for the giant magnetocaloric effect in these compounds. Strain and grain size effect can be some of these phenomenon and they are discussed in detail in the following section.

Recalling the basic characteristic of the alloy i.e., shape memory effect is directly related with the structure of the material. Shape memory alloys are established to exhibit large volume changes (ΔV/V or ΔL/L) across their structural transition. This property should depend more on the elasticity of material compared to the composition itself. So it is interesting to probe effect of grain shape of the material on the observed physical properties. This will also felicitate in unveiling the fact, does the large entropy observed is related with structural or elasticity of the material.

3.2.4. Microstructural – microstrain effect

Unlike any other compounds $Ni_2Mn_{1-x}Cu_xGa$ series or even shape memory alloys in general inherit different physical properties. Here we make an effort demonstrate the relation of grain size/morphology to the observed physical properties. The blocks (Figure 11 a) when ground (without too much pressure) using mortar and pestle initial separate to look something like shown in Figure 11 b). It infers that blocks are formed with combination of tiny fiber like structures. With further grinding, they take shape of plate like form before being able to get them in powder form ((Figure 11 c). The x-ray diffraction from these three samples is presented in Figure 11 d. X-ray pattern on bulk is mostly of the cubic phase, and as we break them we see increase of tetragonal/orthorhombic phase. This has been highlighted by arrow symbols in Figure 11 e, which present expanded view around the most intense peak. So to compare, the intensity of the peaks marked with arrow symbol increase with grinding. Similar results were observed on other composition, for magnetic measurements to follow in couple of paragraph we restrict to only bulk and the powder.

At this point it is noteworthy to mention some crucial features expected for shape memory alloys, in particular Ni-Mn-X Heusler alloys. In single crystal of $Ni_{52}Mn_{24}Ga_{24}$ alloys it has been demonstrated that microstrain in the grain can be introduced due to grinding. From x-ray diffraction data, average microstructural strain ε (%), due to grinding can be calculated using following relation, $\varepsilon = \left|\frac{\Delta d}{d}\right| = \frac{\beta}{4 \cdot \tan\theta}$ which is based on Scherrer formula. In the relation, d represents the interplanar spacing, θ is the Bragg angle and $\beta = \sqrt{W_1^2 - W_2^2}$ where W_1 and W_2 are the FWHM (Full Width of the Half Maxima) of corresponding Bragg peaks for the ground and annealed samples respectively. By evaluating the microstrain (ε)

for samples with different particle size it was shown that particles with size≤200 the strain starts to increase exponentially [48]. Further by obtaining similar values of ε on different Bragg peaks, it was confirmed the so observed microstrain to be isotropic for the given sample. Using the value of microstrain one can also deduce (i) Elastic energy of the material, $E = \frac{1}{2}C\varepsilon^2$ (ii) average internal stress $\sigma = C\varepsilon$, where C is the bulk Young's modulus. In the case study mentioned above it was shown that with decreasing particle size a monotonic increase of average internal stress is observed.

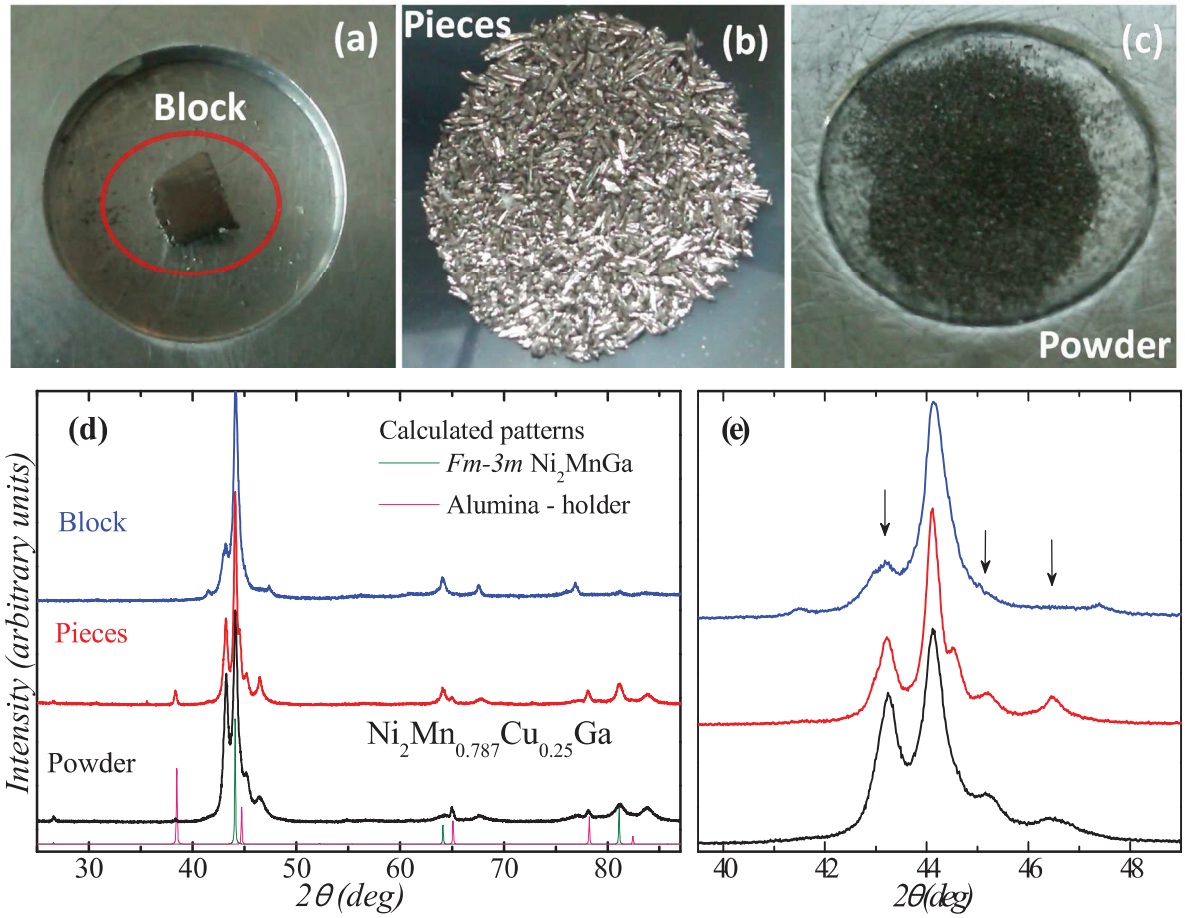

Figure 11: Photographic images of (a) Block highlighted by red circle (b) Pieces and (c) powdered sample. And comparison of their x-ray diffraction pattern (d) and (e).

In our case, at room temperature the compositions are biphasic as we are just around magnetic and structural transition. The appearance of multiple peaks due to two-phase along with peaks broadening due to grinding makes it complicated to extract such qualitative information. The trials to extract microstrain for samples shown in Figure 11 (d)

resulted in different values of ε for different Bragg peaks however; increase in value of ε with grinding was confirmed.

For each sample discussed in the previous sections (3.3.2 and 3.3.3), temperature dependent magnetization measurements were carried out on two different morphological specimens – *(i) fine powder* ground from the heat treated ingot (Figure 11 c) and *(ii) single block* cut from heat treated ingot (Figure 11 a). As is evident from the graphs (Figure 12), in case of all composition, blocks result in sharper transition compared to those obtained on powders where the transition is much continuous and is over long range of temperature. Inset of Figure 12(a) show the data along complete temperature range collected during field cooling, it helps one to better differentiate the transition nature displayed by block and powder samples.

As magnetization curves on powder samples are already discussed in detail in section 3.2.2 and 3.2.3, here we will discuss only results on bulk samples.

$Ni_2Mn_{0.8}Cu_{0.2}Ga$ exhibits sharp ferromagnetic to paramagnetic transition at 304.5 K (under FCC) and 307.2 K (under FCW) with a hysteresis of 2.7 K between the FCC and FCW at transition (Figure 12 a). Similar change in the order of transition is observed in case of other two copper substituted samples. Magnetic transition temperature for $Ni_2Mn_{0.75}Cu_{0.25}Ga$ read $(335.5\ K)_{FCC}$, $(334.2\ K)_{FCW}$ and for $Ni_2Mn_{0.7}Cu_{0.3}Ga$ was $(309.6\ K)_{FCC}$ and $(310.2\ K)_{FCW}$. In these two samples the opening between FCC and FCW was almost zero near transition and shifted to just below transition, extending to lower temperature (280 K to 330 K) in case of $Ni_2Mn_{0.75}Cu_{0.25}Ga$. While for $Ni_2Mn_{0.7}Cu_{0.3}Ga$ the hysteresis in FCC-FCW is observed between 306.2 K and 259 K similar to former just below transition. Such opening can be often referred to structural transition from martensitic to austenitic with increasing temperature, similar to one observed in parent compound Ni_2MnGa [43]. The reasoning for hysteresis between FCC and FCW curves can also be the phase co-existence, i.e., with in the temperature of hysteresis between FCC, FCW low temperature and high temperature phase coexist. Implying the temperature range observed for the hysteresis is temperature range required for structural transition to complete, in present case the transition from cubic to tetragonal/orthorhombic (during cooling) and vice versa while heating. This infers the structure transition to occur at same interval compared to magnetic transition temperature in $Ni_2Mn_{0.8}Cu_{0.2}Ga$, while for other two samples it looks like the two transitions occur at

different temperature. These results are much different from those observed on powder samples, the microstains on the grains of crystallite due to grinding can be the main reason behind.

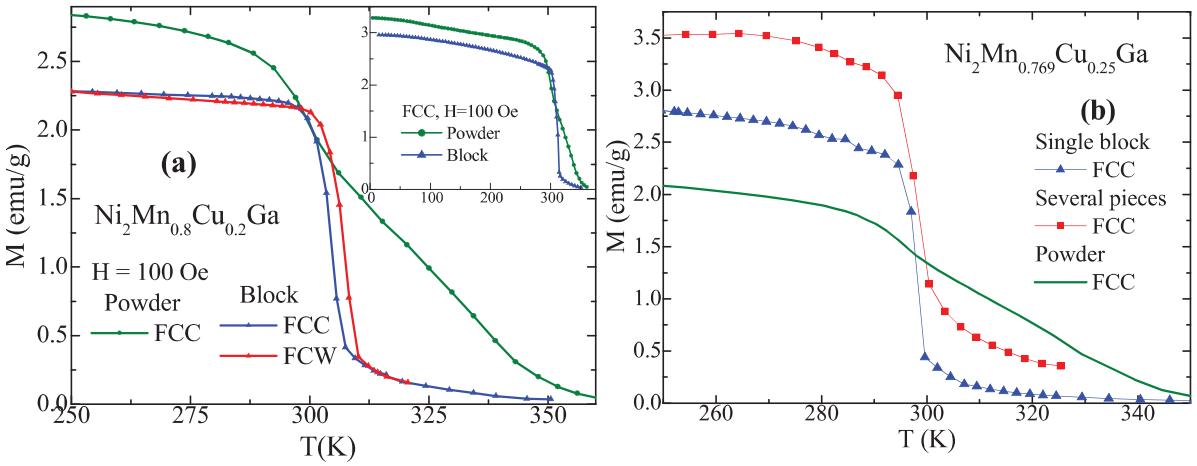

Figure 12: Magnetization as a function of temperature for two samples with different morphology.

We extend similar studies to the manganese samples presented in 3.2.3 and observe sharper transitions then the once observed on powder samples for example, Figure 12 b. For $Ni_2Mn_{0.769}Cu_{0.25}Ga$ temperature dependent magnetization are carried out on three different morphologies similar to the once shown in Figure 11 a, b and c. The resulting field cooled data for single-block; pieces and fine powder of the sample are presented in Figure 12 b. It is interesting to see that the sharpness in magnetic transition decreases monotonically with grinding. This suggest that the structural or/and magnetic transition depend on strain applied on grains and hence more the strain lower is the degree of first order transition.

Recalling the x-ray diffraction on bulk and powder samples, we can link changes in magnetization of these two samples with changes in structural phase. The effect of such changes can be better understood by probing temperature dependent x-ray/neutron diffraction on bulk and powder along transition temperature. If our assumptions, the link between structure and magnetism are true, then we should expect sudden change in structure on bulk sample, whereas, on powder sample one should see continuous/dragged phase change over wider temperature range as is the magnetic transition. As discussed in introduction of this chapter Heusler alloys are better known for their shape memory effect.

This could mean, by destroying morphology of the grain we destroy the elastic nature associated with the material and hence large entropy change associated with it.

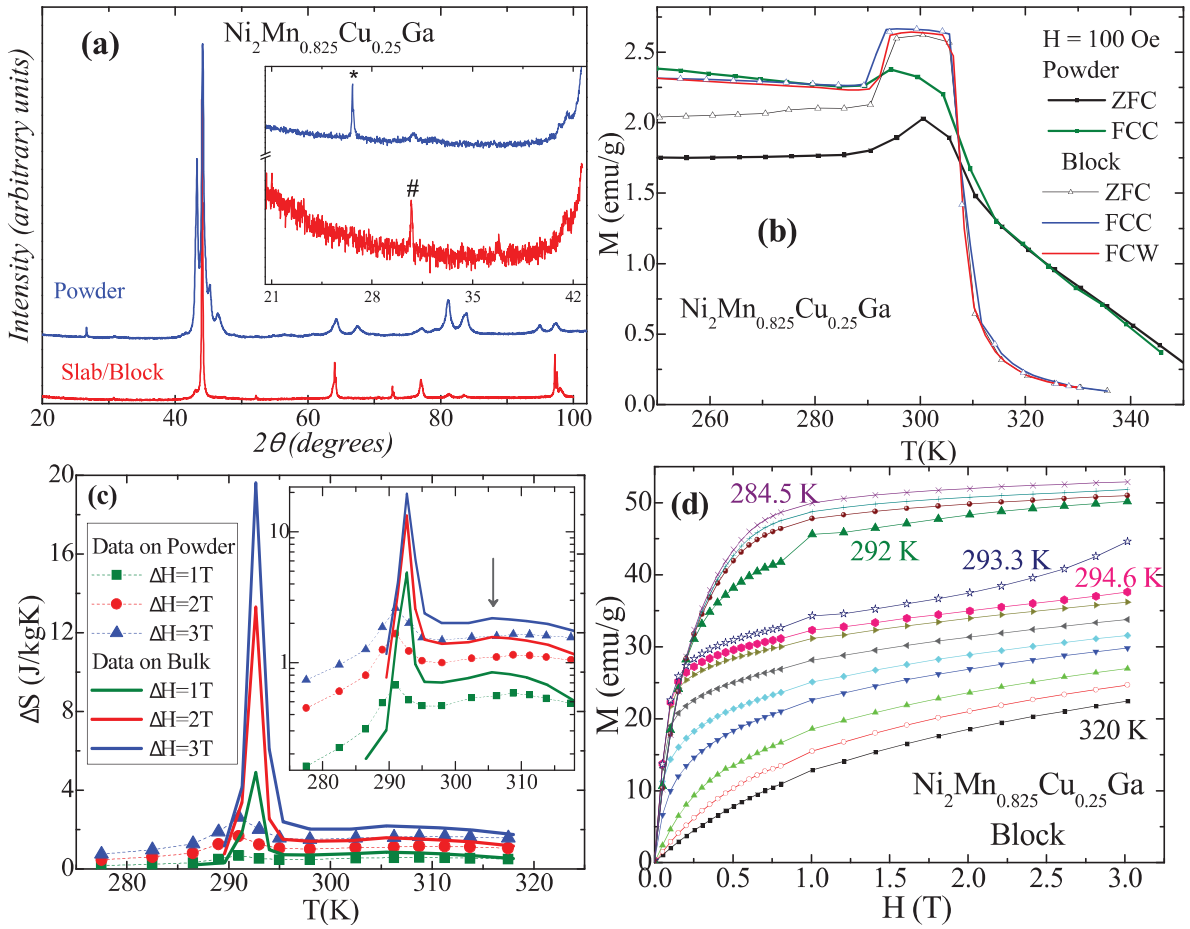

Figure 13: $Ni_2Mn_{0.825}Cu_{0.25}Ga$ - microstructure effect demonstrated on powder and block sample. Comparison of powder and block data of (a) x-ray diffraction pattern; (b) magnetization curve, (c) the observed entropy and (d) isothermal magnetization profile of block.

Figure 13 (a) display the x-ray diffraction patterns for powder and block for the composition with 10 atomic % excess Mn. It is clear that the slab display almost cubic phase, whereas the powder is biphasic. The inset shows the low angle peaks which distinguish the two phases. Temperature dependence magnetization curves on powder and bulk morphological samples are present in Figure 13 (b). The powder sample showed a broader transition extending from 300K to 350K. Magnetization curves probed on bulk of the sample show two well separated transitions (i) around 290 K, a decrease in the magnetization during FCC and increase on FCW characterized with hysteresis of about 3 K (ii) around 308 K a ferromagnetic transition with merged FCC and FCW. The transition (i) is characteristic of

structural transition while (ii) should be magnetic. So it is interesting in couple of aspects to evaluate the magnetocaloric effect in $Ni_2Mn_{0.825}Cu_{0.25}Ga$ samples. Room temperature (T>295 K) x-ray diffraction for the two samples is shown in inset of the figure. It was clear from observations, the bulk has cubic structure as majority of the phase while the powder had majority phase of tetragonal/modulated structure. This will support our assumption, the low temperature transition in magnetization to be a structural transition (T_M<290K). As we observe magnetic and structural transition to be close but not completely merged in this compound, it will give us opportunity to address if the coexistence of both transitions is a must to observe the so highlighted giant MCE in these compounds [49]. The isothermal magnetization curves for both the samples were probed between 320 K and 275 K so that we cover complete range of transition. The M(H) curves on powder sample (data not shown) are similar to the once observed for any typical second order ferro to paramagnetic magnetic transition. The entropy changes from these curves are plotted using solid symbol with dotted line in Figure 13 c (is same data that was presented in Figure 10 d1).

Isothermal magnetization curves for bulk sample show similar behavior between 320 K and 295 K but at temperatures 293 K and 292 K they are characterized with anisotropy. The effect of such anisotropy can be seen on the observed entropy change. The entropy change calculated from M vs H curves applying Maxwell's equation is presented with solid line in Figure 13 c. The peak values of observed entropy change at T=292K read as ΔS = 4.89, 13.31 and 19.61 J kg^{-1} K^{-1} corresponding to the field change of 1, 2 and 3 T. Inset of same figure display entropy change in logarithmic scale where a secondary peak can be observed at 305.5 K, from the derivative of M (T) curve this peak should correspond to the magnetic transition. The peak value in this case are very low (ΔS= 0.844, 1.566 & 2.178 J kg-1 K-1 for ΔH = 1, 2 & 3T), but they are comparable to the once observed in most of second order magnetic transition. However, there is still need to address the contributions of anisotropy observed on isothermal magnetization curves towards these large values.

Comparing the set of values mentioned, we can propose that the major contribution for observed high values of entropy change in Heusler alloys is from structural transition. This is in agreement with some recent reports where it was shown, (in case of Ni-Mn-In-(Co) alloy) that the structural transition is what that drive the so called giant magnetocaloric effect [50]. The authors also suggest some feasible solutions that help overcome some of

the obstacles such as the large thermal irreversibility, limited operating temperature window.

Table 7 : Comparison of transition temperature, entropy change from block and powder specimen.

Composition	T_{C-FCC} (K)	T_{C-FCW} (K)	$T = \Delta S_{peak}$ (K)	ΔS ($Jkg^{-1}K^{-1}$)		
	H = 100 Oe			1 (T)	2 (T)	3 (T)
$Ni_2Mn_{0.80}Cu_{0.20}Ga$-Pow	301.5	--	302.5	0.86	1.85	2.49
$Ni_2Mn_{0.80}Cu_{0.20}Ga$ block†	304.5	308.28	304	7.74	--	--
$Ni_2Mn_{0.80}Cu_{0.20}Ga$ block‡			306.6	5.93	--	--
$Ni_2Mn_{0.769}Cu_{0.25}Ga$-Pow			305	0.35	0.73	1.09
$Ni_2Mn_{0.769}Cu_{0.25}Ga$-block	303	307.8	307.5	4.28	9.25	14.1
$Ni_2Mn_{0.787}Cu_{0.25}Ga$-Pow	310		308	1.45	2.71	3.71
$Ni_2Mn_{0.787}Cu_{0.25}Ga$-block	299.7	301.2	298.75	4.05	10.02	13.44
$Ni_2Mn_{0.825}Cu_{0.25}Ga$-Pow	289.5	--	291	0.67	1.66	2.61
$Ni_2Mn_{0.825}Cu_{0.25}Ga$-block	291.5	292.3	292.6	4.89	13.31	19.61

Pow = data on powder; † - calculated from FCC data under different applied field; ‡ - calculated from FCW data under different applied field.

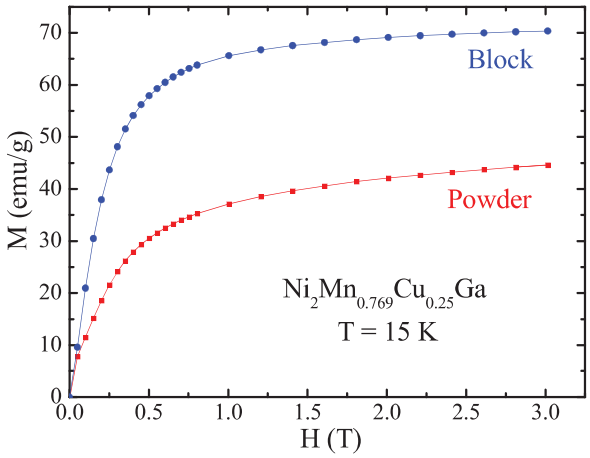

Figure 14: Isothermal magnetization curve measured at 15 K for block and powder specimen of $Ni_2Mn_{0.769}Cu_{0.25}Ga$.

Isothermal magnetization curves for the powder and block $Ni_2Mn_{0.769}Cu_{0.25}Ga$ sample up to applied field of 3 Tesla is shown in Figure 14. Magnetization curve for powder does not saturation for the current applied field. It has value of 44.55 emu/g which is very

low compared to value on block sample (70.31 emu/g). In literature there are few attempts to remove the strains by annealing the ground powder, like in case of Ni-Fe-Ga-Co based Heusler alloy [51]. The authors report effect of powderization of the material on the observed physical properties. Their results show total disappearance of the martensitic transformation in powder sample. This indeed decreases the transition temperature as well as effective magnetic moment. After annealing the powder they recover some of the martensitic transition, but fail to gain the original properties completely.

Entropy change for other compositions presented in previous section is calculated using block instead of powder specimen and the results are summarized in Table 7. By comparison the block specimen exhibit larger entropy change (10 fold more) compared to their respective powder sample. The MCE figures of merits are comparable for different excess Mn samples, when they are probed in bulk form. However, only 2.5 at %excess Mn sample showed clear hysteresis across the ferro to paramagnetic transition, suggesting coupled structural and magnetic transition.

From our experiments on microstructure it is clear that the destruction of grain due to micro-strain during grinding lead to destroy of the physical properties (structural and magnetic) of the sample. Recollecting the basic properties of shape memory effect, we propose that grain morphology plays very crucial in these materials. In our further investigation on exploring the effect of annealing condition we will present data only on the bulk sample.

3.2.5. Effect of annealing

In early literature on $Ni_2Mn_{0.75}Cu_{0.25}Ga$, there was mention of fact that the observed entropy change is a strong dependent of the heat treatment – the annealing temperature, duration, as well as cooling rate. However, none of the reports specify the numerical values for these experimental conditions. Following our experimental results of strong composition dependence on entropy change and nature of transition we have investigated effect of heat treatments on one of the promising material and will be discussed in detail. Composition with 2.5 at. % excess Mn, $Ni_2Mn_{0.769}Cu_{0.25}Ga$, with convincing first order magneto-structural transition was chosen for the task (Figure 12 b). Interestingly, the so resulting sharp

transition lies near room temperature (≈298K) which is advantageous for near room temperature magnetocaloric effect. It is thereby interesting to optimize the composition in order to obtain better MCE figure of merit. The As-Cast ingot was broken into 4 parts and each of them was treated for different annealing. Two pieces were annealed at 800°C for 145 hours followed by first sample was allowed to *slowly cool (60°C per hour) to room temperature* (here after referred as *sam (i)*) and other was *quenched from 800 °C into ice cooled water (*referred as *sam (ii))*. Other piece was annealed at 900 °C for 145 hours and quenched into ice cooled water referred as *sam (iii)*.

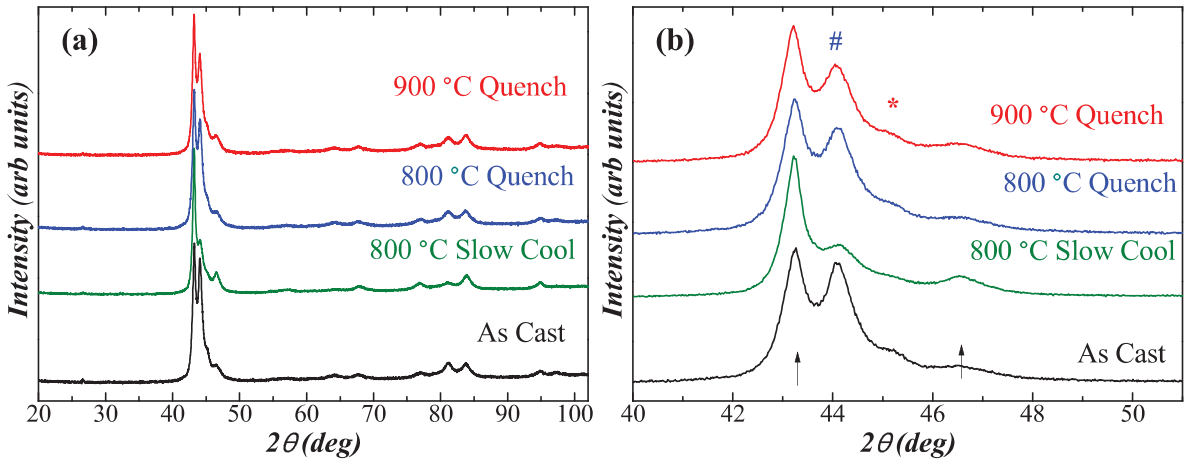

Figure 15: (a) Room temperature x-ray diffraction pattern for different heat treatments. (b) Expanded view around main peak.

X-ray powder diffraction patterns are presented in Figure 15 (a), all the samples look to be either biphasic or to have modulated structure, similar to $Ni_2Mn_{0.8}Cu_{0.2}Ga$ described in 3.2.2. Figure 15(b) highlight some of the differences: (i) As cast sample and the two samples quenched in to water show similar structural properties, with close to equal amount of cubic and tetragonal/modulated phase(marked with arrow and star). The intensity of cubic phase (marked with #) is highest for As Cast and decrease with lowering temperature. (ii) The sample after slow cooling showed more tetragonal/modulated structure with considerably low contribution of cubic phase. Even intensity of extra peak (*) is reasonable low as compared with other three samples. These changes follow the ordering phase diagram presented in Figure 3 b, the highest temperature stabilizing ordered cubic phase, and cooling stabilizing the lower temperature phase in present case the tetragonal phase.

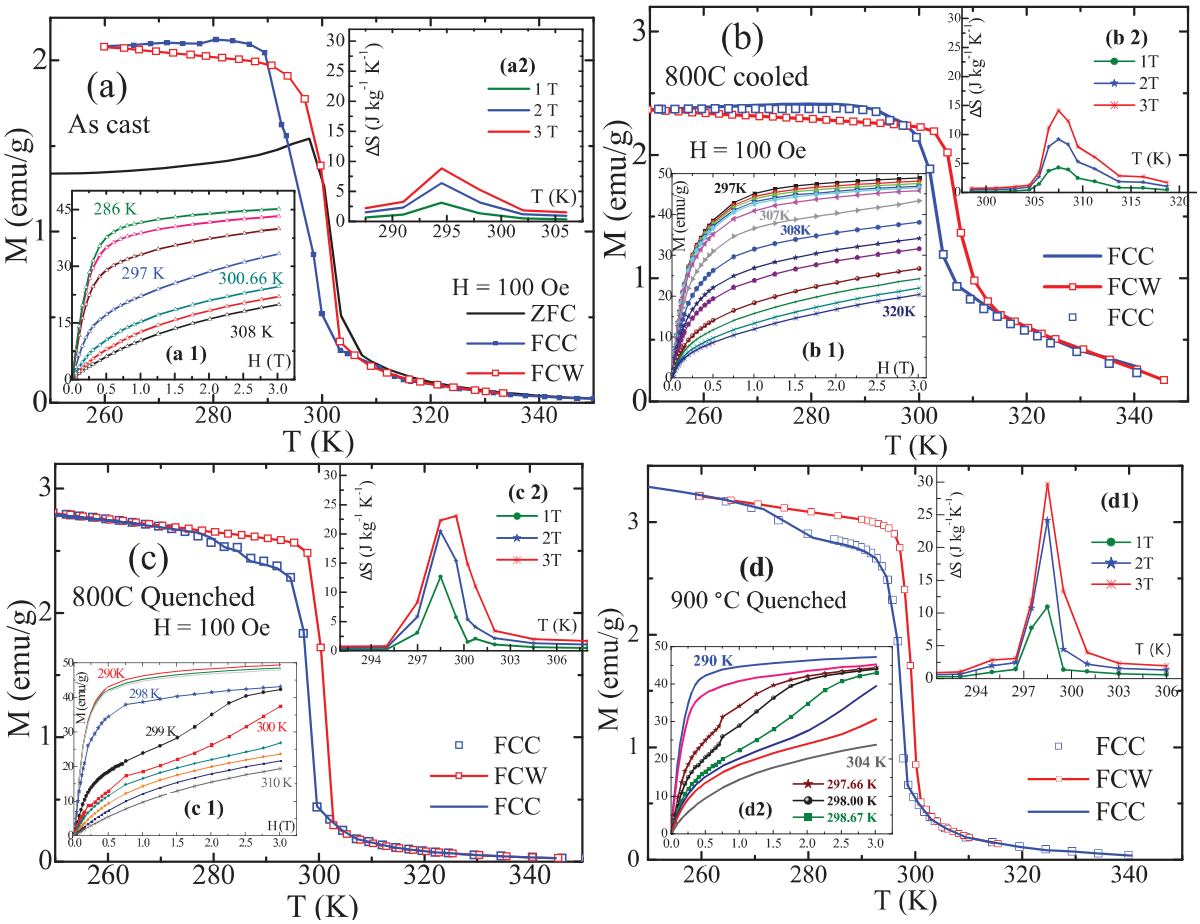

Figure 16: Magnetization around transition along with observed entropy change and isothermal in inset for $Ni_2Mn_{0.769}Cu_{0.25}Ga$ samples block after different annealing treatment.

Table 8: Magnetic properties obtained on block of $Ni_2Mn_{0.769}Cu_{0.25}Ga$ samples heat treated under different condition.

Heat treatment	Magnetization at 15 K, 3 T (emu/g)	$(T_C)_{FCC}$ (*K*)	$(T_C)_{FCW}$ (*K*)	ΔS_{peak} (*K*)	ΔS ($J\ kg^{-1}K^{-1}$) **RCP** ($J\ kg^{-1}$)		
					1 T	2 T	3T
As Cast	70.89	288.43	299.8	294.5	3.16 **18.67**	6.41 **41.09**	8.87 **65.64**
(i) 800 °C Slow Cooling	72.63	303	307.8	307.5	4.28 **15.75**	9.25 **34.04**	14.1 **52.03**
(ii) 800 °C Quench	70.31	297.1	300.4	298.5	12.66 **24.05**	20.46 **50.33**	22.31 **75.85**
(iii) 900 °C Quench	72.99	296.8	299.2	298.5	10.93 **20.82**	24.16 **35.76**	29.68 **52.83**

Temperature dependent magnetization measurements are performed on different heat treated samples using single block. As-cast ingot itself showed first order like transition but the transition occurs over long range of temperature Figure 16 a. The isothermal curves (inset a2) across the transition and the entropy change (inset a1) calculated from these curves is shown as inset in the Figure 16 a. The entropy values obtained are ΔS = 3.16, 6.41 and 8.87 J kg^{-1} K^{-1} for applied field change of ΔH = 1, 2, 3 T, which are much better compared to the once obtained on annealed '*powder*' sample (Figure 10 b). Further, blocks after annealing at 800°C show single and sharper transitions Figure 16 b, c. Field dependent isothermal curves around the transition were performed for sample *(i)* and *(ii)* as shown in inset (b 2) and (c 2) respectively. The entropy change calculated from these isothermal curves using Maxwell's relation is displayed in inset (b 1) and (c 1). To check the effect of temperature, one of the samples was treated at 900°C (referred as sample *(iii)*) followed by quenching into ice cooled water analog to sample *(ii)*. The magnetization, isothermal and entropy responses for this sample showed similar features to that of sample *(ii)* (Figure 16 d). But with sharpened transition leading to narrow, higher entropy change. For better comparison the observed physical properties for all the samples are summarized in Table 8.

We also need to consider other figure of merit in evaluating the MCM's such as Relative Cooling Power (RCP) = $\Delta S_{peak} \times \Delta S_{FWHM}$, which depends not just on height but also the width of the entropy peak. RCP for samples *(i), (ii) and (iii)* read respectively 15.75, 24.05 and 20.82J/kg under ΔH=1T and 34.04, 50.33 and 35.76 J/kg under ΔH=2T. Hence it is notable that sample (*ii*) has better magnetocaloric potential compared to other samples.

As it was mentioned in chapter 1 (*1.3.2.2*), the so addressed 'giant' or 'colossal' that was reported for compounds like $Gd_5Si_2Ge_2$, $Mn_{1-x}Fe_xAs$ near their first order transition. Such high value for magnetic entropy was questioned mainly for the way the values were derived [52, 53]. The critical factor behind such large entropy values in these compounds was attributed to presence of anisotropy in the isothermal magnetization curves. To avoid overestimation of the entropy change it is suggested to take into account the anisotropy in isothermal magnetization when encountered (for instance, Figure 16 e). Ideally in such cases, it is necessary to evaluate entropy using two methods, Maxwell relation and Clausius-Claperyon equation [54] preferably using latter one (i) hysteresis during field heating and cooling, (ii) meta-magnetic transition, (Figure 17 a) [55].

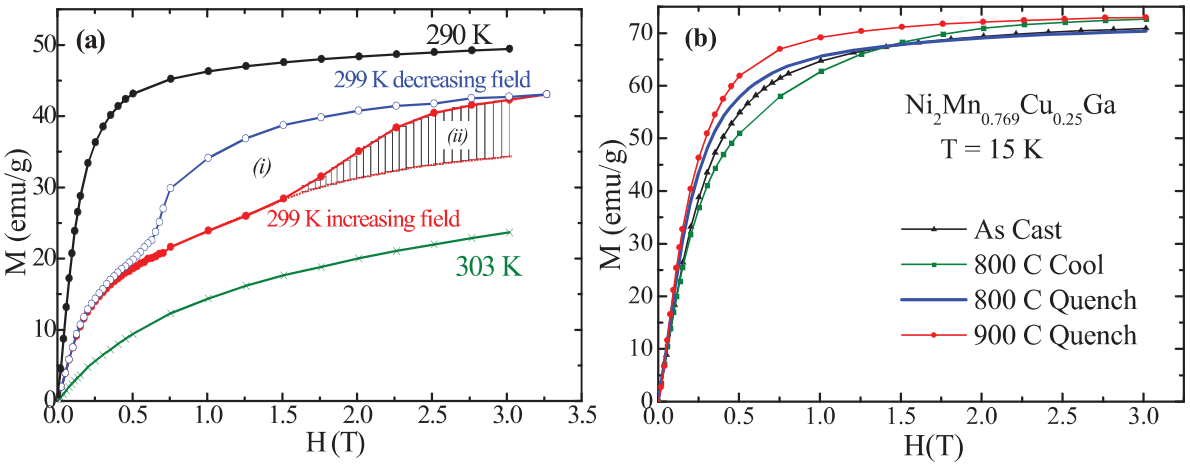

Figure 17: (a) Anisotropy in isothermal magnetization curves around transition temperature. (b) Isothermal magnetization curves at 15 K for different heat treated samples of $Ni_2Mn_{0.769}Cu_{0.25}Ga$.

Isothermal magnetization curves for all samples of $Ni_2Mn_{0.769}Cu_{0.25}Ga$ at 15K are presented in Figure 17 b. Samples quenched from either 900 °C or 800 °C show sharp rise in magnetization against the applied field and close to saturation at higher fields (H>2.5 Tesla), suggesting the spin arrangements in the system are mostly in easy axis. It is possible this can also suggest mostly single phase. The magnetization value for sample quenched from 900 °C is higher (72.99 emu/g) than for its analog sample of 800 °C (70.31 emu/g). The as cast sample requires slightly higher applied field to attain higher magnetization values in comparison with that required for quenched sample. This sample does not completely saturate till the probed field of 3T. The sample with slow cooling on other hand needs still higher field implying the spin arrangement to be in more towards harder axis of magnetization. And magnetization still keeps slowly increasing even at higher external fields.

Elemental analysis to know the overall distribution of elements was carried out by electron probe microanalysis. We have performed these measurements on all the compounds. However, to keep it simple we shall present data only on selected compound, $Ni_2Mn_{0.769}Cu_{0.25}Ga$, and discuss in detail distribution observed in as cast, cooled and quenched sample. From backscattered electron image on all three samples, left panel of Figure 18 (a - c), we observe homogeneous distribution without any trace of prominent impurity phases at the micron level. The images presented in left panel of Figure 18 give average composition and might not provide information on distribution of the individual element.

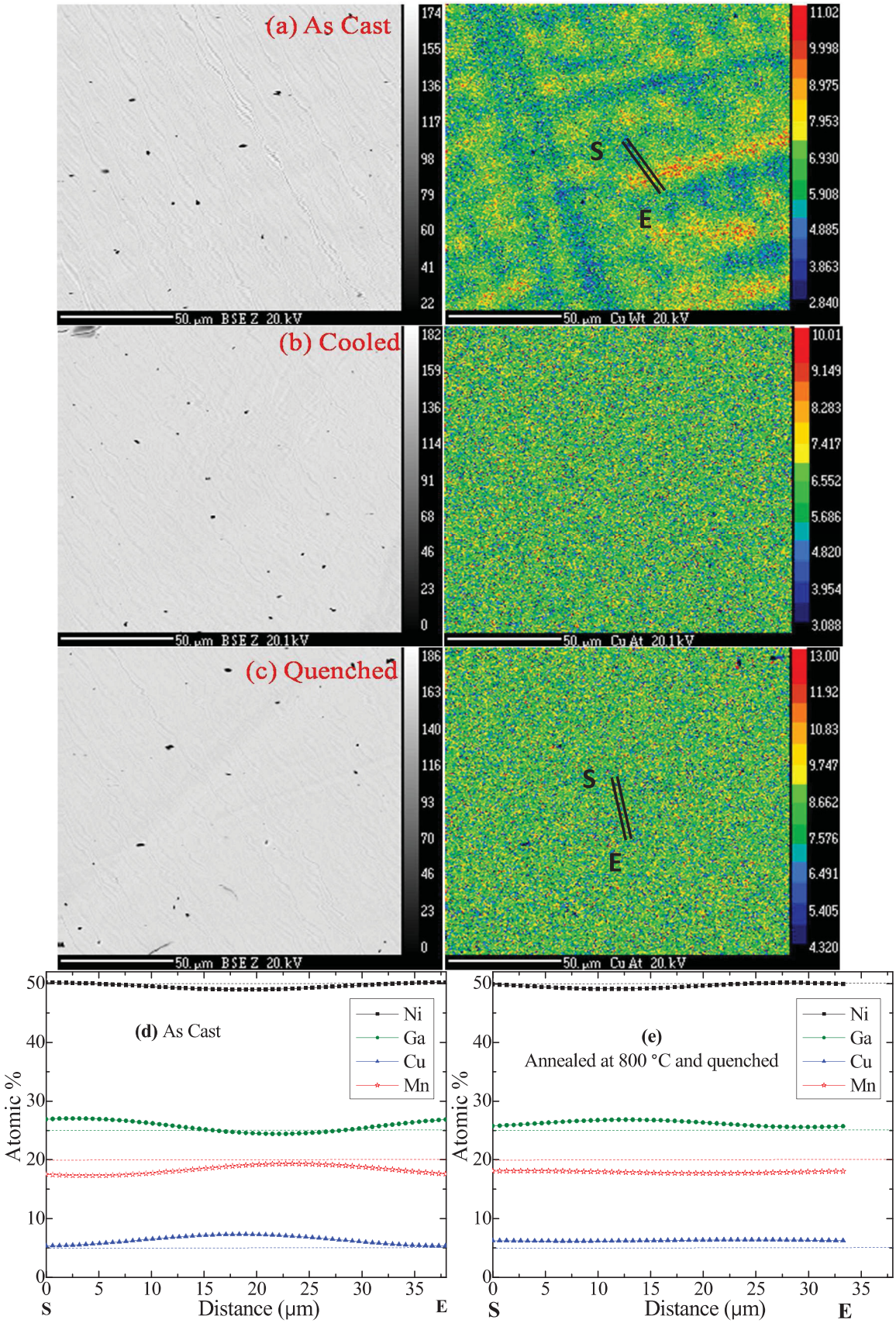

Figure 18: Electron Probe microanalysis left panel is the backscattered electron image and right is 'Cu' elemental distribution in the scanned area for (a) As cast (b) Annealed and slow cooled (c) Annealed followed by quenching. Elemental mapping for (d) as cast (e) quenched sample.

To accomplish better understanding, it is necessary to perform the elemental mapping along defined region. For the samples discussed, elemental mapping of one of the constituent elements 'Cu' are presented in the right panel. As evident, the copper distribution on as cast sample is not homogeneous; there is copper deficient and rich areas such observations are common over entire probe area. However, rest of the elements, Ni, Mn and Ga are found well distributed all over the scanned area. On annealing, the copper looks to redistribute all over the sample and no discrepant area were further detected. These observations suggest that even after thorough melting the heat treatments are necessary in order to obtain chemically homogenized samples. Our analysis support possibility of chemical segregation in as cast sample as previously reported. For instance, chemical segregations during preparation of single crystals of Ni-Mn-Ga alloys has been reported [56].

Elemental mapping on selected area are presented on the as cast (Figure 18 d), as well as quenched samples (Figure 18 e). In both these figures the marking S and E refer to the starting and end point of mapping. Markings S, E on Figure 18 d and e correspond respectively the marking S, E on Figure 18 a and c. From the plots on As-cast sample, it looks like the variation of Mn and Ga looks to follow one trend whereas Ni and Cu variation trend are linked to each other. Suggesting possible chemical modulation/ordering between Ni-Cu and Mn-Ga. After annealing however, the variation of Mn and Cu seems to be constant (at micron level) over the entire range of probe. And the variation of Ni and Ga behavior seems to be linked. However, we cannot draw any strong conclusion based on these results, as Ga is lighter element can exhibit such variation independently. In summary the as cast samples exhibit chemical inhomogeneity, so further heat treatment are necessary in attaining the chemical redistribution of the elements.

3.3. Ageing effect on $Ni_2Mn_{0.825}Cu_{0.25}Ga$

With the promising giant magnetocaloric effect that we observe in the compounds under study, we were motivated to study the stability of these materials in the flux of heat transport fluid. Ageing process was carried out on $Ni_2Mn_{0.825}Cu_{0.25}Ga$ which exhibit moderate magnetocaloric effect around its structural transition (292 K) when probed in its

bulk form (Figure 13 c). Several thin slabs were cut from the annealed block of sample and they were exposed to the flux of the deionized water working as heat transport fluid (as described in detail in Chapter 2). Here we present few of our initial results as the experiments were in progress during writing of this thesis. Xrd, xps and electrochemical reactions responsible for the oxidation or corrosion on two month aged sample are reported. The x-ray diffraction pattern on the thin slab after 2 months, 4 month of ageing do not show any extra peaks as compared to the starting slab. So it is necessary to probe changes at micron level, unfortunately, results from Auger and micro probe analysis are not available to detail the microstructural changes on surface. We however, present detailed XPS results in the following sections.

3.3.1. XPS

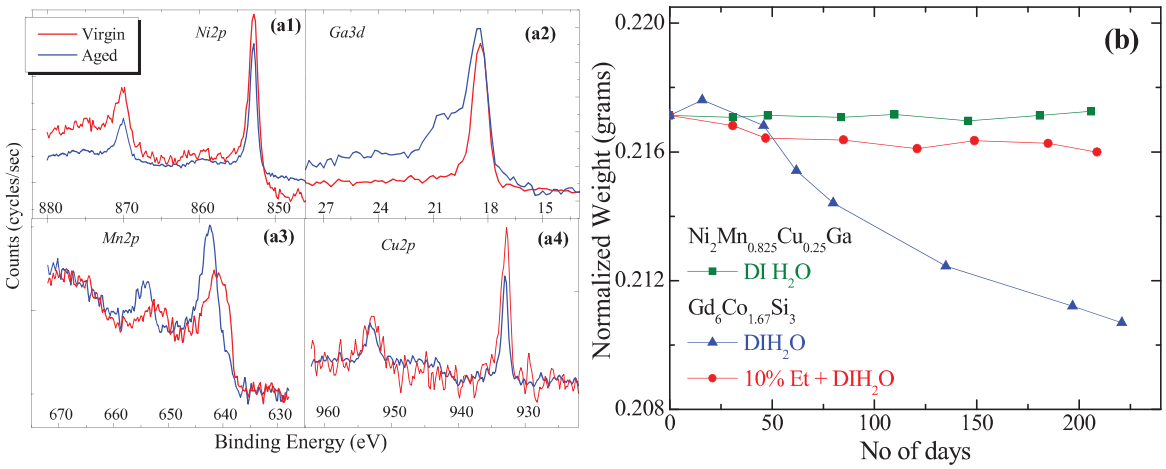

Figure 19: (a) X-ray photoelectron spectroscopy (XPS) spectra from as prepared and 2 months aged sample, (b) weight loss tracking during ageing.

We have successfully demonstrated in our chapter 2, that the oxidation state of individual constituent element is better qualitatively measured in understanding the basic corrosion and erosion. X-ray photoelectron spectroscopy (XPS) experiments were performed on both *(i)* pristine that will be used as standard and *(ii)* the 2 month aged samples. For XPS on the pristine we make sure through in-situ scratch, the carbon signal was as low as possible. Initially the survey spectra was obtained using Al-kα source. By using this source we notice that the higher binding energy for multiplet and satellite structure of *Mn2p3/2* (B.E. ≈ 645 eV) overlap with the contribution from auger structure of NiLM2 (eV).

Such overlap when analyzing metals with close binding energy require the use of an offset for the higher binding energy as it has been demonstrated by few earlier reports [57]. In our analysis we therefore switch to twin Mg x-ray source. XPS for each of the constituent elements of as prepared and 2 month aged samples are compared in Figure 19 (a1 to a4). It is evident from the comparison that only *Mn2p* and *Ga3d* spectra are different for the two samples while no major difference is seen on $Cu2p_{3/2}$ and *Ni2p* spectra [58, 59]. Detailed qualitative analysis of these spectra is underway.

As we had discussed in chapter 2 (section 2.4), one of the blind characterizations of corrosion and erosion is tracking weight loss at regular interval of time. We record at regular interval of time the weight of the sample during the ageing and results are shown in Figure 19 (d). For comparison the results for $Gd_6Co_{1.67}Si_3$ are also reproduced from chapter 2. Even though these might not provide a qualitative analysis considering the error bar of measurement, what is interesting is the overall trend of the curve. The trend of decrease in weight for Heusler alloy with time (after 210days/7 month) is much low compared to the once observed for Gd-based compound under same conditions (ageing in DI H_2O). However, till date, the sample even after ageing for period of 6 months or more did not show any discoloration of the surface or weight loss. The detailed characterization of these samples will be presented elsewhere. In summary, the ageing of the Ni-Mn-Ga alloys results in formation of oxidation/hydroxide of Mn and Ga, which stay in solid state on surface. However, the fluid does not carry them away.

3.3.2. Electrochemical Oxidation

In previous section we observe that only Mn and Ga are oxidized while the Ni and Cu are not affected much. The spontaneous electrochemical oxidation of elements helps us to understand the reason behind such selective element oxidation. Following the reduction potentials required for electrochemical oxidation of each element listed below. We infer oxidation and reduction between equations (5) and (1) occur. Resulting in oxidation of Mn as confirmed from the shift on XPS peaks. Once the oxidation of is complete with time the next low potential reaction equation (4) with (1) occurs, resulting Ga oxidation.

For the present study for the time of 2 months may be low to see through the other reactions namely (2) and (1). So we believe it is necessary to characterize samples after

ageing them for longer duration of time. To the brighter side, our initial inspect of the 4 months and 6 months aged sample do not show any visual discoloration or any extra peaks on x-ray diffraction. More detailed investigations of microprobe and XPS are under way.

Reduction potentials for the metals

$$4OH^- \rightleftharpoons O_2g + 2H_2O + 4e^- \quad + 0.40\ eV \ldots (1)$$
$$Cu_s \rightleftharpoons Cu^{2+} + 2e^- \quad + 0.34\ eV \ldots (2)$$
$$Ni_s \rightleftharpoons Ni^{2+} + 2e^- \quad - 0.25\ eV \ldots (3)$$
$$Ga_s \rightleftharpoons Ga^{3+} + 3e^- \quad - 0.53\ eV \ldots (4)$$
$$Mn_s \rightleftharpoons Mn^{2+} + 2e^- \quad - 1.03\ eV \ldots (5)$$
$$Mn_s \rightleftharpoons Mn^{3+} + 3e^- \quad - 1.185\ eV \ldots (6)$$

3.4. Conclusion and perspectives

Detailed and systematic studies on $Ni_2Mn_{1-x+\delta}Cu_xGa$ (*(i)* x=0.2, 0.25, 0.3 and δ=0; *(ii)* x=0.25, δ=2.5, 5, 10 at. % excess Mn) has been presented. Structural, magnetic and magnetocaloric properties in each case are presented. The importance of manganese concentration, synthesis conditions on observed entropy change has been demonstrated based on elemental probe investigations. Ordering of individual constituent element depending on the history of heat treatment needs to be taken into account in this system of interest. The possible destruction of the giant magnetocaloric effect from microstructure damage of the shape memory alloy is demonstrated. The Heusler composition with moderately high entropy change was tested against the flux of the heat transport fluid, which showed lesser corrosion compared to some other promising MCM. Alongside being already known as economic and environmental friendly, we are confident these results will add to the potential of the Ni-Mn-Ga based Heusler alloys towards being leading candidate for realistic applications.

More convincing structural studies for samples exhibiting multiphase/modulated structure still need to be addressed though temperature dependent diffraction studies. The neutron powder diffraction experiments (on block) all along transition will be carried out. We expect such studies to also assist in better understanding the relation between magnetic and structural transitions in observing high entropy changes. They can also help answer right symmetry and modulation of the samples. The diminish in entropy change and

possible change in symmetry due to destruction of grains during grinding as demonstrated in section 3.2.5 are still open challenges. *(i)* One of the possibilities is subjecting the ground fine powder for further annealing treatments and check if one can recover the degree of first order transition. *(ii)* Second possibility to address such problem is by probing block of sample with assumption of no grain anisotropic/specific crystallographic orientation contribution. *(iii)* Alternative possibility is microstructures such as ribbons which are obtained by material synthesis engineering might help to reduce grain microstrain and the internal stress. To the brighter side of all these disadvantages, the application of these materials in magnetocaloric refrigeration requires bulk material in form of thin slabs. These can even be obtained through molding just at end of melting. Further, so obtained thin slabs can be subjected to required annealing treatment. So it becomes obvious that much attention should be paid in understanding the properties of bulk sample then the powder. The evaluation of entropy change from magnetization curves with anisotropic nature should be dealt with care, may be the direct MCE measurement methods come for great help in these situations.

3.5. References

1. Skokov K P, et al., *Influence of thermal hysteresis and field cycling on the magnetocaloric effect in LaFe11.6Si1.4.* Journal of Alloys and Compounds, 2013. **552**(0): p. 310-317.
2. Mejía C Salazar, Gomes A. M., and de Oliveira L.A. S., *A less expensive NiMnGa based Heusler alloy for magnetic refrigeration.* Journal of Applied Physics, 2012. **111**(7): p. 07A923.
3. Heusler, F., *Über die Synthese ferromagnetischer Manganlegierungen* Verhandlungen der Deutschen Physikalischen Gesellschaft, 1903. **5**: p. 219.
4. Bradley, A.J. and J.W. Rodgers, *The Crystal Structure of the Heusler Alloys.* Proceedings of the Royal Society of London. Series A, 1934. **144**(852): p. 340-359.
5. Oxley, D.P., R.S. Tebble, and K.C. Williams, *Heusler Alloys.* Journal of Applied Physics, 1963. **34**(4): p. 1362-1364.

6. Graf, T., C. Felser, and S.S.P. Parkin, *Simple rules for the understanding of Heusler compounds.* Progress in Solid State Chemistry, 2011. **39**(1): p. 1-50.

7. Bacon, G.E. and J.S. Plant, *Chemical ordering in Heusler alloys with the general formula A_2BC or ABC.* Journal of Physics F: Metal Physics, 1971. **1**(4): p. 524.

8. Luo, H.Z., et al., *Half-metallic properties for the Mn_2FeZ (Z=Al, Ga, Si, Ge, Sb) Heusler alloys: A first-principles study.* Journal of Applied Physics, 2008. **103**(8): p. 083908.

9. Graf, T., et al., *Crystal Structure of New Heusler Compounds.* Zeitschrift für anorganische und allgemeine Chemie, 2009. **635**(6-7): p. 976-981.

10. Bao, B., et al., *Phase transition processes and magnetocaloric effect in $Ni_{2.15}Mn_{0.85-x}Co_xGa$ alloys.* Journal of Applied Physics, 2008. **103**(7): p. 07B335-3.

11. Basso, V., et al., *Hysteresis and magnetocaloric effect at the magnetostructural phase transition of Ni-Mn-Ga and Ni-Mn-Co-Sn Heusler alloys.* Physical Review B, 2012. **85**(1): p. 014430.

12. Brown, P.J., et al., *Magnetic shape memory behaviour.* Journal of Magnetism and Magnetic Materials, 2007. **310**(2, Part 3): p. 2755-2760.

13. Manfred Kohl, et al., *Ferromagnetic Shape Memory Microactuators* Materials Transactions, 2006. **47**: p. 639 - 644.

14. Ullakko, K., et al., *Large magnetic-field-induced strains in Ni_2MnGa single crystals.* Applied Physics Letters, 1996. **69**(13): p. 1966-1968.

15. Sozinov, A., et al., *Giant magnetic-field-induced strain in NiMnGa seven-layered martensitic phase.* Applied Physics Letters, 2002. **80**(10): p. 1746-1748.

16. Abhyankar, A.C., et al., *Thermal and transport properties of Ni2MnGa1-xAlx alloys.* Intermetallics, 2010. **18**: p. 2090 - 2095.

17. Overholser, R.W., M. Wuttig, and D.A. Neumann, *Chemical ordering in Ni-Mn-Ga Heusler alloys.* Scripta Materialia, 1999. **40**(10): p. 1095-1102.

18. Barman, S.R., S. Banik, and A. Chakrabarti, *Structural and electronic properties of Ni_2MnGa.* Physical Review B, 2005. **72**: p. 184410.

19. Umetsu, R.Y., et al., *Phase diagram and magnetic moment of $Ni_{50+x}Mn_{27-x}Ga_{23}$ ferromagnetic shape memory alloys.* Journal of Alloys and Compounds, 2013. **579**(0): p. 521-528.

20. Brown, P.J., et al., *The field and temperature dependence of the magnetic and structural properties of the shape memory compound $Ni_{1.84}Mn_{1.64}In_{0.52}$.* Journal of Physics: Condensed Matter, 2011. **23**(45): p. 456004.

21. Inoue, K., et al., *Martensitic and magnetic transformations of Ni_2MnGa-based shape-memory alloys.* Appl Phys A 2002. **74**: p. S1061.

22. Kustov, S., et al., *Isothermal and athermal martensitic transformations in the B2 – R – B19′ sequence in Ni – Ti shape memory alloys.* Scripta Materialia, 2010. **63**(12): p. 1240-1243.

23. Kashchenko, M.P. and V.G. Chashchina, *Dynamic Model of the Formation of an Intermediate Mesorcopic State During B2 → B19 Martensitic Transformation.* Russian Physics Journal, 2013. **56**(5): p. 557-561.

24. L. A. Bendersky, A. Roytburd, and W.J. Boettinger, *Transformation of BCC and B2 High Temperature Phases to HCP and Orthorhombic Structures in the Ti-Al-Nb System. Part I: Microstructural Predictions Based on a Subgroup Relation Between Phases* Journal of Research of the National Institute of Standards and Technology, 1993. **98**: p. 561-583.

25. Cong, D.Y., et al., *Crystal structure and phase transformation in $Ni_{53}Mn_{25}Ga_{22}$ shape memory alloy from 20K to 473K.* Applied Physics Letters, 2005. **87**(11): p. 111906.

26. Banik, S., et al., *Structural studies of $Ni_{2+x}Mn_{1-x}Ga$ by powder x-ray diffraction and total energy calculations.* Physical Review B, 2007. **75**(10): p. 104107.

27. J. PONS, et al., *CRYSTAL STRUCTURE OF MARTENSITIC PHASES IN Ni-Mn-Ga SHAPE MEMORY ALLOYS.* Acta Materialia, 2000. **48**: p. 3027.

28. Umetsu, R.Y., et al., *Magnetic properties and stability of $L2_1$ and B2 phases in the Co_2MnAl Heusler alloy.* Journal of Applied Physics, 2008. **103**(7): p. 07D718-3.

29. A. N. Vasil'ev, et al., *Structural and magnetic phase transitions in shape-memory alloys $Ni_{2+x}Mn_{1-x}Ga$.* Physical Review B, 1999. **59**: p. 1113.

30. Khan, M., et al., *The structural and magnetic properties of $Ni_2Mn_{1-x}M_xGa$ (M = Co, Cu).* Journal of Applied Physics, 2005. **97**(10): p. 10M304-3.

31. Chernenko, V.A., et al., *Ferromagnetism of thermoelastic martensites: Theory and experiment.* Physical Review B, 2003. **67**(6): p. 064407.

32. Castillo-Villa, P.O., et al., *Caloric effects induced by magnetic and mechanical fields in a $Ni_{50}Mn_{25-x}Ga_{25}Co_x$ magnetic shape memory alloy.* Physical Review B, 2011. **83**(17): p. 174109.

33. Karaca, H.E., et al., *Stress-induced martensite to austenite phase transformation in Ni_2MnGa magnetic shape memory alloys.* Smart Mater. Struct. , 2012. **21**: p. 045011.

34. Feng-xia Hu, Bao-gen Shen, and J.-r. Sun, *Magnetic entropy change in $Ni_{51.5}Mn_{22.7}Ga_{25.8}$ alloy.* Applied Physics Letters, 2000. **76**: p. 3460.

35. Aksoy, S., et al., *Tailoring magnetic and magnetocaloric properties of martensitic transitions in ferromagnetic Heusler alloys.* Applied Physics Letters, 2007. **91**(24): p. 241916-3.

36. Banik, S., et al., *Phase diagram and electronic structure of $Ni_{2+x}Mn_{1-x}Ga$.* Physical Review B, 2006. **74**(8): p. 085110.

37. L. Pareti, et al., *Giant entropy change at the co-occurrence of structural and magnetic transitions in the $Ni_{2.19}Mn_{0.81}Ga$ Heusler alloy.* European Physics Journal B, 2003. **32**: p. 303.

38. Porcari, G., et al., *Reverse magnetostructural transformation and adiabatic temperature change in Co- and In-substituted Ni-Mn-Ga alloys.* Physical Review B, 2012. **85**(2): p. 024414.

39. Shane Stadler, et al., *Magnetocaloric properties of $Ni_2Mn_{1-x}Cu_xGa$.* Applied Physics Letters, 2006. **88**: p. 192511.

40. Marcos, J., et al., *Magnetic field induced entropy change and magnetoelasticity in Ni-Mn-Ga alloys.* Physical Review B, 2002. **66**(22): p. 224413.

41. Pasquale, M., C.P. Sasso, and L.H. Lewis, *Magnetic entropy in Ni_2MnGa single crystals.* Journal of Applied Physics, 2004. **95**(11): p. 6918-6920.

42. Gomes, A.M., et al., *Magnetocaloric properties of the $Ni_2Mn_{1-x}(Cu,Co)_xGa$ Heusler alloys.* Journal of Applied Physics, 2006. **99**(8): p. 08Q106.

43. Xuezhi Zhou, et al., *A criterion for enhancing the giant magnetocaloric effect (Ni–Mn–Ga)—a promising new system for magnetic refrigeration.* Journal of Physics Condensed Matter, 2004. **16**: p. L39 - L44.

44. Brown, P.J., et al., *The crystal structure and phase transitions of the magnetic shape memory compound Ni_2MnGa.* Journal of Physics: Condensed Matter, 2002. **14**(43): p. 10159.

45. Pons, J., et al., *Long-period martensitic structures of Ni-Mn-Ga alloys studied by high-resolution transmission electron microscopy.* Journal of Applied Physics, 2005. **97**(8): p. 083516.

46. Roy, S., et al., *Delocalization and hybridization enhance the magnetocaloric effect in Cu-doped Ni_2MnGa.* Physical Review B, 2009. **79**(23): p. 235127.

47. Gautam, B.R., et al., *Effect of small changes in Mn concentration on phase transition temperatures and magnetic entropy variations in $Ni_2Mn_{0.75}Cu_{0.25}Ga$ Heusler alloys.* Journal of Alloys and Compounds, 2009. **472**(1–2): p. 35-39.

48. Wang, W.H., et al., *Thermoelastic intermartensitic transformation and its internal stress dependency in $Ni_{52}Mn_{24}Ga_{24}$ single crystals.* Physical Review B, 2002. **66**(5): p. 052411.

49. Khovailo, V.V., et al., *Influence of intermartensitic transitions on transport properties of $Ni_{2.16}Mn_{0.84}Ga$ alloy.* Journal of Physics: Condensed Matter, 2004. **16**(12): p. 1951.

50. Jian Liu, et al., *Giant magnetocaloric effect driven by structural transitions.* Nature Materials, 2013. **11**: p. 620.

51. J. Liu, N. Scheerbaum, and O. Gutfleisch, *Comparative Study of Structural and Magnetic Properties of Bulk and Powder $Ni_{52}Fe_{17}Ga_{27}Co_4$ Magnetic Shape Memory Alloy.* IEEE Transactions on Magnetics, 2008. **44**: p. 3025 - 3027.

52. Balli, M., et al., *The "colossal'' magnetocaloric effect in $Mn_{1-x}Fe_xAs$: What are we really measuring?* Applied Physics Letters, 2009. **95**(7): p. 072509-3.

53. Giguère, A., et al., *Direct Measurement of the "Giant" Adiabatic Temperature Change in $Gd_5Si_2Ge_2$.* Physical Review Letters, 1999. **83**(11): p. 2262-2265.

54. Cui, et al., *The origin of large overestimation of the magnetic entropy changes calculated directly by Maxwell relation.* Applied Physics Letters, 2010. **96**(22): p. 222509-3.

55. Bing, L., et al., *Intrinsic magnetocaloric effect at a first-order magnetic transition.* EPL (Europhysics Letters), 2012. **97**(5): p. 57002.

56. Schlagel, D.L., et al., *Chemical segregation during bulk single crystal preparation of Ni–Mn–Ga ferromagnetic shape memory alloys.* Journal of Alloys and Compounds, 2000. **312**(1–2): p. 77-85.

57. Biesinger, M.C., et al., *Resolving surface chemical states in XPS analysis of first row transition metals, oxides and hydroxides: Cr, Mn, Fe, Co and Ni.* Applied Surface Science, 2011. **257**(7): p. 2717-2730.

58. Hinkle, C.L., et al., *Detection of Ga suboxides and their impact on III-V passivation and Fermi-level pinning.* Applied Physics Letters, 2009. **94**(16): p. 162101-3.

59. Grosvenor, A.P., et al., *New interpretations of XPS spectra of nickel metal and oxides.* Surface Science, 2006. **600**(9): p. 1771-1779.

Chapter 4

Nuclear – magnetic phase diagram around magnetic transition and magnetocaloric effect in metallic ferromagnet manganese perovskites $Pr_{1-x}Sr_xMnO_3$ (0.25≤x≤0.45)

4.1. Introduction

Oxides in general, either in stable simple form (ZnO, SiO_2, TiO_2, Fe_3O_4, V_2O_5) or complex (P_4O_{10} and P_4O_9) have gained lot of attention and have fascinated the material scientists through their chemical and physical properties. The other reason is their flexibility in terms of synthesis and stability thereafter.

In introduction of this chapter the manganese based perovskite oxides that have shown magnetocaloric figure of merits comparable to that of the well established intermetallic materials are summarized. Following this we walk through basic phenomenon for one of the interesting family of oxide, *the perovskite*. Brief summary of the results on the praseodymium manganese based perovskite oxide, $Pr_{1-x}Sr_xMnO_3$, focusing nuclear as well as the magnetic structure phase diagram. The observed MCE around room temperature from different literature is also introduced. Considering the key factors of stability, reproducibility along with moderate MCE with in this oxide family, we restrict our experimental investigations to perovskite manganite system $Pr_{1-x}Sr_xMnO_3$ defined in the range $0.25 \leq x \leq 0.45$. Detailed and systematic studies of structural and magnetic properties of several compositions in the range of interest will be presented. Before conclusion, effect of corrosion due to heat transport fluid on the compound $Pr_{0.66}Sr_{0.34}MnO_3$ is presented.

4.1.1 The magnetocaloric effect in oxides and our choice for study

In general, intermetallics like Ln-based (lanthanides Ln- La, Gd... Ex: Gd-Ge-Si, Gd-Co-Si, La-Fe-Co-Si, etc.) or M-based (transition metal M-Mn, Ni, Co… Ex: Mn-Fe-P-As, Ni-Mn-Ga, etc.) have dominated the field of magnetocaloric for decades [1]. Oxides are believed to enjoy advantage over these intermetallics concerning few key factors such as low cost (economical), good chemical stability, higher electrical resistivity with good heat conductivity and simple preparation process. Manganite based oxides, especially perovskite have succeeded to show reasonable competition with the large magnetocaloric effect exhibited by the intermetallics. As mentioned in chapter 1, lanthanum perovskite manganite $La_{1-x}A_xMnO_3$ with group 2 alkaline A = Ca, Ba, showed promising signs of MCE around their first order magneto-structural transition. Large entropy change even under low applied field of 1 T or 1.5 T can be obtained by playing with the doping level [2]. Promising value of entropy

change are reported for $La_{0.67}Ca_{0.33}MnO_3$ (T_C = 257 K, ΔS = 4.3 $Jkg^{-1}K^{-1}$, ΔH = 1.5 T) and a-site cation defficient $La_{0.54}Ca_{0.32}MnO_{3-\delta}$ (T_C = 272 K, ΔS = 2.9 $Jkg^{-1}K^{-1}$, ΔH = 0.9 T) [2]. Doping with group 1 alkali elements, like A = Na, K, Ag, also resulted in much similar magnetocaloric properties.

$Sr_3Ti_2O_7$-type layered manganite's perovskites SUCH AS $La_{2-2x}A_{1+2x}Mn_2O_7$ (a= Ca, Sr, Ba) can be obtained with n=2 in the Ruddlesden-Popper phase $A_{n-1}A_2'B_nX_{3n+1}$. $La_{2-2x}Ca_{1+2x}Mn_2O_7$ systems in particular are subsequently proposed to exhibit large entropy values $T_C \approx$ 270 K, ΔS= 11.3 $Jkg^{-1}K^{-1}$, ΔH = 2 T as in $La_{1.4}Ca_{1.6}Mn_2O_7$ [3]. These large values are highlighted to be better than the once observed for pure Gd ($T_C \approx$ 292 K, ΔS= 13.7 $Jkg^{-1}K^{-1}$, ΔH = 8T). Even the relative cooling power (RCP) is also reported to be same as compared to the prototype-Gd, $Gd_5Ge_2Si_2$ and $MnFeP_{0.45}As_{0.55}$ alloys.

Unfortunately, there are few disadvantage and also large differences in physical properties reported for these La-based manganite compounds: *(i) T_C and ΔS – criticality of stoichiometry:* Enormous difference in T_C even for very close compositions for example, $La_{0.666}Sr_{0.333}MnO_3$ is reported to have $T_C \approx$ 305 K and $La_{0.65}Sr_{0.35}MnO_3$ has $T_C \approx$ 370 K [4, 5]. For applied field change of ΔH= 1 T, the former composition exhibit entropy change of 2.12 $Jkg^{-1}K^{-1}$ and the later 1.5 $Jkg^{-1}K^{-1}$. This will complicate the large scale manufacturing procedure, forcing it to be more precise and accurate. The other oxides, $(La,Ca)MnO_3$ and $(La,Ba)MnO_3$ have lower T_C, also inherit anisotropic magnetization with first order transition which is still to be addressed. Minute change in oxygen stoichiometry can result in large change of observed properties. For instance, in case of $La_{0.66}Ba_{0.33}MnO_{3-\delta}$, the T_C reduce from 337 K to 268 K as δ change from 0 to 0.1 and their respective entropy change is lowered from 2.7 to 1.7 $Jkg^{-1}K^{-1}$ [6]. *(ii) Narrow temperature range*: As most of the composition exhibiting large entropy change is due to nature of first order transition, the temperature range for observed magnetocaloric effect is very narrow. This is big drawback as the RC which is one of the major MCM's evaluating parameter greatly depends on ΔT. *(iii) stacking default :* Layered manganite's ($La_{2-2x}Ca_{1+2x}Mn_2O_7$) have been debated for the competing phases that affect the overall properties to great extent, more over several discrepancy on obtained large entropy change also exist. As for case of $La_{1.4}Ca_{1.6}Mn_2O_7$ few report with much lower figure of merits, $T_C \approx$ 265 K, ΔS= 4.7 $Jkg^{-1}K^{-1}$, ΔH = 2 T [7] are reported against once discussed above. These drawbacks individually or in combined form make them doubtful candidates for the long and consistent performance.

The analog perovskites of $La_{1-x}Sr_xMnO_3$, with different rare earth elements in place of La = Nd, Sm, Pr, Gd are also explored. Out of these only the system with praseodymium-strontium showed magnetic transition close to mark of room temperature and rest had lower transition temperatures. The potential results in terms of magnetocaloric effect for the perovskite-manganite $Pr_{1-x}Sr_xMnO_3$ system was first reported for single crystal of $Pr_{0.63}Sr_{0.37}MnO_3$. Entropy change (2.57 $Jkg^{-1}K^{-1}$, $T_C \approx$ 305 K, ΔH=1 T) that comparable to the prototype material gadolinium (2.80 $Jkg^{-1}K^{-1}$, $T_C \approx$293 K, ΔH=1 T) was reported [8]. It was further reported that even the adiabatic temperature change (ΔT) that can be achieved on this single crystal was better than the one observed for either single crystal or polycrystalline $La_{0.7}Ca_{0.3}MnO_3$. Much recently the magnetocaloric merits of polycrystalline $Pr_{0.65}Sr_{0.35}MnO_3$ (ΔS=2.3 $Jkg^{-1}K^{-1}$, $T_C \approx$295 K, ΔH=1 T) were demonstrate to be close to gadolinium [9]. Comparable figure of merits were obtained for polycrystalline $Pr_{0.66}Sr_{0.34}MnO_3$, this material was tested on prototypes (ΔS=2.5 $Jkg^{-1}K^{-1}$, ΔT_{ad} = 1.2 K at $T_C \approx$294 K, ΔH=1 T) [Thesis U LEGAIT, Institut Néel]. Much detailed summary on the complete series of $Pr_{1-x}Sr_xMnO_3$ will be discussed in 4.1.3.

4.1.2 Perovskites structure- ABO_3

Oxides have been categorized into several families based on their chemical formula, crystal structure. ABX_3 represents general form of perovskites (***oxide*** ex: $MgSiO_3$, $GdFeO_3$). Generally A and B represent the two cations of different size while X being anion that bond to both of these cations. These are some of the widely studies oxide materials due to their rich physical and chemical properties [10]. Depending on the oxidation of A, B cations, we can have two possible configurations, $\boldsymbol{A^{3+}B^{3+}(O^{2-})_3}$ Ex: $R^{3+}Mn^{3+}O_3$ (R=La, Pr, Nd, Sm, Gd, …, Lu) or $\boldsymbol{A^{2+}B^{4+}(O^{2-})_3}$ Ex: $BaTiO_3$, $SrTiO_3$, $CaTiO_3$ [11]. The resulting combination of parent compound can then be stabilized.

The general perovskite structure described with in cubic symmetry has B cation in 6-fold coordination surrounded by an octahedron of anions, the A cation is in 12-fold cuboctahedral coordination (Figure 1 (a)). In ideal cubic perovskite the cell axis '*a*' which is geometrically related to the ionic radii can be expressed as, $a = \sqrt{2}(r_B + r_O) = (r_A + r_O)$. Where, r_A, r_B *and* r_O represent respectively the ionic radius of A cation atom, B cation atom and anion atom.

One can derive wide range of composition of perovskite with mixing of cations, like $A_{1-x}A'_xB_{1-y}B'_yO_{3\pm\delta}$, when parent compounds are mixed. By such doing the ideal cubic perovskite structure is forced to deviate to lower symmetry structure like hexagonal, tetragonal, orthorhombic or monoclinic. $CaTiO_3$ is one of the good examples for perovskites. It has been demonstrated in three structures cubic ((Figure 1 a), tetragonal ((Figure 1 b) and orthorhombic (Figure 1 c) as function of the temperature.

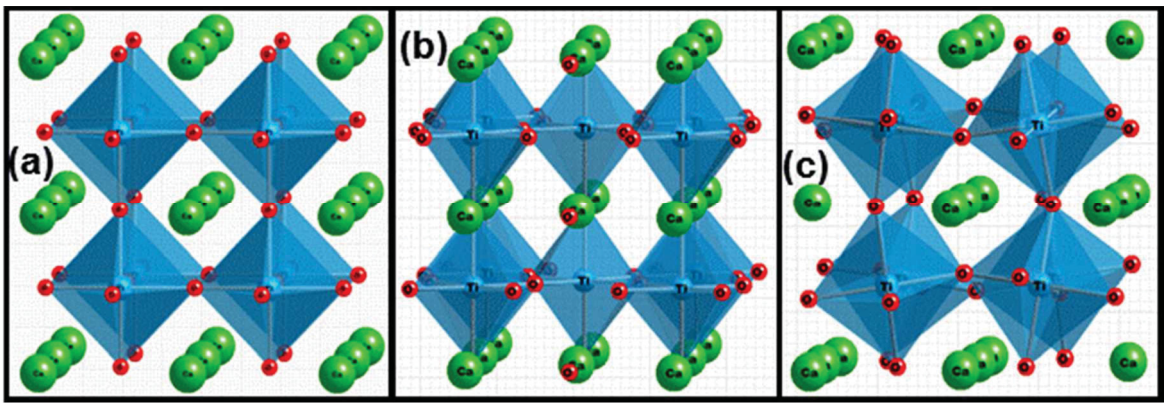

Figure 1: $CaTiO_3$ defined with symmetry of (a) cubic (b) tetragonal distortion (c) orthorhombic distortion. Green, red and light blue represent respectively Ca, O and Ti atom.

Such modification of composition will results in several new compositions with interesting physical properties. For example, $LaMnO_3$ is antiferromagnetic, by introducing Sr^{2+} ($\langle r_{Sr}^{IX}\rangle = 1.31$ Å) in place of La^{3+} $\left(\langle r_{La}^{IX}\rangle = 1.21 \text{ Å}\right)$ the A-site size is increased. Also the oxidation of Sr^{2+} is different compared to La^{3+}. This could force some Mn^{3+} change oxidation state to Mn^{4+} amount of which is equal to that of doped Sr^{2+} in order to maintain the overall stoichiometry, in turn leading to new stoichiometry, $La_{1-x}^{3+}Sr_x^{2+}Mn_{1-x}^{3+}Mn_x^{4+}O_3^{2-}$. To keep the perovskite structure deformations comes into act resulting in tilting/distortions. New arrangement will lead to either enhancement or decrement of the interatomic interactions (magnetic/spin/orbital) and hence change in the properties.

Some common phenomenon that relate the structure and physical properties in perovskites are briefed in following sections. They also serve as conditions/rules governing the perovskite structure to still exist even under several possible deformations.

(i) *Goldschmidt's Tolerance factor*

Some of the structural deformation depends on the ionic radii of the cation and anion. If the ionic radii of A-site anion is r_A, that of B-site anion is r_B and the ionic radii of

cation site is r_O. Then, the Goldschmidt's tolerance is defined by, $t = \frac{(r_A + r_O)}{\sqrt{2}\,(r_B + r_O)}$. For ideal cubic structure the value of *t* is unity, for valid perovskite structure to exist the allowed tolerance value is 0.75 ≤ t ≤ 1.02. For instance, the ideal cubic perovskites, $SrTiO_3$ has tolerance *t* = 1.00 ().

Related to the Goldschmidt's factor, the *average A-site ionic radius* $\langle r_A \rangle$ controls the physical and chemical properties, for instance, structure of $A_{1-x}Sr_xMnO_3$ change with $\langle r_A \rangle$ [12]. Similarly the magnetic transition temperature (T_C) can be varied by controlling the$\langle r_A \rangle$. Ionic radii from literature for some of the commonly used alkaline elements are, $\langle r_{Ca}^{IX} \rangle = 1.18$ Å, $\langle r_{Sr}^{IX} \rangle = 1.31$ Å and $\langle r_{Ba}^{IX} \rangle = 1.47$ Å, the same for few lanthanides read as $\langle r_{Gd}^{IX} \rangle = 1.107$ Å, $\langle r_{Sm}^{IX} \rangle = 1.132$ Å, $\langle r_{Nd}^{IX} \rangle = 1.163$ Å, $\langle r_{Pr}^{IX} \rangle = 1.179$ Å and $\langle r_{La}^{IX} \rangle = 1.216$ Å.

(ii) Jahn-Teller distortions

This is second parameter that acts on structural deformation. The relation between the structure and the emerging properties of the perovskite manganite can be found elsewhere [10, 13]. We try to brief some of them here. Jahn-Teller distortion explains the origin of ferromagnetism in doped perovskite materials (Ex: $La_{1-x}Sr_xMn^{3+}Mn^{4+}O_3$) based on the super exchange between mixed valence stare (Mn^{3+} and Mn^{4+}). While Double exchange phenomenon address the coexistence of the metal-insulator transition across the ferromagnetic-paramagnetic transition [14]. However, the metal-insulator transition cannot be understood completely by the double exchange mechanism. Sometime they can be explained using coupling between the carriers and phonons through Jahn-Teller distortions, and the high temperature conduction mechanism through variable range hopping mechanism [15] .

(iii) Size mismatch

When the size difference between two A-site cation, A^{3+}, M^{2+} (in $A_{1-x}M_xBO_3$) is large, so formed steric size effect can affected the physical properties to greater extent. The effect of A-site cation size mismatch leading to large change in electrical and magnetic properties is demonstrated for perovskite manganite [16]. $Pr_{1-x}Ca_xMnO_3$ is a hole doped (Ca^{2+} in place of Pr^{3+}) system with special case of close average radius of A-site cations ($\langle r_A \rangle_{Pr3+}$ =1.179 Å, $\langle r_A \rangle_{Ca2+} = 1.18$ Å). In agreement with the minimum ionic radii requirement for ferromagnetic metal ($\langle r_A \rangle > 1.18$ Å) it exhibit insulator behavior [17]. By introducing elements in A-site with larger atomic radii (La^{3+}, $\langle r_A \rangle_{La3+}$ = 1.216 Å), the appearance of

metallic and ferromagnetic behavior was demonstrated. The degree of size mis-match is expressed by variance expressed as, $\sigma^2 = \sum y_i r_i^2 - \langle r_A \rangle$ [18].

(iv) Glazer notations and the group-subgroup relations

The cationic size mismatch forces the structure to distort/tilt in order to maintain the valid perovskite structure. By doing so the symmetry of the system is reduced and hence system crystallizes in different space group. Often the relations between resulting lattice constant and a given distortion of an octahedral is expressed using Galzer notations [19]. The relation between the tilting of the octahedral and the corresponding glazer notation for three crystal structures cubic Pm-3m ($a^0a^0a^0$), orthorhombic Pnma ($a^-b^+a^-$) and tetragonal I4/mcm ($a^0a^0c^-$) is demonstrated in Figure 2 (a to c).

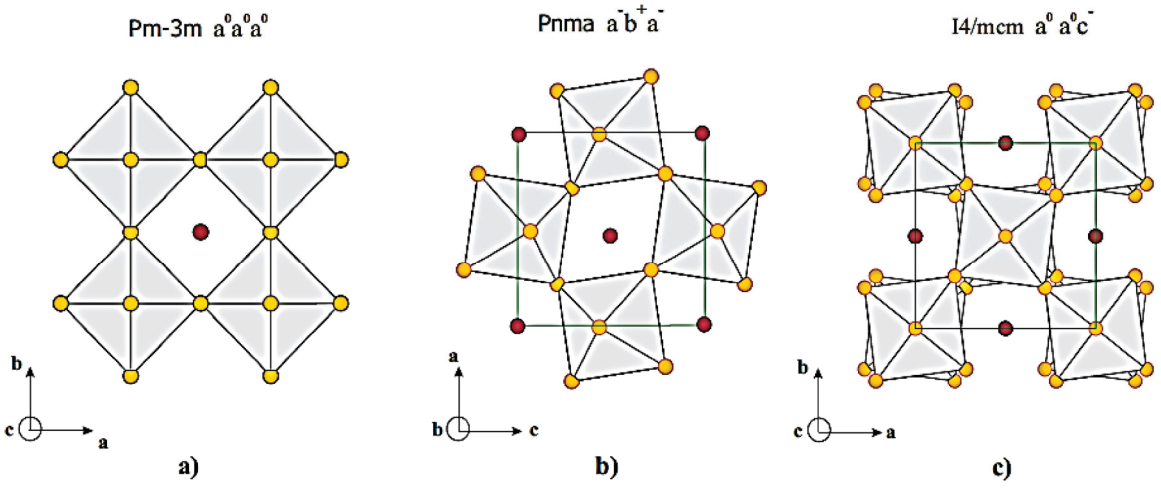

Figure 2: Glazers notation and tilting/distortions for (a) cubic, (b) orthorhombic and (c) tetragonal structure [From Thesis of Cecile Autret, CRISMAT].

These notations of Glazer are constructed as follows: (i) the sequence of symbol indicate the axis of tilt, ex: along a-axis, (ii) identical characters indicate the same amplitude of tilt and (iii) the superscripts indicate the subsequent layers of octahedral namely zero-tilt (0), in-phase-tilt (+) and anti-phase-tilt (-). Cubic phase $a^0a^0a^0$ is known as zero-tilt system, does not have any tilting on the structure. While in case of tetragonal structure the tilting is anti-phase on c axis, forming twisted like structure when viewed along c-axis.

The space groups Pnma and Imma crystallize in similar perovskite-like structures with unit cells defined by, $a_p\sqrt{2} \times 2a_p \times a_p\sqrt{2}$, with $a_p$being lattice parameter of the ideal perovskite unit cell. The Glazer notation for *Pnma* is $a^+b^-b^-$and for *Imma* is $a^0b^-b^-$. One

major difference is the rotation of the oxygen octahedral with respect to symmetry axis of the unit cell, this is evident on their glazer notations [20].

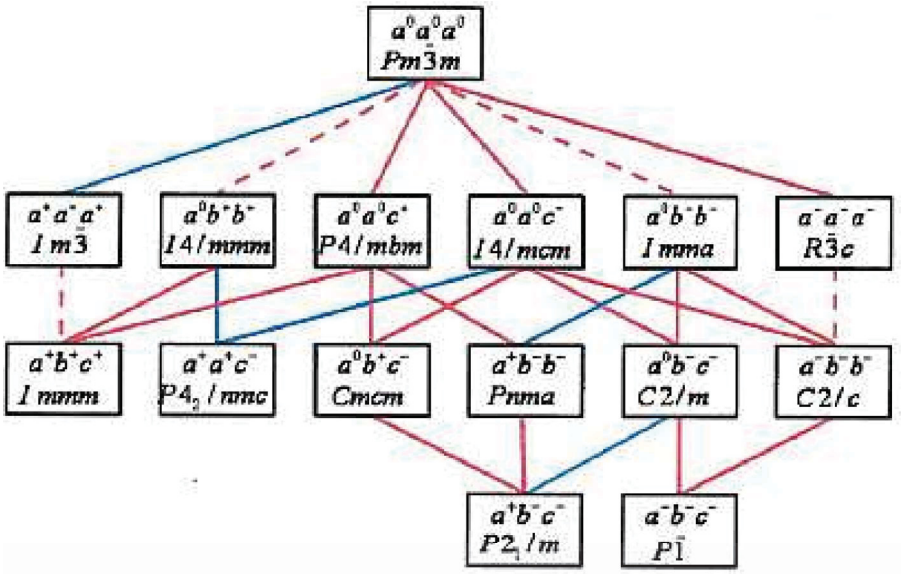

Figure 3: Group- sub group relations based on Glazers notations [21].

The relation between space group and nature of transitions between them was proposed by Howard and Stokes. Figure 3 represents the schematic general diagram found by them [21]. According to this transitions within group-group and group-subgroup does occur and they are respectively first-order and second order by nature [21]. In the figure the full lines joining tilt systems denote phase transitions that may be continuous, while dashed lines indicate first-order transitions. Red lines are those for which the crystal structure changes, while blue lines connect phases in the same crystal systems. Following these rules one can predict the nature of transition occurring between any given space groups. For instance, $SrSnO_3$ which is one of the simple perovskite, show an orthorhombic symmetry transition between *Pnma* (low temperature phase) and *Imma* (high temperature phase) around 600 °C. As evident from neutron diffraction experiment such transition due to orthorhombic tilting was continuous [22]. While in case of $PbRuO_3$ an orbital ordering near metal-insulator transition accompanied with first order structural transition was reported. Based on high resolution synchrotron x-ray diffraction experiments this structural transition was confirmed to be *Pnma* (high temperature phase) to *Imma* (low temperature phase) which is an unconventional reversal of the group-subgroup symmetry relationship [23]. A short note on the difference between the group and subgroups is given in Appendix I.

Phase transition due to even very small change in anionic size was demonstrated in the series $Ba_{1-x}Sr_xSnO_3$, where composition from x=0 to x=1 results in change in symmetry and space group in the order *Pm-3m* → *I4/mcm* → *Imma* → *Pnma*. Such change was attributed to introduction of cooperative tilting of the corner sharing SnO_6 octahedra [24]. Transition from Pnma to Imma symmetry under applied external pressure is also reported in case of $Pr_{0.7}Sr_{0.3}MnO_3$ [20].

(vi) *% orthorhombic deformation*: The high symmetry cubic structure with change of cation or anion environment results in distortion/tilting of octohedra favoring the structure to take lower symmetry, either tetragonal/orthorhombic/monoclinic. The deformation, orthorhombic in particular is defined by $= \frac{1}{3}\sum_1^3 \left|\frac{\alpha_i - \bar{\alpha}}{\bar{\alpha}}\right| \cdot 100$; $\alpha_1 = a,\ \alpha_2 = b\ and\ \alpha_3 = c/\sqrt{2}$; $\bar{\alpha} = \left(abc/\sqrt{2}\right)^{1/3}$ [25].

Focusing our concentration on relation between structure and magnetic properties and hence the magnetocaloric effect. Goldsmiths Tolerance factor can be used as direct parameter to trace deviation of perovskite structure and can help to explain changes in related physical properties. In case of the $La_{2/3}(Ca_{1-x}Sr_x)_{1/3}MnO_3$ solid solution, change in crystal structure from orthorhombic (*Pbnm*) to rhombohedral (*R-3c*) around 0.05 ≤ x ≤ 0.15 was correlated to system going from first order to second order magnetic transition, it was traced that such change coincide for tolerance factor of t= 0.92 [4]. The reduced symmetry also lead to decrease of the observed total entropy from 3.7 J $kg^{-1}K^{-1}$ for x=0 to 1.5 J $kg^{-1}K^{-1}$ for x=1.

Introduction to manganese based perovskites is not complete until one mentions the colossal magneto resistance they exhibit. As discussed before the perovskites with $\langle r_A \rangle > 1.18\ \text{Å}$, exhibit metal insulator transition across the ferromagnetic-paramagnetic ordering following the double exchange phenomenon. The property of the material to drastically change value of its resistance (2 – 3%) in presence of applied magnetic field is termed as magnetoresistance (MR). When the value of such magnetoresistance is large enough (≥ 11%) it is called giant magnetoresistance (GMR); when sufficiently large (≥ 40%) it is named colossal magnetoresistance (CMR) [26]. Depending on the origin of such CMR we can distinguish two type of CMR, (i) type I – around ferromagnetic metal and paramagnetic semiconductor transition; (ii) type II – from antiferromagnetic nonmetal to ferromagnet

metal with increasing temperature [27]. The former is explained based on double exchange phenomenon, while later is mostly due to orbital ordering.

4.1.3 Praseodymium manganite perovskite ($Pr_{1-x}Sr_xMnO_3$) : the nuclear and magnetic structures

$Pr_{1-x}Sr_xMnO_3$ exhibits rich phase diagram with interesting magnetic properties as well as promising near room temperature MCMs as shown in Figure 4 a and b. Unlike other members of the $R_{1-x}A_xMnO_3$, this particular phase diagram exhibits a wider window of compositions with near room temperature ferromagnetic to paramagnetic transition. With moderate entropy change which is mainly attributed to second order magnetic transition. Most of these compositions also obey double exchange theory and show metal-insulator transition along their magnetic transition T_C (ferromagnetic - paramagnetic).

One of the end member of the phase diagram $PrMnO_3$ i.e., $Pr^{3+}Mn^{3+}O_3^{2-}$, is orthorhombic perovskite crystallizing in Pbnm with *A-type* antiferromagnetic ordering below T_N=100 K [28]. Much recently it was demonstrated, nanoparticles of $PrMnO_{3+\delta}$ with average diameter 500 nm(with δ=0.13) have ferromagnetic ordering around TC = 120 K [29]. However, with further lowering the average size the ferromagnetism weaken with decrease in Curie temperature. Finally, spin glass behavior appears for particle size less than 120 nm (δ=0.15). The change in magnetic behavior was attributed to excessive oxygen and its consequent surface effects. With self-doping of oxygen (cation deficiency - reduced size) forces Mn^{4+} ions to appear and the double exchange between Mn^{3+} and Mn^{4+} results in ferromagnetism. With further decrease of particle size the MnO_6 distortion increase leading to increase of Mn-O bond length and decrease of Mn-O-Mn bond angle resulting lowering of the magnetic interactions.

$Pr_{1-x}Sr_xMnO_3$ i.e., $Pr_{1-x}^{3+}Sr_x^{2+}Mn_{1-x}^{3+}Mn_x^{4+}O_3^{2-}$, remains antiferromagnetic (canted) till x=0.1. Ferromagnetic ordering due to spin-only moment only with application of high fields appears for 0.1≤x≤0.2. These are reported to be insulating. Metallic behavior appears below ferromagnetic transition for compositions x≥0.25 [30]. The magnetic transitions from the report are represented by blue symbols + line in Figure 4 (b).

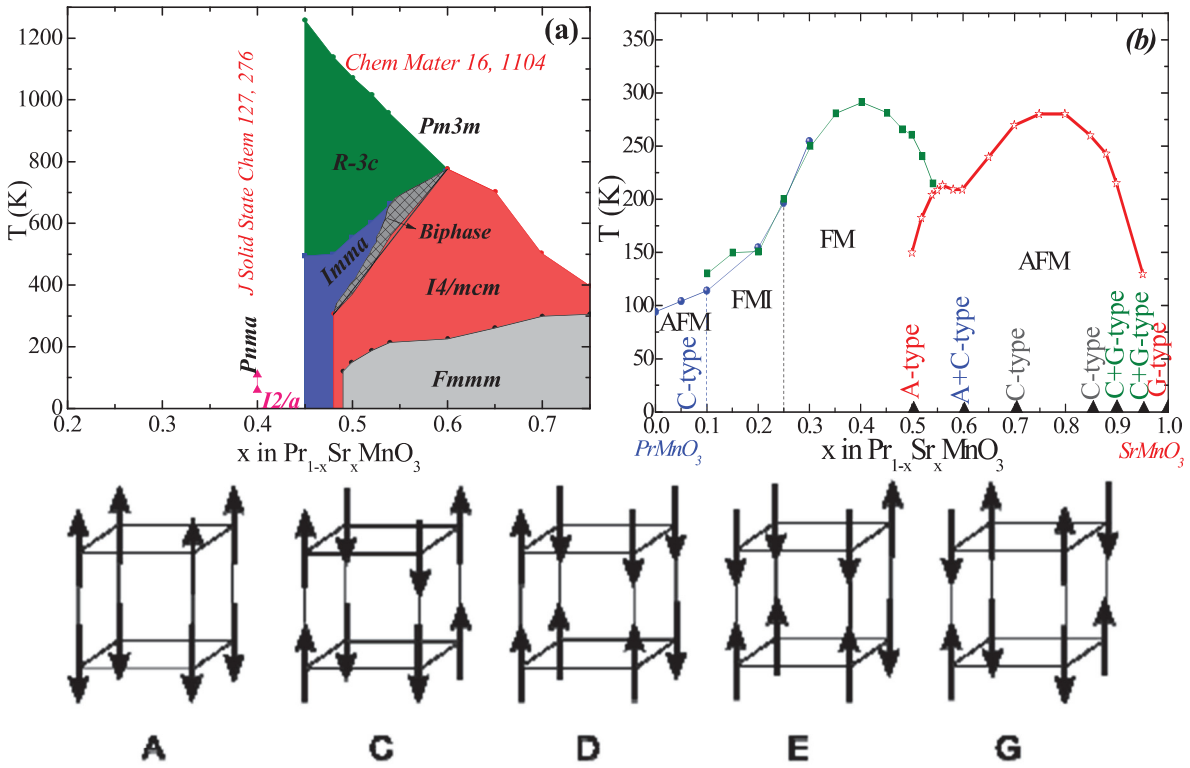

Figure 4: Nuclear (a) and magnetic (b – 0.48≤x≤1 from neutron diffraction) phase diagram as proposed in different literature. (c) Unique arrangements of spins defining each type of antiferromagnetic couplings (Source: Thesis of *Maud GIOT*).

At room temperature $Pr_{0.7}Sr_{0.3}MnO_3$ is reported to have orthorhombic structure define by *Pnma.* The ferromagnetic transition in this sample is reported as T_C = 250 K or 273 K by two different reports [20]. Recently, the nanoparticles of $Pr_{0.7}Sr_{0.3}MnO_3$ are reported to have cubic structure (*Fm-3m, a= b= c= 0.366 nm*) at room temperature [31]. They show second order ferromagnetic transition at T_C= 235 K characterized with large entropy change, ΔS= 1.6, 6.3 $Jkg^{-1}K^{-1}$ (ΔH = 1 T, 5 T). $Pr_{0.67}Sr_{0.33}MnO_3$ single crystal has [32] show second order magnetic transition around room temperature.

For $Pr_{0.6}Sr_{0.4}MnO_3$ there are several discrepancies for the room temperature structure, some reports mention the structure to be described by *Pnma* while few others as *Imma [33, 34]*. C. Ritter et al for first time reported $Pr_{0.6}Sr_{0.4}MnO_3$ to undergo phase transition from high temperature orthorhombic *Pnma* to low temperature monoclinic *I2/a* based on their neutron diffraction results [35]. Volume fractions of the monoclinic space group *I2/a* at 60 K, 90 K and 120 K was reported to be 87%, 38% and 9% respectively, wider transition temperature indicating the phase transition to be second order. Also, the structural and magnetic refinement on neutron diffraction spectra down at 1.6 K still showed traces of *Pnma* (12% volume fraction) as well as *I2/a* (88%). Phase transformation

rules within various perovskite *allotypes* based on the glazers notations was also presented. According to these rules, phase transition from space group *I2/a* or *I4/mcm* to *Pnma* should be of first order in case if it do not involve other phases during the transition, also following group – subgroup relations. Few parallel reports also claim much similar results, but with slight difference in distribution of fraction of each phase [36]. For example, at 10K weight percentage of *Pnma* and *I2/a* are reported to be 26.5% and 73.5% respectively as against 12% and 88% [35].

Much recently a decrease in magnetization curve at low temperature (below 100 K) was seen on dc magnetic measurements of $Pr_{0.6}Sr_{0.4}MnO_3$ by [36]. It was commented by the authors, such decrease in magnetization may be due to a canted spin state or mixture of magnetic phases or the structural transition at low temperature. Even if one correlates these different reports (C. Ritter & Boujelben et al) and link the drop in magnetization to the structural change, *we still need to address possible magnetic arrangement that results in decrease of total moment*. In parallel reports, the refinements on neutron diffraction focusing ferromagnetic ordering suggest magnetic moments alignments to be along longer crystallographic axis, such as along b-axis in case of orthorhombic cell (*Pnma* or *Imma*) for compositions with x≤0.48. While for tetragonal compound described using *I4/mcm* the magnetic moments are reported to be along the c-axis (for x=0.48) [34].

Sample with x= 0.49, 0.5 exhibit two magnetic transitions, a low temperature antiferromagnet (AFM) and high temperature ferromagnetic ordering [33]. For example x=0.5, the magnetic measurements during field cooled cooling confirm ferromagnetic ordering around T_C = 267K and a drop around T_N =135 K which is due to A-type AFM ordering which remains down to low temperature. The electrical resistivity show a metal to insulator transition near the ferromagnetic transition, while increase in resistivity is seen when cooled below the AFM transition [33]. It is not same straight forward when it comes to structural studies is concerned. Similar to sample with x=0.4, different groups claim different structural properties. Especially on space group that can define the lower temperature AFM phase, very interesting debate exists and still needs a definite conclusion. Llobet et al report the A-type AFM phase to be defined by $P2_1/n$ $\left(a_p\sqrt{2} \times 2a_p \times a_p\sqrt{2}\right)$ [37]. While Raveau et al based on their coupled NPD-ED studies had already claimed the same phase to be *Fmmm* $\left(2a_p \times\right.$

$2a_p \times 2a_p$) [38]. Damay et al and A Llobert et al further justify their results in the debate [37, 39, 40].

For all compositions with x≥0.57 only antiferromagnetism appears without any trace of ferromagnetic ordering as presented by Jirak et al [33] in their phase diagram. In independent investigations, compounds with higher Sr concentration (x≥0.5) were shown to exhibit anti-ferromagnetic ordering. Specific type (A/C/G-type) of antiferromagnetic ordering which can be distinguished by unique peaks on neutron diffraction was also reported by same groups [33, 41]. The summary of these reports on magnetic ordering for x≥0.48 is presented in Figure 4 (b). General spin arrangements in different type of antiferromagnetic ordering are presented in Figure 4 (c).

$SrMnO_3$ with complete oxygen stoichiometry $Sr^{2+}Mn^{4+}O_3^{2-}$ forms a cubic perovskite structure defined by *Pm-3m* space group with lattice parameter of *a*= 3.805 Å. Crystal structure is constructed with three-dimensional stacking of corner-sharing MnO_6 regular octahedral formed by six equivalent Mn-O bonds. It is reported to be G-type antiferromagnetic (T_N= 233 K) insulator with electronic configuration, t_{2g}^3 [42]. $SrMnO_3$ is reporter to exist in both cubic (high-temperature) and a hexagonal (low-temperature) perovskite polymorph [43]. This hexagonal structure is formed with corner-sharing bioctahedral Mn_2O_9 entities along the *c* axis. The hexagonal structures exhibit antiferromagnetic coupling both within Mn_2O_9 entities as well as Mn-ions in the corner-sharing octahedra.

4.1.4 Magnetocaloric effect in $Pr_{1-x}Sr_xMnO_3$

The entropy change reported from different groups for the compositions $Pr_{1-x}Sr_xMnO_3$ 0.25≤x≤0.5 are summarized in Figure 5 (a). For simplicity, and to be realistic we shall consider the values in case of polycrystalline samples, for applied field of 1T (the data from single crystal and nanoparticles are presented in different color, to help in distinguish them). It is interesting to see (i) the sudden drop in entropy as we move from x=0.34 to x=0.4; (ii) the values reported by different studies sometimes agree (for example in x=0.45) with each other, in few case they may differ (x=0.4). Magnetocaloric effect for metallic-ferromagnets of the series $Pr_{1-x}Sr_xMnO_3$ was reported by Chen et al., with highest entropy value of 7.1 $Jkg^{-1}K^{-1}$ (ΔH=1 T, T_N≈161 K) in case of x=0.5 sample across its antiferromagnet-

ferromagnet transition [44]. While around ferromagnetic transition they report entropy change of 2.07(T_C≈203 K), 1.51 (T_C≈244 K) and 1.38 (T_C≈260 K) respectively for x=0.5, 0.4 & 0.3 for field change of ΔH=1T. The lowered values of the observed T_C for x=0.4 is bit of surprising. The large entropy values observed at AFM transition are attributed for the first order charge ordering leading to anisotropy in the isotherm curves [45].

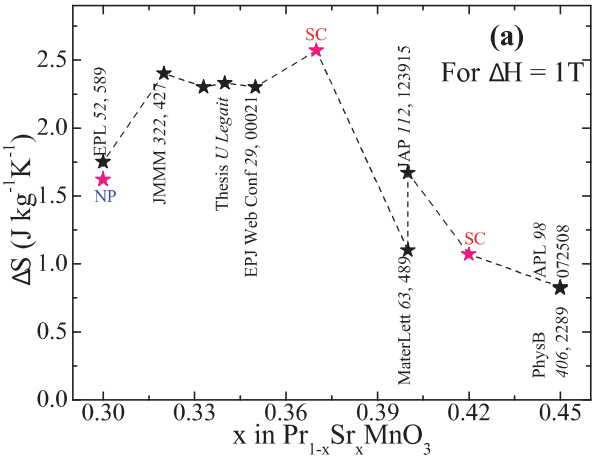

Figure 5: (a) Entropy change from different report in the literature for the series $Pr_{1-x}Sr_xMnO_3$ (0.25≤x≤0.45).

In order to clarify the discrepancy on structural and magnetic properties we investigate in detail the structural and magnetic properties of $Pr_{1-x}Sr_xMnO_3$ in the range 0.25≤ x≤ 0.45. This is also interesting with perspective of magnetocalorics as most of the compositions have their ferromagnetic transition around room temperatures. To extract structural information temperature dependent neutron diffraction studies are carried out and nuclear and magnetic structures are presented. After which the temperature and field dependent magnetic measurements are presented with special focus on entropy change. Apart from the applications discussed before, some compositions of the series $Pr_{1-x}Sr_xMnO_3$ have also been tested for application in solid oxide fuel cells (SOFC) due to their stabile chemical and physical properties up to higher temperatures.

4.2. Synthesis:

Samples were prepared by solid state reaction of metal oxides. Pr_2O_3 (Alfa Aesar 99.9%) was fired at 1000 °C during overnight and Pr_6O_{11} was obtained, confirmed by x-ray diffraction. $SrCO_3$ (Alfa Aesar, 99.5%) was preheated at 275 °C for overnight to remove any

possible absorbed hydroxide. Stoichiometric amount of Pr_6O_{11}, preheated $SrCO_3$ and MnO_2 (Alfa Aesar, 99.9%) were weighed and mixed using mortar and pestle. Well mixed and ground powder was heat treated at 900 °C, 1100 °C, 1250 °C each for 12 hours each with intermediate grinding. From this powder pellet of 10 mm diameter were pressed under hydrostatic pressure (≈ 100 bars or 20 T/cm^2) and heated at 1375 °C for 14 hours. For final sintering, the pellets were reground, pelletized and reheated at 1375 °C for further 50 hours followed by slow cooling (2.5 °C/min) to room temperature.

We like to remark that the final sintering temperature however varies for each individual report between 1200 °C to 1500°C. For example: 1200 °C [32, 46], 1350 °C [35], 1400 °C [36], 1500 °C [9, 34]. The complete solid state reaction involved can be written as,

$$(1-x)Pr_6O_{11} + xSrCO_3 + 6MnO_2 \rightarrow 6Pr_{1-x}Sr_xMnO_3 + \delta(1-x)O_2 + 6xCO_2$$

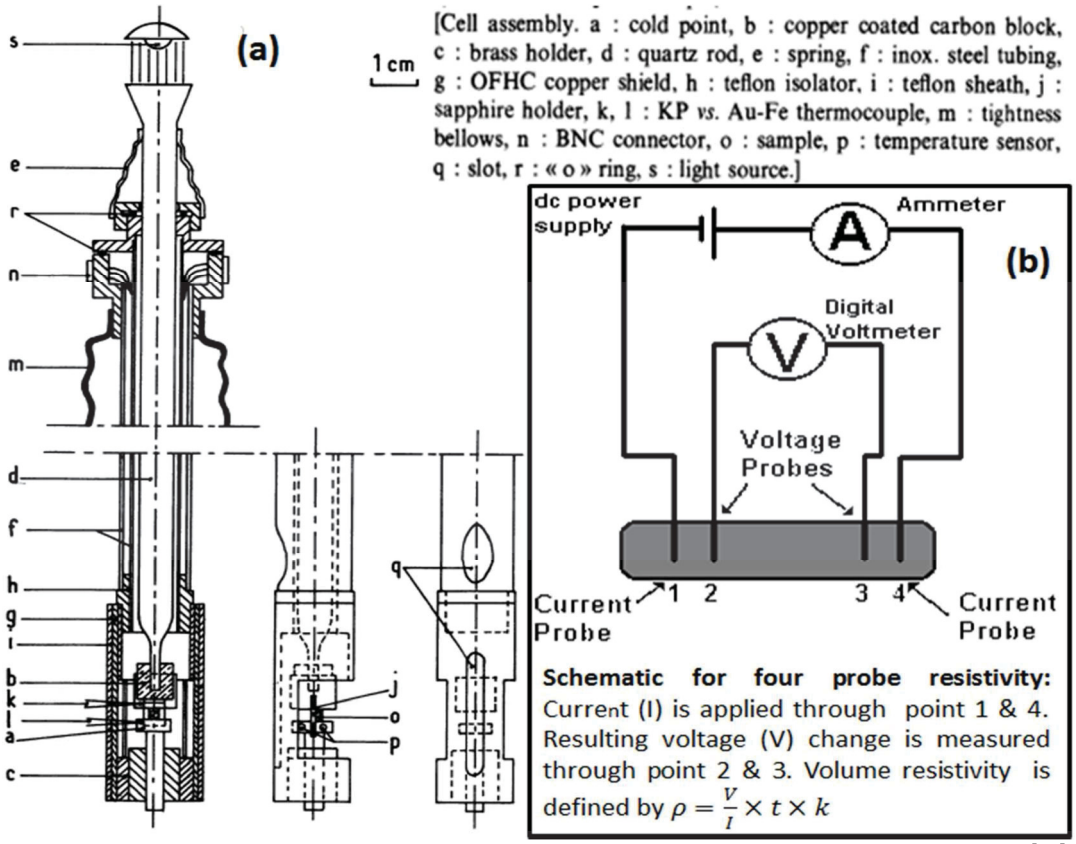

Figure 6: Schematic diagram of a home built apparatus for measuring (a) Seebeck [47] and probe arrangement of a (b) four probe resistivity measurements.

Powder x-ray diffraction (xrd) to ensure phase purity was carried out on PANalytical X'Pert Pro diffractometer using Cu Ka1 monochromatic radiation. The high temperature x-ray diffraction spectra are collected on PANalytical X'pert diffractometer (Cu K_α radiation) at

ICMCB, as well as on Bruker D8 machine at Institut Carnot CIRIMAT CNRS, Toulouse. Neutron diffraction on well ground powders were collected on D20 (ILL, Grenoble), 3T-2, G4-1 (LLB, Saclay) and HRPT (PSI, Switzerland) spectrometers. Details on each of these spectrometer is provided in Appendix G. Structural (nuclear and magnetic) refinements based on Rietveld refinement were carried out using FULLPROF program [48]. The magnetic structures were determined using simulated annealing and structure analysis (SARAh) program [49]. Magnetization measurements were carried out on SQUID MPMS system (Quantum design). Temperature dependent (5 K≤T≤350 K) resistivity measurements were performed on home built four probe unit displayed in Figure 6(b), capable of measuring resistivity in the range 10^{-4} to 10^{5} Ω m and the temperature range 4.2 to 1100 K [50]. Seebeck's coefficient was measured on another home built system which can work in temperature interval of 4 to 300 K [47].

4.3. Phase diagram for nuclear, magnetic structure – case of $Pr_{1-x}Sr_xMnO_3$

The experimental investigations towards providing a complete structural phase diagram will be presented in the following sections. Initially, the nuclear structure at room temperature is addressed through Rietveld refinements carried out on the lab x-ray patterns. Then the refinement results on neutron diffraction patterns for most of these compositions collected at 393 K is presented. In final part of this section detailed nuclear and magnetic structure derived from temperature dependent neutron diffraction are summarized. The Rietveld refinement are initially carried out to with the higher symmetry space group and moved to lowering symmetry only if necessary.

4.3.1. Room Temperature – xrd – the ambient nuclear structure

The room temperature x-ray diffraction over complete range (20° ≤ 2θ ≤ 100°) for all the samples under study $Pr_{1-x}Sr_xMnO_3$ is shown in Figure 7. It is evident from observed peaks (two insets (a) and (b)), that a phase change takes place from space group *Imma* (for x=0.45) to *Pnma* (for x=0.25). Some of the reflections that help to distinguish them are (111) at 2θ≈25.7 °, (210) at 2θ≈34.8 ° which are taken into account only by *Pnma* space group. These peaks start to appear for composition with x≤0.4 and are absent for x=0.42, 0.45. With these

observations we consider compositions x=0.4 and x=0.42 to be the limit for phase transition from *Pnma* to *Ibmm* with in orthorhombic subgroups.

Unlike any other perovskite manganite's (like $La_{1-x}A_xMnO_3$), the present series is reported not to accompany any structural transition alongside magnetic transition. So for now we shall ignore any structural transition around magnetic transition. The Rietveld refinements were carried out on all the samples under study, this should help us in addressing whether the transition between *Imma* and *Pnma* is first order or continuous along the variation of x (i.e., composition) in present case.

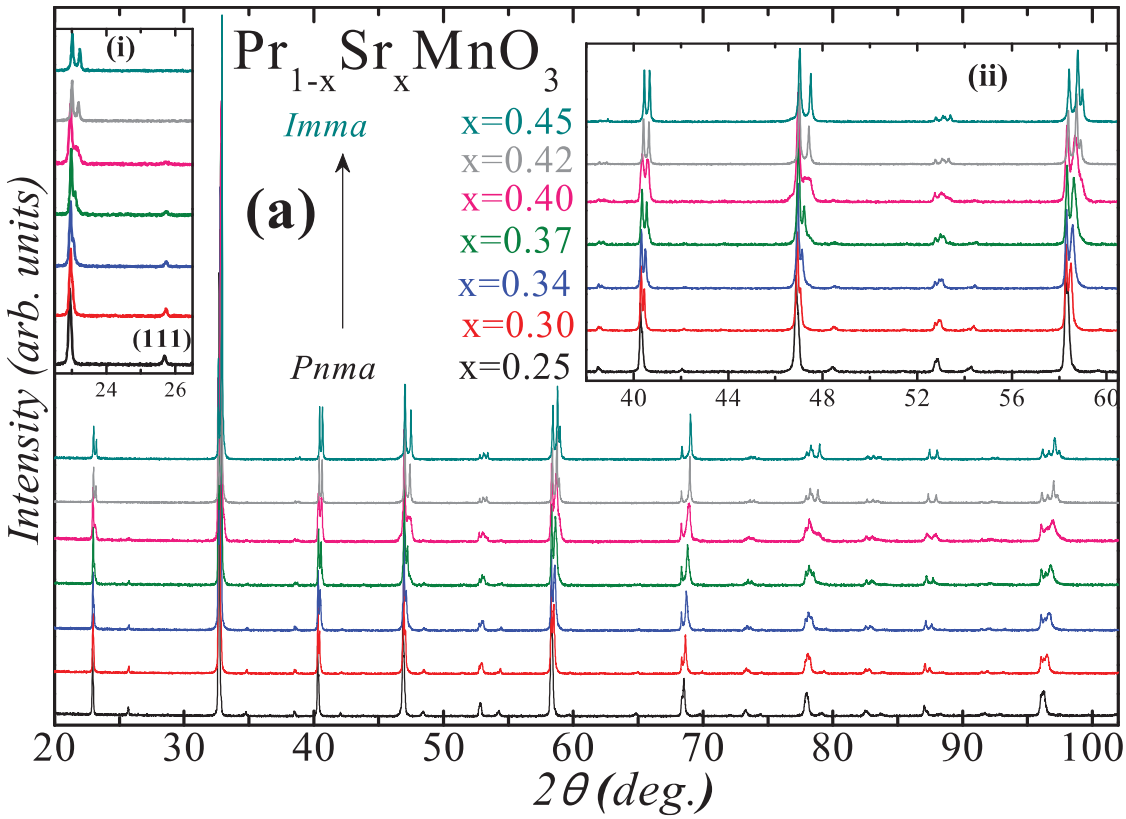

Figure 7 (a) X-ray diffraction patterns collected at ambient temperature. The insets (i) and (ii) display patterns in narrower 2θ range to highlight the continuous phase change from Pnma (for x=0.25) to Imma (for x=0.45).

Profile matching and Rietveld refinements on $Pr_{0.55}Sr_{0.45}MnO_3$ performed using *Imma* space group result in some extra accounted peaks. By comparing the x-ray pattern of x=0.42 and x=0.45 (inset of Figure 9), we could differentiate these extra peaks and match them with *I4/mcm*. So refinements are made considering a secondary phase of *I4/mcm* which gave comparatively better fit (Figure 9). The weight percentage for *Imma* and *I4/mcm* obtained

from refinement results are respectively 94.82 % and 5.18 %. Such biphasic regime is also observed for small range of temperature in case of 0.48≤x≤0.60 as evident on Figure 4 a. The Rietveld refinements on the x=0.42 sample using only *Imma* still had very small amount of the residual, so the secondary phase of *I4/mcm* had to be included to improve goodness of fit. The weight percentage of *I4/mcm* is found to be very low, 6.95%. So we conclude that such biphasic region also exists for x>0.40.

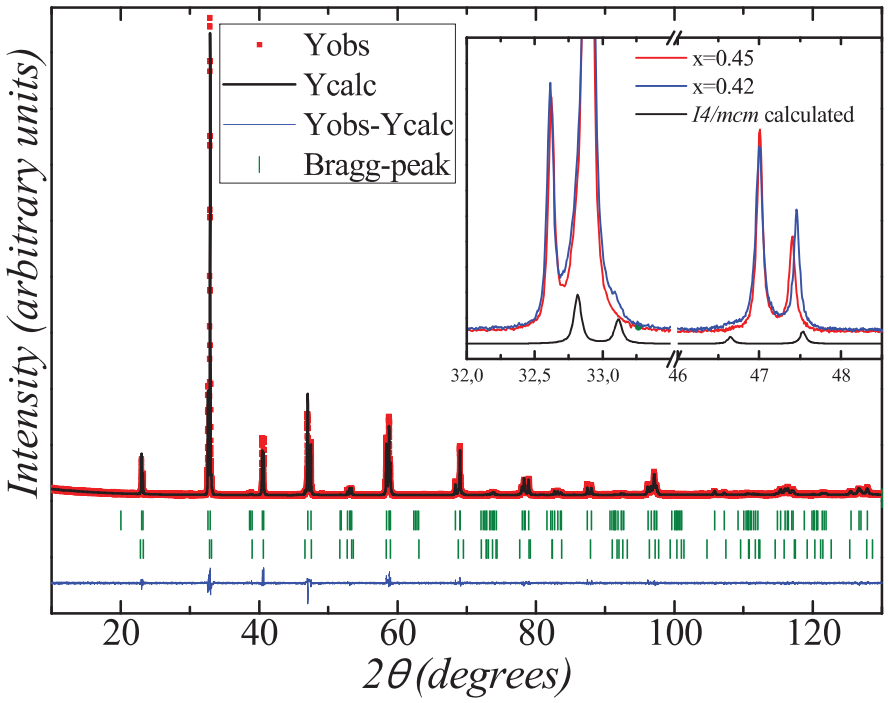

Figure 8: Results from Rietveld refinements of x=0.45

As we approach x=0.40, the A-site radii reaches $\langle r_A \rangle$= 1.23 the critical value at which the phase transition from *Pnma* to *I2/a* is expected at lower temperature as it was well explained by C Ritter et al [35]. In the same report the structure of this composition is reported to be Pnma upto 180 K. For our samples the initial refinements trials with *Imma* or *Pnma* did not provide good fit. Combination of one of these with I4/mcm still resulted in high reliability factors. As clearly seen in the inset of Figure 9 , xrd peaks of sample x=0.4 are slightly wide and can be considered as some ratio of pattern for *Pnma* and *Imma*, small peak which cannot be accounted by either of these (marked by arrow) can be taken care by *I4/mcm* space group. So refinements with all three space group was carried out. The observed and calculated patterns so obtained are presented in Figure 9 b, the three different

Bragg peaks shown represent respectively, from top to bottom, the reflections from space group – *Pnma* (36.67 wt %), *Imma* (56.99 wt %) and *I4/mcm* (6.95 wt %). These results suggest the possibility of the phase segregation for given limit of strontium doping. Most of the reports have assigned the structure for the same composition to be either Ibmm [51] or Pbnm [33]. It is possible because the reflections from both these space groups are much similar, except few extra peaks appearing for Pnma (elaborated in inset of Figure 7 a (i) and (ii)). Inset of Figure 9 (b) display the expanded view of x=0.4 sample along with calculated patterns for three different phases namely *Pnma*, *Imma* and *I4/mcm*.

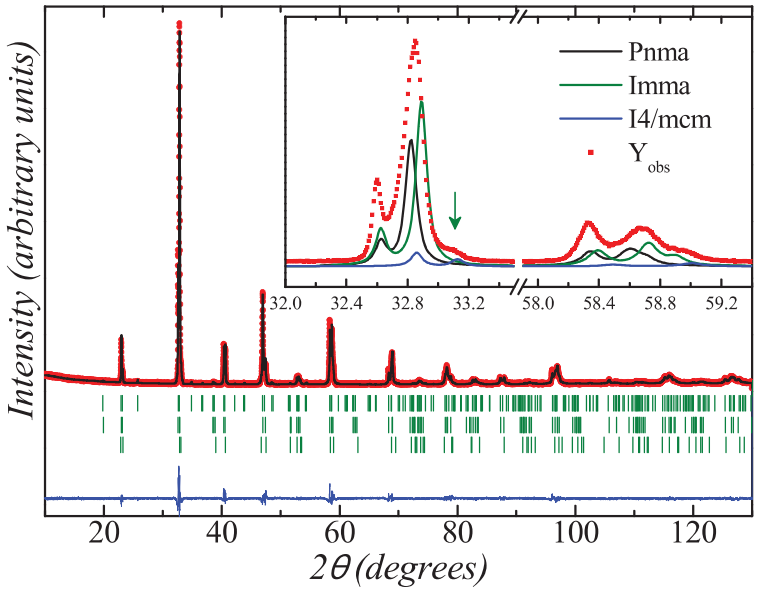

Figure 9: Results from Rietveld refinements for x=0.4. Inset of (b) demonstrate possibility for 3 phase co-existence in x=0.4 at room temperature.

Rietveld refinement on $Pr_{0.63}Sr_{0.37}MnO_3$ yield similar phase coexistence with lowered Imma contribution. With further lowered strontium content tetragonal phase disappear leaving only orthorhombic contribution with majority or only *Pnma (for x≤0.3)*. All these results from refinements are summarized in supplementary table 1 provided at the end of the chapter. The orthorhombic distortion calculated from the refined unit cell parameters decrease continuously with reduced strontium content (for x=0.45, D= 0.466 % to D= 0.092 % for x=0.34). This gives the amount of stress applied by the distortion on the structure and hence the necessary change of the space group.

4.3.2. Neutron diffraction studies at 393 K

Our neutron diffraction experiments should help address the following: (i) one needs to address if the symmetry transitions from Pnma to Imma as compositions change from x=0.40 to x=42 is first order or a continuous as we see on our x-ray diffraction. (ii) the phase co-existence at low temperature especially for higher Sr concentration need to be evaluated (similar to once for x=0.5 to 0.6 in Figure 4 a/ Figure 7 b). By probing temperature dependence structural changes we look forward to address the above mentioned points. We prefer neutron diffraction as our probe as it will allow us to extract information on magnetic structure along with nuclear structure.

Refining room temperature neutron diffraction in order to obtain clear nuclear structural details is not straight forward, considering the fact that the present series of composition exhibit paramagnetic to ferromagnetic transition around 300 K. So in order to obtain better information on nuclear structure the neutron diffraction patterns were collected at 393 K well above ordering temperature with no or lowered magnetic contribution. The so obtained neutron diffraction spectra for x=0.45, 0.42, 0.4, 0.34 and 0.25 are shown in Figure 10. As each of them is collected on different diffractometer using different wavelength, they are presented in Q ($Å^{-1}$) to help compare identical reflections. It is clear that there are few extra reflection which start to appear for x=0.4 and are better differentiable in x=0.25 (black arrow in Figure 10).

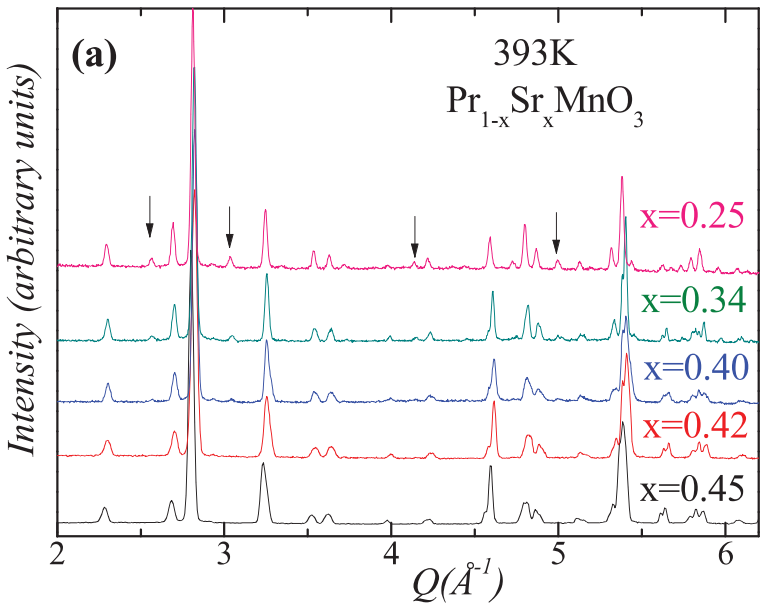

Figure 10: Neutron diffraction pattern at 393 K.

The Q values corresponding to position of these extra peaks are, 2.57, 3.03, 3.717, 4.13, 4.36, 4.44, 4.72, 4.99, 5.95 $Å^{-1}$. These are similar to the observations that we made on room temperature x-ray diffraction where phase change from *Imma* to *Pnma* was shown. Qualitative analysis on these patterns should justify the reliability of the room temperature x-ray diffraction refinements presented earlier.

The lattice parameters, phase distribution along with reliable factors of the refinements of these compositions are summarized in supplementary table 2. It is interesting to see these results as most of them exhibit majority of single phase. Samples with x=0.25, 0.34 have single *Pnma* and x=0.42, 0.45 the *Imma* same as the room temperature phase as we see on lab XRD. However, x=0.4 sample could be refined with majority of *Pnma* phase contrary to three phase model as proposed on lab x-ray data. To address this we need to compare neutron diffraction around room temperature.

4.3.3. Synchrotron diffraction on $Pr_{0.55}Sr_{0.45}MnO_3$

Very recently we receive some synchrotron x-ray diffraction on $Pr_{0.55}Sr_{0.45}MnO_3$, they have to be still subjected to qualitative analysis. First we will highlight the changes observed on temperature dependent synchrotron. Then the results of refinement on temperature dependent neutron diffraction spectra of $Pr_{0.55}Sr_{0.45}MnO_3$ will be presented.

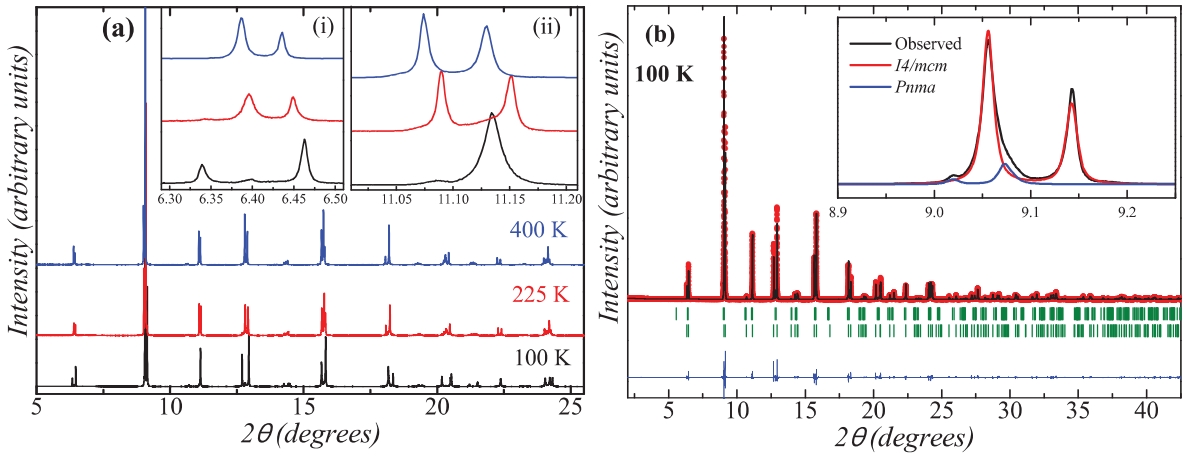

Figure 11: $Pr_{0.55}Sr_{0.45}MnO_3$ - Synchrotron x-ray diffraction (a) at 400 K, 225 K and 100 K. Rietveld refinement for the spectra at 100 K.

High energy synchrotron x-ray diffraction patterns are obtained at 400 K, 225 K and 100 K on ID31 High-resolution powder diffractometer using incident x-ray of λ = 0.430459 Å

(Figure 11 a). Due to smaller wavelengths and high resolution, the distance between the peaks is widened hence the peaks can be better differentiated from each other. The inset (i) and (ii) of Figure 11 (a) display selected peaks that highlight the phase transition between 225 K and 100 K.

Table 1 : Structural parameters, reliability factors for the refinements on synchrotron x-ray diffraction patterns collected at 100 K for $Pr_{0.55}Sr_{0.45}MnO_3$. Last column present the same for neutron diffraction pattern at 100 K.

Temperature		**100K**		**100K**		100 K - ***neutron***	
Space group		***Imma***	***I4/mcm***	***Pnma***	***I4/mcm***	*Pnma*	*I4/mcm*
Phase fractions (%)		11.66 %	88.34 %	30.68 %	69.32 %	12.16 %	87.84 %
Wavelength		0.430459 Å				1.494 Å	
Cell parameters							
a (Å)		5.474	5.401	5.436	5.401	5.438	5.398
b (Å)		7.677	5.401	7.677	5.401	7.666	5.398
c (Å)		5.436	7.786	5.474	7.786	5.477	7.784
Atomic positions							
Pr/Sr	x	0.00	0.00	0.01	0.00	0.010	0.00
	y	0.25	0.50	0.25	0.50	0.25	0.5
	z	0.508	0.25	0.503	0.25	0.526	0.25
Mn		0 0 0	0 0 0	0 0 0	0 0 0	0 0 0	0 0 0
O1		0.00	0.0	0.997	0.0	-0.028	0.0
		0.25	0.0	0.25	0.0	0.25	0.0
		0.999	0.25	0.091	0.25	0.062	0.25
O2		0.25	0.213	0.283	0.213	0.222	0.21
		0.45	0.713	0.541	0.713	0.526	0.71
		0.25	0.00	0.265	0.00	0.273	0.00
Reliability factors							
χ^2		3.22		3.16		4.12	
Rp		13.0		12.8		7.13	
Rwp		16.1		15.9		9.11	
Mtot (μ_B)		--		--		3.36	3.565

Most of the reports claim the low temperature phase as monoclinic *I2/a* (as in $Pr_{0.6}Sr_{0.4}MnO_3$) or *$P2_1/n$* (as in $Pr_{0.5}Sr_{0.5}MnO_3$). The unit cell parameters used in case of $Pr_{0.6}Sr_{0.4}MnO_3$ at 105 K using I2/a are a =7.7858 Å, b = 5.4083 Å, c =5.4028 Å, α=γ= 90 ° and β= 90.132 ° [35]. It can be noticed that b and c have quite close values, with small amount of distortion provided by β. In our case, for synchrotron spectra at 100 K we obtain reasonable good refinement with *I4/mcm* using unit parameters, a=b= 5.4007 Å, c= 7.7858 Å, α = β = γ = 90 °. The resulting fit is presented in Figure 12 b, the inset show expanded portion of the main peak observed around 2θ ≈ 9 ° along with fitted/calculated *I4/mcm* and *Pnma* curves. There were no extra peaks that were not accounted by these space groups. So we believe it is not necessary to reduce the symmetry of the system to monoclinic to address the present structural change. Refinement considering I4/mcm and Imma was also performed and the results are compared in Table 1.

Space Group→		***I4/mcm***	***Imma***	***Pnma***
No. of space group		*140*	*74*	*62*
General multiplicity		*32*	*16*	*8*
Pr/Sr		*site 4b*	*site 4e*	*site 4c*
x,y,z		0, 0.5, 0.25	0, 0.25, ***0.508***	***0.02***, 0.25, ***0.502***
Mn		*site 4c*	*site 4a*	*site 4a*
		0 0 0	0, 0, 0	0, 0, 0
O1 apical		*site 4a*	*site 4e*	*site 4c*
		0, 0, 0.25	0, 0.25, ***0.98***	***0.98***, 0.25, ***0.098***
O2 equatorial		*site 8h*	*site 8g*	*site 8d*
		0.21, ***0.71***, 0	0.25, ***0.46***, 0.25	***0.28***, ***0.53***, ***0.247***
Magnetic structure	**k-vector**	k [0, 0, 0]	k [0, 0, 0]	k [0, 0, 0]
	gamma	Γ(1)ψ(1)	Γ(1)	Γ(5)

Table 2 Detailed atomic positions for different space group used to carry out Rietveld refinements. Refined/refine able atomic site positions are present in bold-italic.

As it was highlighted before, the Imma and Pnma have very similar reflections, and even atomic positions are quite similar Table 2. So the refinements with both these space

group results in almost same reliable values. Refinement results on the synchrotron pattern presented are summarized in supplementary Table 1. Rietveld refinements on 400 K and 225 K pattern need to be performed to better understand the phase transitions at higher temperature.

4.3.4. Detailed neutron diffraction studies

Temperature dependent (10 K to 393 K) neutron diffraction patterns were collected on the selected composition. We shall present in detail the Rietveld analysis on each of them one after another.

$Pr_{0.55}Sr_{0.45}MnO_3$ was probed on D20 neutron diffraction spectrometer using wavelength of λ=1.39Å. Diffraction spectra were collected during cooling and warming. Long time acquisition was made at selected temperatures of 393 K, 235 K, 75 K, 30 K and 2K.

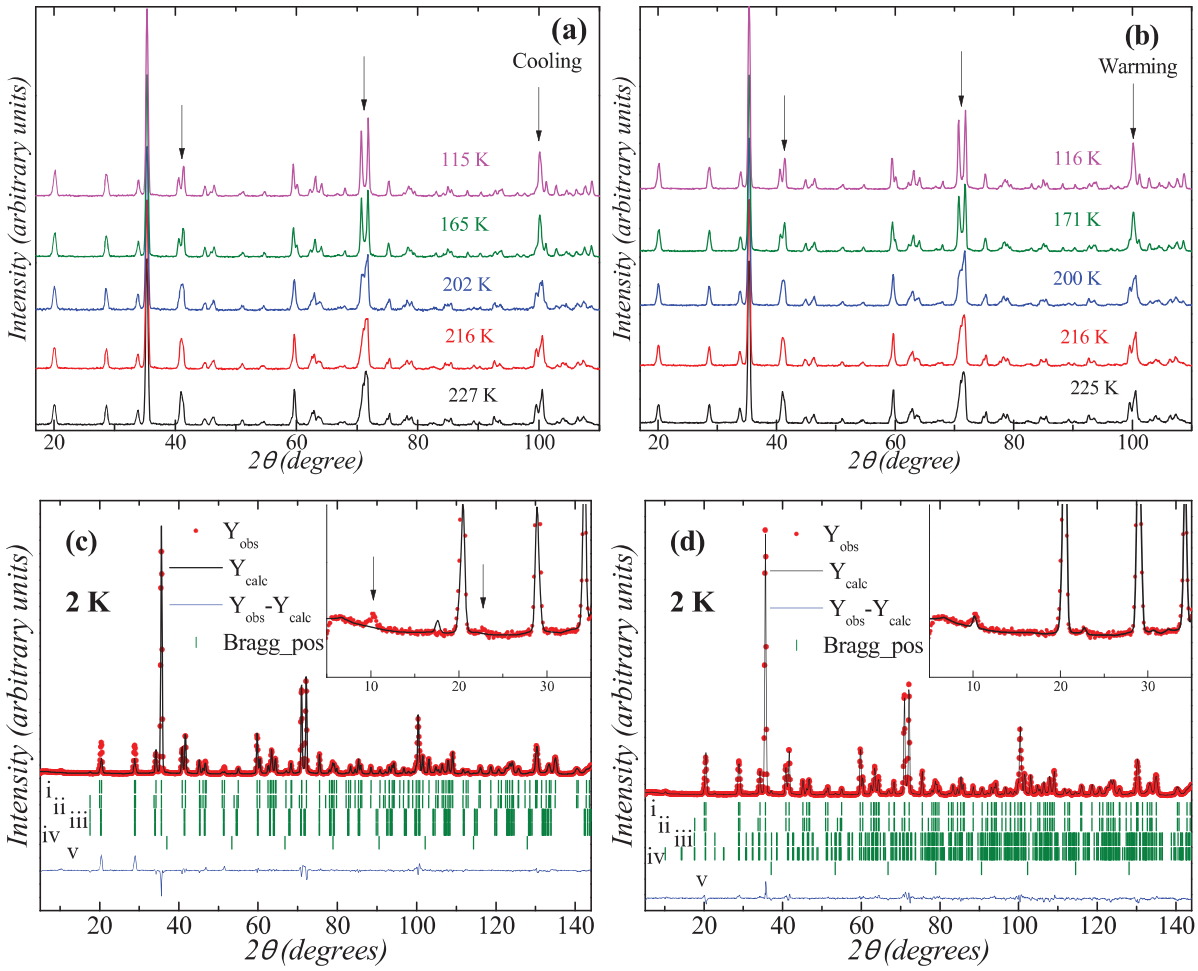

Figure 12: Temperature dependent neutron pattern for $Pr_{0.55}Sr_{0.45}MnO_3$ around low temperature phase transition (a) during cooling (b) during warming. Results from rietveld refinements for data at 2 K (c) *I4/mcm + Imma*, (d) *I4/mcm + Pnma*.

Rietveld refinements considering both nuclear and magnetic contribution have been performed. For diffraction pattern at 393 K reasonable good fit could be obtained using *Imma* space group with a= 5.4913(6) Å, b=5.4507(5) Å and c= 7.6771(8) Å. As we decrease the temperature, alongside the ferromagnetic transition at room temperature additional reversible phase transition (Figure 12 a, b) was observed between 200 K and 175 K with in the ferromagnetic regime. The black arrows in both the figures highlight some of the peaks that show better splitting around the transition. Rietveld refinements were performed taking into account some facts mentioned in previous reports. C Ritter et al during their initial trial of refinement suggest index of Bragg peaks of the secondary phase belong to orthorhombic lattice satisfying a≈ c≈ 5.39 Å, b= 7.77 Å. Along with extinction conditions of the resulting symmetry to better satisfy the *I*-centered lattice. So to address low temperature phase we try using different space group, in the order of lowered symmetry, orthorhombic (*Imma*) → monoclinic (*I2/a*) as well in order of higher symmetry, orthorhombic (*Imma*) → tetragonal (*I4/mcm*).

Refinements on neutron diffraction spectra collected at 2 K are performed using I4/mcm and Imma. The resulting curves are presented in Figure 12 c, each of the five Bragg position in the figure corresponds to (i) nuclear *I4/mcm*, (ii) magnetic *I4/mcm*, (iii) nuclear *Imma*, (iv) magnetic *Imma* and (v) vanadium (sample container) phases. It can be seen in inset (black arrows) that few peaks are not accounted by any of these phases. The new peaks at low angles (corresponding to d≈ 7.5 Å, 3.435 Å, and 2.581 Å) appear only at temperatures below the observed transition (175 K). Peaks at such low angles are, in general, characterized to be signature of *A*-type antiferromagnetic ordering for instance in $Pr_{0.5}Sr_{0.5}MnO_3$ [41]. It is also surprising that such important observations was not mentioned/ highlighted in any of the previous reports demonstrating structure transition with in ferromagnetic regime [35, 36].

The refinements considering the monoclinic I2/a phase for low temperature phase keeping the secondary high temperature phase of Imma improve reliability factors but, do not account these peaks. In our refinements we could index them using magnetic phase (Γ(5)) of the Pnma space group (inset of Figure 12 f). The Bragg positions in the figure correspond to (i) nuclear I4/mcm, (ii) magnetic I4mcm, (iii) nuclear Pnma, (iv) magnetic Pnma and (v) vanadium (sample container) phases. By replacing I4/mcm low temperature phase with monoclinic I2/a did not have any large impact on the refinement. So these are

quite consistent to the once observed in refinements on our synchrotron diffraction at 100 K with majority of I4/mcm and minority of Pnma. With advantage of neutron diffraction carrying the information on magnetic phase, one can better differentiate with the additional magnetic peaks that are specific for each type of ordering.

Details of all refined parameters and magnetic moments at each temperature for the sample $Pr_{0.55}Sr_{0.45}MnO_3$ is presented in supplementary table 3 provided at end of the chapter.

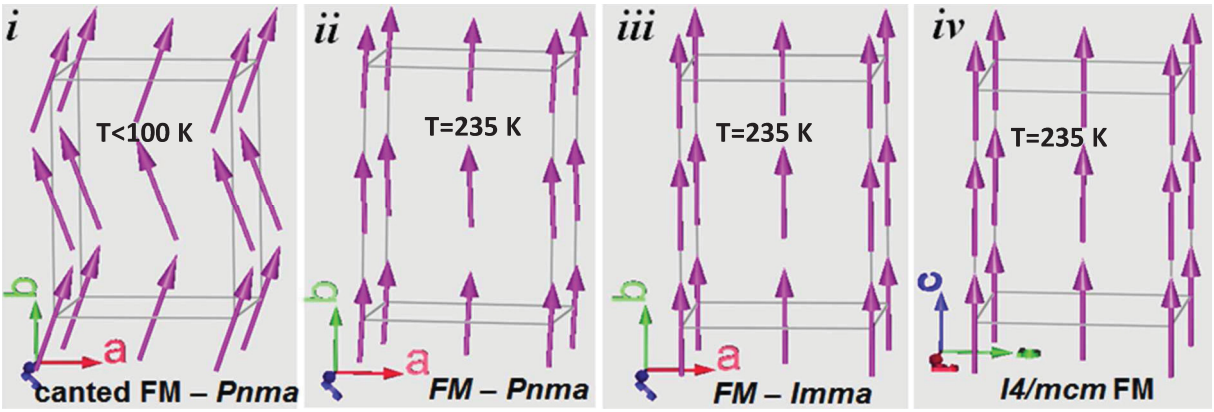

Figure 13: Magnetic structures observed at different temperatures in $Pr_{0.55}Sr_{0.45}MnO_3$.

The magnetic structures obtained from refinements at different temperature are displayed in Figure 13, where structure (i) refers to the magnetic structure obtained for minority *Pnma* phase below 100 K as discussed just before. It shows that the spin arrangement in this case is more distorted or canted compared to the spin arrangement in (ii) which is the magnetic structure at 235 K using same space group. Figure 13 (iii) is arrangement at 235 K obtained with Imma space group. The magnetic spins are slightly distorted in Pnma compared to the one with Imma. The final ferromagnetic spin arrangement (iv) is for the I4/mcm symmetry. It should be noted that, in each case, the magnetic moment is along the longer crystallographic axis.

At this stage of analysis, we still need to better understand at which temperature the structural transition *Imma* to *Pnma* occurs. As observed on $SrSnO_3$ there may exist the phase transition from high temperature Imma to low temperature Pnma a second order transition [22], along with large temperature range showing phase coexistence. Interestingly, the tolerance factor of $SrSnO_3$ (t=1.0808) and some of our samples are quite close (t=1.087 for x=0.45, t=1.083 for x=0.42, and t=1.08 for x=0.4), so we can expect similar behavior in our

sample. Analysis of our synchrotron xray diffraction data are in progress, we expect the outcomes will help in addressing such very small change.

Phase separation with in the orthorhombic subgroups, that looks to be dependent on size of anion (<r_A> or t), in our case controlled by concentration of Sr/Pr, is addressed using neutron diffraction experiments. Recollecting the room temperature x-ray diffraction it is convincing that the sample $Pr_{0.58}Sr_{0.42}MnO_3$ is in the limit of subgroup to sub-sub group transformation, Ibmm to Pnma. The experiments on 3T-2 using λ=1.225 Å (Figure 14 a) will help in resolving nuclear structure along with magnetic structure over the temperature of interest. Whereas, neutron diffraction with incident wavelength of λ=2.423Å on G4-1 (Figure 14 b) is used to provide details on magnetic structure of the sample.

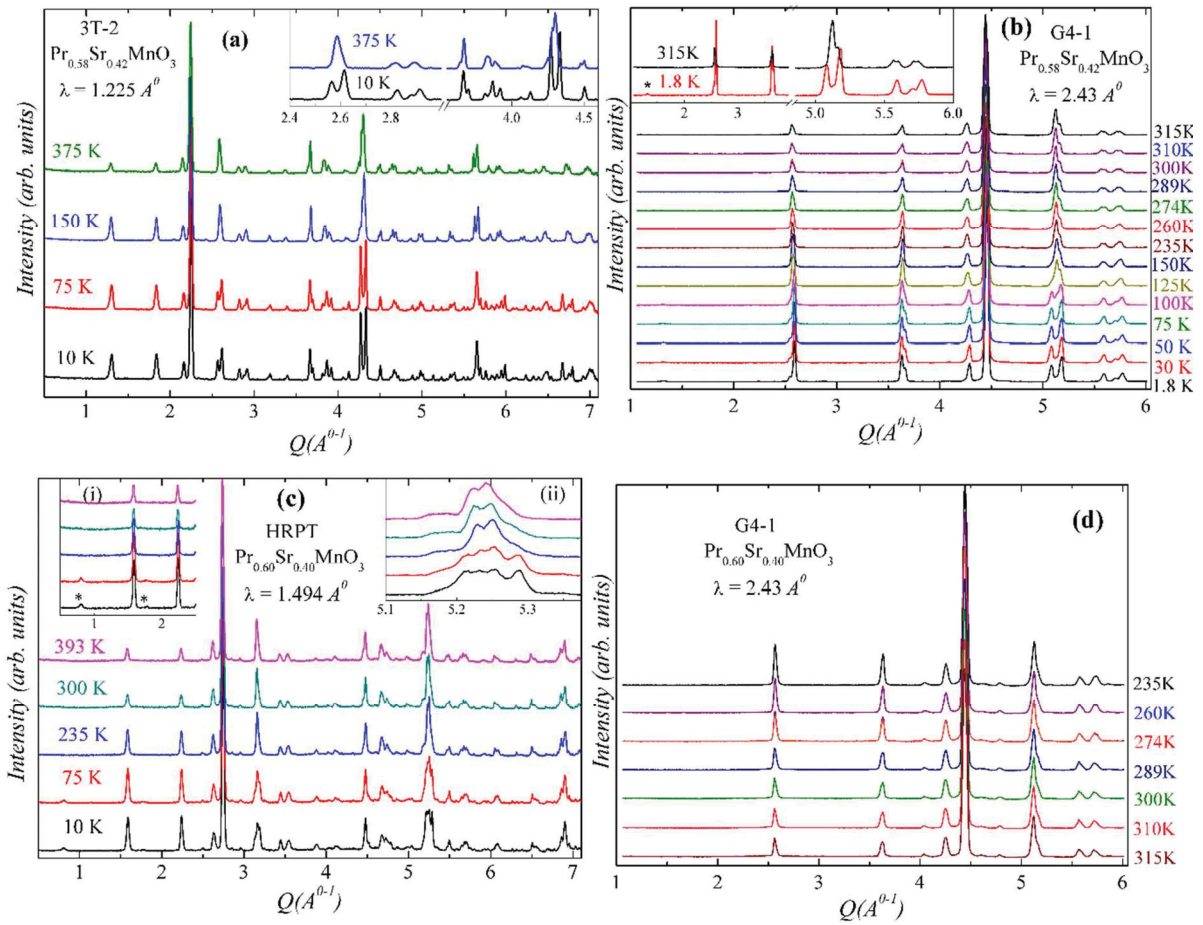

Figure 14 Neutron diffraction pattern for (a, b) $Pr_{0.58}Sr_{0.42}MnO_3$ (c, d) $Pr_{0.6}Sr_{0.4}MnO_3$

Rietveld refinements on neutron diffraction pattern for $Pr_{0.58}Sr_{0.42}MnO_3$ collected at 10 K confirm the coexistence of *I4/mcm* and *Pnma* with the canted ferromagnet as discussed

in previous sample of $Pr_{0.55}Sr_{0.45}MnO_3$ as highlighted by '*' in Figure 14 b. The phase fraction *of I4/mcm* decrease to 85.27 % compared to previous sample of 91.11 %. With increasing the temperature both phase still appear upto 100 K as confirmed on our diffraction patterns on *G4-1* Figure 14 b. Upon further increasing temperature to 125 K only single phase starts to appear and remains till the highest probed temperature 315 K. One of the interesting features observed on these set of data is the transition between phases *Imma-Pnma* is broad. This confirms the fact that the transition between sub space group *Imma* and *Pnma* is second order/continuous following the Howard and Stokes diagram [52, 53]. More qualitative refinements on these spectra is yet to be performed in order to extract change of magnetic moment and phase fraction as function of temperature.

Neutron diffraction patterns at different temperatures for $Pr_{0.6}Sr_{0.4}MnO_3$ are presented in Figure 14 c and d. As in case of previous two samples, we observe lower temperature phase transition between 100 K and 50K, these changes are highlighted in inset (i), (ii) of Figure 14 c. The low angle peaks below the transition are highlighted using '*' in inset (i) of Figure 14 c. The phase fraction of I4/mcm derived from Rietveld refinement of 10 K diffraction spectra further drops to 44.41 %.

Neutron powder diffraction experiments on $Pr_{0.66}Sr_{0.34}MnO_3$ and $Pr_{0.75}Sr_{0.25}MnO_3$ are carried out on HRPT diffractometer using incident wavelength of λ = 1.494 Å. The neutron spectra collected at different temperatures 10K, 75K, 235K and 393K are presented in Figure 15 (a & b). Except increase in intensity of the magnetic peaks (at low angles) with lowering of temperature, no significant change in nuclear structure was observed over complete scanned temperature. Inset of Figure 15 (a) compares the neutron spectra of $Pr_{0.6}Sr_{0.4}MnO_3$ and $Pr_{0.66}Sr_{0.34}MnO_3$ recorded at 10 K. The low angle extra peaks are marked with '*' symbol and closed '◊' symbol represent peaks from the nuclear *Pnma*. It is clear that in former case there is no more extra magnetic contribution which was addressed as due to canted spins. The phase for all temperatures can be well indexed and refined using orthorhombic *Pnma* space group using parameters given in Table 2. The variation of lattice parameter with temperature for both these samples is plotted in Figure 15 c.

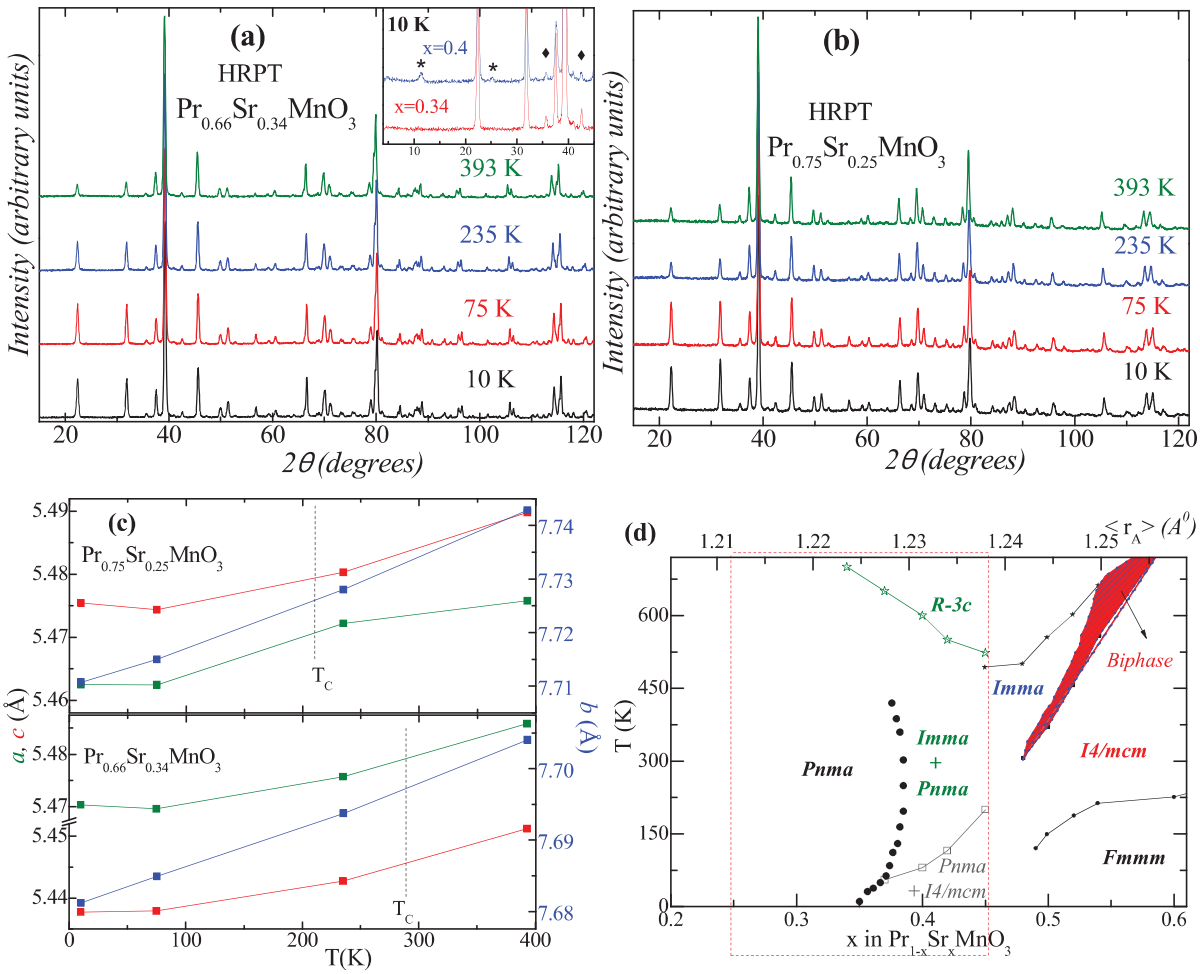

Figure 15 Neutron diffraction patterns at different temperatures for (a) $Pr_{0.66}Sr_{0.34}MnO_3$ (b) $Pr_{0.75}Sr_{0.25}MnO_3$. (c) Lattice parameter *a* (green), *b* (blue) and *c* (red) variation as function of temperature extracted from Rietveld refinements. (d) Structural phase diagram from our investigations with in red dotted box.

A tentative complete magnetic and nuclear structural phase diagram based on neutron diffraction investigations for $Pr_{1-x}Sr_xMnO_3$ ($0.25 \leq x \leq 0.45$) is presented in Figure 15 d (highlighted in red). The new region representing *Pnma+Imma* in low temperature for samples with x= 0.45 to 0.4 is proposed. The magnetic structure of *Pnma* in the region is found to be canted ferromagnet. Single phase of *Pnma* for x=0.34 to 0.25 is confirmed between 400 K ≤ T ≤ 10 K. These samples are found not to show any canted structures until the lowest temperature probed (10 K). The high temperature phase transition denoted by *R-3c* line are derived from high temperature lab x-ray diffraction experiments performed at ICMCB, Bordeaux and CIRIMAT, Toulouse. The line represented by black circle symbols

separating *I4/mcm+Imma* and *Pnma* for composition 0.34<x<0.37 is tentative line. This needs to be confirmed from further detailed analysis of neutron diffraction patterns.

The values of cell parameter, atomic position, magnetic moment and reliability factors for Rietveld refinement at 393 K and 10 K for all the samples presented are summarized in supplementary table 2 and 4 respectively.

4.4. Magnetization

Magnetization as function of temperature under conditions of ZFC (Zero Field Cooled), FCC (Field Cooled Cooling) and FCW (Field Cooled Warming) was measured for all the samples in presence of external applied field of 100 Oe. In all our investigations, the Curie temperature is defined by derivative (dM/dT) of ZFC curve.

4.4.1. Temperature dependence magnetization and ordering temperature :

All samples show more convincing second order like magnetic transition around room temperature as displayed in Figure 16 (a) and (b). The so obtained Curie temperature almost matches with those reported. We shall discuss only few salient features that are not expected in conventional case.

Drop in magnetization during FCC: $Pr_{0.5}Sr_{0.5}MnO_3$ is AFM below T_N= 155 K which is well below its ferromagnetic temperature T_C= 265 K. However with small decrease of Sr content, even $Pr_{0.52}Sr_{0.48}MnO_3$ is believed to be ferromagnetic below T_C= 270 K, without any AFM transition. In our studies we observe a sudden drop in FCC curve of $Pr_{0.55}Sr_{0.45}MnO_3$ at temperature T_{FCC}' = 180K < T_C= 296 K (highlighted by arrows in Figure 16 b). Such drop in FCC curve is extended to $Pr_{0.58}Sr_{0.42}MnO_3$ (T_{FCC}'= 107 K), $Pr_{0.6}Sr_{0.4}MnO_3$ (T_{FCC}'= 75 K), the intensity of drop weakens with decrease of Sr. The possibilities for such drop can be *(i)* secondary phase transition similar to one that was observed by C Ritter et al during neutron diffraction studies for $Pr_{0.6}Sr_{0.4}MnO_3$ [35], *(ii)* weak AFM clusters within dominant FM domain. However, the neutron diffraction confirms the phase transition from Imma to Pnma, with canted ferromagnetic arrangement. We believe that these canting reduce the overall ferromagnetic contribution and hence drop in magnetization.

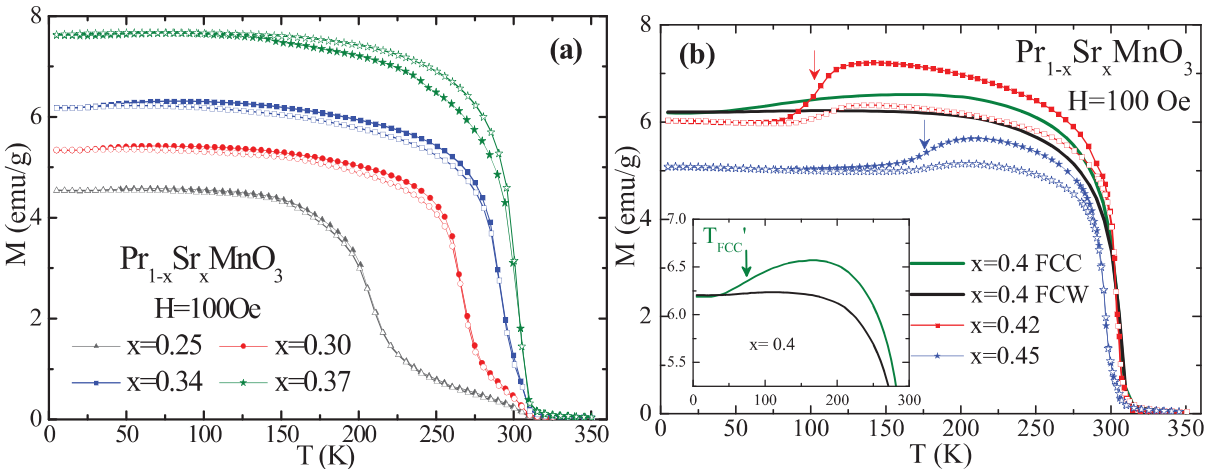

Figure 16: (a), (b) Magnetization curves during Field Cooled Cooling (FCC) and Field Cooled Warming (FCW) for all samples of interest.

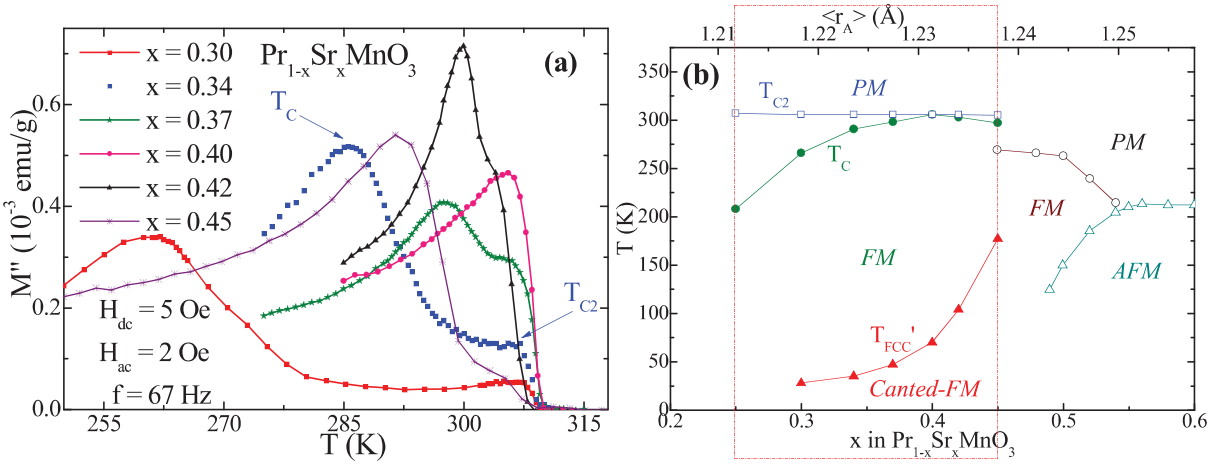

Figure 17: (a) Imaginary part of the AC susceptibility measurements around magnetic transition. (b) Magnetic phase diagram based on dc and ac susceptibility measurements from literature and from present study (with in red dotted box). Where, FM- ferromagnet, PM- paramagnet, AFM – anti-FM.

Thermal hysteresis between FCC and FCW: In most of the case, for second order transition which is described as controlled/clamed system one do not expect any difference in path traced by FCC and FCW, as can be seen in $Pr_{0.75}Sr_{0.25}MnO_3$. As strontium concentration increases we start to observe small hysteresis between them and gets prominent (we will consider FCC-FCW of $Pr_{0.52}Sr_{0.48}MnO_3$, Figure 16(b), throughout the discussion). Interestingly, such opening is seen from Curie temperature (T_C=303 K) down to

the temperature where FCC drops (T_{FCC}'= 103 K) and below this temperature FCC and FCW looks to trace single path. One reason for such hysteresis to appear can be the coexistence of two different magnetic phases. As recently demonstrated, by applying higher fields (H > 1 kOe) it is possible to close this hysteresis over long temperature range, with still small opening near the drop in magnetization [46].

Secondary peak around room temperature on AC Susceptibility: AC susceptibility measurements with different frequencies were performed (H_{ac}= 2Oe, H_{dc}= 5Oe) around magnetic transition and the results are summarized in Figure 17 (a). It could be noticed in all of the samples under study appearance of two peaks *(a)* preliminary prominent peak associated to be with magnetic transition (T_C); *(b)* secondary peak which is different from first one, however, looks to occur at almost same temperature (T_{C2}≈305 K). At this stage it is noteworthy to recall, a deviation of Curie-Weiss law which was reported for x≥0.3, such deviation was justified to be due to *(i)* formation of super-paramagnetic clusters in PM region [54], *(ii)* A-site cationic size mismatch due to difference in larger ionic radii of Sr in comparison with Pr ions can cause complex magnetic structures. The other possible origin can be (iii) in homogeneity in stoichiometry, (iv) presence of two different ferromagnetic clusters/structures [55] and in some case (v) grain boundary effects [5]. Comparing our magnetic and nuclear phase studies we propose that T_{C2} to be para to ferromagnetic transition associated with *Imma*. In which case we should expect *Imma* on neutron diffraction of other samples (x=0.34, 0.25). From peak height of T_{C2} it is clear that the fraction of *Imma* is reduced. So the fraction may be small enough to be detected on the neutron.

Magnetic phase diagram considering all the aforementioned transitions along with some of the reports is summarized in the Figure 17 (b). It would be worth to notice that the drop in FCC which was reported in case of $Pr_{0.6}Sr_{0.4}MnO_3$ is indeed extended to other compositions with in the metallic ferromagnetic regime (represented by red-solid triangles). These correspond to the appearance of canted *Pnma* and the associated phase transition (*I4/mcm*) as proposed from our neutron diffraction studies. Following both magnetic diagram as well as nuclear phase diagram (Figure 15 d) a smooth transition can also be explained at lower temperatures which can be due to canting of magnetic spins.

4.4.2. Isothermal curves at 5 K

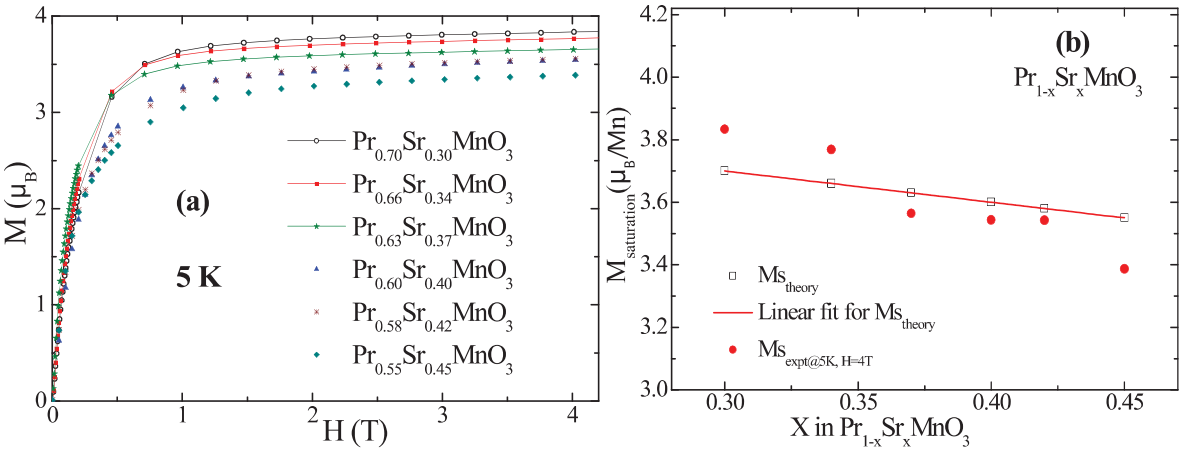

Figure 18: (a) Isothermal magnetization versus applied field at 5K. (b) Comparing saturation magnetization from experimental curves presented in (a) with theoretical values.

Magnetization at 5K: The spin fluctuations, thermal vibrations are believed to be lowered or frozen at low temperatures (technically close to absolute zero). In such cases, magnetization should saturate to its maximum empirical value with application of moderate fields. Isothermal magnetization is collected for all the samples under study at 5 K up to applied field of about 4 T Figure 18 (a). The saturation magnetization obtained from these curves is plotted in Figure 18 (b) along with the theoretical values. The theoretical values are obtained from, $M_S = g\,(1-x)\,S^{Mn3+} + g\,S^{Mn4+}$ where $S^{Mn4+} = 3/2$, $S^{Mn3+} = 2$ and g=2 (in spin-only contribution). The solid line is linear fit to the theoretical data points. It can be noticed that the experimental values for sample x=0.3 and x=0.34 are slightly higher than the theoretical once. This can be attributed to the magnetic moment due to Pr-4f ordering. And we observe sudden drop in these values around x=0.37, the reason could be the canted ferromagnetism as discussed previously.

4.5. Magnetocaloric effect -- *Entropy using Maxwell's equation:*

In order to clarify the discrepancy seen in the reported values and to choose the composition for the ageing process we will evaluate magnetocaloric effect for all our compositions that we have discussed earlier. The samples under study show second order magnetic transition, hence no anisotropy or strain effect is expected/observed for these

samples. The magnetic entropy for all the samples was calculated from isothermal magnetization curves collected around magnetic transition using Maxwell's equation.

Magnetocaloric effect around T_C

The so obtained magnetic entropy values under 1, 2, 3T are plotted against composition in the Figure 19 a. We also observe smooth drop in this plot near x=0.4, similar to that we discussed in previous paragraph. The values from our samples are lower than the once found in literature. And in some case they are higher than the once reported. For example in case of $Pr_{0.55}Sr_{0.45}MnO_3$ our entropy values are 0.92, 1.71, 2.36 $Jkg^{-1}K^{-1}$ compared to the reported values of 0.82, 1.3, 1.71 $Jkg^{-1}K^{-1}$ (for magnetic field change of 1.0, 2.0, 3.0 T) [56] [Appl. Phys. Lett. **98**, 072508]. Even though the values of entropy changes are low in case of $Pr_{0.55}Sr_{0.45}MnO_3$, they have large FWHM, and hence increase in the RCP [56]. Figure 19 (b) compares the entropy curves for the samples with temperature normalized to their respective T_C. In our case, we do not see peak broadening for any particular sample, all sample have similar width. Only $Pr_{0.66}Sr_{0.34}MnO_3$ has noticeable bigger width and looks to be broader enclosing all the curves.

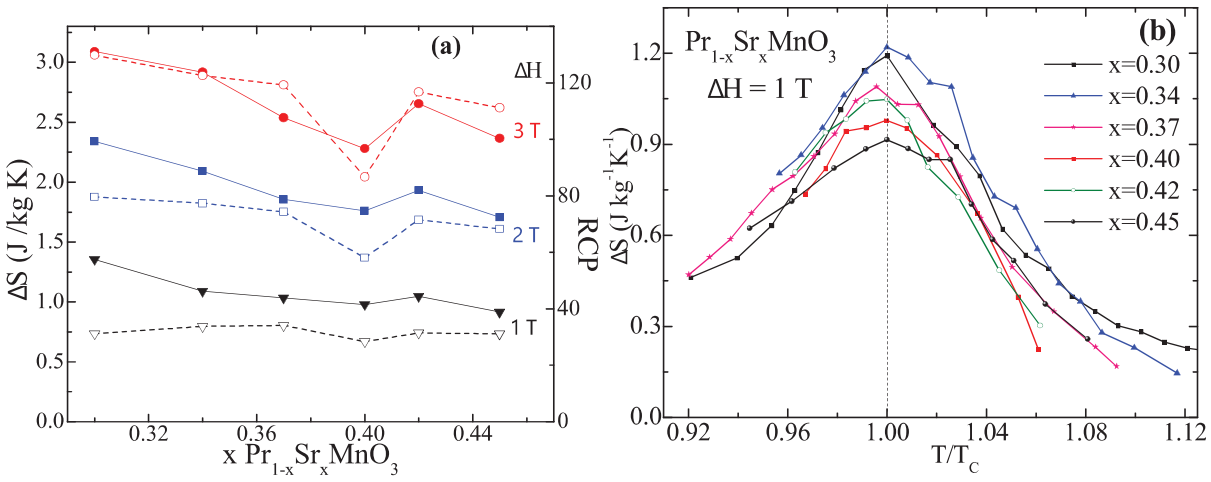

Figure 19: (a) Entropy change (solid symbol) their corresponding RCP (open symbol) for all samples. (b) Entropy change for field change of 1 T for all samples, temperature is normalized with their T_C.

The differences in entropy values between the reported and our investigation can be due to one of the following: *(a) synthesis condition* – it is well known in case of most of the oxides, the observed physical properties (resistivity, magnetization - T_C, entropy change) strongly depend on synthesis route used to obtain them. Some reported claim the

nanocrystalline $Pr_{0.7}Sr_{0.3}MnO_3$ show large magnetic entropy [31]. It should be noted these large values are observed at high fields and for lower applied field they are within the values for bulk polycrystalline sample (Figure 19 a). For bulk polycrystalline sample the final sintering conditions play key role in obtaining single phase, crystalline, dense samples. Each of these factors play very important role on the observed physical properties (structural, magnetic, electrical and heat transport). Recently, the effect of the sintering temperature on the observed entropy change was reported for $Pr_{2/3}Sr_{1/3}MnO_3$ [57]. The sample sintered at 1260 °C showed slightly lower entropy values (ΔS = 1.72, 3.2 $Jkg^{-1}K^{-1}$ for ΔH = 1, 2 T) in comparison with that of 1400 °C sintered sample (ΔS = 2.3, 3.9 $Jkg^{-1}K^{-1}$). They highlight enhancement in electrical transport properties, and assign such change to variation in grain size/boundaries.

(b) morphology – alignment of the spins[58]. Magnetization carried out with different orientation of bulk sample (in form of rectangle) show different behavior (inset of Figure 20 c). The sample was warmed above 320K, then FCC (Field Cooled Cooling) followed by FCW (Field Cooled Warming) under applied field of 100 Oe was performed near the magnetic transition. The magnetization was higher with length of rectangle along axis of applied field (indicated as b in inset of Figure 20 c) compared to that when sample was perpendicular (illustrated as a) to direction of field. Magnetization isotherms at 15 K for these two directions confirm that the parallel configuration is in easier axis of magnetization (Figure 20 c). Magnetization curve at 15 K of the powder sample looks much similar to parallel configuration, with slightly higher saturation values. However the FCC and FCW curves are much lower near magnetic transition. Such dependence of the observed magnetization can be correlated to the magnetic arrangements in the sample which is normally on longest crystallographic axis as confirmed from the neutron diffraction. However, the saturation value for magnetization curve at 15K for parallel configuration is almost same as that of the powder sample. Even the values of entropy change ΔS are same for both powder and block parallel to applied field. Hence the discrepancy observed in values reported in literature could be from grain size effect – heterogeneous grain size.

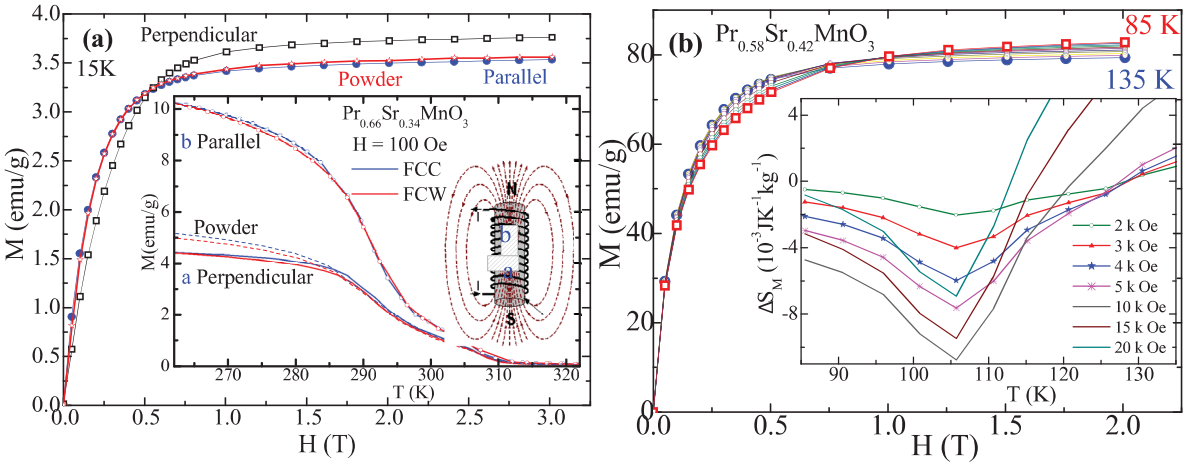

Figure 20: (a) Magnetization curve for different sample orientation (b) Isothermal magnetization curves across the drop in FCC curve for sample $Pr_{0.58}Sr_{0.42}MnO_3$, inset display the entropy change calculated from these curves.

Magnetocaloric effect across the drop in FCC

Recently very small entropy change (-0.578 $Jkg^{-1}K^{-1}$) independent of the applied field for $Pr_{0.6}Sr_{0.4}MnO_3$ was reported near 100 K across the structural transition [46]. The entropy change we obtain near T = 105 K for x=0.42 are very small compared to the once around magnetic transition at room temperature. Applied field direction dependence entropy change, ΔS = 0.3 $Jkg^{-1}K^{-1}$ ($H_{parallel}$) and 0.08 $Jkg^{-1}K^{-1}$ (H_{perp}) is reported for $Pr_{0.52}Sr_{0.48}MnO_3$ single crystal around similar drop of magnetization [59]. Unlike this, the direction of external field ($H_{parallel}$ or H_{perp}) had no effect on the entropy (3.3 $Jkg^{-1}K^{-1}$, ΔH = 4 T) observed around magnetic transition (T_C).

The reason for which was explained as *(i)* the structure transition associated with AFM as in case of $Pr_{0.5}Sr_{0.5}MnO_3$. Similar crossover in isothermal curves is observed in case of Ni-Mn-Ga Heusler alloys where in small inverse magnetocaloric effect across martensitic transition is reported [60]. *(ii)* Ordering of praseodymium at lower temperatures (across 50 K). The second possibility can be ruled out as it occurs at very low temperatures then the drop in FCC. Let us recall the first order transition from low temperature antiferromagnetic charge-ordered state to ferromagnetic charge-disordered state observed around 165 K in $Pr_{0.5}Sr_{0.5}MnO_3$. The entropy change in this case was very high (ΔS=-7.5 $Jkg^{-1}K^{-1}$, ΔH = 5 T) even compared with the one around T_C (ΔS = 3.2 $Jkg^{-1}K^{-1}$, ΔH = 5 T) for the same sample.

Isothermal magnetization curves for our $Pr_{0.58}Sr_{0.42}MnO_3$ sample are measured across the temperature where FCC drop is observed (135 K and 85 K). The results are displayed in Figure 20 b. The values observed are very low as in case of Pr0.52Sr0.48MnO3 single crystal. From our neutron diffraction experiments we have confirmed the transition to result in the canted ferromagnetic structure. So we believe the drop in magnetization curve and the crossover of isothermal curves to be from these canted arrangements of the ferromagnetic spins. We propose that the small entropy values observed for our samples is due to lower energy necessary for the canting of spins then the flipping that is necessary to observe the AFM. This justifies our results of choosing *Pnma* with canted spins rather than any other possible lower symmetry (monoclinic) with antiferromagnetic ordering.

4.6. Ageing

The polycrystalline $Pr_{0.65}Sr_{0.35}MnO_3$ material was tested in magnetic refrigeration (MR) system by Guillou et al [9]. They are able to produce the oxide material in large scale and demonstrate its real refrigeration capacity for room temperature cooling. The interesting outcome from those experiment is however the performance of Pr,Sr based manganite to be close to the prototype materials Gd. In similar independent experiments, the same group has confirmed the stability of $Pr_{0.65}Sr_{0.35}MnO_3$ in water, but without subjecting it to any flux. Apart from this report there are no other investigation dedicated for testing the stability of oxides against the heat transport fluids or mimic the refrigeration workspace atmosphere.

Considering the physical properties from experiment results, like (i) near ambient temperature transition (T_C= 290 K), (ii) moderate magnetocaloric performance of the materials (ΔS= 1.08 $Jkg^{-1}K^{-1}$; RCP= 33 Jkg^{-1} for ΔH= 1 T) (iii) and lower structural deviation. We adopt $Pr_{0.66}Sr_{0.34}MnO_3$ as our choice of material for testing its stability against the flux of heat transfer fluid (DI H_2O).

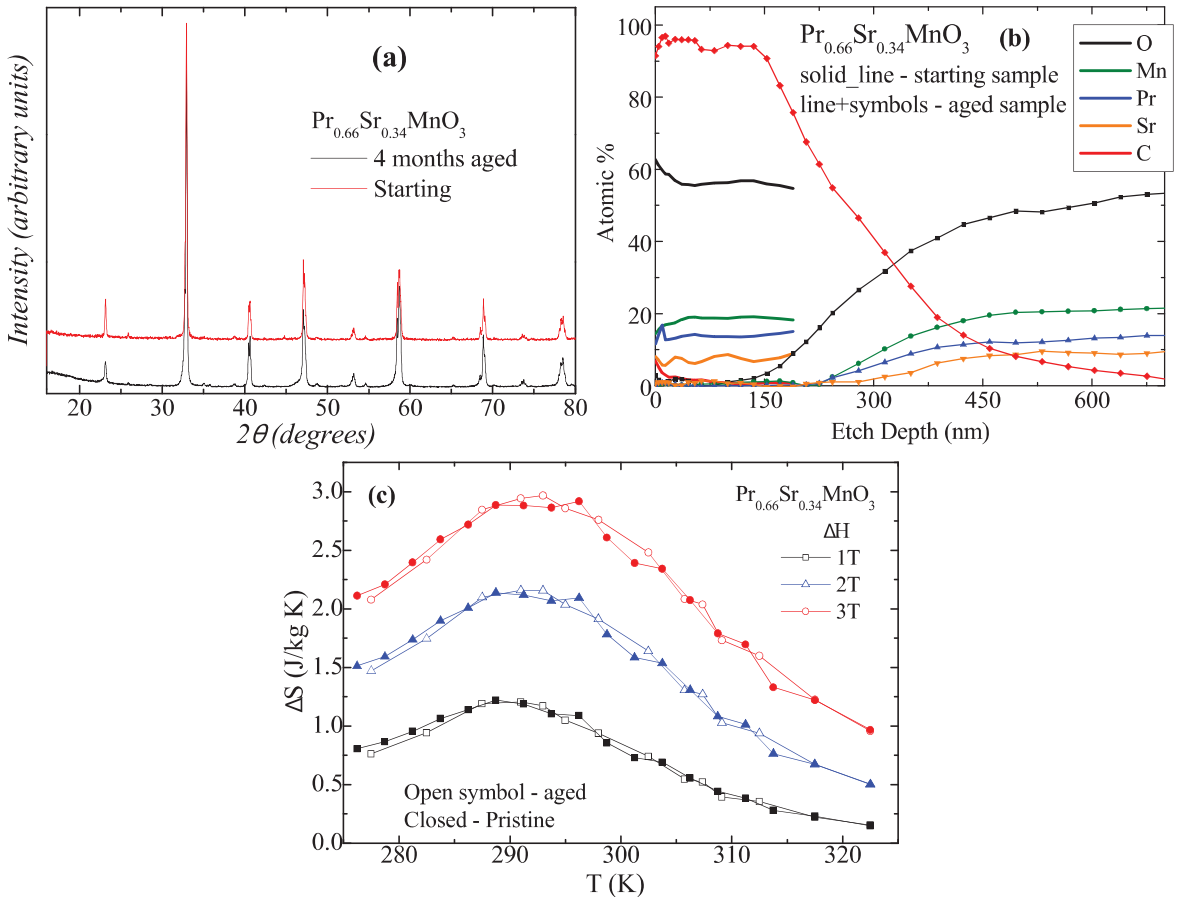

Figure 21: (a) XRD pattern for starring and 4 month aged sample. (b) Depth profile by auger spectroscopy pristine (solid line) and 2 months aged sample (line+symbols) (colors represent individual element). (d) Entropy change for the pristine and aged sample.

Pellets of the composition $Pr_{0.66}Sr_{0.34}MnO_3$ are placed in the ageing cell and treated with water flux (as described in chapter 2). At regular interval of time these pellets were removed and subject to xrd, microstructure, and magnetic characterization. The xrd spectra did not show any considerable changes even up to probe period of 4 months (Figure 21 a). Similar results are seen even with further ageing. This confirms the chemical stability of the material to the flux. Also there was no visible evidence of any mechanical damage, such as erosion of the pellets. The weight loss recorded along the period of ageing show no change.

The possible microstructure change cannot be ignored so further characterization focusing microstructural changes are made. The depth profile for pristine and two month aged samples using auger spectrometer are shown in Figure 21 (b). For starting or pristine sample nominal stoichiometry is observed just below 25 nm depth. The carbon found up to this level can be pollutant carbon due to the atmospheric exposure of the pellet. However,

after exposure of the pellet to the flux of DI H_2O carbon was found to deeper level of the pellets, after on month carbon content extent up to 320nm and 550nm after 2 months of aging (as shown by red symbol + line on Figure 21 (b)). The predictable possible pollutant or the impurity formation during ageing of carbon can be explained as from formation of strontium carbonate. However, from the depth profile it is clear that for area around high carbon we do not see any trace of oxygen, so we can rule out the possibility of $SrCO_3$. So we still need to establish better reasoning for the formation of the carbon layer.

Meanwhile we also notice that the carbon variations described is not consistence throughout the pellet. These observations suggest that the carbon can also be contribution from inter-granular pores. The repeated trials of ageing on this particular composition with further densified pellets are in progress. The results from these experiments should provide better information on the change of chemical state of the material.

The magnetic properties are not affected to any considerable extent by aging. The entropy change for 3 months aged sample is compared with the starting sample in Figure 21 (c). As evident there is no significant decrease of either transition temperature (T_C = 290 K) or the observed entropy change ($\Delta S \approx 1.08$ $Jkg^{-1}K^{-1}$, $\Delta H \approx 1T$) due to aging.

4.7. Conclusion:

Detailed structural, magnetic and magnetocaloric characterizations for the complete metallic–ferromagnet perovskite manganite $Pr_{1-x}Sr_xMnO_3$ ($0.25 \leq x \leq 0.45$) are carried out for first time. Based on the neutron diffraction experiments a new phase diagram of nuclear and magnetic structures over temperature range is presented.

The drop in magnetization within ferromagnetic regime of sample $Pr_{0.6}Sr_{0.4}MnO_3$ was reported by most of literatures as due to structure transition from orthorhombic (*Pnma*) to monoclinic (*P2/a*). While the extra peaks at very low angle observed on neutron diffraction were not addressed. We address this issue in our investigation and propose such peaks to be magnetic contribution due to canted *Pnma* structure. This is further assigned as the reason for the drop in the field cooled magnetization anomaly which was debated as orthorhombic to monoclinic transition in most of the literature. It has been further demonstrated that such canting does appear for other higher strontium concentration (x=0.42, 0.45). Summing all the results a new nuclear-magnetic structural phase diagram has been proposed.

$Pr_{0.64}Sr_{0.34}MnO_3$ is mostly free from any such low temperature magnetization anomalies, with mostly orthorhombic structure over the temperature range of interest. It exhibit second order magnetic transition close to room temperature characterized with moderate entropy change. Even though there is still room to improve the observed performance by optimizing some steps in synthesis procedure.

We have performed the ageing of the sample for defined period of time. The results show that the composition $Pr_{0.64}Sr_{0.34}MnO_3$ is stable to the environment and flux of DI H_2O, confirming some of the previous reports where samples were allowed to stay in water. The remarkable changes with time were emerging of carbon. This still need to be addressed through more precise characterization. The overall outcomes from ageing however should inspire the further developments of oxide materials for room temperature magnetocaloric applications.

4.8. References:

1. Gschneidner, K.P., VK, *Magnetocaloric materials.* ANNUAL REVIEW OF MATERIALS SCIENCE, 2000. **30**: p. 387-429.

2. Phan, M.-H. and S.-C. Yu, *Review of the magnetocaloric effect in manganite materials.* Journal of Magnetism and Magnetic Materials, 2007. **308**(2): p. 325-340.

3. Zhu, H., H. Song, and Y. Zhang, *Magnetocaloric effect in layered perovskite manganese oxide $La_{1.4}Ca_{1.6}Mn_2O_7$.* Applied Physics Letters, 2002. **81**(18): p. 3416-3418.

4. Mira, J., et al., *Drop of magnetocaloric effect related to the change from first- to second-order magnetic phase transition in $La_{2/3}(Ca_{1-x}Sr_x)_{1/3}MnO_3$.* Journal of Applied Physics, 2002. **91**(10): p. 8903-8905.

5. Phan, M.H., et al., *Large magnetic-entropy change above 300 K in CMR materials.* Journal of Magnetism and Magnetic Materials, 2003. **258–259**(0): p. 309-311.

6. Zhong, W., et al., *Dependence of the magnetocaloric effect on oxygen stoichiometry in polycrystalline $La_{2/3}Ba_{1/3}MnO_{3-\delta}$.* Journal of Magnetism and Magnetic Materials, 2003. **261**(1–2): p. 238-243.

7. Taşarkuyu, E., et al., *Effect of high temperature sintering on the structural and the magnetic properties of $La_{1.4}Ca_{1.6}Mn_2O_7$.* Journal of Alloys and Compounds, 2011. **509**(9): p. 3717-3722.

8. Manh-Huong Phan, Hua-Xin Peng, and S.-C. Yu, *Large magnetocaloric effect in single crystal $Pr_{0.63}Sr_{0.37}MnO_3$.* Journal of Applied Physics, 2005. **97**: p. 10M306.

9. F. Guillou, et al., *Development of a new magnetocaloric material used in a magnetic refrigeration device.* EPJ Web of Conferences, 2012. **29**: p. 00021.

10. Rao, C.N.R. and B. Raveau, *Colossal magnetoresistance, charge ordering and related properties of manganese oxides*. 1998: World Scientific.

11. Manthiram, A., et al., *Crystal chemistry and properties of mixed ionic-electronic conductors.* Journal of Electroceramics, 2011. **27**(2): p. 93-107.

12. Radaelli, P.G., et al., *Structural Phase Diagram of Perovskite $A_{0.7}A'_{0.3}MnO_3$ (A= La, Pr; A′ = Ca, Sr, Ba): A New Imma Allotype.* Journal of Solid State Chemistry, 1996. **122**(2): p. 444-447.

13. J M D Coey, M Viret, and S.V. MOLNAR, *Mixed-valence manganites.* Advances in Physics, 1999. **48**(2): p. 167 - 293.

14. Yurii, A.I. and N.S. Yu, *Double exchange model and the unique properties of the manganites.* Physics-Uspekhi, 2001. **44**(2): p. 109.

15. Nevill, M., *Conduction in Non-Crystalline Materials*. 1993: Clarendon, Oxford. 17.

16. Sundaresan, A., A. Maignan, and B. Raveau, *Effect of A-site cation size mismatch on charge ordering and colossal magnetoresistance properties of perovskite manganites.* Physical Review B, 1997. **56**(9): p. 5092-5095.

17. Hwang, H.Y., et al., *Lattice Effects on the Magnetoresistance in Doped $LaMnO_3$.* Physical Review Letters, 1995. **75**(5): p. 914-917.

18. Rodriguez-Martinez, L.M. and J.P. Attfield, *Cation disorder and size effects in magnetoresistive manganese oxide perovskites.* Physical Review B, 1996. **54**(22): p. R15622-R15625.

19. Glazer, A., *The classification of tilted octahedra in perovskites.* Acta Crystallographica Section B, 1972. **28**(11): p. 3384-3392.

20. Dang, N.T., et al., *Structural and magnetic phase transitions occurring in $Pr_{0.7}Sr_{0.3}MnO_3$ manganite at high pressures.* JETP Letters, 2013. **97**(9): p. 540-545.

21. Howard, C.J. and H.T. Stokes, *Group-Theoretical Analysis of Octahedral Tilting in Perovskites. Erratum.* Acta Crystallographica Section B, 2002. **58**(3 Part 2): p. 565.

22. Mountstevens, E.H., S.A.T. Redfern, and J.P. Attfield, *Order-disorder octahedral tilting transitions in $SrSnO_3$ perovskite.* Physical Review B, 2005. **71**(22): p. 220102.

23. Kimber, S.A.J., et al., *Metal-Insulator Transition and Orbital Order in $PbRuO_3$.* Physical Review Letters, 2009. **102**(4): p. 046409.

24. Prodjosantoso, A.K., Q. Zhou, and B.J. Kennedy, *Synchrotron X-ray diffraction study of the $Ba_{1-x}Sr_xSnO_3$ solid solution.* Journal of Solid State Chemistry, 2013. **200**(0): p. 241-245.

25. Kostogloudis, G.C., N. Vasilakos, and C. Ftikos, *Preparation and characterization of $Pr_{1-x}Sr_xMnO_{3\pm\delta}$ (x = 0, 0.15, 0.3, 0.4, 0.5) as a potential SOFC cathode material operating at intermediate temperatures (500–700 °C).* Journal of the European Ceramic Society, 1997. **17**(12): p. 1513-1521.

26. von Helmolt, R., et al., *Giant negative magnetoresistance in perovskitelike $La_{2/3}Ba_{1/3}MnO_x$ ferromagnetic films.* Physical Review Letters, 1993. **71**(14): p. 2331-2333.

27. Wolfman, J., et al., *Increase ofTNup to 190 K in the Type II CMR Manganite $Pr_{1/2}Sr_{1/2}MnO_3$.* Journal of Solid State Chemistry, 1996. **123**(2): p. 413-416.

28. Hemberger, J., et al., *Magnetic properties and specific heat of $RMnO_3$ (R=Pr, Nd).* Physical Review B, 2004. **69**(6): p. 064418.

29. Zhang, T., et al., *Nanometer size effect on the structure and magnetic properties of high oxygen content ferromagnetic $PrMnO_{3+\delta}$ nanoparticles.* Journal of Applied Physics, 2010. **108**(11): p. 113901-6.

30. Hassen, A., *A comparative study between $Pr_{1-x}Sr_xMnO_3$ and $Pr_{1-x}Ca_xMnO_3$ at $0 \leqslant x \leqslant 0.30$.* Journal of the Korean Physical Society, 2008. **52**: p. 98.

31. Mahato, R.N., et al., *Large magnetic entropy change in nanocrystalline $Pr_{0.7}Sr_{0.3}MnO_3$.* Journal of Applied Physics, 2010. **107**(9): p. 09A943-3.

32. Hcini, S., et al., *Size mismatch, grain boundary and bandwidth effects on structural, magnetic and electrical properties of $Pr_{0.67}Ba_{0.33}MnO_3$ and $Pr_{0.67}Sr_{0.33}MnO_3$ perovskites.* Journal of Alloys and Compounds, 2011. **509**(5): p. 1394-1400.

33. Jirak, Z., et al., *Magnetic ground states in $Pr_{1-x}Sr_xMnO_3$ (x = 0.48 - 0.75).* Journal of Applied Physics, 2001. **89**(11): p. 7404-7406.

34. Knížek, K., et al., *Structure, Magnetism, and Transport Properties of $Pr_{1-x}Sr_xMnO_3$ (x = 0.45−0.75) up to 1200 K.* Chemistry of Materials, 2004. **16**(6): p. 1104-1110.

35. Ritter, C., et al., *A New Monoclinic Perovskite Allotype in $Pr_{0.6}Sr_{0.4}MnO_3$.* Journal of Solid State Chemistry, 1996. **127**(2): p. 276-282.

36. Boujelben, W., et al., *Neutron diffraction, NMR and magneto-transport properties in the $Pr_{0.6}Sr_{0.4}MnO_3$ perovskite manganite.* Journal of Alloys and Compounds, 2002. **334**(1–2): p. 1-8.

37. Llobet, A., et al., *Tetragonal to monoclinic transition in the metallic antiferromagnet $Pr_{0.5}Sr_{0.5}MnO_3$.* Physical Review B, 1999. **60**(14): p. R9889-R9892.

38. Damay, F., et al., *Structural transitions in the manganite $Pr_{0.5}Sr_{0.5}MnO_3$.* Journal of Magnetism and Magnetic Materials, 1998. **184**(1): p. 71-82.

39. Raveau, B., M. Hervieu, and A. Maignan, *Comment on "Tetragonal to monoclinic transition in the metallic antiferromagnet $Pr_{0.5}Sr_{0.5}MnO_3$".* Physical Review B, 2000. **62**(10): p. 6820-6821.

40. Frontera, C., et al., *Reply to "Comment on 'Tetragonal to monoclinic transition in the metallic antiferromagnet $Pr_{0.5}Sr_{0.5}MnO_3$'".* Physical Review B, 2000. **62**(10): p. 6822-6824.

41. Hervieu, M., et al., *Structural and Magnetotransport Transitions in the Electron-Doped $Pr_{1-x}Sr_xMnO_3$ ($0.85 \leqslant x \leqslant 1$) Manganites.* Chemistry of Materials, 2000. **12**(5): p. 1456-1462.

42. Chmaissem, O., et al., *Relationship between structural parameters and the Néel temperature in $Sr_{1-x}Ca_xMnO_3$ ($0<x<1$) and $Sr_{1-y}Ba_yMnO_3$ ($y<0.2$).* Physical Review B, 2001. **64**(13): p. 134412.

43. Søndenå, R., et al., *Electronic structure and magnetic properties of cubic and hexagonal $SrMnO_3$.* Physical Review B, 2006. **74**(14): p. 144102.

44. Chen, P., Y.W. Du, and G. Ni, *Low-field magnetocaloric effect in $Pr_{0.5}Sr_{0.5}MnO_3$.* EPL (Europhysics Letters), 2000. **52**(5): p. 589.

45. Bingham, N.S., et al., *Magnetocaloric effect and refrigerant capacity in charge-ordered manganites.* Journal of Applied Physics, 2009. **106**(2): p. 023909-5.

46. Repaka, D.V.M., et al., *Magnetocaloric effect and magnetothermopower in the room temperature ferromagnet $Pr_{0.6}Sr_{0.4}MnO_3$.* Journal of Applied Physics, 2012. **112**(12): p. 123915-9.

47. P. Dordor, E. Marquestaut, and G. Villeneuve, *Dispositif de mesures du pouvoir thermoélectrique sur des échantillons très résistants entre 4 et 300 K.* Rev. Phys. Appl. (Paris) 1980. **15**: p. 1607.

48. Rodríguez-Carvajal, J., *Recent advances in magnetic structure determination by neutron powder diffraction.* Physica B: Condensed Matter, 1993. **192**(1–2): p. 55-69.

49. Wills, A.S., *A new protocol for the determination of magnetic structures using simulated annealing and representational analysis (SARAh).* Physica B: Condensed Matter, 2000. **276–278**(0): p. 680-681.

50. P. Dordor, et al., *Dispositif automatique de mesures de résistivité entre 4 et 1 100 K.* Rev. Phys. Appl. (Paris), 1985. **20**: p. 795.

51. Tan, T.-Y., et al., *Valence changes of manganese and structural phase transitions in $Sr_{1-x}Pr_xMnO_3$ ($0.1 \leqslant x \leqslant 0.6$).* Journal of Solid State Chemistry, 2013. **201**(0): p. 115-127.

52. C. J. Howard and H.T. Stokes, *Group-Theoretical Analysis of Octahedral Tilting in Perovskites.* Acta Crystallographica B, 1998. **54**: p. 782-789.

53. Christopher J. Howard and H.T. Stokes, *Structures and phase transitions in perovskites - a group-theoretical approach.* Acta Crystallographica B, 2004. **61**: p. 93-111.

54. Paraskevopoulos, M., et al., *Magnetic properties and the phase diagram of $La_{1-x}Sr_xMnO_3$ for x ⩽0.2.* Journal of Physics: Condensed Matter, 2000. **12**(17): p. 3993.

55. Sun, Y., W. Tong, and Y. Zhang, *Large magnetic entropy change above 300 K in $La_{0.67}Sr_{0.33}Mn_{0.9}Cr_{0.1}O_3$.* Journal of Magnetism and Magnetic Materials, 2001. **232**(3): p. 205-208.

56. Fan, J., et al., *Magnetic and magnetocaloric properties of perovskite manganite $Pr_{0.55}Sr_{0.45}MnO_3$.* Physica B: Condensed Matter, 2011. **406**(11): p. 2289-2292.

57. Bhatt, R.C., et al., *Impact of sintering temperature on room temperature magneto-resistive and magneto-caloric properties of $Pr_{2/3}Sr_{1/3}MnO_3$.* Journal of Alloys and Compounds, 2013. **580**(0): p. 377-381.

58. Wolfman, J., et al., *Low temperature magnetic and transport anisotropy in $Pr_{0.7}Sr_{0.3}MnO_3$: The magnetostriction scenario.* Journal of Applied Physics, 2000. **87**(9): p. 6752-6754.

59. Patra, M., et al., *Anisotropic Magnetocaloric Effect in Single-crystalline $Pr_{0.52}Sr_{0.48}MnO_3$.* Journal of Superconductivity and Novel Magnetism, 2011. **24**(1-2): p. 775-777.

60. Marcos, J., et al., *Magnetic field induced entropy change and magnetoelasticity in Ni-Mn-Ga alloys.* Physical Review B, 2002. **66**(22): p. 224413.

Supplementary Table 1: Structural parameters, reliability factors from the refinements on room temperature lab x-ray diffraction patterns for compounds under study of the series $Pr_{1-x}Sr_xMnO_3$.

Composition	X=0.45		X=0.42		X=0.40			X=0.37			0=0.34		X=0.30	X=0.25
Space group	***Imma***	***I4/mcm***	*Imma*	*Pnma*	*Pnma*	*Imma*	*I4/mcm*	*Pnma*	*Imma*	*I4/mcm*	*Pnma*	*Imma*	*Pnma*	*Pnma*
Phase fractions (%)	94.82	5.18	93.05	6.95	36.67	56.99	6.95	75.5	12.24	12.25	92.66	7.34	100	100
Wavelength	1.5406 Å													
a (Å)	5.484	5.406	5.486	5.462	5.451	5.485	5.4061	5.447	5.464	5.461	5.452	5.468	5.461	5.474
b (Å)	7.655		7.666	7.687	7.696	7.667		7.695	7.737		7.706	7.744	7.72	7.733
c (Å)	5.440	7.783	5.441	5.4835	5.4845	5.444	7.7416	5.486	5.483	7.662	5.485	5.482	5.484	5.484
Volume (Å^3)														
D†	*0.466*	--	*0.446*	0.297	0.306	*0.423*	--	0.338	*0.123*	--	0.277	*0.092*	0.192	0.102
Pr/Sr	0.00	0.00	0.00	0.0146	0.208	0	0.00	0.14	0	0.00	0.016	0	0.021	0.022
x y z	0.25	0.5	0.25	0.25	0.25	0.25	0.50	0.25	0.25	0.50	0.25	0.25	0.25	0.25
	0.498	0.25	0.496	0.525	0.504	0.507	0.25	0.501	0.499	0.25	0.504	0.499	0.504	0.453
Mn	0 0 0	0 0 0	0 0 0	0 0 0	0 0 0	0 0 0	0 0 0	0 0 0	0 0 0	0 0 0	0 0 0	0 0 0	0 0 0	0 0 0
O1 – apical	0.00	0.00	0.00	0.859	0.998	0.00	0.00	0.999	0	0.00	0.992	0.000	0.997	0.993
	0.25	0.00	0.25	0.25	0.25	0.25	0.25	0.25	0.25	0.25	0.25	0.25	0.25	0.25
	0.953	0.25	0.974	0.951	0.0998	0.956	0.9924	0.045	0.966		0.057	0.991	0.064	0.08
O2 –	0.25	0.211	0.25	0.178	0.292	0.25	0.25	0.214	0.25	0.215	0.219	0.25	0.223	0.285
equatorial	0.482	0.711	0.484	0.445	0.529	0.467	0.469	0.529	0.426	0.715	0.534	0.583	0.528	0.478
	0.25	0.00	0.25	0.187	0.253	0.25	0.25	0.260	0.25	0.00	0.264	0.25	0.262	0.277
χ^2	1.65		1.54		3.24			1.98			2.33		2.08	2.47
Rp	5.20		5.08		6.69			5.20			5.97		5.09	6.79
Rwp	6.79		6.54		9.11			7.06			8.00		7.61	9.13

†Orthorhombic deformation, $D = \frac{1}{3}\sum_{i=1}^{3}|(a_i - \bar{a})/\bar{a}| \times 100\,; with\ a_1 = a; a_3 = b/\sqrt{2}\,; a_3 = c;\ \bar{a} = \left(abc/\sqrt{2}\right)^{1/3}$

Supplementary Table 2: Nuclear structure parameters and reliability factors for the refinements on neutron diffraction patterns at 393 K for $Pr_{1-x}Sr_xMnO_3$.

Composition	X=0.45	X=0.42	X=0.4		X=0.34	X=0.25
Space group	*Imma*	*Imma*	*Pnma*	*I4/mcm*	*Pnma*	*Pnma*
Phase fractions (%)	100	100	99.11	0.89	100	100
Wavelength	1.36 Å	1.225 Å	1.494 Å			
a (Å)	5.451 (6)	5.440 (4)	5.449 (7)	5.414 (3)	5.451 (2)	5.459 (2)
b (Å)	7.677 (9)	7.667 (8)	7.685 (11)	5.414 (4)	7.704 (3)	7.742 (1)
c (Å)	5.491 (6)	5.483 (4)	5.487 (7)	7.735 (4)	5.486 (2)	5.489 (2)
Volume ($Å^3$)	*229.79*	228.7	229.77	226.69	230.38	231.7
Pr/Sr x	0.021 (8)	0.019 (18)	0.009 (7)	0.00	0.013 (5)	0.026 (6)
y	0.25	0.25	0.25	0.50	0.25	0.25
z	0.508 (5)	0.498 (12)	0.502 (7)	0.25	0.502 (4)	0.503 (7)
Mn	0 0 0	0 0 0	0 0 0	0 0 0	0 0 0	0 0 0
O1	0.00	0.00	0.998 (5)	0.00	0.995 (5)	0.990 (7)
	0.25	0.25	0.25	0.00	0.25	0.25
	0.999 (5)	0.9948 (8)	0.056 (7)	0.25	0.057 (3)	0.066 (6)
O2	0.25	0.25	0.235 (9)	0.224 (11)	0.231 (3)	0.224 (4)
	0.45 (3)	0.58 (10)	0.528 (12)	0.725 (8)	0.530 (1)	0.533 (2)
	0.25	0.25	0.261 (3)	0.00	0.269 (2)	0.277 (4)
χ^2	13.6	3.14	2.80		1.79	1.60
Rp	5.78	2.95	5.11		4.89	2.85
Rwp	8.53	3.86	6.61		6.36	3.63

Supplementary Table 3: Nuclear structural parameters, reliability factors for the refinements on synchrotron diffraction patterns at different temperature for $Pr_{0.55}Sr_{0.45}MnO_3$

Temperature	2 K		30 K		75 K		393 K
Space group	I4/mcm	Pnma	I4/mcm	Pnma	I4/mcm	Pnma	*Imma*
Phase fractions (%)	91.11	8.89	89.99	10.01	88.42	11.58	100
Wavelength	1.36 Å on ***D20***						
a (Å)	5.404 (1)	5.439 (3)	5.4037	5.442	5.4035	5.442	5.451 (6)
b (Å)	5.404 (1)	7.674 (3)	5.4037	7.654	5.4035	7.658	7.677 (9)
c (Å)	7.796 (3)	5.473 (5)	7.796	5.479	7.7939	5.479	5.491 (6)
Volume ($Å^3$)	*227.71*	*228.46*	*227.65*	*228.24*	*227.7*	*228.39*	*229.79*
Pr/Sr x	0.00	0.02 (8)	0.00	0.024	0.00	0.025	0.021 (8)
y	0.5	0.25	0.5	0.25	0.5	0.250	0.25
z	0.25	0.504 (8)	0.25	0.502	0.25	0.504	0.508 (5)
Mn	0 0 0	0 0 0	0 0 0	0 0 0	0 0 0	0 0 0	0 0 0
O1	0.00	0.016 (5)	0.00	0.0089	0.00	0.0087	0.00
	0.00	0.25	0.00	0.25	0.00	0.25	0.25
	0.25	0.054 (6)	0.25	0.057	0.25	0.058	0.999 (5)
O2	0.21 (2)	0.238 (2)	0.21	0.233	0.21	0.233	0.25
	0.71 (4)	0.523 (6)	0.71	0.523	0.71	0.524	0.45 (3)
	0.00	0.274 (2)	0.00	0.273	0.00	0.274	0.25
Mtot	3.52	3.77	3.39	3.75	3.363	3.68	--
χ^2	9.14		12.3		11.7		13.6
Rp	5.50		5.08		4.79		5.78
Rwp	7.33		6.71		6.59		8.53

Supplementary Table 4: Nuclear and magnetic structure parameters, reliability factors for the refinements on neutron diffraction patterns at 10 K for $Pr_{1-x}Sr_xMnO_3$ (0.25≤x≤0.45).

Composition	X=0.45 at 2 K		X=0.42		X=0.4		X=0.34	X=0.25
Space group	*I4/mcm*	*Pnma*	*I4/mcm*	*Pnma*	*I4/mcm*	*Pnma*	*Pnma*	*Pnma*
Phase fractions (%)	91.11	8.89	85.27	14.73	44.41	55.59	100	100
Wavelength	1.36 Å		1.225 Å		1.8857 Å		1.494 Å	
a (Å)	5.404	5.439	5.400	5.441	5.396	5.440	5.437	5.434
b (Å)	5.404	7.674	5.400	7.646	5.396	7.675	7.69	7.71
c (Å)	7.796	5.473	7.787	5.479	7.82	5.471	5.47	5.475
Volume ($Å^3$)	227.71	*228.46*	227.07	227.98	226.73	228.59	228.45	228.39
Pr/Sr x	0.00	0.02	0.00	0.011	0.00	0.019	0.016	0.026
y	0.5	0.25	0.50	0.25	0.50	0.25	0.25	0.25
z	0.25	0.504	0.25	0.505	0.25	0.498	0.502	0.503
Mn	0 0 0	0 0 0	0 0 0	0 0 0	0 0 0	0 0 0	0 0 0	0 0 0
O1	0.00	0.016	0.00	0.01	0.00	0.016	0.993	0.99
	0.00	0.25	0.00	0.25	0.00	0.25	0.25	0.25
	0.25	0.054	0.25	0.067	0.25	0.06	0.058	0.066
O2	0.21	0.238	0.21022	0.265	0.2115	0.229	0.227	0.22
	0.71	0.523	0.71022	0.521	0.7115	0.529	0.531	0.533
	0.00	0.274	0.00	0.234	0.00	0.269	0.272	0.277
Mtot	3.52	3.77 [C]	3.55	3.73 [C]	3.55	3.73 [C]	3.46	3.334
χ^2	9.14		8.72		3.85		1.84	1.94
Rp	5.50		5.31		4.98		5.03	3.1
Rwp	7.33		6.73		6.79		6.58	4.0

[C] – *Canted ferromagnetic alignment*

Chapter 5

General Conclusion and perspectives

Magnetocaloric materials are growing important in view of the technological transfer with increasing number of refrigerators put forward each year (Figure 1 a) [1]. At the same time MCM's keep offering fascinating interest for the material scientist through their unique properties. In this thesis, second chapter address factors close to the first point while following two chapters address some more fundamental aspect such as structure, microstructure and magnetic properties relations.

In general, a satisfactory study to understand basic problems that might arise due to interaction of thermal transport fluid on working material was carried out. Even if we did not adapt the used thermal fluid flow rate to those that can find on prototypes Detailed studies of microstructural changes of the MCM $Gd_6Co_{1.67}Si_3$ using EPMA, Auger spectroscopy are presented.The explanation of corrosion-erosion process is justified on basis of spontaneous electrochemical reaction of constituent element with the fluid. Such reactions result in a micron size core-shell of $SiO_{2\pm\delta}$–Gd_2O_3 self-coating on top of pristine/virgin sample. Interestingly, the magnetic measurements and entropy change calculated from these measurements did not show difference between aged and virgin sample. As the magnetization measurements are made on bulk samples, it is necessary to use more appropriate and sensitive methods (surface sensitive magnetization, thermal conductivity) to better probe effect of such corrosion on physical properties.The possibility of reducing the corrosionby changing the pH of the transport fluid was also demonstrated.

Concerning the ageing of the magnetocaloric materials discussed within this thesis, what we have demonstrated here is one of the key factors that would influence the performance of magnetocaloric material in complete working conditions. To evaluate potential MCM's it is necessary to test them for stability and performance reproducibility under effect of different parameters such as applied field, temperature, fluid flow rate/pressure and so on. To accomplish such systematic studies it becomes obvious to design prototype/unit close to real working unit. Such tasks further involve multidisciplinary expertise, but can result to more realistic problem and possibly leading to address solutions in much effective way. In case of the studies on ageing in thermal transport fluids there were few trials exploring the possibility of surface protection by coating the MCM with other material such as gold. Even though such attempts resulted in protecting the MCM for time being, later with time the coating itself accelerate the corrosion. Based on results from our studies we believe that the preferable materials for surface coating of any MCM should satisfy (i) high reduction potential with working fluid as well as working material (MCM) along with well-known factors of (ii) high thermal conductivity and (iii) transparent to the magnetic field.

In third chapter, conditions for reproducibility of the giant magnetocaloric effect are addressed by studying in detail the effect of composition and synthesis conditions on the resulting magnetocaloric effect shown by Heusler phase derived materials. Structural deviation from non-modulated structure (cubic or tetragonal) to modulated structure (monoclinic or orthorhombic) due to the off stoichiometry of the composition is also presented. The effect played by the microstrain artificially introduced during grinding of the sample on magnetic, structural and magnetocaloric properties was demonstrated. One of the selected Heusler compositions showed good resistance to the flux of heat transport fluid during our preliminary ageing experiments. These results are promising as the stability of the material during performance is the key factor when realizing the material in devices.

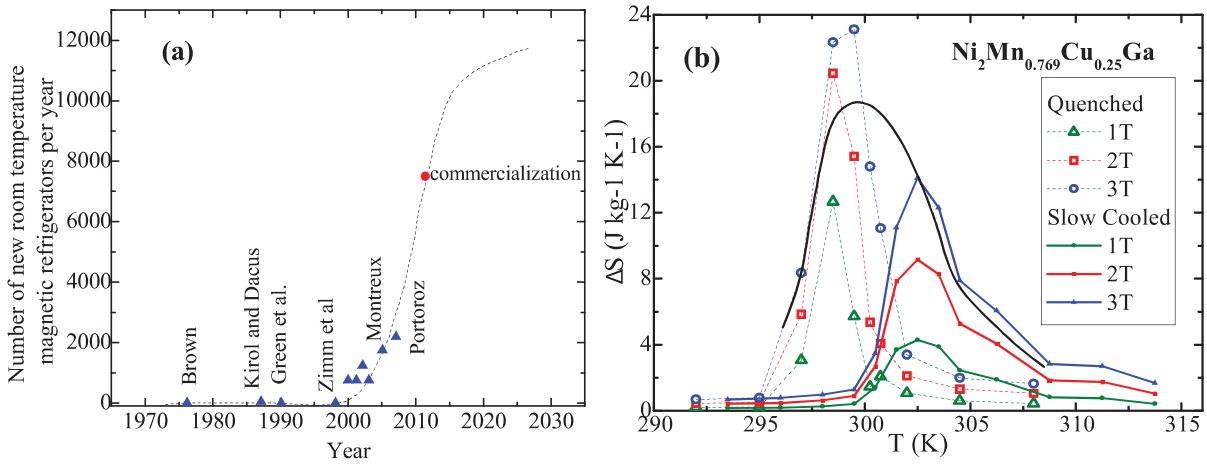

Figure 1: (a) Number of new room temperature magnetocaloric refrigeration per year [1]. (b) Expected performance of the two magnetocaloric materials with nearby magnetic transition.

One of the major issues with materials exhibiting first order transition, as we see in Heusler alloys, is narrow operating temperature interval. Due to their sharp transition the observed entropy change/cooling effect is limited to very small temperature range (3 to 4 °C) which can be disadvantage when it is necessary to operating under wider temperatures (25 to 40 °C) in realistic applications. However, it has been numerically predicted and demonstrated that one can stack the materials with close transition and obtain wider operating temperatures [2, 3]. For example let us consider $Ni_2Mn_{0.769}Cu_{0.25}Ga$, the quenched and slow cooled samples show, the entropy change ΔS =23 and 14.05 $Jkg^{-1}K^{-1}$ respectively and the corresponding RCP = 76.13 and 55.36 Jkg^{-1} (for ΔH = 3 T). However by coupling these two samples one should expect the resulting entropy curve to trace black line in Figure 1 b (just approximation actual

results are subject to change). This new curve then should exhibit the entropy change of 18.6 $Jkg^{-1}K^{-1}$ and RCP of 124.4 Jkg^{-1}which can increase the interest of the material.

Detailed and comprehensive nuclear and magnetic structure phase diagram for $Pr_{1-x}Sr_xMnO_3$ ($0.25 \leq x \leq 0.45$), based on qualitative analysis of neutron powder diffraction as well as results from dc magnetometer is presented in chapter 4. A convergence between both the probes is observed. Such results also further lead to a complete phase diagram for the metallic-ferromagnet ($0.25 \leq x \leq 0.45$) characterized with modest near room temperature magnetocaloric effect. Initial glimpse of the ageing are presented, however, more detailed studies which are in progress at the time of writing of this thesis will help better understand the initial results. Up to date, an electrocatalytic conversion of CO_2 is proposed to explain the carbone shell around the manganties. For oxide based materials, even though the series that is presented with in the context of this thesis, $Pr_{1-x}Sr_xMnO_3$ is a moderate choice. One cannot ignore possibility of better material with improved magnetocaloric figure of merits as well as stability. Towards which regard it gives opportunities for the scientists to explore and propose new material satisfying all or most of the critical figure of merits demanded for an ideal magnetocaloric material.

One of the issues that should be addressed for any device application based material is the reproducibility along with consistency of the properties with number of operating cycle or often addressed withterm*cycling*. In real operating magnetocaloric system, material is demanded to withstand cycling with variation of temperature, field, and so on. We have made one of the attempts in this regard to verify the reproducibility of the material property with temperature cycling. Considering the fact the entropy of the material can also be evaluated from DSC measurements, as discussed in section 1.3.1 of chapter 1. And exploring the advantage of cycling the temperature with wide range of sweep rate (2°C/min to 20°C/min) on our DSC instrument we perform cycling test on our samples for 20 to 50 cycles. Figure 2 (a to c) summarizes the results from the temperature cycling on three different class of material that were studied during course of the thesis i.e., $Gd_6Co_{1.67}Si_3$ (Figure 2 a) $Ni_2Mn_{0.75}Cu_{0.25}Ga$ (Figure 2 b), and $Pr_{0.66}Sr_{0.34}MnO_3$ (Figure 2 c). It is clear that the entropy change during cycling in case of Heusler looks much disturbed during heating while is converged and smooth for cooling. DSC curves on $Gd_6Co_{1.67}Si_3$ trace same path even up to 35 cycles, suggesting the consistent reproducibility of the entropy change in this compound. DSC curves on perovskite oxide show two peaks while heating, broad prominent one signifying the second order magnetic transition (T_C), secondary small peak just above T_C. These peaks can be assigned to the two peaks observed on the ac-susceptibility measurements (T_{C1}, T_{C2})

presented in chapter 4. There is no change or noise on first peak for complete set of 17 cycles, while the secondary peak moves randomly with each cycle. Comparing this effect with one on Heusler we propose the secondary peak to be associated with some structural phase transition/transformation. Even though this small peak may affect the total entropy change, comparing with the magnitude of the effect of magnetic transition it can be neglected. From these tests we conclude that the properties of Gd-based intermetallics and manganese based perovskites with second order transition are much precisely reproducible compared to Heusler compounds with first order transition.

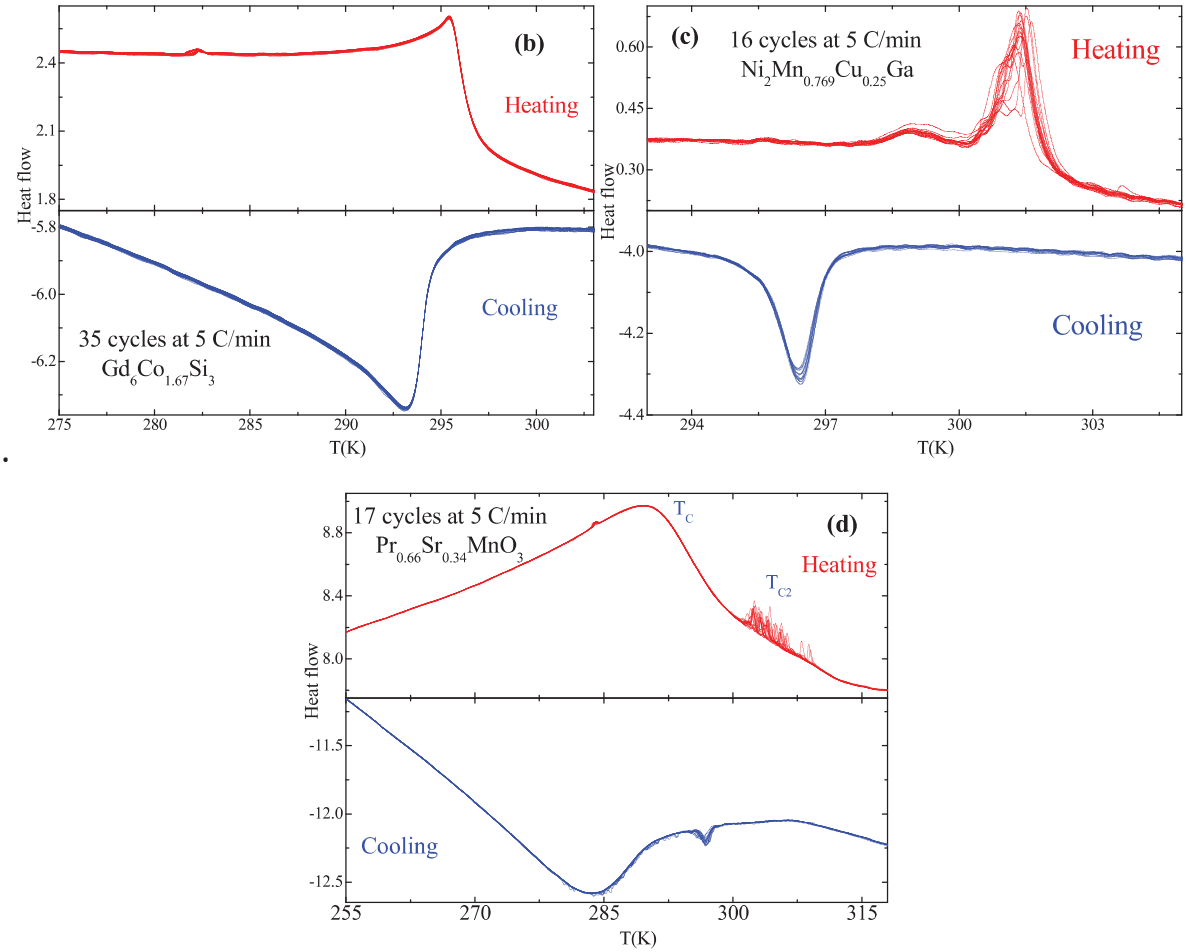

Figure 2 Continuous cycling of DSC curves at rate of 5 °/min for (a)) Gd-based $Gd_6Co_{1.}$, (b $_{67}Si_3$Heusler phase and (c) $Pr_{0.66}Sr_{0.34}MnO_3$.

5.1. References :

1. Gschneidner Jr, K.A. and V.K. Pecharsky, *Thirty years of near room temperature magnetic cooling: Where we are today and future prospects.* International Journal of Refrigeration, 2008. **31**(6): p. 945-961.
2. R. Caballero-Flores, et al., *Magnetic Multilayers as a Way to Increase the Magnetic Field Responsiveness of Magnetocaloric Materials.* Journal of Nanoscience and Nanotechnology, 2012. **12**: p. 7432.
3. Jian Liu, et al., *Giant magnetocaloric effect driven by structural transitions.* Nature Materials, 2013. **11**: p. 620.

Appendix

Appendix A. Acronyms scientific terms, symbols and miscellaneous

ABO_3 – General formula of Perovskite

COP – Coefficient of performance

et al. – and others; et (and) alii (others) – from latin

ICMCB –Institut de Chimie de la MatièreCondensée de Bordeaux, Pessac, France

ILL –Institut Laue-Langevin, Grenoble, France

IUPAC – International Union of Pure and Applied Chemistry

LLB –Laboratoire Léon Brillouin, Saclay, France

LNS –Laboratory for Neutron Scattering, PSI, Switzerland

MCE – MagnetoCaloric Effect

MCM – MagnetoCaloric Materials

PSI – Paul Scherrer Institute, Switzerland

RCP –Relative Cooling power

RC – RefrigerantCapacity

SINQ – The Swiss Spallation Neutron Source, PSI, Switzerland

SLS– Swiss Light Source, PSI, Switzerland

T_C – Curie temperature

T_{MI} – Metal to insulator transition

XYZ – General form for half Heusler

X_2YZ – Heusler phase

ΔS – Entropy change

ΔT – adiabatic temperature change

ΔH – Change in applied magnetic field

Appendix B. Acronyms for fewjournals

Acta Mater – ActaMaterialia

Adv Mater – Advanced Materials

ApplPhysLett – Applied Physics Letters

Chem Mater – Chemistry of Materials

EurophysLett – Europhysics Letters

Int J Refrig – International Journal of Refrigeration

J Alloys Comp – Journal of Alloys and Compounds

J Am Ceram Soc – Journal of the American Ceramic Society

J ApplPhys –Journal of Applied Physics

J KorPhysSoc – Journal of Korean Physical Society

JMagnMagnMater – Journal of Magnetism and Magnetic Materials

J NanosciNanotechnol – Journal of Nanoscience and Nanotechnology

J Phys:Condens Matter – Journal of Physics: Condensed Matter

J PhysSocJpn -Journal of the Physical Society of Japan

J Sol Stat Chem – Journal of Solid State Chemistry

J Supercond Nov Magn – Journal of Superconductivity and Novel Magnetism

Mater Res Bull –Materials Research Bulletin

Mater Lett– Materials Letter

Nat Mater – Nature Materials

Phys Rev – Physical Review

Phys Rev B – Physical Review B

Phys Rev Lett – Physical Review Letters

Rev Mod Phys – Reviews of Modern Physics

Rep ProgPhys–Reports on Progress in Physics

Rev SciInstrum – Review of Scientific Instruments

Scri Mater – ScriptaMaterialia

ScrMetall Mater - ScriptaMetallurgicaetMaterialia

Solid State Comm –Solid State Communications

Z anorgallgChem - Zeitschriftfűranorganischeund allgemeineChemie

Appendix C. Conferences and Symposiums

C.1. 18th International Conference on Solid Compounds of Transition Elements – SCTE 2012, Lisbanne, Portugal, 1st to 5th of April, 2012**.** *Oral contribution:* ***"Microstructure analysis of ageing of magnetocaloric materials"***http://scte2012.itn.pt/

C.2. **Journées de l'EcoleDoctorale des Sciences Chimiques,** Université Bordeaux 1, Talence, 12th and 13th April, 2012.*Poster contribution:* **"Magnetoaloric materials – ageing and structural studies"***http://www.edsc.u-bordeaux1.fr/index.php/*

C.3. IECB Young Scientist Symposium 2012, IECB, Bordeaux, 21st and 22nd of May, 2012. *Oral contribution:****"Structural, magnetic, and magnetocaloric investigations for ferromagnet-metals*** $Pr_{1-x}Sr_xMnO_3$ ***(0.3≤x≤0.45)"****http://www.iecb.u-bordeaux.fr/jjc/*

C.4. 4th International symposium on structure property relations in solid state materials, ICMCB, Bordeaux, 24th to 29th of June, 2012**.** *Poster contribution: "****Phase transition along with magnetic and transport transitions in ferromagnet metals*** $Pr_{1-x}Sr_xMnO_3$ ***(0.25≤x≤0.45)****"http://www.spssm4.com/*

C.5. **Project MAGCOOL (Stock-E 2010 project ANR) meeting,** CRISMAT, Caen, France, 28th and 29th March, 2013. *Oral presentation:****"Ageing on MagnetoCaloric Materials – Microstructural Studies".****http://www.agence-nationale-recherche.fr/projet-anr/?tx_lwmsuivibilan_pi2[CODE]=ANR-10-STKE-0008*

Appendix D. School, visits for experiments

D.1. Neutron diffraction experiments on D20, Institut Laue-Langevin, Grenoble, France. 12th of October 2012.

D.2. School on Advanced Neutron Diffraction data treatment using *FULLPROF,* Institut Laue-Langevin, Grenoble, France. 23rd to 28th of January, 2012.

D.3. Neutron diffraction experiments on 3T2 and G4.1, Laboratoire Léon Brillouin, CEA, Saclay, France. 14rd to 17th of June, 2012.

D.4. Joint Synchrotron and Neutron diffraction experiments on HRPTatLNS-SINQ and**MS –X04SA** at SLS, Paul Scherrer Institute, Switzerland. 1st to 8th of August, 2012.

D.5. Neutron diffraction experiments on HRPT, LNS-SINQ, Paul Scherrer Institute, Switzerland. 23st to 28th of August, 2012.

D.6. Neutron diffraction experiments on D1B, Institut Laue-Langevin, Grenoble, France. 16 and17 of May, 2013.

Appendix E. Magnetic moments

Depending on the oxidation state/coordination/the neighboring ion each element exhibits its unique magnetic moment. Magnetic moment depends on the unpaired electrons, so more the number of unpaired electrons higher is the magnitude of moment in case of d-block metals. The other ……. Here effort to bring most of them at one place along with their electron configuration and we expect this to serve as quick hand note.

E. 1. Magnetic susceptibility (μ) associated with different oxidation of individual elements is presented in the following table. It refers to spin only moment resulting due to the spinning of unpaired electrons (d-block metal ions). The magnetic moment is expressed as $\mu_{(spin-only)} = \sqrt{n(n+2)}$ Bohr Magneton, n being the number of unpaired electrons. Another way to represent the spin-only magnetic moment is based on the electron spin quantum number (S), $\mu_{(spin-only)} = 2S(S+1)$Bohr Magneton.

Element	Config.	Moment μ_B/(f.u.)
Cobalt (Co) $Co^{2+}_{H.S.}$ $Co^{2+}_{L.S.}$ Co^{3+} Co^{4+}		 3.87 4.90
Chromium (Cr) $Cr^{2+}_{L.S.}$ $Cr^{2+}_{H.S.}$ Cr^{3+}	 $t_{2g}4$ $t_{2g}3e_g1$	 4.90 3.87
Copper (Cu) Cu^{2+}	$t_{2g}6e_g3$	1.73
Gadolinium(Gd) Gd^{3+}		
Iron (Fe) $Fe^{2+}_{L.S.}$ $Fe^{2+}_{H.S.}$ Fe^{3+}		 4.90 5.92
Fe^{4+}		
Manganese(Mn) Mn^{2+} Mn^{3+} Mn^{4+}		 5.92 4.90
Nickel (Ni) Ni^{2+} Ni^{3+} Ni^{4+}		 2.83
Praseodymium		
Vanadium (V) V^{2+} V^{3+}		 3.87 2.83

Source: http://wwwchem.uwimona.edu.jm/spectra/MagMom.html;Lecture notes-19

Table 4.7. The 3*d* ions. m_{eff} is in units of μ_B

$3d^n$		S	L	J	g	$m_{eff} = g\sqrt{J(J+1)}$	$m_{eff} = g\sqrt{S(S+1)}$	m_{eff}^{exp}
1	Ti^{3+}, V^{4+}	$\frac{1}{2}$	2	$\frac{3}{2}$	$\frac{4}{5}$	1.55	1.73	1.7
2	Ti^{2+}, V^{3+}	1	3	2	$\frac{2}{3}$	1.63	2.83	2.8
3	V^{2+}, Cr^{3+}	$\frac{3}{2}$	3	$\frac{3}{2}$	$\frac{2}{5}$	0.78	3.87	3.8
4	Cr^{2+}, Mn^{3+}	2	2	0			4.90	4.9
5	Mn^{2+}, Fe^{3+}	$\frac{5}{2}$	0	$\frac{5}{2}$	2	5.92	5.92	5.9
6	Fe^{2+}, Co^{3+}	2	2	4	$\frac{3}{2}$	6.71	4.90	5.4
7	Co^{2+}, Ni^{3+}	$\frac{3}{2}$	3	$\frac{9}{2}$	$\frac{4}{3}$	6.63	3.87	4.8
8	Ni^{3+}	1	3	4	$\frac{5}{4}$	5.59	2.83	3.2
9	Cu^{2+}	$\frac{1}{2}$	2	$\frac{5}{2}$	$\frac{6}{5}$	3.55	1.73	1.9

E. 2. Magnetic susceptibility due to superexchange, spin and orbital contributions.

Interaction	**Config.**	**Moment μ_B/(f.u.)**
Co^{3+}-O^{2-} - Fe^{3+}		
Co $^{2+}$-O^{2-}-Mn^{4+}		
AFM in plane SuperExchange Mn^{3+}-$O^{2-}$$MN^{3+}$	Half filled t_{2g}-t_{2g}	

Source: SlidesBrown.ppt

Mn^{4+}-$O^{2-}$$MN^{4+}$	d_{z2}-d_{z2}	

Appendix F. Electrochemical oxidataion

Figure 1 (Left to Right): English scientists Michael Faraday and John Frederic Daniell; German scientist Walther Nernst; Swedish chemist Svante Arrhenius

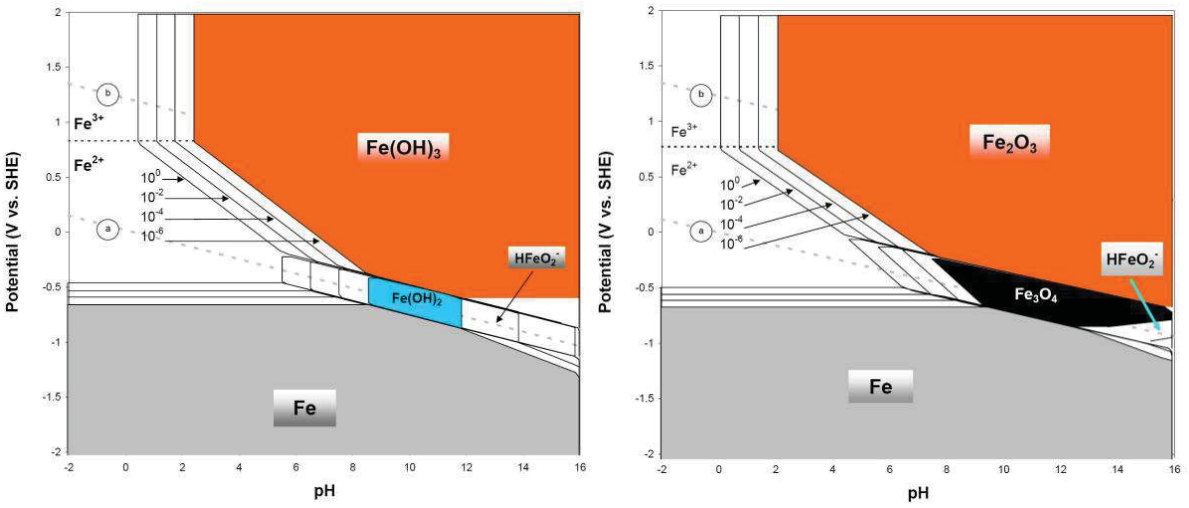

Figure 2Left:E-pH diagram of iron or steel with four concentrations of soluble species, three soluble species and two wet corrosion products (25°C). Right:E-pH diagram of iron or steel with four concentrations of soluble species, three soluble species and two dry corrosion products (25°C)

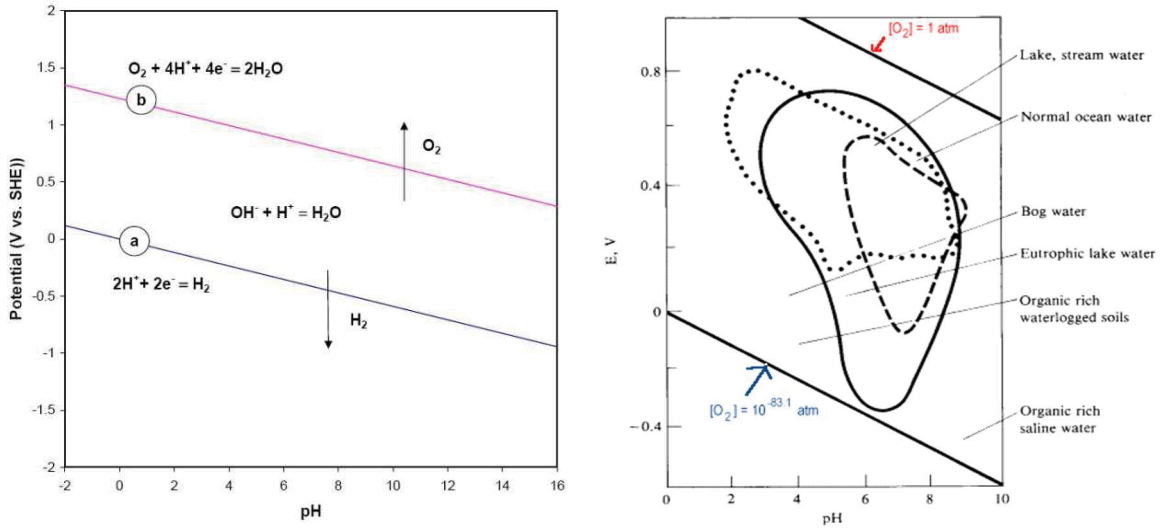

E-pH stability diagram of water at 25°C

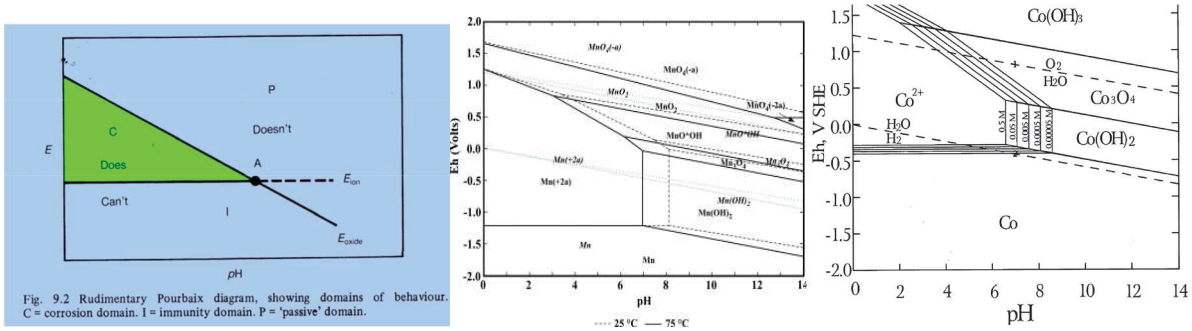

$$Mn^{2+} + H_2O = MnO_2 + 4H^+ + 2e^-$$

Reference: Materials Engineering 24, 1658 (2011)

Appendix G. Diffraction and diffractometers

F.1. X-ray diffraction, scattering:

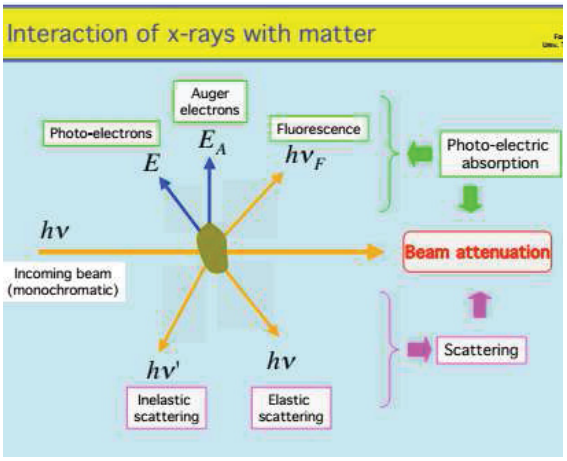

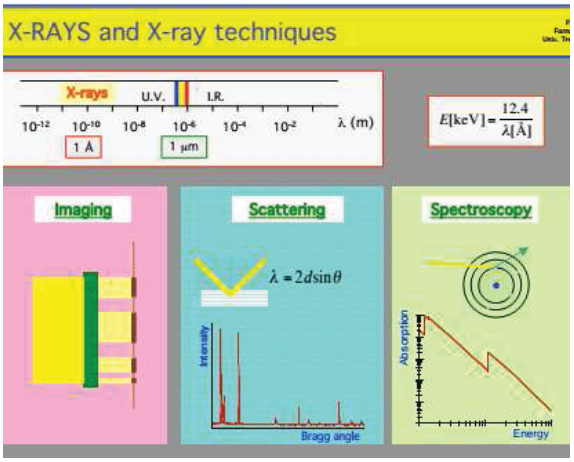

F.2. X-ray and neutron diffraction what are the differences:

What does each see?

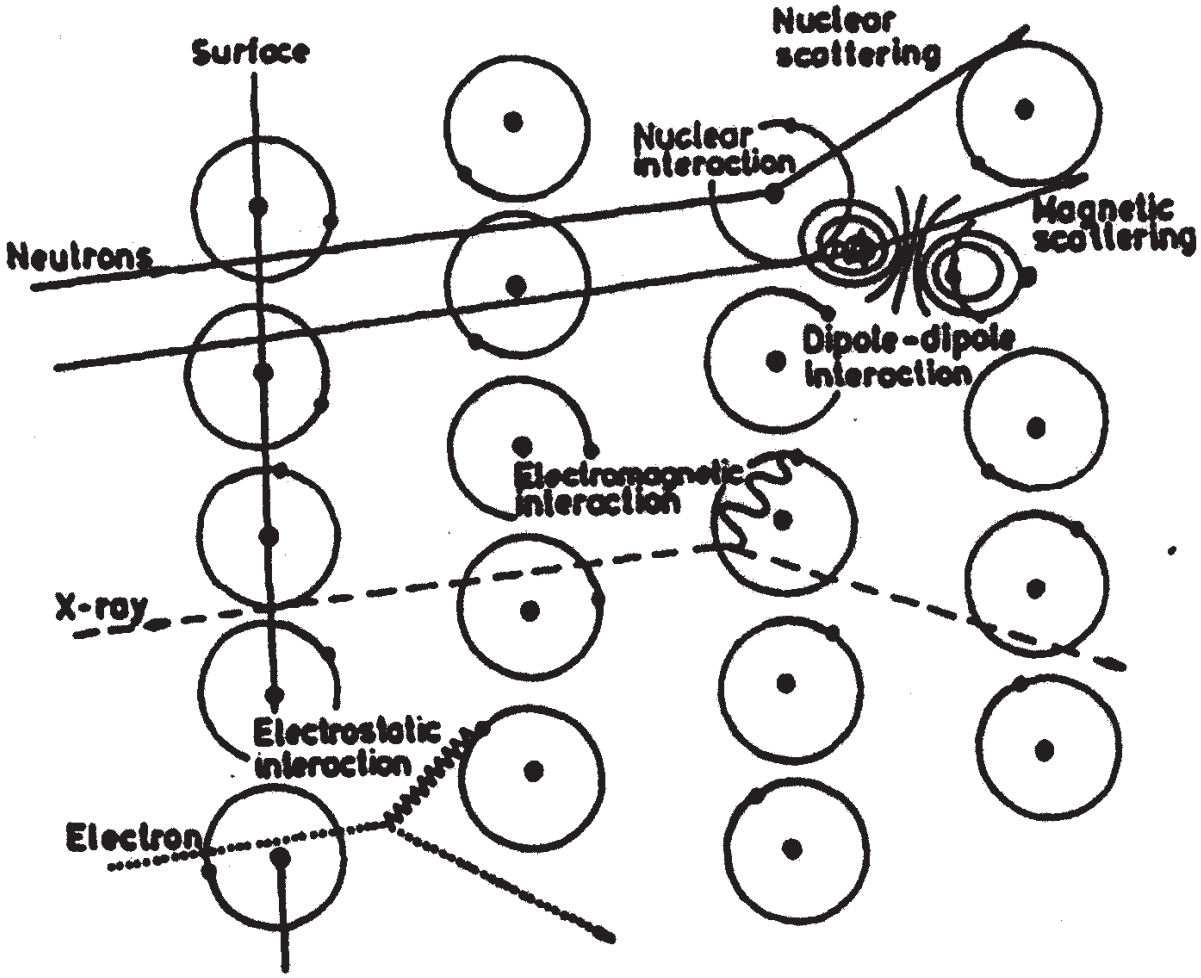

Neutron scattering length and xray scattering length-

F.3. Neutron diffraction: Nuclear and magnetic contributions- cold and thermal neutrons:

F.4. Nuclear diffractometers:

The resolution which is expressed as……. is unique and critical parameter for each diffractometer. It should be taken into account when proposing qualitative analysis. For instance, the

Refereces: http://sinq.web.psi.ch/sinq/instr/hrpt/doc/pomjakushin_magdif08_pdf.pdf

Table 1: Comparison and summary of different neutron diffractometer.

Specifications	D20	D1B	3T-2	G4-1	HRPT
Description	High-intensity two-axis diffractometer with variable resolution	High resolution neutron two-axis powder diffractometer	High resolution powder diffractometer	Cold neutron two-axis diffractometer PYRRHIAS	High-Resolution Powder diffractometer for Thermal neutrons
Location	LLB, Grenoble, France		LLB, Saclay, France		LNS, PSI, Switzerland
Type	Two-axis	Two-axis	Two-axis	Two-Axis	
Beam			thermal	cold neutron	thermal
Monochroma-tor		Pyrolytic graphite(002)‡ or Germanium (311)†	Vertically focusing Ge (335)	Pyrolytic graphite (002) vertical focus	Vertically focusing wafer Ge (hkk)
Incident wavelength		λ=2.52 Å‡ λ=1.28 Å †		2.43<λ(Å)<5.5	0.94≤λ≤2.94
Collimation			A1 variable (10', 14', 21')		Oscillating mylar-Gd_2O_3 radial
Max. beam size at specimen		5 × 2 cm^2	20 ×60 mm^2	10 × 50 mm^2	
Detectors		$^3He/CF_4$ position-sensitive detector	50 ^8He, 2.4 ° apart	Linear multidetector 800 cells (BF_3)	Position sensitive (PSD) ^3He (3.6 bar) +CF_4 (1.1 bar) detector
Angular range		128 °	5<2θ °<122	3<2θ °<105	0<2θ °<165
Typical step size			0.05°	0.02 ° (2θ)	0.05 ° or less
Max. Flux at specimen		‡6.5×$10^6$to †0.4 × 10^6ncm^{-2}s^{-1}	10^8 n cm^{-2} s^{-1}	4.10^6 n cm^{-2} s^{-1}	
Sample environment			1.5 K – 550 K or T<1000°C, P≈10^{-4}mbar	1.5K<T<500K Or T<100O °C Pressure<23bar Vertical magnet H<1.5T	80mK≤T≤1800K H = 5T (vertical) Zero matrix cells (9, 15, 100 kbar)

Appendix H. Ordering - disordering in Heusler alloys

ICSD notation	Strukturberichte (SB)	Ordering	Space group	Remark	Symm.	Superstructure reflections
Cubic systems						
Cu_2MnAl	$L2_1$	X=X`, Y, Z	*Fm-3m*	Ordered	FCC	(111) (200)
BiF_3	DO_3	X=X`=Y, Z	*Fm-3m*		BCC	(111) (200)
CsCl-type	*B2*	X=X`, Y=Z	*Pm-3m*	Partially ordered		(001)
W-type	*A2*	X=X`=Y=Z	*Fd-3m*	Random ordering		
NaTl-type	$B32_a$	X=Y, X`=Z	*Im-3m*			(111)

Ref: Graf et al, Prog Solid State Chem 39, 1 (2011)

The name *Martensite*is is associated with the german Scientist Martens.

Appendix I. Space groups: group-subgroup relations

Structural transitions can be transformations between either

(i) different symmetry (cubic – tetra, cubic – orthorhombic, tetra – orthorhombic, hexagonal-monoclinic *R-3m* to *C2/m*…)or

(ii) within the same symmetry transition between subgroup (Ex: orthorhombic-Pnma to Imma, monoclinic P2/m – C2/m…).

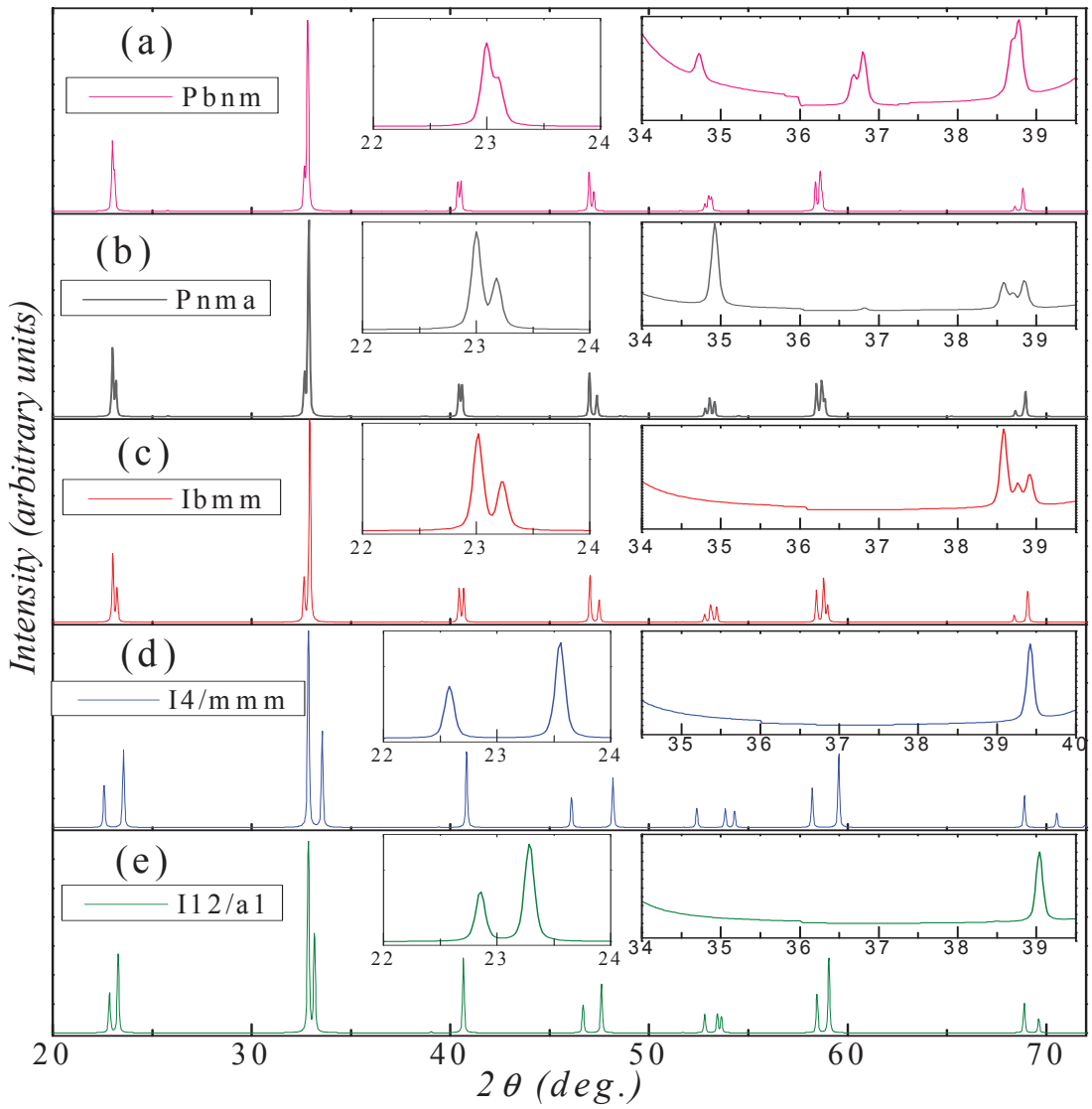

Figure 3: Calculated x-ray pattern for $Pr_{0.6}Sr_{0.4}MnO_3$ (a) at 293 K with space group *Pbnm* a=5.45, b=5.48, c=7.692 nm; (b) *Pnma* a=5.4483, b=7.6681, c=5.4786; (c) (only this pattern is for $Pr_{0.55}Sr_{0.45}MnO_3$) at 300 K space group *Ibmm* with a=5.4826, 5.4380, c=7.6417; (d) 10 K, *I4/mmm* a=5.337, b=5.337, c=7.8687 and (e) 10K, *I12/a1* a=7.7758, b=5.3981 and c=5.3975. Insets highlight the unique reflections for each space group.

Glazer Notation:

The cationic size mismatch forces the structure to distort/tilt in order to maintain the valid perovskite structure. By doing so the symmetry of the system is reduced and hence system crystallizes in different space group. Often the relations between resulting lattice constant and a given distortion of an octahedral is expressed using Galzer notations [19]. The relation between the tilting of the octahedral and the corresponding glazer notation for three crystal structures cubic Pm-3m ($a^0a^0a^0$), orthorhombic Pnma ($a^-b^+a^-$) and tetragonal I4/mcm ($a^0a^0c^-$) is demonstrated in figure below.

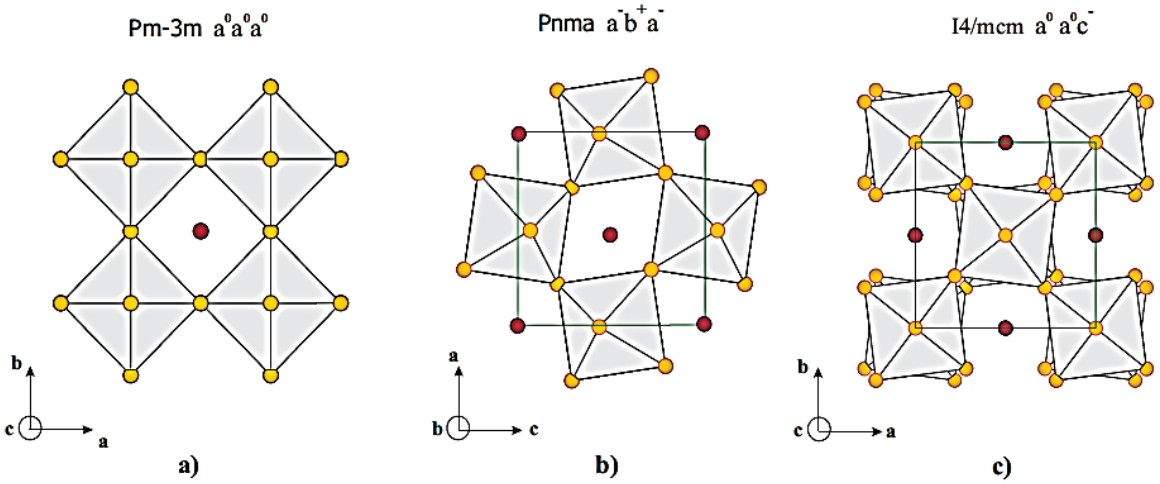

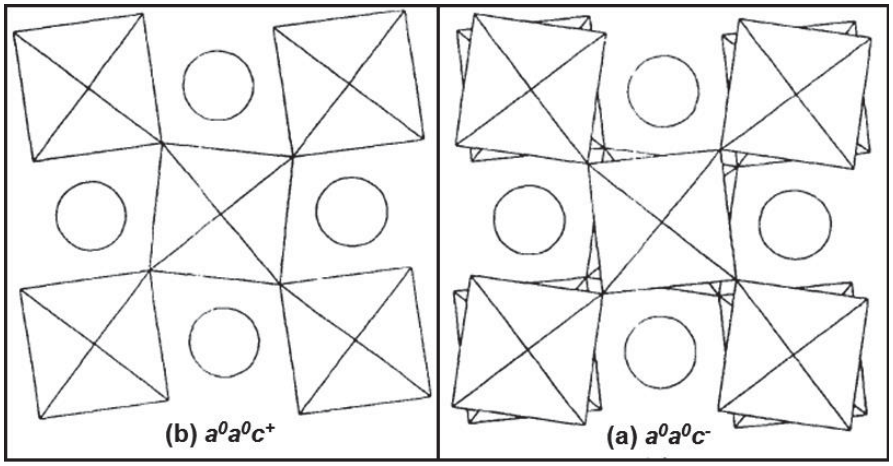

ActaCrystallogr.B **28**, 3384 (1972).

These notations of Glazer are constructed as follows: (i) the sequence of symbol indicate the axis of tilt, ex: along a-axis, (ii) identical characters indicate the same amplitude of tilt and (iii) the superscripts indicate the subsequent layers of octahedral namely zero-tilt (0), in-phase-tilt (+) and anti-phase-tilt (-). Cubic phase $a^0a^0a^0$ is known as zero-tilt system,

does not have any tilting on the structure. While in case of tetragonal structure the tilting is anti-phase on c axis, forming twisted like structure when viewed along c-axis.

The space groups Pnma and Imma crystallize in similar perovskite-like structures with unit cells defined by, $a_p\sqrt{2} \times 2a_p \times a_p\sqrt{2}$, with $a_p$being lattice parameter of the ideal perovskite unit cell. The Glazer notation for *Pnma* is $a^+b^-b^-$and for *Imma* is $a^0b^-b^-$. One major difference is the rotation of the oxygen octahedral with respect to symmetry axis of the unit cell, this is evident on their glazer notations

http://www.unf.edu/~michael.lufaso/spuds/

Here is some of the supporting information concerning the details of space group, the symmetry, glazers' notation they inherit.

x in $Pr_{1-x}Sr_xMnO_3$	Structural details for room temperature			Remark
	Space group	Glazers notation†	Symmetry, Unit cell	
0.9	*Pm-3m*	$a^0a^0a^0$	Cubic a_P=a≈3.8Å	
0.85 to 0.75	*Pm-3m + I4/mcm*	$a^0a^0a^0$+ $a^0a^0c^-$	Cubic + Tetragonal $a_P\sqrt{2}\cdot a_P\sqrt{2}\cdot a_P2$	
0.70 to 0.60	*I4/mcm with121 super lattice reflection*	$a^0a^0c^-$	Tetragonal $a_P\sqrt{2}\cdot a_P\sqrt{2}\cdot a_P2$	
0.55	*I4/mcm without 121 super lattice reflection*	$a^0a^0c^-$	Tetragonal	
0.55 to 0.475	*I4/mcm + Imma*	$a^0a^0c^-$ + $a^-b^0a^-$	Tetragonal +Orthorhombic $a_P\sqrt{2}\cdot a_P2\cdot a_P\sqrt{2}$	
0.5 to 0.6	*Imma*	$a^0b^-b^-a^-a^-c^0$	Orthorhombic $a_P\sqrt{2}\cdot a_P2\cdot a_P\sqrt{2}$	
	Ibmm			
	Pbnm	$a^+b^-b^-$		$a_P\sqrt{2}\cdot a_P\sqrt{2}\cdot a_P2$
	Pnma	$a^-b^+a^-a^-c^+$		$a_P\sqrt{2}\cdot a_P2\cdot a_P\sqrt{2}$
	I2/m	$a^0b^-c^-$		
	I2/a	$a^-a^-c^-$	Monoclinic	
	R-3c	$a^-a^-a^-$	Rhombohedra	

†J Solid State Chem 127, 276 ; Classification of tilted octahedral in perovskites, Acta Crystallographica 28, 3384

References:

Chem Mater DOI: 10.1021/cm401942t
Symmetry-raising orbital order in $PbRuO_3$, ESRF highlights (2009)
Phys Stat Sol a 85, 359 (1984)

Appendix J. Spectroscopies for surface analysis

This is an effort to bring at one place details of different spectroscopies used to characterize the microstructural and chemical state of the materials in general. Working principle, the strength and limitations of these spectroscopies, the possible alternatives or higher precisions for each of them is tabulated.

Function	Surface morphology	Depth Profile	Chemical State/ESCA
Technique	Electron probe micro-analyzer	Auger Electron Spectroscopy	X-Ray Photoelectron Spectroscopy (XPS) /UPS
History			
Principle			
Schematic representation of working unit and working principle	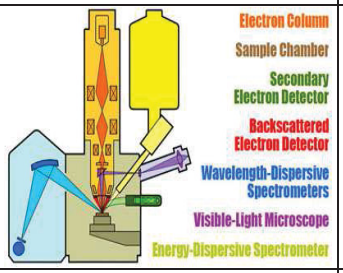	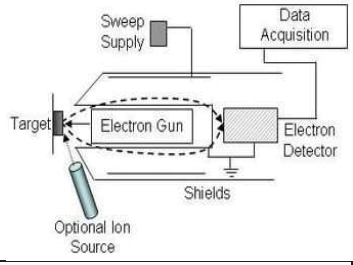	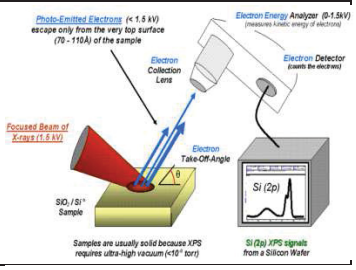
		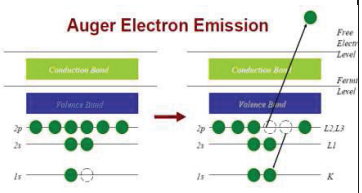	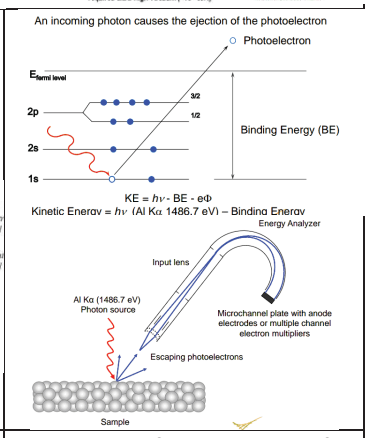
Advantage	Backscattered electrons help in obtaining morphology and the secondary electrons help in qualitative analysis	Combined with sputtering facility this canbe used to obtain depth profile	Possibility for extraction of detailed information about chemical, electronic state of compositional element
Limitations	! The applied voltage should be choosen carefully taking into account the properties of the material		Surface sensitive not useful in obtaining information from depth composition
Alternatives or Higher version	FESEM	SIMS	XAS

Appendix K. Further readings

- **Solid State Physics, *Charles Kittle***
- **Solid State Chemistry, *A R West***
- **Magnetism in Solids, *Derek. H. Martin*,** Cambridge: M.I.T. Press, [1967].
- **Laboratory Course Neutron Scattering Lectures, *Thomas Brückel, Gernot Heger, Dieter Richter, Georg Roth and Reiner Zorn(Editors)*,** RWTH Aachen University Münster.
- P. J. Webster and K. R. A. Ziebeck, "Heusler Alloys", in *Landolt-B_rnstein New Series Group III, Vol. 19C*, H. R. J. Wijn (Ed.) (Springer, Berlin, 1988) p. 75.

Remerciements

I like to express my sincere thanks to members of the jury Dr. Vincent HARDY, Dr. Olivier ISNARD and Dr. Philippe TAILHADES for their valuable suggestions, time and encouragement. I really appreciate their cooperation for agreeing to read the manuscript and to provide their report in shortest time. Special thanks for Dr Vincent for his fruitful discussions during different meetings and conferences.

"Patience, persistence and perspiration make an unbeatable combination for success" – Napoleon Hill. I would wish to express my deepest gratitude towards Dr. Olivier TOULEMONDE and Dr. Bernard CHEVALIER. For giving the opportunity to work with them which in deed lead to my doctoral degree. For their encouragement, keeping me motivated during the duration of the entire thesis. For their valuable guidance towards improvement of my scientific skills and also progress intellectually. I am moved by your humbleness and dedication towards science.

I like to acknowledge former director of ICMCB Claude Delmas for accepting my PhD candidature and present director Mario Maglione for continued support, as well as for his valuable scientific suggestions, time within his busy schedule.

I wish to acknowledge each person and institute involved on data acquisition and data treatment of all our neutron diffraction experiments specifically for their time, resource and scientific discussions. Namely, Dr Gwilherm Nénert (D20 & ID31), Dr Vivian NASSIF (D1B), Dr Emmanuelle SUARD (D2B) at Institut Laue-Langevin (ILL), Grenoble France. Dr Florence PORCHER (3T-2), Dr Gilles André (G4-1) at Laboratoire Léon Brillouin (LLB), Saclay, France. As well, Dr Vladimir Pomjakushin and Dr Denis Sheptyakov for data on HRPT located at Paul Scherrer Institute (PSI), Switzerland.

I like to acknowledge Dr Antoine Barnabe for high temperature xrd on Bruker D8 machine at Université Paul Sabatier, Institut Carnot CIRIMAT CNRS, Toulouse. Anna Llobet, Françoise DAMAY for quick discussions and for providing softcopy of the respective thesis. Etienne GAUDIN, Michaël POLLET, Sophie TENCE, Stéphane GORSSE at ICMCB for suggestions in specific topics.

I have my deep gratitude towards each person in Service collective of ICMCB for their assistance in different experiments and support : ***XRD*** *– Eric LEBRAUD, Stanislav PECHEV;* ***EPMA, Auger*** *– Michel LAHAYE;* ***Resistivity, Seeback*** *– Rodolphe DECOURT;* ***XPS*** *– Christine LABRUGERE ;* ***SQUID*** *– Olivier NGUYEN;* ***DSC, TGA*** *– Dominique DENUX;* ***ICP*** – Laetitia Etienne*;* ***Administration***; ***Cryogénie; Informatique; Bibliothèque; Hygiène et sécurité***

"The highest forms of understanding we can achieve are laughter and human compassion" Richard P. Feynman. One of the most excited experiences for me during my

stay was sweet relation of wonderful people with in ICMCB. Group 1(ancient) in particular was literally my home away home, I will cherish for rest of the life the hospitality and encouragement shown by every members of the group for last three years (group lunch, cycle trip(Rodolphe Decourt), countless apéro, as well group meetings – which stopped in midway unfortunately! ….). Nevertheless were all the members of ICMCB – petonque, journey doctoral are memories that I will remember forever. I also specially thank families of Dr Oliveir, Dr Aline, Dr Jean-Claude and Dr. Rodolphe for the kind and warm hospitality.

"The source of inspiration need not necessarily be searched in the woods; it mostly resides in the home" – anonymous. I would wish to felicitate Prof Jean-Claude GRENIER, Prof Claude DELMAS, Prof Bernard CHEVALIER, Prof Michel POUCHARD, Prof Jean ETOURNEAU and Prof Alain TRESSAUD for their individual contribution towards their respective field as well for inspiring young generation for decades through their words and action. I feel honored to have been able to have interacted even for shortest possible time.

"As we think, so we become! The thought manifests as the word; the word manifests as the deed. The deed develops into habit; and habit hardens into character. So watch the thought and its way with care" - Lord Buddha reads signature in every email of Prof A. Sundaresan, working at Jawaharlal Nehru Centre for Advanced Scientific Research, Bangalore, India. In 2005 just after couple of months of completion of my MSc (Physics) as I walked into his chamber with no experience or knowledge about research I was about to be encountered with questions on crystallography. By end of rather average interview he said, "It is clear you have no experience in research, but, I will give you chance and you need to prove yourself". It turned out it was not just chance but, he trained me in solid-state chemistry (which I had left three years back then), thinfilms and also hands on then booming nano-science. I thank him for that 'chance' and his constant support thereafter; it means a lot for me. I would wish to thank all nice people that I come across during my stay there, Dr M. Eswaramoorthy, my friends KKR Datta, Rajashekaraih, Gurunatha, Vengadesh, Pranab, Shipra, Gomathi, list never ends. I also like to thank my previous supervisor and labmates - Dr Mani, Brandon, Mike, Josh, Tanja, Kausik, Anish, and Rishi at Colorado State University, Fort Collins for making my stay a memorable one.

It is worth quoting famous words of Richard Feynman, "There's Plenty of Room at the Bottom", at Caltech, 1959.

Thank you for all the help during arc melting experiments, ***"Rest in Peace"*** - Joël VILLOT

Resumé

La réfrigération magnétique attire beaucoup d'attention ces dernières années parce qu'elle est considérée comme une technologie respectueuse de l'environnement et énergétiquement efficace. Aujourd'hui, cette technologie avancée est encore en phase de recherche que des dispositifs de réfrigérations magnétiques soient déjà opérationnels. Ce travail de thèse consiste à étudier la potentialité de résistance à la corrosion de différents types de matériaux magnétocaloriques ($Gd_6Co_{1.67}Si_3$, $Ni_2Mn_{0.75}Cu_{0.25}Ga$ et $Pr_{0.66}Sr_{0.34}MnO_3$) en contact avec un fluide caloporteur. Afin de comprendre les propriétés magnétocaloriques des matériaux, nos recherches se sont aussi focalisées sur les relations entre la transition magnéto-structurales d'alliages Heusler $Ni_2Mn_{0.75}Cu_{0.25}Ga$ et (i) la distribution cationique au sein de la structure cristalline et/ou (ii) la microstructure. Finalement, le diagramme de phase magnétique et nucléaire en lien avec les effets magnétocalorique obtenu grâce à la diffraction de neutrons et de pérovskite $Pr_{1-x}Sr_xMnO_3$ ($0.25 \leq x \leq 0.45$) est également présenté.

Abstract

Magnetic refrigeration has gained lot of importance and attention as they are highlighted to be environmental friendly, energy efficient. Presently, though at research stage, the magnetic refrigerators are pushed towards realization in domestic application with extensive work on materials and with few working models. One critical issue, the potential resistance to corrosion in case of different class of magnetocaloric materials ($Gd_6Co_{1.67}Si_3$, $Ni_2Mn_{0.75}Cu_{0.25}Ga$ and $Pr_{0.66}Sr_{0.34}MnO_3$) against the heat transport fluid is addressed. To better understand and improve the observed magnetocaloric properties in Heulser alloys $Ni_2Mn_{0.75}Cu_{0.25}Ga$ and to elaborate the same with the magneto-structural relation, studies on (i) cation distribution with in crystal structure and/or (ii) microstructural dependence are presented. Nuclear and magnetic phase diagram based on detailed neutron diffraction and magnetism studies for magnetocaloric perovskite oxide $Pr_{1-x}Sr_xMnO_3$ ($0.25 \leq x \leq 0.45$) is also presented.

Keywords: Magnetocaloric effect, magnetic refrigeration, magnetocaloric materials, first and second order transition, Magneto-structural relation, corrosion, ageing, spontaneous electrochemical oxidation, Heusler alloys, perovskite manganite, Nuclear-magnetic phase diagram.